UNIVERSITY OF SOUTHAMPTON

Faculty of Social Sciences
School of Mathematical Sciences

Gravitational Radiation and the formation of Neutron Star Thermo-elastic Mountains

by

Thomas James Hutchins

ORCiD: 0000-0001-8185-665X

A thesis for the degree of
Doctor of Philosophy

May 2024

University of Southampton

Abstract

Faculty of Social Sciences
School of Mathematical Sciences

Doctor of Philosophy

Gravitational Radiation and the formation of Neutron Star Thermo-elastic Mountains

by Thomas James Hutchins

Advancing sensitivity of LIGO-Virgo-KAGRA gravitational-wave instruments has led to much anticipation for the first detection of quasi-monochromatic continuous gravitational radiation from single, rapidly rotating neutron stars. This thesis is concerned with one specific scenario to facilitate gravitational radiation from such stars: the development of a non-axisymmetric quadrupolar deformation of the solid crust. In accreting systems in particular, deformations may manifest as so-called '*thermal mountains*'; whereby the mass distortion is supported by elastic strains sourced via large-scale non-axisymmetric temperature gradients misaligned from the star's rotation axis.

In this work we present for the first time a fully self-consistent calculation of the size of neutron star thermal mountains. In doing so, we will introduce a new class of deformations that we term '*thermo-elastic*' mountains, in which we consider different sources of temperature-dependence in the crustal equation of state than the conventional picture of the so-called 'wavy electron capture layer'. Over the course of this thesis, we shall present a scheme to develop a mechanism to source a temperature perturbation in the accreted crust, compute the associated density perturbations, and calculate the resultant mass quadrupole moment.

Models of the hydrostatic structure of spherically-symmetric accreting neutron stars are constructed using realistic equations of state. The thermal structure of these stars is then computed, assuming them to be accreting steadily. Temperature perturbations are subsequently introduced onto the homogeneous background via the insertion of a weak internal quadrupolar magnetic field, restricting the flow of heat orthogonal to the field lines and establishing a non-axisymmetric temperature distribution within the star. Such a calculation requires a detailed description of relevant heat generation, neutrino cooling, and heat transport mechanisms, each of which are discussed. The elastic readjustment of the crust in response to the aforementioned temperature asymmetry is then calculated. A piece of the crustal pressure that is generated by the ionic lattice is identified, and shown to have some temperature dependence. Perturbations of this 'thermal lattice pressure' are necessarily tied to the star's elastic phase, and not easily convected away. We find that the mountains sustained by the lattice in response to anisotropic heat conduction are small, and unlikely to be dictating the spin-equilibrium of rapidly rotating neutron stars, but may still be playing a contributory role in determining the long-term spin-evolution of accreting systems.

Contents

3 Gravitational-waves from Thermal Mountains 59

4 Thermal Structure of Accreting Neutron Stars 75

List of Figures

List of Tables

Declaration of Authorship

I declare that this thesis and the work presented in it is my own and has been generated by me as the result of my own original research.

I confirm that:

1. This work was done wholly or mainly while in candidature for a research degree at this University;
2. Where any part of this thesis has previously been submitted for a degree or any other qualification at this University or any other institution, this has been clearly stated;
3. Where I have consulted the published work of others, this is always clearly attributed;
4. Where I have quoted from the work of others, the source is always given. With the exception of such quotations, this thesis is entirely my own work;
5. I have acknowledged all main sources of help;
6. Where the thesis is based on work done by myself jointly with others, I have made clear exactly what was done by others and what I have contributed myself;
7. Parts of this work have been published in Hutchins and Jones (2023):
   - Chapter 2: Section 2.5.1
   - Chapter 3: Section 3.2.2.1.1
   - Chapter 4: Sections 4.7.1; 4.8
   - Chapter 5: Sections 5.1; 5.2; 5.3; 5.4; 5.5; 5.6
   - Chapter 7: Sections 7.1; 7.3.1; 7.3.2

Signed:

Date: 03/05/2024

Acknowledgements

It should be no secret that the task of completing of this Ph.D would have been made impossible without the unwavering support of those around me. Throughout this journey, help has come in many ways; from those who have directly contributed to my development as a scientist, to those who have simply provided a welcome respite from any and all matters relating to neutron stars. Most fortuitously, my gratitude for distractions extends even so far as my neighbour's cat, Autumn, who, as I write these very words, has climbed through my window and onto my desk.

First and foremost, I would like to thank my supervisor, Ian Jones, for his endless support and guidance over the past four years. His friendly, welcoming approach to all his students allowed me to ask questions without hesitation, and regardless of triviality. Even after the fourth tap on his office door of the afternoon (something which I am sure happened on more than one occasion), he would always turn around with a smile, eager to help solve my latest problem. Certainly I could not have asked for a kinder and more knowledgeable mentor.

I would also like to thank all of those who have passed over the desks of Office 54/2019 during my tenure; Oliver Long, Alex Wright, Garvin Yim, Marcus Hatton, and Shanshan Yin. Alex, as well as Andrei Donko, were always available to fill the snooker-shaped void in my afternoons. Never was the suggestion of 'a few frames' to be turned down lightly.

With the outbreak of the COVID-19 virus closing the world down only a few months into my Ph.D, I would also like to recognize the continued support of friends from before my time at Southampton. I'd like to thank them for keeping me sane through the lockdowns. George Gill, for all of the evenings of online chess - which, with the help of a little wine, was always of a calibre that would make even a child wince; Luke Romeo, for seemingly endless nights spent dropping into Verdansk (the days of the DMR meta will be sorely missed); and Beni Hofmann, for letting me keep you up to date with my flat-sharing escapades. I would also like to thank Oliver Long (again), Patrick Buck, Elliot Thomas, and Charlie Lyth for all the games of Among Us during the pandemic - I was never the imposter, honest.

These acknowledgments can also not be complete without paying a special thank you to my dearest, Emma Weston, who made emerging from post-isolation better than I ever could possibly have anticipated. For all the adventures we have taken together, from the Roman Colosseum to the Alpine peaks of Rochers-de-Nayes, the time we've spent together has been very precious to me, and I am incredibly grateful to have her in my life.

Finally, I owe an eternal debt of gratitude to my parents, Ian and Alison, for supporting me through all my many endeavours. Though they often comment my work is of 'another language', for all they have done for me, a part of this thesis will forever be theirs.

Notation and Conventions

Before we begin, we will briefly outline a number of general notation rules and conventions that pertain to any and all subsequent symbols, definitions, and calculations of physical quantities. This serves to reduce ambiguity, as well as reduce the need for repetition of said conventions in subsequent chapters. A list of acronyms is also provided, which also serves to avoid repetition of common phrases, as well as frequently cited works.

Indices

Spacetime indices run from 0 to 3 and are denoted by ‘early’ Latin letters in *italic* typeset, e.g. a, b, c, ... etc. Spatial indices on the other hand run from 1 to 3 and are denoted by the ‘late’ Latin letters (also in *italic* typeset) i, j, k ... etc.

As is customary in the *theory of general relativity*, we shall adopt the Einstein summation convention. For any arbitrary four-vector u^a or three-vector v^i, repeated indices are assumed to imply a summation over all possible values of said index, i.e.

$$u^a u_a = \sum_{a=0}^{3} u^a u_a = u_0 u^0 + u_1 u^1 + u_2 u^2 + u_3 u^3 \,,$$

$$v^i v_i = \sum_{i=1}^{3} v^i v_i = +v_1 v^1 + v_2 v^2 + v_3 v^3 \,.$$

There is a fundamental distinction between raised and lowered indices, which determines the covariance and contravariance of the vector. Consider, for example, the four-vector u^a. To obtain the covector u_a, one need contract with the space-time metric g_{ab}, such that

$$g_{ab} u^b = u_a \,.$$

Similarly, contracting the covector u_a with the *inverse* metric g^{ab} gives a vector

$$g^{ab} u_b = u^a \,.$$

As a matter of choice, the signature of the space-time metric g_{ab} is taken to be $(-,+,+,+)$, leading to time-like four-vectors having negative lengths.

Latin and Greek indices in a roman typeset, e.g. n, p, e, ... etc. are constituent indices. They are placed either 'upstairs' or 'downstairs' at convenience and do not conform to any type of summation convention.

Covariant and partial derivatives

The covariant derivative is a generalization of the gradient operator of conventional vector calculus. Covariant derivatives with respect to some coordinate basis x^a are written as ∇_a. In much of this work we shall specialise to spherical polar coordinates (see Fig. 1), where, for example $x^a = (t, r, \theta, \varphi)$, with $x^t = t, ...$ etc.

For an arbitrary scalar quantity f, the covariant derivative reduces to just the partial derivative for scalars, i.e. $\nabla_a f = \partial_a f$. For brevity, we may sometimes write down radial derivatives with a prime, e.g. $f' = \partial_r f$, and occasionally write down temporal derivatives with a dot, i.e. $\dot{f} = \partial_t f$.

Spherical Harmonics

One exception to the rule of italic Latin indices are the symbols ℓ and m, which are reserved solely to denote the degree and order of the spherical harmonics $Y_{\ell m}(\theta, \varphi)$. Spherical harmonics are a set of special functions that are defined on the surface of a sphere. In Euclidean flat-space, the spherical harmonics appear as solutions to *Laplace's equation*. Laplace's equation requires that the Laplacian (∇^2) of an arbitrary scalar field f is zero.

The multipole expansion of any *scalar* function f may be written as

$$f(r, \theta, \varphi) = \sum_{\ell=0}^{\infty} \sum_{m=-\ell}^{\ell} f_{\ell m}(r) Y_{\ell m}(\theta, \varphi) .$$

Similarly, any arbitrary *vector* field also admits a multipole expansion. Vector spherical harmonics are an extension of the scalar spherical harmonics, and may be written

$$\begin{aligned}
\mathbf{Y}_{\ell m} &= Y_{\ell m} \hat{\mathbf{r}} , \\
\boldsymbol{\Psi}_{\ell m} &= r \nabla Y_{\ell m} , \\
\boldsymbol{\Phi}_{\ell m} &= \mathbf{r} \times \nabla Y_{\ell m} ,
\end{aligned}$$

where $\hat{\mathbf{r}}$ is the radial unit vector in spherical polar coordinates and $\mathbf{r}$ is the vector along the radial direction defined as $\mathbf{r} = r\hat{\mathbf{r}}$.

The multipole expansion of any vector field F may be written as

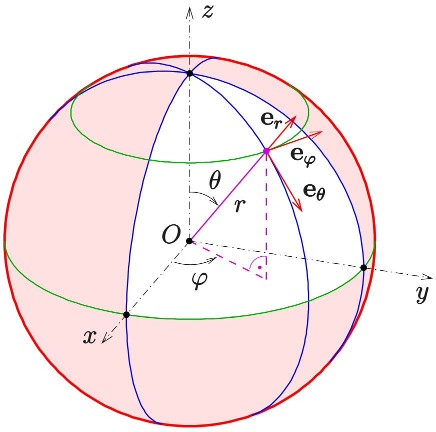

FIGURE 1: Representation of the spherical polar coordinate system with unit vectors $\mathbf{e}_r$, $\mathbf{e}_\theta$ and $\mathbf{e}_\varphi$. The variable r represents the distance from the origin, θ is the polar angle, and φ is the angle of longitude (azimuthal angle). Image credit: Wikipedia, author Ag2gaeh.

$$F = \sum_{\ell=0}^{\infty} \sum_{m=-\ell}^{\ell} \left(U_{\ell m}(r) \mathbf{Y}_{\ell m} + V_{\ell m}(r) \mathbf{\Psi}_{\ell m} + W_{\ell m}(r) \mathbf{\Phi}_{\ell m} \right),$$

where $U_{\ell m}(r)$ is the radial component of the vector field, while $V_{\ell m}(r)$ and $W_{\ell m}(r)$ represent its transverse components (with respect to $\mathbf{r}$).

Acronyms

AC Accreted crust.
AMXP Accreting millisecond X-ray pulsar.

CPBF Cooper pair breaking and formation.

DCH Deep crustal heating.
Durca Direct URCA.

EDF Energy-density functional.
EoS Equation of state.

F+18 Fantina et al. (2018).

GC Ground state crust.
GC20 Gusakov and Chugunov (2020).
GR General relativity.
GRB Gamma-ray burst.
GS Ground state.
GW Gravitational-wave.

HM High-mass.
HZ08 Haensel and Zdunik (2008).
HZ90 Haensel and Zdunik (1990a).

LIGO Laser Interferometer Gravitational-Wave Observatory.
LM Low-mass.
LMXB Low-mass X-ray binary.

Murca Modified URCA.

NS Neutron star.

OCP One-component Plasma.
ODE Ordinary differential equation.
OJ20 Osborne and Jones (2020).

SCH Shallow crustal heating.

TOV Tolmann-Oppenheimer-Volkoff equation.

UCB Ushomirsky et al. (2000).
ULX Ultraluminous X-ray source.

VSH Vector spherical harmonic.

Nomenclature

Physical Constants

c	Speed of light in a vacuum	$2.997\,924\,58 \times 10^{10}\,\mathrm{cm\,s^{-1}}$
h	Planck constant	$6.62607015 \times 10^{-27}\ \mathrm{erg\,s}$
$\hbar$	Reduced Planck constant	$1.05457266 \times 10^{-27}\ \mathrm{erg\,s}$
G	Newtonian Gravitational constant	$6.67430 \times 10^{-8}\ \mathrm{cm^3\,g^{-1}\,s^{-2}}$
e	Elementary charge	$4.8032047 \times 10^{-10}\ \mathrm{cm^{3/2}\,g^{1/2}\,s^{-1}}$
k_B	Boltzmann constant	$1.380649 \times 10^{-16}\ \mathrm{erg\,K^{-1}}$
σ	Stefan-Boltzmann constant	$5.6704 \times 10^{-5}\ \mathrm{g\,s^{-3}K^{-4}}$
m_{b}	Baryon mass	$1.67377585 \times 10^{-24}\ \mathrm{g}$
m_μ	Muon mass	$1.8835327 \times 10^{-25}\ \mathrm{g}$
m_{e}	Electron mass	$9.1093897 \times 10^{-28}\ \mathrm{g}$
ρ_0	Nuclear saturation mass density	$2.8 \times 10^{14}\ \mathrm{g\,cm^3}$
n_0	Nuclear saturation density	$0.16\ \mathrm{fm^{-3}}$
α	Fine-structure constant	7.297352×10^{-3}
G_F	Fermi weak interaction constant	$1.496 \times 10^{49}\ \mathrm{erg\,cm^3}$

Astronomical Units

$M_\odot$	Solar mass	$1.9891 \times 10^{33}\ \mathrm{g}$
$\dot{M}$	Eddington accretion rate	$2 \times 10^{-8}\ \mathrm{M_\odot\,yr^{-1}}$
pc	Parsec	$3.08567758 \times 10^{18}\ \mathrm{cm}$
yr	Year	$3.156 \times 10^{7}\ \mathrm{s}$
erg		$1\ \mathrm{cm^2\,g\,s^{-2}}$

1

Motivation

This thesis begins with a characterisation of the phenomenon of gravitational-waves (GWs), with a specific focus on the role that rotating neutron stars (NSs) play in their creation. Section 1.2 presents scenarios in which these stars may generate different types of gravitational radiation, followed in Section 1.3 with a review of different potential sources of *continuous* gravitational radiation from rotating NSs, known as pulsars. In Section 1.4 we shall then present an outline of what is to come in the remainder of the thesis.

1.1 Introduction: A brief history

Gravitation is one of the four fundamental interactions that describe our Universe (alongside the electromagnetic, strong, and weak interactions). The field equations of the *general theory of relativity*, derived by Albert Einstein over a century ago, represents a defining moment in our understanding of gravitational theory. This seminal work (Einstein, 1915a,b,c)[1] superseded the long-standing interpretation held by Sir Isaac Newton in his *Philosophiae Naturalis Principia Mathematica* that gravity manifests as the geometry of a curved, four-dimensional spacetime, rather than as a physical 'force'.

The sophistication of general relativity (GR) predicts a number of more subtle effects of gravity than we experience in our day-to-day lives here on planet Earth. Indeed, to further understand his theory, Einstein himself proposed three initial tests (Einstein, 1915d) which would establish observational evidence for his theoretical predictions. These tests were:

- i) the 'anomalous' precession of the perihelion of Mercury,
- ii) the bending of light in gravitational fields,

---

[1] English translation of these works may be found here: `https://einsteinrelativelyeasy.com/index.php/einstein/83-the-einstein-field-equations-series`.

- iii) gravitational redshifting.

By the end of 1954, each of these tests had been successfully verified (see e.g. Bambi, 2018), leading to further probes of the theory in the so-called ‘weak-field limit’, and beyond.

Soon after the initial publications, Einstein posited the existence of *gravitational-waves*, a gravitational analogue of electromagnetic waves. This idea was not unique to Einstein, though, having been first discussed by Heaviside (1893), and later by Poincaré (1905)[2], who also proposed that gravity might be transmitted as a ‘wave’. Einstein, was, however, the first to write down the potential existence of these waves through the mathematical framework of GR.

The reception to this conjecture, however, was met with varied criticism - not least by Einstein himself who doubted the legitimacy of his own proposal - and the question of the existence of GWs would plague the relativity community for decades. Einstein had, for a time, believed he had found a solution to his field equations that predicted three different kinds of GWs. Yet, soon after, Eddington argued that two of these waves were simply ‘geometric artifacts’ of the coordinate system Einstein had used and not really waves at all (Eddington, 1922). Later, in 1936, Einstein wrote to Max Born claiming

> ”*I arrive at the interesting result that gravitational-waves do not exist, though they have been assumed a certainty to the first approximation*”.

The issue of the legitimacy of these waves would not be settled until Felix Pirani used the coordinate-independent Riemann curvature tensor to prove their existence (Pirani, 1956). A year later, at the Chapel Hill conference in North Carolina, Pirani went on further to argue the *physical* significance of such waves, postulating that a pair of freely falling particles subjected to a GW would experience genuine motions with respect to one another.

The outcome of the Chapel Hill conference would be to unite the relativity community in agreement of the *theoretical* existence of GWs. Yet, proving their existence *experimentally* was a much more challenging prospect. Compared to the other three fundamental interactions, gravitation is very much the ‘weakest’, particularly at the atomic scale. Gravitational-waves interact with matter so weakly that only the most cataclysmic of astrophysical events are likely to produce gravitational radiation at a level where one might hope to detect them.

It would in fact not be too long before the first detection of GWs would be announced by Joseph Weber. Resonant-mass bar detectors - large cylinders of aluminium (roughly one meter thick and two meters in length) - were purported to act as GW antennae (Weber, 1969). In the presence of passing GWs, these ‘Weber bars’ would (theoretically) ring out, akin to an oversized tuning fork. Weber asserted that the probability of false-detection was ‘incredibly small’. Yet, other

---

[2] English translation available here: `https://en.wikisource.org/wiki/Translation:On_the_Dynamics_of_the_Electron_(July)`.

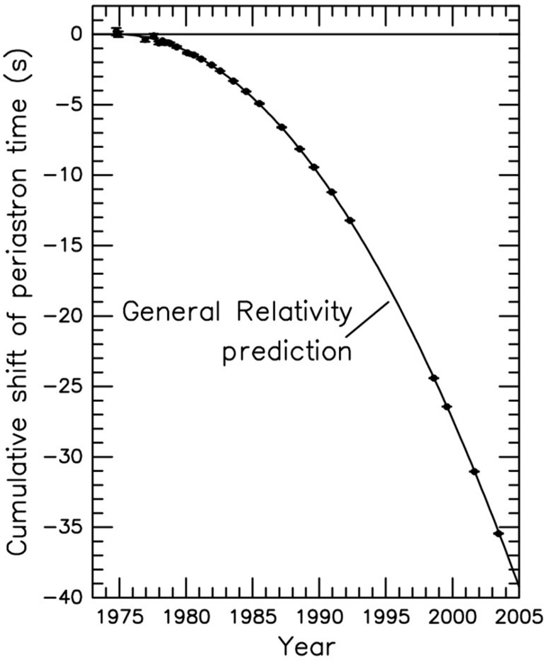

FIGURE 1.1: The observed orbital decay of the Hulse-Taylor pulsar (PSR B1913+16). Data points indicate the *observed* change in the epoch of periastron in time, whilst the curve indicates the equivalent *theoretical* change in epoch due to the emission of gravitational-waves. Image credit: reproduced from Weisberg and Taylor (2004).

independent groups at the time failed to replicate Weber's results with similar equipment, and the claim would ultimately fall into disrepute.

The existence of GWs in Nature would instead be first demonstrated *indirectly*, following the discovery of the Hulse-Taylor binary pulsar system PSR B1913+16 (Hulse and Taylor, 1975). Monitoring of the system over several years showed an incredible agreement between the observed change in the epoch of periastron of the system over time, and the theoretically expected change predicted by GR due to the loss of energy and angular momentum from the system through gravitational radiation (Taylor et al., 1979; Taylor and Weisberg, 1982), as shown in Fig. 1.1.

This indirect 'confirmation' led to a fever of excitement amongst the community, and shortly afterwards proposals for long-baseline broadband laser interferometers began to surface. Among them, the **L**aser **I**nterferometer **G**ravitational-Wave **O**bservatory (LIGO) group emerged by the end of the 20th century as the first group to most likely to experimentally verify their existence.

Indeed, on the 14th September 2015, after a century of painstaking theoretical (and experimental!) turmoil, LIGO made scientific history. The twin H1 and L1 detectors, located in Hanford, Washington and Livingston, Louisiana in the United States respectively observed a GW signal that matched extraordinarily well the waveforms predicted by GR for the inspiral and merger of two orbiting black holes (Abbott et al., 2016c). The signal, dubbed *GW150914* lasted ~ 0.2 seconds and had a peak strain in the H1 and L1 detectors of $\sim 10^{-21}$ (see Fig. 1.2). The passing of the GW resulted in a fractional change in the lengths of the two 4km arms of the LIGO

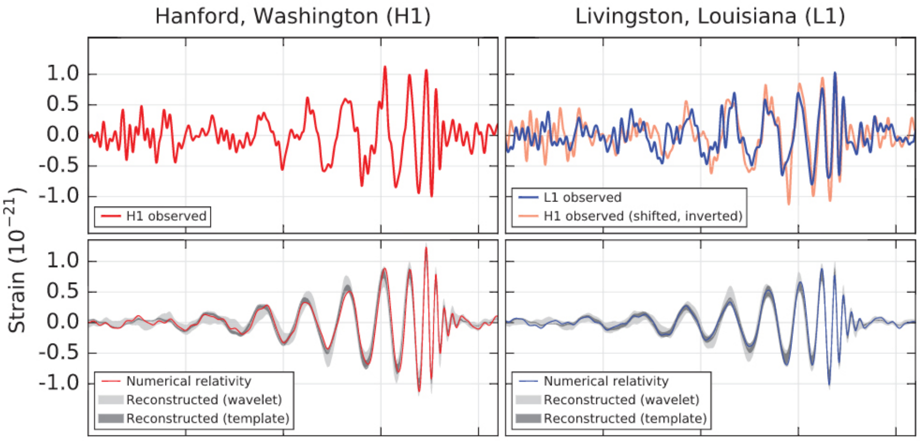

FIGURE 1.2: The landmark gravitational-wave event GW150914 as observed by the LIGO Hanford (H1, left column panels) and Livingston (L1, right column panels) interferometers. The top panels show the strain data in the H1 and L1 detectors. The bottom panels show the gravitational-wave strain projected onto each detector in the 35 – 350 Hz band. The solid red (*left*) and solid blue (*right*) lines indicate a numerical relativity waveform for a system with parameters consistent with those recovered from GW150914 (Mroué et al., 2013). The dark grey shaded regions show models of the signal using binary black hole template waveforms (Abbott et al., 2016b). The light gray shaded regions show models that do not use an astrophysical model, but instead calculates the strain signal as a linear combination of sine-Gaussian wavelets (Cornish and Littenberg, 2015; Abbott et al., 2016a). Image credit: adapted from Figure 1 of Abbott et al. (2016c).

interferometers of the order 10^{-18} m, a thousandth the width of a single proton. To put such a feat into perspective, it was equivalent to measuring a change in the distance to the nearest star outside our Solar System (40,208,000,000,000 km), Proxima Centauri, by just the width of a single hair. Enter, the modern era of *gravitational-wave astronomy*.

The 'advanced' interferometers have completed three observing runs to-date, with the collaboration fast approaching its 100th detection of a GW signal. Within this exhaustive catalog, on the 17th August 2017, a particularly exceptional event occurred. Within a few seconds of an initial gravitational-wave trigger, the Gamma-ray Burst Monitor atop NASA's Fermi space telescope detected a burst of γ-rays. At the time, the origin of short γ-ray bursts (GRBs) had remained a mystery, but now it appeared that the answer to this question may lie buried deep within the data of the twin LIGO interferometers.

This signal, since dubbed *GW170817* was quite unlike any other that had been seen in the detectors up to that point. Binary black hole mergers produce what is commonly referred to as a 'chirp' in a small region of the detector's sensitivity band ($\sim 50-350$ Hz), lasting a fraction of a single second (see the right-column panels in Fig. 1.3). In the case of GW170817, however, the 'chirp' lasted $\sim$ 100 seconds, sweeping through a greater frequency range of detector's sensitivity band (see the left-column panels in Fig. 1.3). Initial matched-filtering of the signal against a bank of theoretical waveforms suggested that the masses of the progenitors were likely too small to be black holes, and instead in the range of another type of compact object - two *neutron stars* (Abbott et al., 2017b). It had been suspected for decades that GRBs might be powered by the

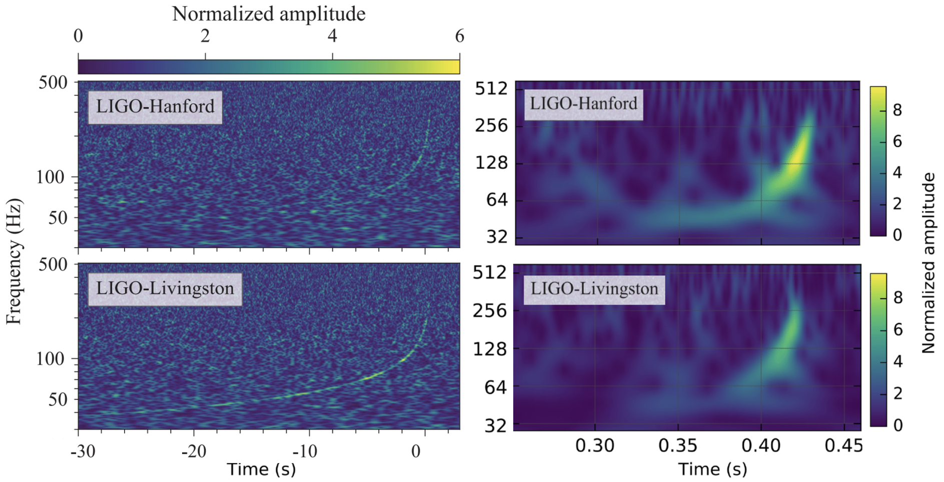

FIGURE 1.3: Time-frequency plots as observed by the LIGO Hanford (H1, left column panels) and Livingston (L1, right column panels) interferometers. The top panels show data containing GW170817 in the H1 and L1 detectors. The bottom panels show the data containing GW150914 in the H1 and L1 detectors. Image credit: adapted from Figure 1 of Abbott et al. (2017b) and Figure 1 of Abbott et al. (2016c).

collisions of NSs (Blinnikov et al., 1984; Eichler et al., 1989; Berger et al., 2013), and thus the near-simultaneous temporal and spatial observations of the GW trigger and GRB appeared to be conclusive proof (Abbott et al., 2017c).

The detection of GW170817 also benefited from the incorporation of the 'Virgo' GW interferometer, hosted by the European Gravitational Observatory and located in Pisa, Italy, that joined the LIGO network just two weeks before the detection was made. Though less sensitive than either L1 or H1, improved sky localisation of the signal allowed it to be pinpointed to have originated from the galaxy NGC 4993. In the days following the initial GW and GRB trigger, a host of observations across the electromagnetic spectrum from radio to X-rays were made from the galaxy. Such detections were unprecedented, with the marriage of gravitational *and* conventional astronomy spawning a new era of *multi-messenger astronomy*.

The union of gravitational and electromagnetic astronomy has facilitated a number of significant scientific breakthroughs since GW170817, underlining the importance that NSs have to play in advancing our understanding of a host of different astronomical phenomena. Such examples include providing an independent method to estimate the Hubble Constant (Abbott et al., 2017a, 2023); placing constraints on the equation of state of dense matter (e.g. Abbott et al., 2018); providing further probes of fundamental aspects of GR, including Lorentz invariance and the equivalence principle (Abbott et al., 2017c); as well as identifying that NSs are Nature's very own alchemists, with merger events now thought to be responsible for producing the majority of the Universe's precious metals (Kasen et al., 2017).

A further milestone of the collaboration would be achieved during the third observing run (O3), coinciding with the additional incorporation of the Japanese 'KAGRA' GW interferometer into the LIGO-Virgo network. In January 2020, during the first half of O3, two neutron star-black

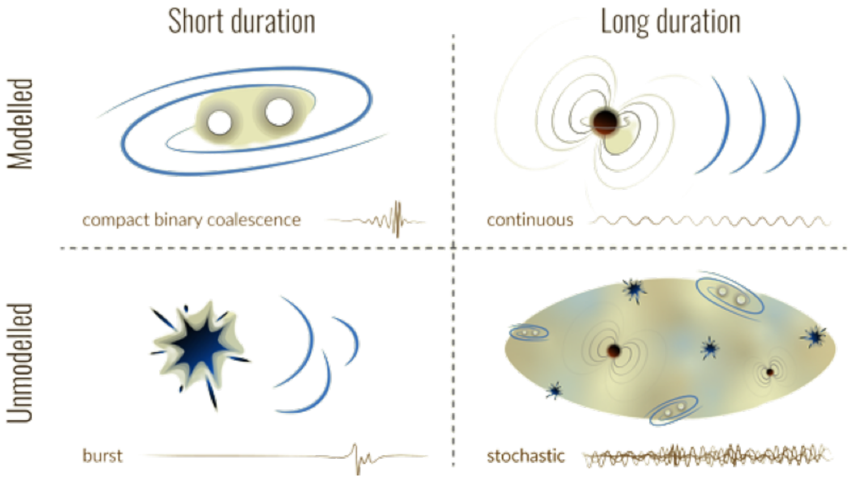

FIGURE 1.4: Graphic displaying the different types of gravitational-wave emission thought to be produced in the Universe, together with the associated signal that would likely be seen in the LIGO-Virgo-KAGRA detectors. Modelled sources (i.e. transient and continuous) are those that have specific mechanisms which generate them. Image credit: adapted from Shanika Galaudage.

hole collisions were observed just 10 days apart (Abbott et al., 2021a). With the fourth observing run currently underway at the time of writing, detections of binary mergers are becoming all but too frequent, owing to continuing advancements in the sensitivity of the instruments. Amongst all these successes, there is now much anticipation for the first detection of a GW signal that originates from something other than compact binary coalescence. If this does indeed occur, then it is likely that neutron stars will have some role to play in its discovery.

1.2 Types of gravitational-wave emission

In principle, any accelerating source of matter will produce gravitational radiation. This means that we humans, our cars, planes, etc. generate GWs to some degree. It is just the case however that they are *far* too small to be seen through the eyes of any detectors. To find ones that aren't, one must look beyond the Earth, and as we saw from the last section, even beyond the solar system.

Broadly speaking, there are four categories of GW signal that any accelerating massive object will fall into. These are: *Transient*, *Continuous*, *Stochastic* and *Burst*. A graphic displaying potential sources of these types of emission is shown in Fig. 1.4, as well as example illustrations of the associated signal that would be seen in the LIGO-Virgo-KAGRA detectors.

Neutron stars in particular are unique objects in the context of GWs in the sense that they possess (at least in theory) the ability to facilitate each of these types of emission, as we shall now discuss.

1.2.1 Transient gravitational-waves

Of the almost 100 signals detected thus far by LIGO-Virgo-KAGRA, each one has been an example of *transient gravitational-waves*; a class of powerful, short-lived signals generated as a result of the inspiral and merger of compact objects such as black holes and NSs. So far, three types of compact binary systems have been observed - binary black hole, binary neutron star, and neutron star - black hole binaries (Fig. 1.5).

In reference to Fig. 1.2, there are three distinct phases of a transient GW signal. The inspiral, the merger, and the so-called 'ringdown'. During inspiral, the orbit of the binary gradually shrinks as the system loses angular momentum to the emission of GWs. This process of emitting GWs and orbiting closer and closer leads to an irreversible, runaway spiraling of the two objects until, eventually, they collide and merge.

The aftermath of the collision depends on the nature of the progenitors. For example, two orbiting NSs may form a heavier neutron star after they collide. Or, perhaps more likely, a black hole is formed after the collision. The emitted GWs are strongest during the merger, but what remains, in the case of a black hole remnant, is one that very distorted. Similar to a struck bell, the distortions of the black hole are quickly radiated away as further GWs (hence the term 'ringdown'), leaving behind a stable black hole in the aftermath.

Each binary system has its own unique GW signature, determined by a range of different parameters. These include (amongst others) the mass of the progenitors, their spins, and their orientations[3]. Generally speaking, a more-massive black hole binary will move through its final inspiral phase much more rapidly than less-massive NSs. This leads to a much shorter merger signal for a binary black hole system than that of a binary neutron star system (recall Fig. 1.3).

1.2.2 Continuous gravitational-waves

A stark contrast to transient signals are *continuous gravitational-waves*, a class of long-lived, quasi-monochromatic signals (that will in fact form the focal point of this thesis). Sources of continuous GWs produce considerably weaker signals that vary in both amplitude and frequency over much longer timescales than transient signals. This type of emission is yet to be detected, but is thought to be most likely sourced by singular, rapidly spinning compact objects - neutron stars. Much like a singer holding a single note, if the spin-rate of the NS is constant, then any GWs that are emitted will do so *continuously* at some multiple[4] of the spin-frequency.

---

[3] A circular binary of two point objects is usually described by a fifteen-dimensional parameter vector $\vec{\lambda} = \{\mathcal{M}, \eta, d_{\rm L}, t_{\rm c}, \phi_{\rm c}, \alpha, \delta_{\rm d}, l, \phi_{\rm p}, a_{\rm spin1}, \theta_{\rm spin1}, \phi_{\rm spin1}, a_{\rm spin2}, \theta_{\rm spin2}, \phi_{\rm spin2}\}$, where $\mathcal{M}$ is the chirp mass, η is the symmetric mass ratio, $d_{\rm L}$ is the luminosity distance to the source; $\phi_{\rm c}$ is an integration constant that defines the phase of the GW at time $t_{\rm c}$ of coalescence, α and $\delta_{\rm d}$ are the right ascension and declination of the source which determines its position in the sky; l defines the inclination of the binary with respect to the line of sight; and $\phi_{\rm p}$ is the polarisation angle of the waveform. The quantities $a_{\rm spin1,2}$ are dimensionless spin magnitudes, and $\theta_{\rm spin1,2}$, $\phi_{\rm spin1,2}$ are the angles of their orientations (Raymond, 2012).

[4] This multiple depends on the mechanism which sources it, and will be discussed in Section 1.3.

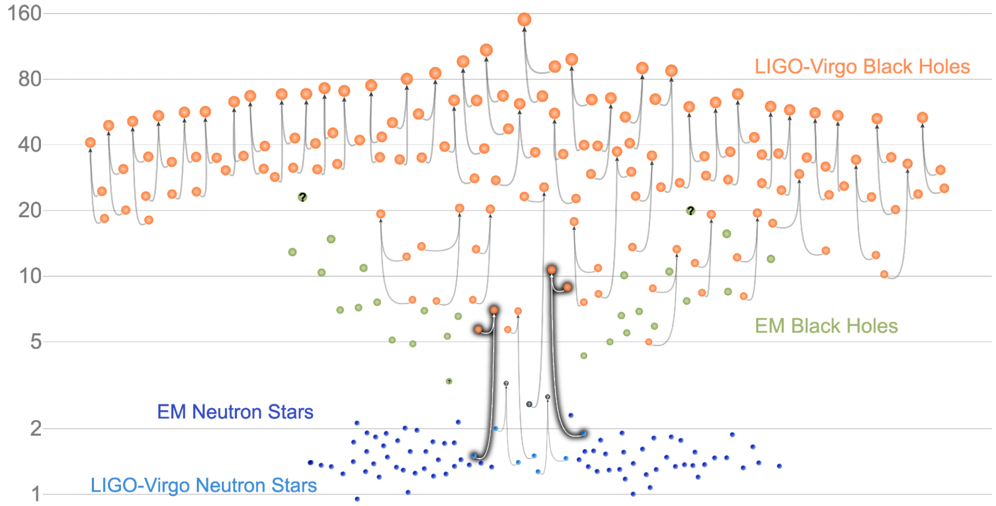

FIGURE 1.5: Graphic displaying the masses (in solar units) of compact objects in the 'Stellar Graveyard'. Black holes measured by gravitational-wave observations are marked in orange, whilst black holes detected through electromagnetic observations are marked in green. Neutron stars measured with electromagnetic observations are given in dark blue, and masses of neutron stars measured from gravitational-wave observations are labelled in light blue. Two neutron star - black hole mergers are highlighted with shaded arrows. Image credit: adapted from LIGO-Virgo/Aaron Geller/Northwestern

For a NS to generate continuous gravitational radiation, it must develop, and sustain, some form of axial asymmetry. There are a number of different candidate mechanisms thought to be able to generate the required asymmetry, including:

- i) fluid instabilities (particularly the excitation of the inertial r-mode) - Section 1.3.1;
- ii) free precession - Section 1.3.2;
- iii) non-axisymmetric quadrupolar deformations - Section 1.3.3.

1.2.3 Stochastic gravitational-waves

Unlike the two previous categories, *stochastic gravitational-waves* are not thought to be generated from any one event or mechanism in particular. It is likely, for example, that many rapidly spinning, non-axisymmetric NSs exist in the cosmos, but the vast majority of these stars will produce GWs that are much too small to be seen individually. Relatively speaking, it is expected that there are few *significant* sources of either transient or continuous GWs that might be singularly identified. Instead, a 'stochastic background', formed through the culmination of numerous *individually-undetectable* GWs, all mixed together at random (hence stochastic), therefore likely permeates the Universe.

Very recently, the **N**orth **A**merican **N**anohertz **O**bservatory for Gravitational Waves (NANOGrav) collaboration published evidence for a stochastic background of extremely low frequency GWs (i.e. with periods of years to decades; Agazie et al., 2023a). As part of a 15-year data release, the NANOgrav team identified (quadrupolar) correlations in the arrival times of electromagnetic radiation from a system of 68 millisecond pulsars (Agazie et al., 2023b). Though too faint to have the origin of the signal singularly identified, possible sources favoured by collaborators include the slow orbital decay of pairs of supermassive black holes (Agazie et al., 2023c).

It is also possible that a stochastic background might have developed from cosmological sources rather than astrophysical ones. Analogous to the cosmic microwave background, GWs generated during the early inflationary period could provide unique insights into the nature of the Universe in its earliest moments (Guzzetti et al., 2016). Perhaps more speculatively, a stochastic background of GWs generated via cosmic strings (topological defects produced by phase transitions in the early universe) could also lead to a deeper understanding of the Universe beyond the Standard Model (Kamada and Yamada, 2015).

1.2.4 Burst gravitational-waves

The final type of GW though to permeate the Universe are *burst gravitational-waves*. Similar to the stochastic background, this category largely represents our agnosticism regarding aspects of GW theory; incorporating signals from sources that we either do not yet know about, or are unsure how to model theoretically.

These signals are the most challenging to search for from a data-analysts perspective. Searches for transient GWs, for example, rely on the ability to match data from the interferometers (after accounting for various sources of noise) to that of a bank of template signals generated from solving the field equations of GR (e.g. Owen and Sathyaprakash, 1999; and recall Fig. 1.2). Put simply, it is difficult to find something if you are not sure what it is exactly you are looking for.

This is not to say that theories for potential sources do not exist, however. The most promising are those that might arise as a result of core-collapse supernovae, the explosive and cataclysmic last evolutionary stage of massive stars. Once the nuclear fuel of such a star has been exhausted, there is nothing left but the degeneracy pressure of Fermions to counteract the inward gravitational force as the outer layers of the star collapse into the center. Exactly what the GW signal from such a process might look like, however, is unknown (though progress on this issue has been made in recent years; e.g. Radice et al., 2019). What is left behind after such an explosion, though, is certainly of interest in the search for GWs. These supernova explosions are thought to be the birthplaces of a particular compact remnant, responsible for transient, continuous, and stochastic GWs alike: *neutron stars*.

1.3 Neutron stars as sources of continuous gravitational radiation

Neutron stars clearly play an incredibly important and diverse role in the production of GWs throughout the Universe; from burst GWs potentially produced as a result of their birth, to transient GWs produced as a result of their timely demise through binary inspiral. In this thesis, however, we consider specifically the role NSs have to play in the intermediate periods of their lives, during the time that they may act as *continuous* GW emitters. As highlighted in Section 1.2.2, there are three primary mechanisms that are thought to generate continuous-wave emission: fluid instabilities, free precession, and non-axisymmetric quadrupolar deformations.

1.3.1 Gravitational-waves from fluid instabilities

The first type of asymmetry-inducing mechanism that may exist within NSs are *unstable* modes of oscillation. Oscillation modes are the set of preferred frequencies at which the star 'vibrates' at when it is perturbed in some way. There are a number of different oscillation modes that NSs are capable of supporting. For example, perturbations of the pressure in fluid regions of the star may generate so-called 'p-modes' of oscillation. Discontinuities in the density profile of the star (which can arise due to changes in the chemical composition of the star) on the other hand may lead to 'g-modes', generating oscillations which are driven by buoyancy forces.

If these oscillations are non-axisymmetric with respect to the star's rotation axis, then whey will generate GWs. However, for most modes of oscillation, gravitational radiation will quickly damp any type of perturbation - be it in the density profile or otherwise - as the initial energy of the mode is quickly converted into gravitational energy (and any other energy losses inside the star, such as viscosity). One type of oscillation mode, however, is actually expected to be *amplified* by the gravitational radiation reaction, rather than be damped by it. These modes are known as unstable *r-modes*.

R-modes are a type of toroidal mode, supported by Coriolis forces, that may be generated both on the surface, and throughout the interior, of *rotating* NSs (Andersson, 1998, 2003). These modes are of particular importance since they are unstable to a phenomenon known as the Chandrasekhar–Friedman–Schutz instability (Chandrasekhar, 1970; Friedman and Schutz, 1978). Consider a NS that is initially stationary, and perturbed in such a way that it excites an oscillation mode that deforms the star and travels with non-zero angular momentum in a positive (anti-clockwise) direction.

Assuming the oscillation mode is non-axisymmetric, the mode will lose energy via the emission of GWs, carrying with it *positive* angular momentum from the star. Positive angular momentum is necessarily subtracted from the positive angular momentum of the mode, causing the amplitude of the mode to shrink until it has dissipated completely. Through symmetry, there must also exist a non-axisymmetric mode that moves in the *opposite sense*, travelling with negative angular momentum in the clockwise direction. This mode will emit negative angular momentum in the form of GWs, which also must be subtracted from the negative angular momentum of the mode causing the amplitude of the mode to shrink as well.

Whilst this may seem intuitive (and uninteresting for GW emission), consider what happens to the mode once the star is set into rotation (assumed to be in the positive, anti-clockwise direction).

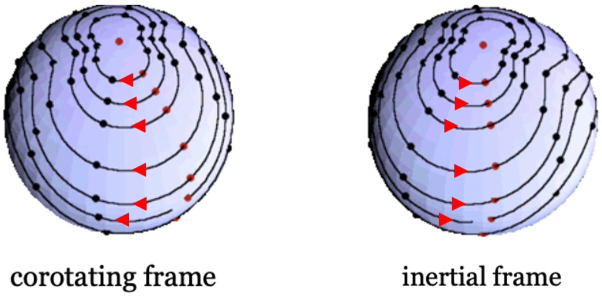

FIGURE 1.6: Schematic picture of the Chandrasekhar–Friedman–Schutz instability in a neutron star, assumed to be rotating in an anti-clockwise direction. Retrograde (clockwise) propagating modes are dragged forward by the anti-clockwise rotation of the star. R-modes on a rotating neutron star are therefore retrograde in the co-moving frame, but prograde in the inertial frame. Image credit: adapted from C. Hanna and B. Owen

Once rotating, the retrograde (clockwise) propagating modes are necessarily dragged forward by the rotation. From the perspective of the star's *rotating frame*, this retrograde mode continues to move backwards. However, in the *inertial frame*, if the star is rotating fast enough, then it will appear to be prograde, moving anti-clockwise and losing energy to GWs carrying *positive* angular momentum. This positive angular momentum must still be subtracted from the negative angular momentum of the mode (it is still moving backwards in the rotating frame), causing the amplitude of the mode to grow. As it grows, the mode continues to emit more and more positive angular momentum, creating a positive-feedback loop that only grows the size of the mode.

Simply put, for rotation rates typical of NSs, r-modes are retrograde in the co-moving rotating frame, but prograde in the inertial frame (see Fig. 1.6), and therefore generically unstable to the Chandrasekhar–Friedman–Schutz instability. If the NS were a perfect fluid, then this instability would grow unabated. However, real NSs are not perfect fluids, and viscosity effects in the interior will, to some degree, damp the system. The amplitude of an excited r-mode is therefore a competition between the GWs that amplify the oscillation amplitude, and the viscous damping that acts to suppress it. It is thought there exists an 'instability window' for which GW emission dominates over viscous dissipation in a small region of parameter space covering both the spin period and temperature of the star (Fig. 1.7). In cold NSs ($\sim 10^8$ K) viscous damping is dominated by frictional shear viscosity, whilst in hot NSs ($\sim 10^{10}$ K) dissipation is dominated by bulk viscosity.

For a NS that is rotating at a given frequency ν_s, the frequency of the emitted GWs will depend on the mechanism that sources it. In the case of an excited r-mode, such a long-lasting oscillation mode will generate GWs at $f_{GW} \sim 4/3\nu_s$ (e.g. Idrisy et al., 2015). Searches for continuous GWs from unstable r-modes have been made, though none have been successful thus far (e.g. Rajbhandari et al., 2021; Fesik and Papa, 2020; Abbott et al., 2021b; Covas et al., 2022).

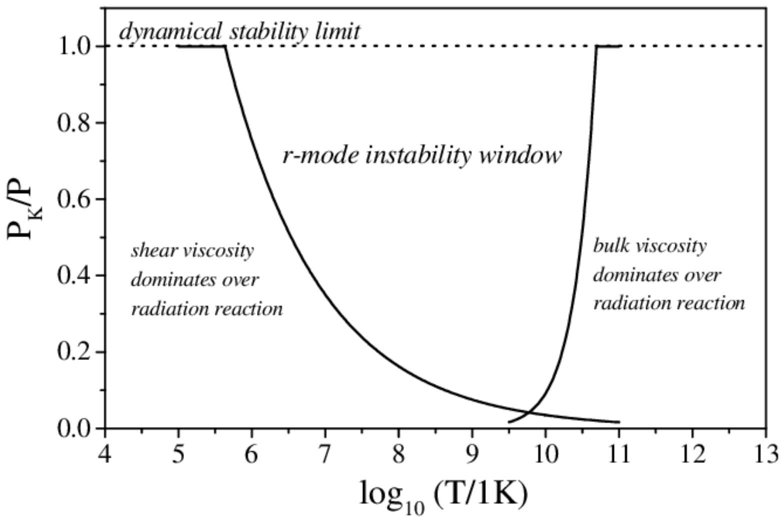

FIGURE 1.7: R-mode instability window for a typical neutron star ($M = 1.4 M_\odot$ and $R = 10$ km). Image credit: reproduced from Kokkotas and Ruoff (2003).

1.3.2 Gravitational-waves from free-precession

In general, the rotation axis of a pulsar need not coincide exactly with one of its principal axes. This can occur in NSs that develop a deformation that is misaligned from its rotation axis. This can cause the star to begin to *precess* around the direction of the total angular momentum vector, with angular frequency $\dot{\phi}$ (e.g. Zimmermann and Szedenits, 1979; Jones and Andersson, 2001).

The precession could be sourced in a variety of ways, including (amongst others) accretion torques, electromagnetic torques, or glitches. These deformations may then be sustained either by elastic strains built up in the solid crust, or by magnetic strains sourced by the presence of strong internal magnetic fields (this will be discussed in greater detail in Section 1.3.3). The amount of precession is determined by the so-called 'wobble angle' θ_W, defined as the angle between the deformation axis $\mathbf{n_d}$ (dependent on the size of the elastic or magnetic strains) and the fixed angular momentum axis $\mathbf{J}$. A schematic illustration of the precession effect may be seen in Fig. 1.8.

In the absence of any dissipative effects, the NS would precess forever. However, much like the presence of viscosity that will damp the inertial r-mode, there are a number of damping effects that will cause the star to halt its precession and return to its original, unperturbed state (Jones and Andersson, 2002). How quickly the precession is damped depends on the nature of the deformation, and the corresponding asymmetry in the moment of inertia tensor ($\Delta I_d = I_3 - I_1$). Consider, for example, a deformation that is built up by magnetic strains. Magnetic fields within NSs are expected to have both a poloidal and toroidal structure (e.g. Rädler et al., 2001). A poloidal magnetic field will result in an *oblate* ($\Delta I_d > 0$) deformation, whilst a toroidal magnetic field will result in a *prolate* ($\Delta I_d < 0$) deformation (e.g. Lander and Jones, 2009).

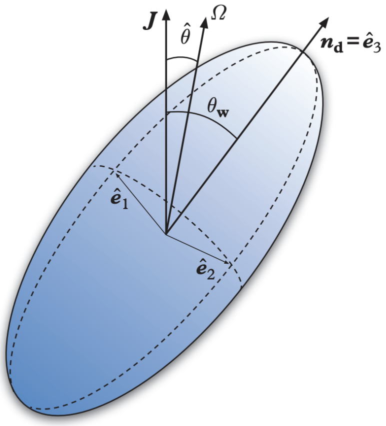

FIGURE 1.8: Schematic picture of a body (such as a deformed rotating neutron star with angular velocity $\mathbf{\Omega}$) undergoing free precession. The angle between the deformation axis $\mathbf{n_d}$ and the fixed angular momentum axis $\mathbf{J}$ is known as the 'wobble angle', θ_W. Image credit: reproduced from Andersson (2019).

The evolution of the wobble angle is approximately $\dot{\theta} \propto \dot{E}/\Delta I_d$, with $\dot{E}$ being the energy lost (and therefore always negative) due to dissipation of mechanical energy into either heat or radiation (Andersson, 2019). It therefore follows that an oblate deformation will tend to *decrease* the wobble angle (since $\Delta I_d > 0$), whilst a prolate deformation will tend to *increase* the wobble angle of the star. However, only strong internal toroidal magnetic fields ($10^{12} - 10^{13}$ G) are thought to be able to produce significant prolate deformations, and elastic strains built up in the crust are thought to almost always lead to oblate deformations only (Jones and Andersson, 2002).

Regardless of the nature of the deformation, GW emission always leads to a decreasing of the wobble angle (Cutler and Jones, 2000). A non-spherical NS that is freely precessing will radiate GWs at three frequencies (Zimmermann, 1980), which can be approximated to be (i) the precession frequency ($f_{GW} = \dot{\phi}$), (ii) twice the precession frequency ($f_{GW} = 2\dot{\phi}$), and (iii) twice the spin-frequency of the star ($f_{GW} = 2\nu_s$). Additionally, freely-precessing NSs should be visible not just through the lens of GW detectors, but in radio telescopes as well. In theory, free precession should introduce modulations in the timing (and width) of the radio signal received from known pulsars. However, such impressions are not typically brought out by observations, with very few pulsars exhibiting radio timing variability consistent with precession effects.

1.3.3 Gravitational-waves from non-axisymmetric deformations: Mountains

Whilst it appears that most neutron stars that we see in the Cosmos do not undergo extended periods of free-precession, it is possible that non-axisymmetric deformations of the NS (which themselves may lead to the precession) may persevere for much longer periods of time.

Quasi-persistent deformations of rigidly rotating NSs are more usually referred to as '*mountains*', and will radiate GWs continuously at twice the spin frequency ($f_{GW} = 2\nu_s$) of the star. As already alluded to, mountains can be divided into two categories. There are so-called '*magnetic* mountains', whereby a mass distortion is supported by Lorentz forces associated with a non-axisymmetric magnetic field , and '*elastic* mountains', where the mass distortion is supported by elastic strains which develop in the star's solid crust.

1.3.3.1 Magnetic mountains

Magnetic mountains may be formed in almost any type of neutron star, ranging from isolated magnetars (those with exceedingly strong $\sim 10^{15}$ G magnetic fields), to accreting systems where the magnetic field is thought to be relatively weak ($\sim 10^{9}$ G; Sec. 2.4).

In strongly magnetised stars, the resulting shape of the deformation is related to the structure of the magnetic field. As mentioned in Section 1.3.2, a purely poloidal field will tend to deform the star into an oblate shape, whilst a purely toroidal field will tend to deform the NS into a prolate shape (see e.g. Glampedakis and Gualtieri, 2018). It follows that a magnetic field that is a mixture of both components will produce a deformation that has both negative and positive contributions, with the relative contributions of the poloidal and toroidal components depending on the exact geometry of the field.

In accreting systems on the other hand, the mountain is more a 'localised deformation' than a global deformation of the star like in a magnetar. They are formed by the accretion of matter onto the NS surface that is sustained in an asymmetric way by the magnetic field via a process known as *magnetic burial* (Payne and Melatos, 2004; Melatos and Payne, 2005; Vigelius and Melatos, 2009; Suvorov and Melatos, 2018; Rossetto et al., 2023). Material that is accreted onto the neutron star accumulates in a column at the polar caps. Intense gravitational fields on the surface of the star act to spread this accreted material down from the poles over the equator. Such a process creates fluctuations in the structure of the magnetic field between the top and base of the accretion column as the magnetic field is compressed into a narrow belt (also referred to as a magnetic 'tutu' in Payne and Melatos, 2004) at the magnetic equator (see Fig. 1.9). Over time, this belt restricts further accreted material from reaching the equator, eventually confining it to the magnetic poles and leading to a build up of accreted matter. If the magnetic poles are misaligned from the axis of rotation, then this will lead to the build up of material in a non-axisymmetric way, leading to GW emission as the star rotates.

1.3.3.2 Elastic mountains

It is expected that neutron stars, much like the Earth, form a solid crust close to their surface. This crust is thought to exhibit *elastic properties* which, in theory, could allow the NS to sustain a non-axisymmetric deformation through elastic strains. Assuming the crust is able to support significant stresses before cracking, elastic mountains could be a promising source of continuous gravitational radiation. In assessing the likelihood of detecting GW emission from

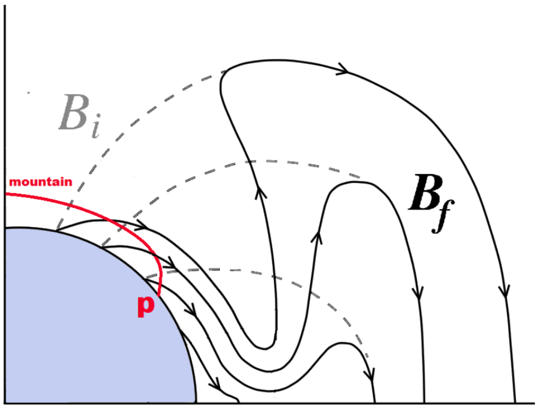

FIGURE 1.9: Schematic illustration of the formation of a magnetic mountain on an accreting neutron star. The magnetic field lines before and after the onset of accretion are denoted by the dashed and solid lines respectively, with the mountain forming in the region bounded by the red curve and the stellar surface. Image credit: reproduced from Suvorov and Melatos (2018).

such mountains, there are, generally speaking, two important considerations one need make: (i) what is the largest possible mountain that the neutron star crust could feasibly maintain? (ii) what physical processes within the NS might be capable of building the necessary asymmetries in the first place?

Many studies have sought to answer this first question in recent years (Ushomirsky et al., 2000; Owen, 2005; Haskell et al., 2006; Johnson-McDaniel and Owen, 2013; Gittins et al., 2021; Gittins and Andersson, 2021). The latter of these studies sought to revisit the approach of Ushomirsky et al. (2000) (hereafter UCB), who calculated the maximum mountain by obtaining the strain tensor associated with the point whereby the entire crust is forced to its elastic yield point (i.e. where it is maximally strained). Both Gittins et al. (2021) and Gittins and Andersson (2021) argued this procedure to be unphysical, since it implies non-zero components of the strain tensor at transitions between the elastic crust and fluid core and ocean, which violates continuity of the traction vector. By introducing a fiducial force to source the mountain instead, Gittins et al. (2021) found that the largest ellipticity (the fractional difference in the star's moments of inertia; Eq. (3.37)) the NS could sustain was $\lesssim 10^{-7}$, an order of magnitude or so smaller than in previous works.

Very recently, Morales and Horowitz (2022) again revisited this problem, seeking to extend the Gittins et al. (2021) formalism by adopting a different forcing function that was chosen to act primarily in the transverse direction. Such a force was shown to be capable of straining the deep crust, whilst not breaking the more fragile outer crust. The maximum ellipticity obtained from this calculation was 7.4×10^{-6}, larger than obtained by Gittins et al. (2021), and in fact consistent with the original calculation by Ushomirsky et al. (2000).

The requirement of some fiducial force leads naturally to the second important question, how exactly might the star be driven away from sphericity? The nature of this problem was not explicitly addressed by Gittins et al. (2021) (or Morales and Horowitz, 2022), who simply introduced the deforming force as a means to give the star a non-spherical shape. One possible *physical* source for the elastic strains are thought to arise from the formation of large-scale temperature asymmetries within the star. For accreting systems in particular, the presence of non-axisymmetric temperature gradients have been shown to alter reaction thresholds for nuclear interactions induced by the compression of accreted material, a process we shall explore in greater depth later on in Section 3.2.2.1. This 'subtype' of elastic mountains are known more commonly as '*thermal* mountains'.

1.3.3.2.1 Thermal mountains

The structure of isolated neutron stars and those that accrete are markedly different. Accreted matter (mostly hydrogen, helium, and other light elements) settles on the star's surface and is subsequently buried under ever-increasing amounts of freshly accreted matter. These layers of hydrogen and helium eventually ignite, and the resulting thermonuclear burning leads to the formation of a layer of nuclear ashes consisting of mostly iron-peak nuclides (Schatz et al., 1999). Continual accretion from the companion star leads to further compression of these heavy nuclides that subsequently sink into the crust, replacing the original crust after $\sim 5 \times 10^7$ years (assuming constant accretion at a rate, $\dot{M} \,/\, 10^{-9}\ M_\odot\ \mathrm{yr}^{-1}$; Ushomirsky et al., 2000).

The accreted crust is defined by a series of density-dependent, non-equilibrium reactions (electron captures, pycnonuclear reactions and neutron emissions) that irreversibly changes the composition of the primordial crust (Sec. 2.4.2). Despite being primarily density-dependent, the threshold energy E_{cap} - which determines when a given electron capture event takes place - has also been shown to have weak temperature sensitivity too (Bildsten and Cumming, 1998). Consequently, in the regions of the crust that are hotter on average, electron-capture events can take place at lower density (i.e. closer to the star's surface) than colder regions. Any temperature asymmetry in the accreted crust therefore results in 'wavy' electron capture layers (Bildsten, 1998) as depicted in Fig. 1.10. If the temperature asymmetry happens to be misaligned with the rotation axis, then the mass distribution itself can inherit the non-axisymmetry and hence develop the mountain.

A description of how the NS might inherit such a non-axisymmetric temperature profile in the first place, however, has been lacking, and motivates this thesis. Indeed, the origin of the required temperature gradients were not given by Bildsten (1998). To reconcile this issue, Osborne and Jones (2020) recently sought to provide substantiation to the 'wavy capture layer' idea by developing a mechanism for which an accreting NS might naturally inherit the necessary temperature gradients. The authors exploited the likely weak internal magnetic fields of these stars to perturb the thermal conductivity tensor, thus rendering it anisotropic (this is to be explored in much greater detail in Chap. 5). By confining their calculation to the accreted crust only, they estimated that large *internal* crustal toroidal magnetic fields ($B \sim 10^{13}$ G) - four orders of magnitude larger than inferred ($B \sim 10^9$ G) *external* field strengths of accreting neutron stars

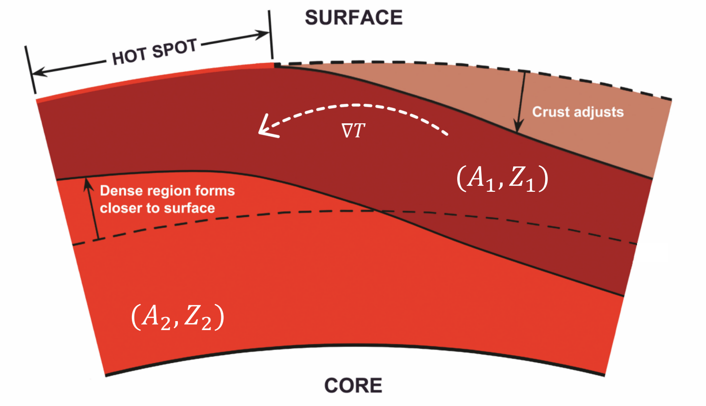

Figure 1.10: Schematic illustration of the formation of a thermal mountain on an accreting neutron star. The dashed line indicates the location of the temperature-sensitive capture boundary between two layers $(A_1,\, Z_1) \longrightarrow (A_2,\, Z_2)$ in a thermally symmetric neutron star. In the presence of a lateral temperature gradient ∇T, the capture boundary shifts closer to the surface in locally hotter regions, and closer to the core in locally colder regions. Image credit: adapted from Emma Osborne.

- were required in order to produce deformations large enough to facilitate GW emission at a significant level.

Estimates of the size of the induced deformations were made through means of a simple fitting formula (which we will discuss later in Sec. 5.6) to the results of Ushomirsky et al. (2000), who calculated the mass quadrupole assuming that there is an elastic readjustment of the solid crust to pre-existing temperature gradients (i.e. those that were assumed present, like Bildsten (1998), *a priori*) as the 'wavy' capture layer is formed. Exactly how these temperature perturbations translate into a perturbation in the star's density profile (this will be the focus of Chap. 6) were assumed to enter through a temperature dependence on the electron mean molecular weight μ_e (where $E_{cap} \equiv \mu_e$) in a two-parameter equation of state whereby $P = P[\rho, \mu_e(\rho, T)]$ (this will be explained in greater detail in Sec. 6.1).

Osborne and Jones (2020) used their fitting formula to estimate the ellipticity from a single value of the temperature perturbation δT in the inner crust at $\rho = 10^{12}$ g cm^{-3}. However, although this simplified their calculations greatly, the fitting formula inherently relies on the existence of capture layers in the deep crust beyond what is predicted by modern crustal equations of state (we will discuss this in greater depth later in Sec. 6.3.2), and therefore likely overestimates the size of the mountains produced from these kinds of temperature asymmetry. The ultimate goal of this thesis is therefore to complete the work initially set out by Osborne and Jones (2020), and compute the ellipticity from the *full* function $\delta T(r)$ that arises from anisotropic heat conduction.

1.4 This thesis

In this thesis we shall indeed develop a scheme to produce the *first fully self-consistent* calculation of the size of neutron star (thermal/thermo-elastic) mountains, bridging the gap between Osborne and Jones (2020), who modelled the formation of non-axisymmetric *temperature* variations only, and Ushomirsky et al. (2000), who modelled the formation of non-axisymmetric *density* variations only.

We focus on providing a physically-motivated estimate for the level of temperature asymmetry that might be realistically developed in the crust, by further developing the Osborne and Jones (2020) mechanism. We shall then discuss, and subsequently implement, a procedure for which these temperature gradients may then generate pressure perturbations, which ultimately result in an elastic readjustment of the crust and form the mountain. A schematic flowchart highlighting the critical stages of our calculation is shown in Fig. 1.11. Each stage of the workflow diagram will be discussed in turn in the relevant chapters indicated in the upper-left corner of each panel in the workflow. The chapters that comprise this thesis are briefly summarised below.

Chapter 2 contains a review of the general structure of neutron stars (and in particular the crust) as they are currently understood. We introduce the concept of the equation of state, and discuss how accretion from a binary companion can irreversibly change the structure of primordial NSs. We outline a method in which one may create analytical representations of realistic accreted equations of state (the light blue panel in Fig. 1.11), and show how they may be used to determine both the microscopic and macroscopic properties of these stars. The equations of stellar structure in Newtonian and relativistic gravity are also presented, and a method to build spherically symmetric stellar models is described (the dark blue panel of Fig. 1.11).

In Chapter 3 we begin with outlining some basic gravitational-wave theory, before discussing the role GWs could be playing in determining the spin-evolution of accreting neutron stars. Specifically, we shall consider different scenarios that may generate spin-up and spin-down torques on the star, and how the presence of thermal mountains may be contributing to the so-called ‘torque balance limit’ of rapidly rotating neutron stars, whereby spin-equilibrium (i.e. the observed spin-rate) of the star is achieved through balancing accretion torques from its main sequence companion.

Following this discussion we move into Chapter 4 where we begin our original work. We discuss existing observations of accreting neutron stars, and how they may be used to infer their internal thermal structure. We then outline how the steady-state thermal profile of such stars may be constructed in a Newtonian framework (the light green panel in Fig. 1.11). This requires a detailed description of relevant heating and cooling processes, as well as a description of the star’s thermal conductivity, all of which are discussed. The implications of baryon superfluidity on each of these processes is also presented. The parameter space of accretion rate, crustal impurities, as well as observationally-inferred shallow-crustal heating is then explored, where we show that our steady-state model is compatible with other theoretical works in the literature.

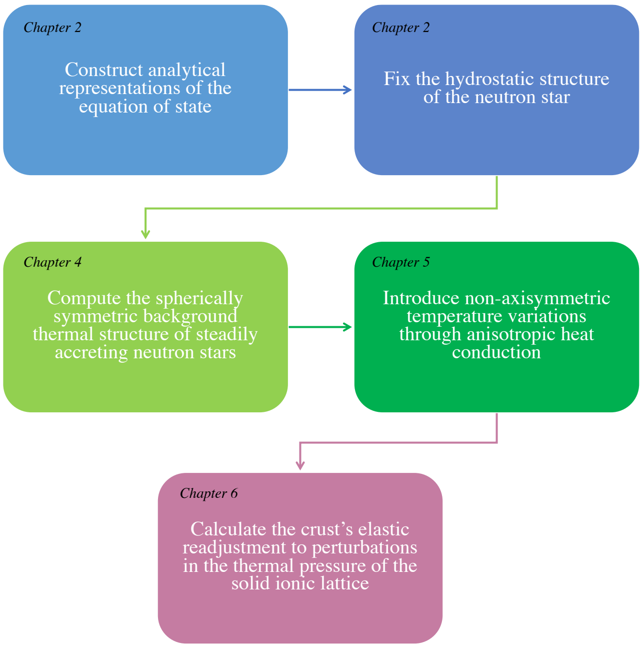

FIGURE 1.11: Workflow diagram for constructing models of thermo-elastic mountains on accreting neutron stars as presented in this thesis.

We continue in Chapter 5 by introducing anisotropy into our model for the thermal background through the addition of a weak magnetic field (the dark green panel in Fig. 1.11). This work was originally developed by Osborne and Jones (2020) to investigate if significant temperature asymmetries can develop in the presence of *crustal* magnetic fields, as discussed in Section 1.3.3.2.1. We revisit and improve various aspects of this mechanism; allowing for the possibility of the magnetic field to permeate the core, with the expectation that non-vanishing temperature perturbations at the crust-core transition will lead to greater asymmetries in the deep crust.

In Chapter 6 we then take one step further the work of Osborne and Jones (2020) and compute self-consistently the mass quadrupole moment generated as a result of temperature gradients sourced by the magnetic field (the purple panel in Fig. 1.11). A small contribution to the pressure within the crust of the star from the Coulomb crystal lattice is identified, and shown to have some temperature dependence. This results in the formation of non-negligible pressure perturbations in regions of the crust that are locally hotter on average, leading to a readjustment of the crustal matter and hence the formation of the mountain.

Finally, we conclude in Chapter 7 by summarising the headline results presented in this thesis, and reviewing some of the finer details of the model. We do this in order to better understand its current limitations, and outline ways in which, in future work, it might be further refined.

2

The Structure of Neutron Stars

In order to understand how mountains form, one must first be armed with an intuitive sense of how neutron stars behave. In this chapter we begin in Section 2.1 by reviewing the different regions that constitute a typical neutron star, followed up with an introduction to the concept of the equation of state (EoS) in Section 2.2. We shall then delve deeper into the structure of the crust in Section 2.3, before discussing how accretion of material from a binary companion can irreversibly change the original composition in Section 2.4. We then continue in Section 2.5 by constructing analytical expressions of unified equations of state based on the Brussels-Montreal energy-density functionals BSk19, BSk20, and BSk21, and show how the parameterised EoS can be used to determine various microscopic properties of the star. Finally, in Section 2.6 we construct both the Newtonian and general relativistic structure equations for a non-rotating, fluid stars and compare the hydrostatic structures of both accreting and non-accreting stars.

2.1 General structure of neutron stars

Neutron stars are among the densest manifestations of matter in the known Universe. With masses typically in the region $1-2\,M_\odot$ (where $M_\odot = 2\times10^{30}$ kg is the solar mass), and diameters of just $20-30$ km, they are extremely compact objects. To put a typical NS into perspective, the Sun's $1\,M_\odot$ is contained within a body 1.4 *million* km in diameter.

First theorised by Baade and Zwicky (1934a,b), the majority of neutron stars are the remnants of medium-sized ($8 \leq M \leq 20\,M_\odot$) main-sequence stars that end their life in the explosive and cataclysmic furnace of a type II supernova explosion[1]. Supported against further collapse into a black hole by neutron-degeneracy pressure, NSs consist primarily of closely packed neutrons, together with a small fraction of protons and electrons.

---

[1] Neutron stars may also be formed as a result of Type 1a or electron-capture supernovae, though this is much more uncommon.

From the surface down to the center, there are believed to be a number of distinct regions that make up the star's internal structure (see e.g. Haensel et al., 2007). Generally speaking, the layers of a typical NS (see Fig. 2.1, and note the approximate thicknesses of each layer) are:

- The ***atmosphere***: A thin gaseous layer surrounding the exterior of the star at densities $\rho \lesssim 10^6$ g/cm^3 composed of ions, atoms, and molecules.
- The ***ocean***: A thin liquid layer that sits atop the surface of the star. Not to be confused with the oceans on Earth, the neutron star ocean is composed of a plasma of strongly coupled electrons and nuclei, which behaves as a fluid.
- The ***outer crust***: When the Coulomb interaction energy between the ions is greater than the thermal energy, the ocean solidifies. This is referred to as the 'crystallization-point', with a crust comprised of a Coulomb lattice of heavy neutron-rich nuclei on a background of relativistic free-electrons being formed.
- The ***inner crust***: Neutrons within the nuclei of the crystal lattice become less and less bound with depth (Sec. 2.3.2). Eventually, some neutrons are able to 'drip out' from the nuclei entirely, forming a lattice of neutron-rich nuclei on a background of both free neutrons and ultra-relativistic electrons. The outer and inner crust is therefore demarcated by the so-called *neutron drip point*, occurring at $\sim 4 \times 10^{11}$ g cm^{-3}.
- The ***mantle***: Sitting just below the Coulomb lattice at densities $\sim 10^{14}$ g cm^{-3} is the mantle, a thin layer that is thought to contain a series of nuclear structures with peculiar geometries. At these densities, nuclei are theorised to undergo a series of transitions into so-called 'pasta' phases, taking on various shapes including cylinders and plane-parallel plates, often refereed to as (comically) the 'spaghetti' and 'lasagna' phases respectively.
- The ***outer core***: At densities exceeding 10^{14} g cm^{-3} it is not energetically favourable for protons to cluster to form nuclei, and instead matter becomes a homogeneous plasma of neutrons, protons, and electrons (maybe muons as well), with some neutrons (protons) also expected to be in a superfluid (superconducting) state.
- The ***inner core***: The central region of the star ($\rho > 10^{15}$ g cm^{-3}) is known as the inner core. Matter at such densities far exceeds what is achievable on Earth, and thus the composition of the inner core is largely unknown. It is speculated that anything from exotic particles such as hyperons, pions or kaons may exist, to mixed phases of both hadronic matter and deconfined quarks.

2.2 The equation of state

To a first approximation, stellar material may be described very well by a perfect fluid. For simplicity, one may think of this fluid as a series of many small fluid elements, with each fluid

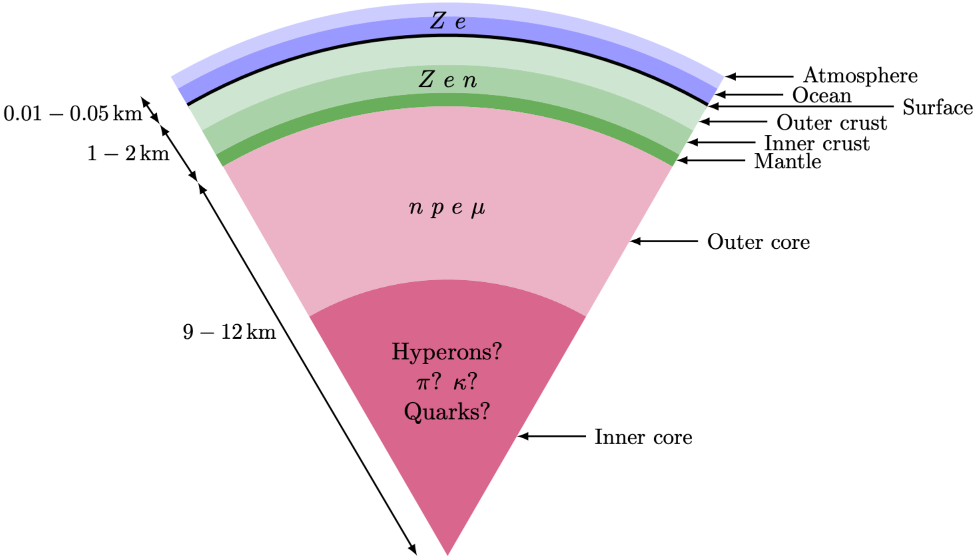

FIGURE 2.1: Schematic illustration of the structure of a typical neutron star, consisting of the exterior layers (blue), the crust (green) and the core (pink). Reproduced from Harpole (2018).

element itself comprised of a large number of individual particles that constitute the star[2]. If the mean-free path of the individual particles (i.e the average distance travelled by a particle in-between collisions) is much less than the characteristic length scales of the flow, then the fluid may be viewed as a *continuum*. In such an instance, the principles of mass, momentum, and energy conservation can be used to describe fluid behavior, which is far more tractable.

Indeed, quantities such as the pressure of the (perfect) fluid can be determined by the local thermodynamic state of the system. For a many-particle-species system (e.g. electrons, neutrons, protons, etc.), the First Law of thermodynamics takes the form

$$dQ = Pd\left(\frac{1}{n_\mathrm{b}}\right) + d\left(\frac{\epsilon}{n_\mathrm{b}}\right) - \sum_\mathrm{x} \mu_\mathrm{x} dY_\mathrm{x} \,, \tag{2.1}$$

where dQ is the change in energy (in this case measured *per baryon*), P is the pressure, n_b is the number density of baryons, ϵ is the energy density (i.e. including rest-mass energy), μ_x is the chemical potential of particle species x, and Y_x is the fraction of species x in the fluid element, defined as

$$Y_\mathrm{x} = \frac{n_\mathrm{x}}{n_\mathrm{b}} \,. \tag{2.2}$$

The Second Law of thermodynamics states that, in general, any process that occurs inside the fluid element must also obey the condition that

---

[2] Though, keep in mind the *true* picture of a neutron star is complicated by the presence of the solid (elastic) crust. This treatment must also be refined when one considers additional physics such as heat transport, strong magnetic fields, as well as baryon superfluidity.

$$dQ \leq TdS\,, \tag{2.3}$$

where T is the temperature and S is the entropy per baryon. Combining Eqs (2.1) - (2.3), the First Law may be written as

$$d\left(\frac{\epsilon}{n_{\rm b}}\right) \leq -Pd\left(\frac{1}{n_{\rm b}}\right) + TdS + \sum_{\rm x} \mu_{\rm x} dY_{\rm x}\,. \tag{2.4}$$

The energy density can be seen to depend on the volume per baryon and entropy per baryon of the system, as well as the relative amounts of each particle species. In equilibrium (see below), we have an *equation of state* for the system, parameterised as $\epsilon(Y_{\rm x}, n_{\rm b}, S)$, from which one extract each of the quantities

$$P \equiv n_{\rm b}^2 \frac{\partial(\epsilon/n_{\rm b})}{\partial n_{\rm b}}\bigg|_{S,Y_{\rm x}}\,, \qquad T \equiv \frac{\partial(\epsilon/n_{\rm b})}{\partial S}\bigg|_{n_{\rm b},Y_{\rm x}}\,, \qquad \mu_{\rm x} \equiv \frac{\partial(\epsilon/n_{\rm b})}{\partial Y_{\rm x}}\bigg|_{S,n_{\rm b},Y_{\rm z}}\,, \tag{2.5}$$

as required, where the sub-scripted variables following a vertical bar indicate that they are being held constant[3]. These relations are crucial, as it allows one to connect the microphysics and thermodynamics to that of the fluid dynamics.

In the context of neutron stars, matter is indeed most often assumed to be in total thermodynamic equilibrium, as well as cold. This is referred to commonly as the *cold-catalyzed matter hypothesis*, where the matter is assumed to be in its ground-state at $T = 0$ K. Of course, this is only an approximation. First and foremost, it is not possible for the interior of the star to be *exactly* 0 K (in fact, it is expected to be hundreds of millions of degrees; Sec. 4.8). Rather, the 'cold' in this statement refers to the fact that the kinetic thermal energy of the nuclei (10^8 K $\simeq$ 0.01 MeV) is actually much less than that of the so-called *Fermi temperature*. Neutron stars are sufficiently dense that there is a non-negligible energy associated with the confinement of atomic nuclei. Under intense gravitational compression, 'squeezing' of the nuclei increases its total energy, with the Fermi energy ($\sim 10 - 100$ MeV) acting as a pressure, usually referred to (as in Section 1.2.4) as *degeneracy pressure*.

In order to remain in total thermodynamic equilibrium, any nuclear interactions that occur within a given matter element are balanced by their inverse (which occurs equally rapidly) and therefore the concentration of each species remains constant. The First Law (2.4) in this instance simplifies to

$$d\left(\frac{\epsilon}{n_{\rm b}}\right) + Pd\left(\frac{1}{n_{\rm b}}\right) = 0\,. \tag{2.6}$$

---

[3] The additional term $Y_{\rm z}$ denotes the set of particle fractions which exclude $Y_{\rm x}$.

Now, rather than an EoS that depends on all three state variables n_b, S, Y_x, the energy density now depends *solely* on just the baryon-number density, and thus $\epsilon = \epsilon(n_\mathrm{b})$.

Since all thermodynamic quantities are related by the First Law, it is also equally valid to express the EoS in terms of the pressure P. The pressure inside a NS composed of cold-catalyzed matter is therefore $P = P(\epsilon) \equiv P(n_\mathrm{b})$. This latter definition is commonly referred to as a *barotropic* equation of state, and features prominently in many neutron star calculations. For reasons that will become clear in Section 2.5, it is most practical to consider the situation whereby equilibrium within the star is achieved at constant pressure. In this specific case, Eq. (2.6) implies that

$$dg = 0\,, \tag{2.7}$$

where g is known as the *Gibbs free energy* per baryon (the mean chemical potential), given by (Shapiro and Teukolsky, 1983)

$$g = \frac{\epsilon + P}{n_\mathrm{b}}\,. \tag{2.8}$$

In the outer regions of the star which are comprised of nuclei (with mass number A and atomic number Z), electrons (and potentially free neutrons), the equilibrium nucleus at a fixed pressure P is determined from the condition that the Gibbs free energy g be minimised at that pressure (this will be discussed in greater detail in the next section).

Determining the EoS is a therefore a two-fold endeavour: one must first determine the equilibrium nuclide present at a given pressure P, and then compute the corresponding density n_b to determine the pressure-density $P(n_\mathrm{b})$ relation. The term ‘equation of state’ can therefore refer to either the pressure-density $P(n_\mathrm{b})$ relation *and/or* the composition (the run of (A, Z) with density) of the matter, assuming some underlying microphysical model. In this Chapter (Chap. 2) we shall refer to the pressure-density relation specifically when we talk about the EoS, rather than the composition. From Chapter 4 onward however, we will in general refer to *both* the pressure-density relation and the composition when we talk about the EoS.

2.3 The crust

The crust constitutes just $\sim 1\%$ of the total mass of the neutron star, and has a radius typically less than one-tenth of the total radius (See Sec. 2.6.4). Yet despite this, the crust plays a pivotal role in determining the evolution and dynamics of the star, as well as generating a plethora of different observational phenomena. These include: oscillations of strongly magnetized NSs (Lander et al., 2010; Leung et al., 2022); quiescent X-ray spectra after periods of accretion from a companion star; energetic type I X-ray explosions (See Sec. 4.1); as well as pulsar glitches (sudden increases in the star’s observed spin frequency; e.g. Zhou et al., 2022) and more. Each of these events provides a unique opportunity to probe the inner structure that would otherwise remain a mystery.

Much of the observed phenomena are indeed attributed to intense magnetic fields which emanate from the top of the crust. The magnetic field evolution of NSs has been a central topic of research for decades, with three main effects thought to influence the dynamics of the evolution. These are (i) Ohmic decay, (ii) Hall drift, and (iii) ambipolar diffusion[4]. Ohmic decay, for example, results as a consequence of finite electrical conductivity (determined by both the structure and composition of the crust), which leads to dissipation of the magnetic field and the conversation of magnetic energy into heat energy. The presence of magnetic fields in the crust can also generate temperature gradients (as a result of anisotropic heat conduction), with the thermal conductivity also being determined by the composition of the crust (Sec. 4.4). This is precisely the mechanism we will explore later on in Chapter 5 to source our mountains.

As described in Section 1.3.3.2.1, the crystalline nature of the crust also makes it a promising source of (continuous) GWs. A solid crust should, in theory, be capable of supporting elastic stresses, which can then build elastic strain as the star undergoes changes in its evolution (perhaps due to temperature gradients induced by magnetic fields, for example!). If these strains *do* develop in an asymmetric way, then the resulting deformation can produce a time-varying quadrupole moment as the star rotates (Sec. 3.1.2).

2.3.1 The outer crust

The outer crust begins at the crust-ocean interface when the ratio of Coulomb energy to thermal energy,

$$\Gamma_{\mathrm{Coul}} = \frac{Z^2 e^2}{k_{\mathrm{B}} T} \left(\frac{4\pi n_{\mathrm{b}}}{3} \right)^{1/3}, \tag{2.9}$$

exceeds the canonical value 175 (and is solid wherever $\Gamma_{\mathrm{Coul}} \geq \Gamma_{\mathrm{m}} = 175$; Haensel et al., 2007). In the above, Z is the atomic number (nuclear charge), e is the elementary charge, and k_{B} is the Boltzmann constant.

It is generally assumed (for simplicity) that matter in the outer crust forms a *perfect crystal*, with a single nuclear species at each lattice site. This is generally referred to as the *one component plasma* (OCP) approximation. In reality however, the crustal layers are expected to contain a number of impurities, violating the OCP approximation (this will be discussed in greater detail in Sec. 4.4). The melting temperature for a *multi-component plasma* can be $\lesssim 20\%$ greater than the canonical value implied by the OCP (corresponding to $\Gamma_{\mathrm{m}} = 175$) for a given crustal layer (Fantina et al., 2020). For a typical NS, the melting temperature is in the region $10^8 - 10^9$ K.

---

[4] Rather than go into details here, the interested reader is referred to Gourgouliatos et al. (2022) for a comprehensive review of the current progress on understanding magnetic field evolution.

The squared-dependence of the nuclear charge in Eq. (2.9) indicates that the state of the matter in the crust strongly depends on composition. Almost all models of the outer crust trace their origins to the seminal paper of Baym et al. (1971). Perhaps the most essential input of this model is the ground-state masses of the nuclei that occupy the lattice sites at a given density. In the low density regions of the crust, these masses can be determined from terrestrial laboratory measurements (e.g. Wang et al., 2017).

The equilibrium values of A and Z at a given pressure are those that minimise the Gibbs free energy (2.8). In the Wigner-Seitz (W-S) approximation, the Gibbs energy of the W-S cell is often written (e.g. Haensel and Pichon, 1994)

$$G_{\rm cell}(A,\,Z) = W_{\rm N}(A,\,Z) + W_{\rm L}(Z,\,n_{\rm N}) + [\epsilon_e(n_{\rm e}) + P]/n_{\rm N}\,, \tag{2.10}$$

where $W_{\rm N}$ is the energy of the nucleus (obtained from a table of known ground-state masses), $W_{\rm L}$ is the body-centred cubic lattice energy (given by Eq. (3) of Baym et al., 1971), $\epsilon_{\rm e}$ is the electron energy density and $n_{\rm e}$, $n_{\rm N}$ are the electron and nuclei number densities respectively. At a given pressure, the latter quantities $n_{\rm e}$, $n_{\rm N}$ are determined from the relations

$$\begin{aligned} n_{\rm e} &= Z n_{\rm N}\,, \\ P &= P_{\rm e}(n_{\rm e},\,Z) + P_{\rm L}(n_{\rm N},\,Z)\,. \end{aligned} \tag{2.11}$$

Experimental nuclear data has come quite a long way since Baym et al. (1971), and the masses of many new neutron-rich isotopes have been measured. A recent review by Chamel and Haensel (2008), for example, state that, at the time of writing, the maximum density at which nuclei have been studied experimentally was $\rho_{\rm max}^{\rm exp} \sim 10^{11}$ g cm^{-3}, up from around $\rho_{\rm max}^{\rm exp} \sim 10^{10}$ g cm^{-3} at the time the Baym et al. (1971) article was written (Haensel and Pichon, 1994). The composition of the outer crust at densities $\lesssim 4\times10^{11}$ g cm^{-3} for a particular recent model is shown in Tab. 2.1, where nuclides with experimentally-measured masses are indicated in boldface.

Beyond this density however, the nuclei are so neutron-rich that there is almost no experimental information. The composition of the rest of the outer crust can only be determined from theoretical extrapolations, and therefore the nuclei predicted to exist in these dense layers becomes model dependent.

2.3.2 The inner crust

As the density inside the crust increases, the (ground-state) value Z/A of nuclei decreases[5]. As it does so, there is a corresponding reduction of the net chemical potential $\mu_{\rm n}$ of neutrons within the nuclei. The neutrons become less and less bound, until eventually, $\mu_{\rm n} = 0$ and the neutrons

---

[5] See the final column of Table 2.1.

TABLE 2.1: Composition (atomic number Z, neutron number N, and atomic mass number A) of the outer crust of a non-accreted neutron star. The maximum density at which each element appears is indicated in the fourth column. Nuclides with experimentally measured masses are indicated in boldface. Adapted from Table VII of Rüster et al. (2006).

Element	Z	N	$\rho_{\max}$ (g cm^{-3})	Z/A
^{56}**Fe**	26	30	8.02×10^{6}	0.464
^{62}**Ni**	28	34	2.71×10^{8}	0.452
^{64}**Ni**	28	36	1.33×10^{9}	0.438
^{66}**Ni**	28	38	1.50×10^{9}	0.424
^{86}**Kr**	36	50	3.09×10^{9}	0.419
^{84}**Se**	34	50	1.06×10^{10}	0.405
^{82}**Ge**	32	50	2.79×10^{10}	0.390
^{80}**Zn**	30	50	6.07×10^{10}	0.375
^{82}Zn	30	52	8.46×10^{10}	0.366
^{128}Pd	46	82	9.67×10^{10}	0.359
^{126}Ru	44	82	1.47×10^{11}	0.349
^{124}Mo	42	82	2.11×10^{11}	0.339
^{122}Zr	40	82	2.89×10^{11}	0.327
^{120}Sr	38	82	3.97×10^{11}	0.316
^{118}Kr	36	82	4.27×10^{11}	0.305

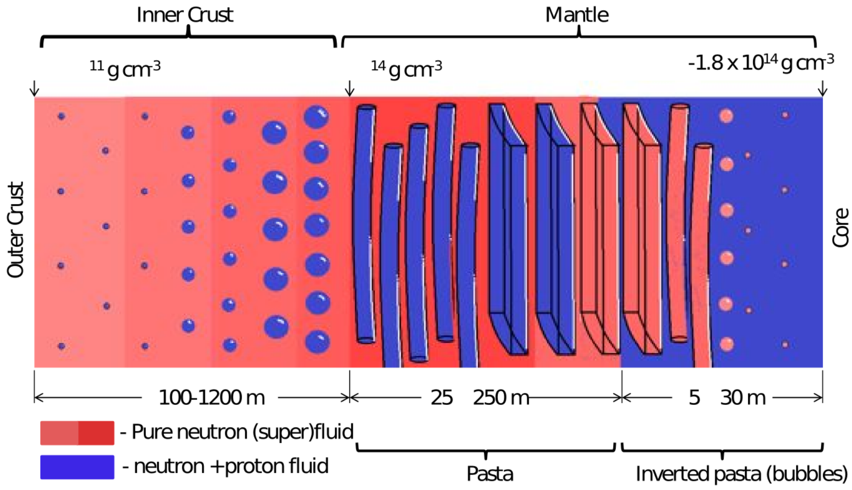

FIGURE 2.2: Schematic illustration of the ground-state structure of neutron stars as a function of density. Reproduced from Newton (2013).

begin to 'drip out' of the nuclei entirely[6]. The layers of the inner crust therefore consist of exceptionally neutron-rich nuclei that are immersed in a gas of dripped neutrons. The system is strongly coupled, and subsequently the constituent layers of the inner crust are more commonly identified as nuclear *clusters* rather than 'individual nuclei' like in the outer crust, in order to account for the presence of the neutron gas.

In principle, the method to compute the equilibrium composition of the inner crust is the same as in the outer crust; one must minimise the Gibbs energy (2.8) at fixed pressure. The total Gibbs

---

[6] One may think of this as a reduction of the energy required to liberate a neutron from a filled sea of degenerate Fermions.

energy of a Wigner-Seitz sphere in the *inner crust* however is different to that of the outer crust (Eq. (2.10)), instead given by (Haensel and Zdunik, 1990a)

$$\begin{aligned} G_{\mathrm{cell}}(A,\, Z) = & W_{\mathrm{N}}(A,\, Z,\, n_{\mathrm{n}}) + W_{\mathrm{L}}(Z,\, n_{\mathrm{N}}) \\ & + [\epsilon_{\mathrm{e}}(n_{\mathrm{e}}) + (1 - n_{\mathrm{N}} V_{N})\epsilon_{\mathrm{n}}(n_{\mathrm{n}}) + P]/n_{\mathrm{N}}\,, \end{aligned} \tag{2.12}$$

and includes two additional quantities which account for the presence of dripped neutrons in the Wigner-Seitz sphere. These are V_{N} and ϵ_{n}, which represent the volume of the nucleus and the energy density of the neutron gas respectively. At a given pressure in the inner crust, the values of n_{e}, n_{N}, n_{n} are determined from the *three* relations

$$\begin{aligned} n_{\mathrm{e}} &= Z n_{\mathrm{N}}\,, \\ P &= P_{\mathrm{e}}(n_{\mathrm{e}},\, Z) + P_{\mathrm{L}}(n_{\mathrm{N}},\, Z) + P_{\mathrm{n}}(n_{\mathrm{n}},\, Z)\,, \\ A_{\mathrm{cell}} &= A + n_{\mathrm{n}}(1/n_{\mathrm{N}} - V_{\mathrm{N}})\,. \end{aligned} \tag{2.13}$$

The additional complication of solving for the equilibrium nuclei in the inner crust are two-fold: (i) the contribution to the total energy density of the neutron gas must be accounted for, and (ii) one must construct a theoretical framework in which to calculate the nuclear masses for a given (A, Z) in the absence of experimental data.

Indeed, recreating a system anything like that of the inner crust in a terrestrial laboratory is far beyond current capabilities. Generally speaking, there are three different theoretical approaches to computing the structure of the inner crust. In order of increasing complexity, they are:

- i) a purely *classical* approach using the ‘Compressible Liquid Drop Model’ (CLDM),
- ii) a *semi-classical* treatment using the ‘Extended Thomas-Fermi’ approximation ,
- iii) a purely *quantum mechanical* treatment using the Hartree-Fock approximation.

The details of such methods are beyond the scope of this thesis, but a comprehensive introductory description of each method can be found in Sections 3.2.1 - 3.2.3 of Chamel and Haensel (2008). To highlight the differences that can arise for different models, the predicted composition of the inner crust as calculated by Negele and Vautherin (1973) (an older calculation) and Baldo et al. (2007a,b) (a more recent calculation) is given in Table 2.2.

2.4 Accreting neutron stars

The narrative of this chapter thus far has pertained specifically to the structure of single, isolated neutron stars. It is the case, however, that many NSs are known to reside in binary systems

TABLE 2.2: Composition (atomic number Z, neutron number N) of nuclear clusters in the inner crust of a non-accreted neutron star calculated by Negele and Vautherin (1973) (*left*) and Baldo et al. (2007a,b) (*right*). In contrast to Table 2.1, N is a sum of the number of neutrons bound in nuclei *and* of those forming a neutron gas, per nucleus (i.e. the number of neutrons in a Wigner–Seitz sphere).

Element	Z	N	$\rho_{\max}$ (g cm^{-3})	$Z/A_{\rm cell}$	Element	Z	N	$\rho_{\max}$ (g cm^{-3})	$Z/A_{\rm cell}$
^{180}Zr	40	140	4.67×10^{11}	0.222	^{212}Te	52	160	4.52×10^{11}	0.325
^{200}Zr	40	160	6.69×10^{11}	0.200	^{562}Xe	54	508	1.53×10^{12}	0.106
^{250}Zr	40	210	1.00×10^{12}	0.160	^{830}Sn	50	780	3.62×10^{12}	0.064
^{320}Zr	40	280	1.47×10^{12}	0.125	^{1020}Pd	46	974	7.06×10^{12}	0.047
^{500}Zr	40	460	2.66×10^{12}	0.080	^{1529}Ba	56	1473	1.22×10^{13}	0.038
^{950}Sn	50	900	6.24×10^{12}	0.052	^{1351}Pd	46	1305	1.94×10^{13}	0.035
^{1100}Sn	50	1050	9.65×10^{12}	0.046	^{1269}Zr	40	1229	2.89×10^{13}	0.033
^{1350}Sn	50	1300	1.49×10^{13}	0.038	^{636}Cr	20	616	4.12×10^{13}	0.031
^{1800}Sn	50	1750	3.41×10^{13}	0.028	^{642}Ca	20	622	5.65×10^{13}	0.031
^{1500}Zn	40	1460	7.94×10^{13}	0.027	^{642}Ca	20	622	7.52×10^{13}	0.031
^{982}Ge	32	950	1.32×10^{14}	0.033	^{633}Ca	20	613	9.76×10^{13}	0.032

alongside a lower-mass companion. It is believed that around 100 of such systems exist in the Milky Way alone (Liu et al., 2007), and are known as *low mass X-ray binaries*[7] (LMXBs) since they are visible primarily in the X-ray region of the electromagnetic spectrum.

2.4.1 Neutron stars in low-mass X-ray binaries

Low mass X-ray binaries are thought to be very long-lived, typically approaching 10^{10} years. Over their lifetime, the NSs in these systems accrete hydrogen, helium and other light elements from their sub-solar companion via a process known as *Roche lobe overflow* (Sec. 3.2.1) at rates typically of the order $10^{-11} < \dot{M} < 10^{-8}$ M$_\odot$ yr^{-1}. This forms an accretion disk around the NS, whereby matter may then fall onto the star's surface (see Fig. 2.3). This process releases gravitational binding energy, most of which is radiated away as X-rays, for which the system is named.

Thermonuclear burning of accreted matter via rapid proton capture (rp) processes generates a layer of mostly iron-peak nuclides ($A \sim 60 - 100$) that settle at the base of the ocean (Fig. 2.4). If the rate of accretion onto the star is low, the burning of helium is unstable, leading to a series of thermonuclear flashes known as type I X-ray bursts[8]. The nature of type I X-ray bursts can vary from system to system. Some are quasi-periodic, occurring every few hours/days at a time; whilst others are more transient in nature, occurring over days/weeks. In the latter case, the bursts are separated by extended periods of quiescence, where there is little to no accretion (see Sec. 4.1).

---

[7] An LMXB system may also contain a black hole rather than a NS, though these are not of relevance for GW emission.

[8] There are also type II X-ray bursts, but these are not released from the NS itself, but from the accretion disk as a result of instabilities in the accretion flow.

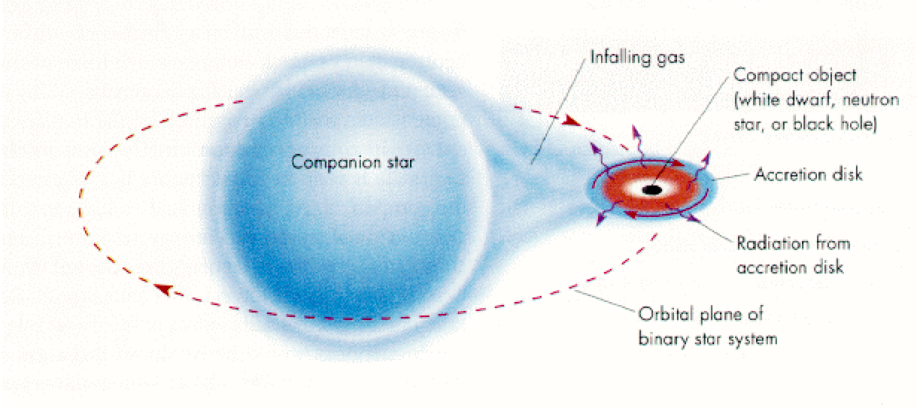

FIGURE 2.3: Schematic diagram of a low-mass X-ray binary. A compact object such as a black hole or neutron star accretes matter from a low-mass companion star leading to characteristic X-ray emission from the accretion disk. Image credit: `astro.ufl.edu`

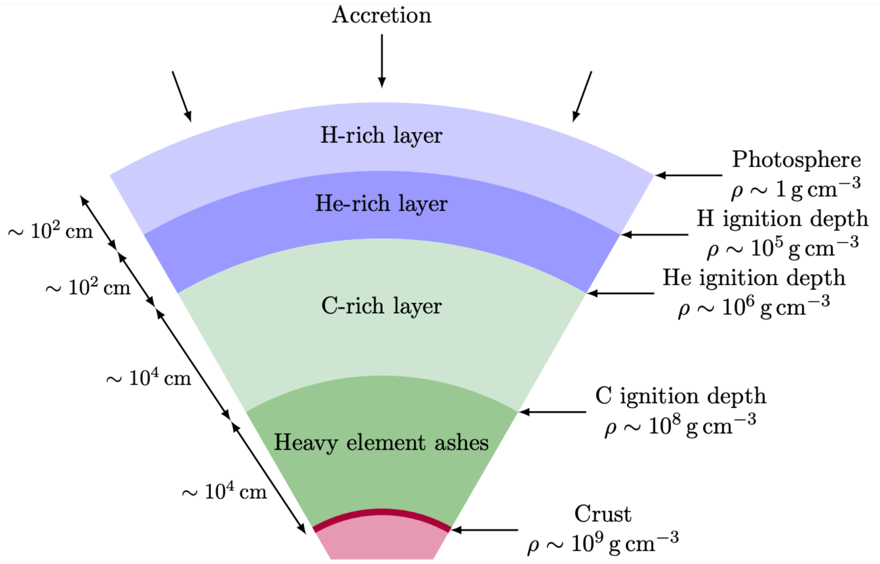

FIGURE 2.4: Schematic illustration of the outer structure of an accreting neutron star, showing the depths at which thermonuclear burning occurs. Image credit: Harpole (2018).

2.4.2 Composition of accreting neutron stars

An isolated neutron star is assumed to comprise matter in its ground-state, in complete thermodynamic equilibrium. In the later stages of the star's evolution, however, it is possible that the matter might be shifted away from this equilibrium state. Such is the case for an old accreting NS, with the process of accreting matter over millions years replacing the primordial crust. During extended periods of accretion, the nuclear ashes produced as a result of thermonuclear burning sink into the crust under the compressive weight of freshly accreted matter. Assuming constant accretion at a rate $\dot{M}$ / 10^{-9} $M_\odot$ yr^{-1}, such a process should occur within $\sim 10^8$ years, well within the lifespan of a typical LMXB.

The composition of accreted NS crusts has been considered by many authors (e.g. Haensel and Zdunik, 1990a; Haensel and Zdunik, 2003; Haensel and Zdunik, 2008; Gupta et al., 2008;

Lau et al., 2018; Fantina et al., 2018; Gusakov and Chugunov, 2020). The general procedure for calculating the composition is to follow the evolution of nuclear ashes (usually pure ^{56}Fe; assuming the one component plasma approximation) as they undergo compression. Inside the crust, the 'cold' nature of the matter restricts further thermonuclear burning due to high Coulomb barriers. Instead, a 'reshuffling' of the nucleons can only be achieved via electron captures, neutron emissions, and pycnonuclear reactions.

Compression of matter increases the magnitude of the Fermi energy E_F of free electrons, to the point whereby an electron capture on a nucleus

$$(A, Z) + e^- \longrightarrow (A, Z-1) + \nu_\mathrm{e} \tag{2.14}$$

is energetically favourable. A nucleus (A, Z) is transformed into a nucleus $(A, Z-1)$, accompanied by the emission of an electron neutrino. The process occurs as soon as the pressure reaches the critical value P_β, such that $g(A, Z, P_\beta) = g(A, Z-1, P_\beta)$, with g being the Gibbs energy of the *nucleus* Eq. (2.8) - related to the Gibbs free energy of the W-S cell Eqs (2.10) and (2.12) as $g = G_\mathrm{cell}/A$ (Fantina et al., 2018). Further captures on the daughter nucleus continue until the most energetically favourable nucleus Z_α is produced, occurring when $g(A, Z_\alpha, P_\beta) < g(A, Z_\alpha - 1, P_\beta)$. Much like the case of the ground-state crust, this corresponds to a local minimum of g at the pressure P_β, except with an additional constraint that the mass number A be fixed to that of the assumed ashes of nuclear burning (Fig. 2.5).

Within the ultra-dense environment of these stars, it is required that nuclei must contain even numbers of protons and neutrons in order to be stable (Haensel and Zdunik, 1990a). In the outer crust (i.e. before the neutron drip point), this condition necessitates a two-step electron capture process such that

$$(A, Z) + e^- \longrightarrow (A, Z-1) + \nu_\mathrm{e} \tag{2.15}$$

$$(A, Z-1) + e^- \longrightarrow (A, Z-2) + \nu_\mathrm{e} + \epsilon_\mathrm{nuc}\,, \tag{2.16}$$

each time the threshold pressure P_β for a single electron capture is reached. The total number of nucleons in the nuclei does not change as a result of electron capture, but does lead to a systematic decrease in Z with increasing density. The first electron capture (2.15) occurs in quasi-equilibrium, taking place very close to the threshold $\mu_e \approx E\{A, Z-1\} - E\{A, Z\}$[9] and leads to negligible heat release. The daughter nucleus, however, being 'odd-odd' (referring to the numbers of protons and neutrons) is unstable, and subsequently captures a second electron in a non-equilibrium way, since the pressure P_β (the threshold pressure for the first e^- capture) is significantly above the threshold pressure on the odd-odd nucleus. As a result, this second

---

[9] This is essentially just the mass difference between the parent and daughter nuclei.

electron capture releases heat energy, equivalent to the change in the Gibbs free-energy per nucleus as

$$\epsilon_{\rm nuc} \equiv \Delta g = \left[G_{\rm cell}(A, Z-1, P_\beta) - G_{\rm cell}(A, Z-2, P_\beta)\right]/A\,. \tag{2.17}$$

As matter is compressed deeper and deeper into the crust, nuclei become progressively more neutron-rich as a result of successive electron captures. Beyond the neutron-drip point, further captures may be accompanied by the spontaneous emission of free neutrons

$$(A, Z) + e^- \longrightarrow (A, Z-1) + \nu_{\rm e} \tag{2.18}$$

$$(A, Z-1) + e^- \longrightarrow (A - \Delta{\rm n}, Z-2) + \Delta{\rm n} + \nu_{\rm e} + \epsilon_{\rm nuc}\,, \tag{2.19}$$

and a nucleus (A, Z) is transformed into nucleus $(A - \Delta{\rm n},\ Z-2)$ with the emission of Δn neutrons and an electron neutrino. Since these reaction chains cannot be experimentally verified, the number of emitted neutrons can vary depending on both the chosen nuclear-mass model and assumed composition of X-ray burst ashes. The possibility of neutron emission results in much more complicated reaction chains in the inner crust than the two-step electron captures in the outer crust. For example, Haensel and Zdunik (1990a) predict that electron capture on a ^{52}S nucleus triggers a series of neutron emissions and further electron captures. Like in the outer crust, captures continue until minimisation of the Gibbs free-energy $g(A, Z_\alpha, P_\beta) < g(A, Z_\alpha - 1, P_\beta)$ is achieved[10].

Minimisation of the Gibbs free energy on a ^{52}S nucleus in the inner crust as calculated by Haensel and Zdunik (1990a) yields the result

$$^{52}{\rm S} \longrightarrow ^{46}{\rm Si} + 6{\rm n} + 2e^- + 2\nu_{\rm e}\,, \tag{2.20}$$

with the entire chain of reactions consisting of

$$\begin{aligned}
&^{52}{\rm S} + e^- \longrightarrow ^{52}{\rm P} + \nu_{\rm e}\,,\\
&^{52}{\rm P} \longrightarrow ^{51}{\rm P} + {\rm n}\,,\\
&^{51}{\rm P} \longrightarrow ^{49}{\rm P} + 2{\rm n}\,,\\
&^{49}{\rm P} + e^- \longrightarrow ^{49}{\rm Si} + \nu_{\rm e}\,,\\
&^{49}{\rm Si} \longrightarrow ^{48}{\rm Si} + {\rm n}\,,\\
&^{48}{\rm Si} \longrightarrow ^{46}{\rm Si} + 2{\rm n}\,.
\end{aligned} \tag{2.21}$$

---

[10] Though, remember that in the inner crust one must account for the presence of the neutron gas.

Ordinarily, large Coulomb barriers in *non-accreting* NSs prohibits nucleus-nucleus interactions. However, consecutive electron captures in accreting systems successively lowers the Coulomb barrier (since Z decreases). At the same time, the compression of matter also squeezes the nuclei into a smaller and smaller volume. This, combined with the associated increase of the zero-point vibration energy of nuclei at each lattice site, may eventually trigger so-called *pycnonuclear reactions*; whereby two identical nuclei tunnel through the depleted Coulomb barrier and fuse to form a single nucleus (e.g. Shapiro and Teukolsky, 1983). Following an electron capture in the inner crust (via the sequence of interactions (2.18) - (2.19)), the pycnonuclear fusion of two nuclei may occur as

$$(A, Z-2) + (A, Z-2) \rightarrow (2A, 2Z-4) + \epsilon_{\mathrm{nuc}} \,. \tag{2.22}$$

The resulting nucleus is usually unstable, and is accompanied by significant energy release (as well as neutron emission) as the daughter nucleus de-excites:

$$(2A, 2Z-4) \rightarrow (2A-\Delta\mathrm{n}, 2Z-4) + \Delta\mathrm{n} + \epsilon_{\mathrm{nuc}} \,. \tag{2.23}$$

The seminal description of the evolution of compressed accreted matter was calculated by Haensel and Zdunik (1990a) (henceforth HZ90). They calculated the composition and full sequence of nuclear interactions using the compressible liquid drop model, assuming ashes of stable nuclear burning to be pure ^{56}Fe. This model was later extended by the same authors (Haensel and Zdunik, 2008; henceforth HZ08) to calculate the composition of the accreted crust assuming X-ray ashes of ^{106}Pd rather than ^{56}Fe, in response to results obtained from newer X-ray burst simulations by Schatz et al. (2001), which utilized a much larger network of nuclei than previous works.

More recently, the composition of accreted NS crusts was considered by Fantina et al. (2018) (henceforth F+18). Rather than use utilize the compressible liquid-drop model, F+18 follow a more microscopic approach; based on self-consistent nuclear energy-density functional (EDF) theory (e.g. Bender et al., 2003; Stone and Reinhard, 2007), utilizing the Brussels–Montreal EDFs BSk19, BSk20, and BSk21 (for which the composition of the crust of *non-accreting* NSs has already been calculated; Pearson et al., 2011, 2012).

The improvements of the F+18 model compared to the HZ90/HZ08 models are twofold:

- i) the use of more recent experimental atomic mass measurements,
- ii) the inclusion of nuclear shell effects.

In Fig. 2.5 we show the run of atomic number Z (solid lines) and mass number A (dashed lines) with density for each of the HZ90, HZ08 and F+18 models. In the outer crust, the composition

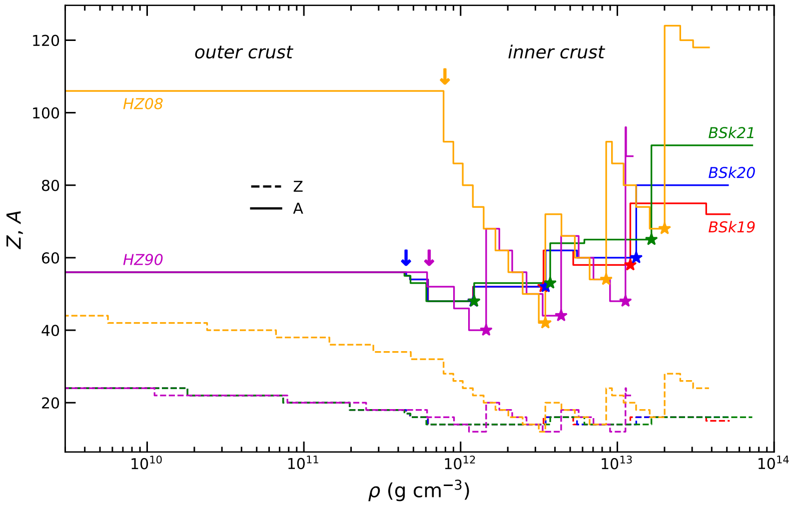

FIGURE 2.5: Atomic number Z (dashed lines) and mass number A (solid lines) of nuclear clusters in the crust of an accreting neutron star as a function of the density for the EoS models BSk19-21 (F+18), HZ90, and HZ08 indicated near the curves. The location of pycnonuclear reactions are marked by stars, and colored arrows denote the transition from the outer to the inner crust (i.e. the neutron drip point).

is strongly tied to the assumed ashes of nuclear burning. The HZ08 model (which assumes ashes of ^{106}Pd) predicts a highly stratified crust, with approximately twice as many electron captures occurring as the HZ90 model (which both assume the compressible liquid drop model). The F+18 model - the more microscopic calculation - also predicts an identical (A, Z) composition to the HZ90 model in the outer crust (both assume ashes of pure ^{56}Fe), differentiated only by the densities at which nuclei first appear.

The structure of the inner crust is also notably different between the three models. Firstly, Fig. 2.5 indicates that once pycnonuclear fusion becomes possible ($\rho \sim 10^{12}$ g cm^{-3}); the compositions of the HZ90 and HZ08 models converge, suggesting that the composition in the inner crust ($10^{12} - 10^{13}$ g cm^{-3}) is largely independent of the burst ashes in the liquid-drop approach. Both HZ90 and HZ08 predict the inner crust to be far more stratified than the micropscopic F+18 approach, however, which instead predicts a freezing of the nuclear composition at $Z = 14$; a result that may be attributed to the inclusion of the proton shell effects. Analogous to that of the atomic shell model (where filled orbital electron shells results in better stability), it is expected that specific numbers of nucleons correspond to complete shells within atomic nuclei. Since the successive electron captures leads to the systematic decrease in Z with density, there are certain points where the binding energy of the next nucleus in the capture sequence is significantly less than the last one; corresponding to nuclei that contain a complete shell. Such a result also corroborates predictions made by Dutta et al. (2004), who suggest that $Z = 14$ is a *magic proton number* in neutron star matter, whereby the protons are arranged into a complete shell and thus more stable against both electron captures and pycnonuclear reactions.

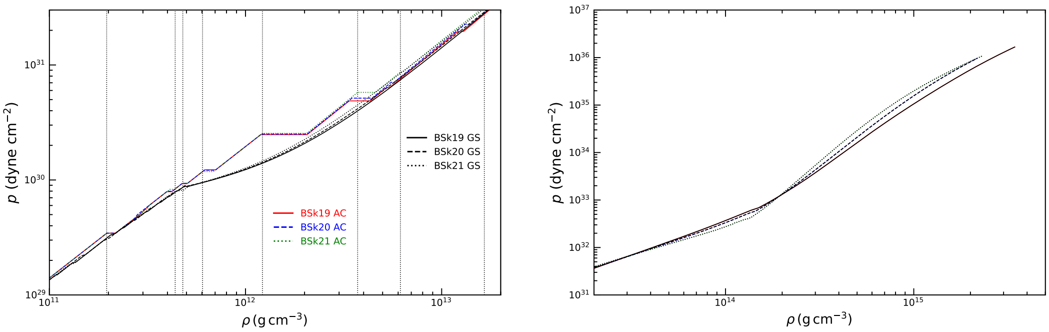

FIGURE 2.6: Pressure versus mass-energy density of the crust (*left panel*) and core (*right panel*) of accreted (AC) and non-accreted (GS) NSs for EoSs based on the EDFs BSk19, BSk20, and BSk21. Vertical dotted lines indicate the approximate location of nuclear transitions across each EoS model.

Pycnonuclear reactions in the inner crust are marked as stars in Fig. 2.5, that (along with individual electron captures) release heat locally in the crust during periods of active accretion. These reactions are thought to source the X-rays observed from LMXBs during later periods of quiescence, as the star cools and heat is transported to the surface (Sec. 4.1). How exactly these non-equilibrium interactions dictate the thermal structure will be discussed in greater detail in Chapter 4.

2.5 Analytical representations of the equation of state: BSk19, BSk20, and BSk21

The equation of state is the fundamental input for many neutron star calculations. In Fig. 2.6 we plot the pressure-density relations calculated from the EDFs BSk19, BSk20, and BSk21 in the crust (left panel) and core (right panel) of both accreted and non-accreted neutron stars[11].

Throughout the star, it is required that the pressure vary *continuously* (Baym et al., 1971). Because of this, at a transition $(A, Z) \rightarrow (A', Z')$ between two nuclear species, the pressure must also be continuous (Haensel and Zdunik, 1990a). This fact necessitates abrupt density discontinuities every time there is a change of nuclear species, which can be seen clearly in Fig. 2.6. In the outer crust, relativistic electrons supply most of the pressure, indicating that the electron number density n_e must also be continuous at each transition. For the accreted crust, the decrease in Z as a result of double electron capture indicates that the baryon number density must change by an amount (Baym et al., 1971)

---

[11] The BSk equation of state tables themselves are freely available from the Centre de Données astronomiques de Strasbourg at `https://vizier.cds.unistra.fr/viz-bin/VizieR?-source=J/A+A/665/A74` for the accreted crust, and `https://vizier.cds.unistra.fr/viz-bin/VizieR?-source=J/A+A/559/A128` for the non-accreted crust.

$$n_{\mathrm{b}}' - n_{\mathrm{b}} \approx n_{\mathrm{e}} \left(\frac{A'}{Z'} - \frac{A}{Z} \right), \tag{2.24}$$

which corresponds to a fractional change in the rest mass density $\rho = \epsilon / c^2$ as

$$\frac{\Delta \rho}{\rho} \approx \frac{\Delta n_{\mathrm{b}}}{n_{\mathrm{b}}} \approx \frac{Z/A}{Z'/A'} - 1 \,. \tag{2.25}$$

The increase in density at each interface $\Delta\rho/\rho$ in the accreted crust for each of the BSk19, BSk20, and BSk21 equations of state can be found in the fifth columns of the composition tables A.1 - A.3, reproduced (for convenience) from Fantina et al. (2018) in Appendix A.1[12].

These density discontinuities can introduce an array of difficulties in numerical calculations at points in the crust where discontinuities occur. This is especially true of calculations that involve derivatives of the mass density ρ (such as the adiabatic index; Sec. 2.5.2.1), or integrals over the density profile of the crust (Sec. 6.2.1.2).

An approximation of the EoS, however, may be implemented to (partially) circumvent these difficulties. To this end, we shall follow a method outlined by Potekhin et al. (2013) who approximated the BSk19-21 EoSs for *non-accreted* NSs, with a fully analytical function which 'smoothly' interpolates across the jumps. By introducing two variables $\zeta = \log_{10}(P/\mathrm{dyne\ \ cm}^{-2})$ and $\xi = \log_{10}(\rho/\mathrm{g\ \ cm}^{-3})$ - which we shall henceforth label as χ in order to avoid future confusion of ξ^i with a displacement vector field (Sec. 6.2) - the authors were able to parameterise the pressure-density relation $P(\rho)$ of non-accreted neutron stars as (*cf.* their Eq. (3))

$$\begin{aligned} \zeta = {} & \frac{a_1 + a_2\chi + a_3\chi^3}{1 + a_4\chi} \{\exp[a_5(\chi - a_6)] + 1\}^{-1} \\ & + (a_7 + a_8\chi)\{\exp[a_9(a_6 - \chi)] + 1\}^{-1} \\ & + (a_{10} + a_{11}\chi)\{\exp[a_{12}(a_{13} - \chi)] + 1\}^{-1} \\ & + (a_{14} + a_{15}\chi)\{\exp[a_{16}(a_{17} - \chi)] + 1\}^{-1} \\ & + \frac{a_{18}}{1 + [a_{19}(\chi - a_{20})]^2} + \frac{a_{21}}{1 + [a_{22}(\chi - a_{23})]^2} \,, \end{aligned} \tag{2.26}$$

where the values of the parameters a_i for the (non-accreted) BSk19, BSk20, and BSk21 EoSs are given in Table 2 of Potekhin et al. (2013).

In order to parameterise the *accreted* EoS, we use the Python `Scipy` routine `curve_fit` to create a non-linear least squared fit to the analytic function ζ using tabulated data specific to the accreted BSk19-21 equations of state. Initial guesses for a_{1-23} were constructed by fixing them to that of values given in Table 2 of Potekhin et al. (2013) for the corresponding non-accreted

---

[12] We reproduce the tables here since we will make use, and refer back to, these tables a number of times at various points throughout this thesis.

TABLE 2.3: Values of a_i that parameterise the analytical fit Eq. (2.26) for the *accreted* equations of state BSk19, BSk20 and BSk21 (see Fig. 2.7).

i	BSk19	BSk20	BSk21
		a_i	
1	3.790	3.916	4.843
2	7.461	7.436	6.989
3	0.00759	0.00766	0.00712
4	0.20818	0.20799	0.19326
5	3.913	3.588	4.078
6	12.260	12.263	12.242
7	13.284	13.752	10.523
8	1.3734	1.3336	1.5900
9	3.898	3.578	4.108
10	- 13.026	- 23.342	- 28.724
11	0.9307	1.6281	2.0854
12	5.91	4.99	4.85
13	14.387	14.191	14.303
14	16.652	23.575	22.880
15	- 1.0530	- 1.5222	- 1.7717
16	2.489	2.135	0.999
17	15.405	14.980	15.329
18	- 0.026	- 0.018	0.035
19	2.25	6.67	4.64
20	11.44	11.64	11.74
21	- 0.028	- 0.031	- 0.082
22	20.3	15.0	10.0
23	14.20	14.19	14.15

EoS. The new (optimal) values of a_i were then found by enforcing that the sum of the squared residuals of $\zeta[\chi(\rho), a_i] - P$, be minimized. The optimal parameters for the accreted EoSs are given in Table 2.3.

In the upper panels of Fig. 2.7 we show BSk19 (left), BSk20 (center), and BSk21 (right), together with their analytical representations. Crosses in the upper panels show rarefied (for clarity) tabulated data for the accreted crust (AC), and the colored lines show the analytical fits computed via Eq. (2.26) and Table 2.3. To aid comparison, we also include the analytic fits for the non-accreted (ground-state) crust (GC) computed via Eq. (2.26) and Table 2 in Potekhin et al. (2013). We plot the function $\zeta - 1.4\chi$ as a function of the density, since this allows for a better inspection of the fit in the crust, which we care most about.

Though the tabular data is rarefied, one can easily identify the density jumps $\Delta\rho/\rho$ with the aid of the vertical dotted lines in the lower panel of Fig. 2.7, which indicate the location of each capture layer in density space across each EoS (see the second columns in Tables A.1 - A.3). The lower panel shows the relative percentage difference between the fits and the tabulated data (of the accreted star). The typical error in the fits is $\approx 0.3\%$, a similar level of accuracy to the fit of the non-accreted EoSs obtained by Potekhin et al. (2013). The maximum error we obtain,

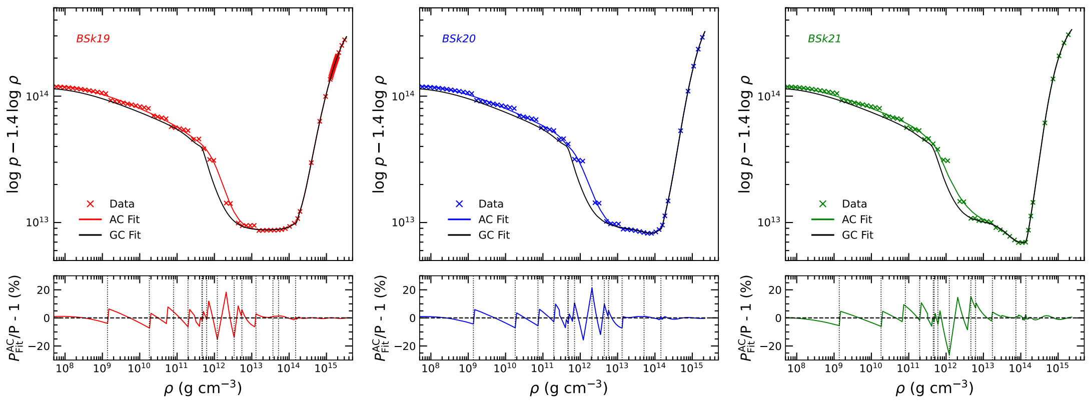

FIGURE 2.7: *Upper panels*: Analytical fits to the pressure-density relations predicted by the EDFs BSk19 (*left*), BSk20 (*centre*) and BSk21 (*right*) for 'AC' accreted (coloured lines; Fantina et al., 2018, 2022) and 'GC' ground-state non-accreted (black lines; Goriely et al., 2010; Pearson et al., 2011, 2012) neutron stars. Symbols denote (rarefied) tabular data points. Coloured lines indicate the analytic fits to the accreted crust obtained via Eq. (2.26) and Table 2.3. Black lines indicate the analytic fits to the non-accreted crust obtained via Eq. (2.26) and Table 2 in Potekhin et al. (2013). *Lower panel*: Relative percentage difference between the tabulated data and analytic fit of the accreted crust. Vertical dotted lines indicate the location of each capture layer from Tables A1 - A3 of Fantina et al. (2018).

however, is 26% (for BSk21), and occurs at $\rho = 1.2 \times 10^{12}$ g cm^{-3}, corresponding to a density jump $\Delta\rho/\rho = 0.68$ at the location of a pycnonuclear reaction in the inner crust (Table A.3). Such a large discontinuity is challenging for the least-squares fit, which attempts to smoothly interpolate between the two points either side of the jump.

In what follows, we shall proceed with the analytical representations of the BSk19-21 equations of state obtained via Eq. (2.26), using the values of a_i given in Table 2.3 for the accreted crust (and values of a_i given in Table 2 of Potekhin et al. (2013) when making use of the non-accreted EoS). The fits do not make any appreciable difference to the hydrostatic and thermal profiles of the star as compared to using only tabulated data (the *average* error in the fits is $\lesssim 1\%$). Any slight losses in accuracy in the thermal calculation, will, in any case, be far outweighed by the fact that we achieve much better numerical convergence when solving the elastic perturbation equations (Sec. 6.2.1) when using the analytical fit as compared to the tabulated data.

2.5.1 Fermion number fractions

Most of the physical parameters inside neutron stars are functions of position. In the accreted crust, many of these parameters are determined by the composition, which also varies with depth (Fig. 2.5). The F+18 composition tables A.1 - A.3 provide a wealth of data, including the values of atomic number Z, mass number A, and the mass fraction of free neutrons $X_{\rm n}$ that comprise the different layers of the crust. From these parameters, a number of other useful density-dependent quantities can be derived.

Firstly, the number density of the nuclei of particular species (A, Z) within a given crustal layer can be computed as

$$n_{\rm N} = \frac{\rho}{A m_{\rm b}}(1 - X_{\rm n}) \,, \tag{2.27}$$

where $m_{\rm b} = 1.67 \times 10^{-24}$ g is the average baryon mass. From this quantity, the number of electrons per unit volume may be obtained via

$$n_{\rm e} = n_N \, Z = \frac{Z}{A} \frac{\rho}{m_{\rm b}}(1 - X_{\rm n}) \,. \tag{2.28}$$

Similarly, past the neutron drip point, the number of free neutrons in the inner crust per unit volume is calculated as

$$n_{\rm n} = n_{\rm b} X_{\rm n} \,, \tag{2.29}$$

where the baryon number density $n_{\rm b}$ is given by

$$n_{\rm b} = \frac{\rho}{m_{\rm b}} \,. \tag{2.30}$$

It is assumed that the cores of both accreting and non-accreting neutron stars are the same (Fantina et al., 2022). The EDFs BSk19-21 predict a npeμ matter composition in the core, as calculated by Pearson et al. (2011, 2012). The number densities of these particles are given by

$$n_{\rm x} = n_{\rm b} Y_{\rm x} \,, \tag{2.31}$$

where $Y_{\rm x} = Y_{\rm n} \,, Y_{\rm p} \,, Y_{\rm e} \,, Y_\mu$ are the number fractions of the neutrons, protons, electrons, and muons respectively. Alongside the analytical expressions for the EoS, convenient fitting formulae for calculating the lepton fractions Y_e and Y_μ in the core were also obtained by Potekhin et al. (2013) (*cf.* their Eq. (9)), and are given by

$$Y_{{\rm e},\mu} = \frac{q_1^{({\rm e},\mu)} + q_2^{({\rm e},\mu)} n_{\rm b} + q_3^{(e,\mu)} n_{\rm b}^4}{1 + q_4^{({\rm e},\mu)} n_{\rm b}^{3/2} + q_5^{({\rm e},\mu)} n_{\rm b}^4} \exp(-q_6^{({\rm e},\mu)} n_{\rm b}^5) \,, \tag{2.32}$$

where the parameters $q_i^{(e,\mu)}$ are given in Table 2.4 (reproduced from Table 6 of Potekhin et al., 2013). The core is usually assumed to be electrically neutral, and so the proton and neutron fractions therefore follow from Eq. (2.32) as

$$Y_{\mathrm{p}} = Y_{\mathrm{e}} + Y_{\mu}\,, \tag{2.33}$$

and

$$Y_{\mathrm{n}} = 1 - Y_{\mathrm{p}}\,. \tag{2.34}$$

It is possible for Eq. (2.32) to return a negative value, in which case it should be replaced by zero (Potekhin et al., 2013). Such a scenario is possible for the muons, in regions of the core where they are forbidden (i.e where the muon chemical potential exceeds than of the electron chemical potential; $\mu_\mu > \mu_e$).

As we shall see, in order to determine the thermal properties of the crust, it is useful to know the Fermi momentum of these particles. Irrespective of whether they are relativistic or not, the Fermi momentum of each of the constituent particles can be calculated from their respective number densities as

$$p_{\mathrm{F}} = \hbar(3\pi^2 n_{\mathrm{x}})^{1/3}\,, \tag{2.35}$$

where $\mathrm{x} = \mathrm{e}, \mu, \mathrm{n}, \mathrm{p}$ denotes the particle of interest. In the crust, the number densities of free electrons and free neutrons are given by Eqs (2.28) and (2.29) respectively. In the core, the number densities of each particle are obtained from Eqs. (2.32) - (2.34). The particle fractions per baryon $Y_{\mathrm{e},\mu,\mathrm{n},\mathrm{p}}$ in both the crust and core of an accreting neutron star are shown in Figs 2.8 and 2.9 respectively, as a function of the baryon density for each of BSk19, BSk20, and BSk21.

If required, to check how relativistic the Fermions are, one can compute the so-called relativity parameter x_{r}, which for a Fermi gas, is

$$x_{\mathrm{r}} = \frac{p_{\mathrm{F}}}{m_{\mathrm{x}}c} = \frac{\hbar}{m_{\mathrm{x}}c}(3\pi^2 n_{\mathrm{x}})^{1/3}\,. \tag{2.36}$$

In general, electrons are relativistic for all but the lowest density regions of the crust, whilst muons are relativistic in the core. The neutrons on the other hand are very much non-relativistic in the crust, but can become (along with the protons) mildy-relativistic in the inner core. When relativistic-effects *are* important, the rest-mass of the particle ($m_{\mathrm{e}} = 9.1 \times 10^{-28}$ g, $m_{\mathrm{n}} \approx m_{\mathrm{p}} = m_{\mathrm{b}}$) must be necessarily replaced by the *effective* mass of the particle

$$m_{\mathrm{x}}^{*} = \sqrt{m_{\mathrm{x}}^2 + \frac{p_{\mathrm{F}}^2}{c^2}}\,. \tag{2.37}$$

TABLE 2.4: Values of $q_i^{(e,\mu)}$ which determine the particle fractions (2.32) for the equations of state BSk19, BSk20 and BSk21. Reproduced from Table 6 of Potekhin et al. (2013).

i	BSk19	BSk20	BSk21
		$q_i^{(\mathrm{e})}$	
1	- 0.0157	- 0.0078	0.00575
2	0.9063	0.075	0.4983
3	0.0	0.508	9.673
4	26.97	22.888	16.31
5	106.5	0.449	38.383
6	5.82	0.00323	0.0
		$q_i^{(\mu)}$	
1	- 0.0315	- 0.0364	- 0.0365
2	0.25	0.2748	0.247
3	0.0	0.2603	11.49
4	12.42	12.99	24.55
5	72.4	0.0767	48.544
6	19.5	0.00413	0.0

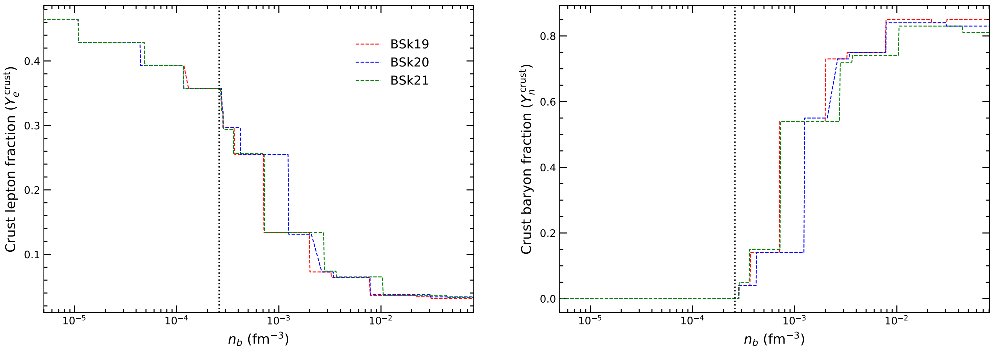

FIGURE 2.8: *Left panel*: Number fraction of electrons Y_e in the crust of an accreting neutron star (relative to the number of nucleons) as a function of the baryon number density n_b for the three *accreting* equations of state BSk19, BSk20, and BSk21. *Right panel*: Number fraction of free neutrons Y_n in the crust. In both panels the vertical dotted lines denotes the (approximate) neutron drip point across each EoS model.

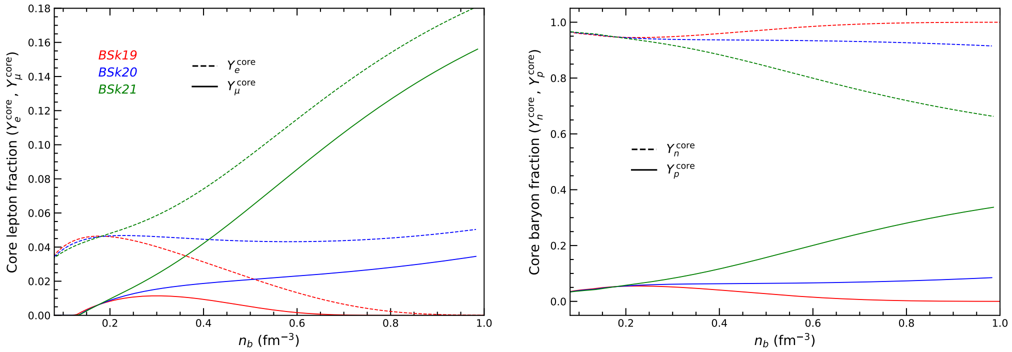

FIGURE 2.9: *Left panel*: Number fractions of electrons Y_e (solid lines) and muons Y_μ (dashed lines) in the core of a neutron star as functions of the baryon number density n_b as computed via Eq. (2.32) and Table 2.4. *Right panel*: Number fractions of protons Y_p and neutrons Y_n in the core.

2.5.2 Microphysical structure of the accreted crust

Having described the composition and equation of state (i.e. the pressure-density relation), there are two more additional pieces of physics (that are determined by EoS) that we require in order to complete the 'physical' picture of the accreted crust. These are the adiabatic index Γ, and shear modulus μ, which we shall now discuss in turn.

2.5.2.1 The adiabatic index

From the analytical expressions Eq. (2.26), differentiation with respect to the mass density ρ allows us to compute the *adiabatic index*, defined by (Potekhin et al., 2013)

$$\Gamma = \frac{n_{\rm b}}{P}\frac{dP}{dn_{\rm b}} = \left[1 + \frac{P}{\rho c^2}\right]\frac{\rho}{P}\frac{dP}{d\rho}\,. \tag{2.38}$$

The run of Γ with density for each of BSk19 (left), BSk20 (center), and BSk21 (right) (Fig. 2.7) is given in Fig. 2.10. First, let us compare the adiabatic index of the accreted crust obtained via finite difference methods (solid lines), with that of the *non-accreted* EoS (dashed lines; as obtained from the analytical fit). In both cases the pressure in the outer layers is supplied almost entirely by ultra-relativistic electrons, and thus $\Gamma \approx 4/3$. At densities $10^{11} \lesssim \rho \lesssim 10^{13}$ g cm^{-3}, however, the adiabatic index of the accreted crust $\Gamma_{\rm AC}$ is significantly different from that of the ground-state crust $\Gamma_{\rm GC}$.

Specifically, the adiabatic index in the two types of crust quickly diverge at the neutron drip point ($\rho \sim 4.5\times10^{11}$ g cm^{-3}). This behavior can be understood in the following way. In the shallowest layers of the inner crust (i.e. where the number fraction of free neutrons is low), the adiabatic index may be approximated as (Fantina et al., 2022)

$$\Gamma \approx \left.\frac{\partial\log(P)}{\partial\log(n_{\rm b})}\right|_{Z/A_{\rm cell}} + \left.\frac{\partial\log(P)}{\partial\log(Z/A_{\rm cell})}\right|_{n_{\rm b}}\frac{d\log(Z/A_{\rm cell})}{d\log(n_{\rm b})} \approx \frac{4}{3}\left[1 + \frac{d\log(Z/A_{\rm cell})}{d\log(n_{\rm b})}\right], \tag{2.39}$$

and the pressure may be assumed to still be dominated largely by the electrons. The number density of electrons in the crust is $n_e \propto Z/A$ (i.e. ensuring charge neutrality). In the inner accreted crust, the ratio $Z/A_{\rm cell}$ ($A_{\rm cell}$ referring to the fact that 'clusters' of nuclei form in the inner crust) can only change at a transition $(A_1, Z_1) \rightarrow (A_2, Z_2)$, and thus $d(Z/A_{\rm cell})/d\log(n_{\rm b}) = 0$. The value of $\Gamma_{\rm AC}$ therefore begins to push slightly above $4/3$ with depth as the number of free neutrons in the crust increases (the fraction of free neutrons at each capture layer is given in the 4th column of Tables A.1 - A.3). In the catalysed crust however, where there are no electron captures, there is a drastic *continuous* fall in $Z/A_{\rm cell}$ (and therefore $d(Z/A_{\rm cell})/d\log(n_{\rm b}) < 0$; *cf.* Fig. 4 of Fantina et al., 2018), leading to a correspondingly drastic fall in $\Gamma_{\rm GC}$ at on the onset of neutron drip.

At densities exceeding that of the heat producing region in the accreted crust ($\rho \gtrsim 10^{13}$ g cm^{-3}), note that the EoSs merge as the fraction of free neutrons X_n increases and neutrons become overwhelmingly the dominant source of pressure in both types of crust (Fig. 2.7 and see Fantina et al., 2022). This leads to a merging of Γ at high density, where they become very similar near the crust-core transition.

Now compare these results with our analytical fit to the accreted EoS (dotted lines), which shows a strong softening compared to that of the tabulated data. Softening occurs since the fit smooths out the density discontinuities that occur at each capture layer (particularly those that occur at $\sim 10^{12} - 10^{13}$ g cm^{-3}). This smoothing of the discontinuities leads to what would otherwise indicate an effective continuous decrease in the ratio Z/A_cell, and a corresponding decrease in Γ_AC, to the point whereby the analytic fit to the accreted EoS largely resembles that of a non-accreted crust.

This is not to say we should be dismissive of our analytical fit, however. On the contrary, a more recent study by Gusakov and Chugunov (2020) indicates that actually the EoS of the accreted inner crust should be very close to that of the ground-state (nonaccreted) EoS (*cf.* their Fig. 1). Unlike the picture of the accreted crust sketched out in Sec. 2.4.2, Gusakov and Chugunov (2020) argue that the treatment of the inner crust in the F+18 model (and by extension HZ90 and HZ08) is thermodynamically inconsistent, since it is predicated on the notion that unbound neutrons move together with nuclei as accreted matter is compressed through the inner crust. The so-called neutron Hydrostatic and Diffusion (nHD) model, which allows free neutrons to filter through different layers of the crust, in fact predicts a dramatic softening of the accreted EoS, and therefore consistent with the analytic representations of the accreted crust derived in the previous section.

The composition of the accreted crust as predicted by the nHD model is not the same as that predicted by the Fantina et al. (2018) model (see Fig. 5 of in Gusakov and Chugunov, 2020). There is therefore some systematic error in pairing the compositional information given in Tables A1 - A3 in Fantina et al. (2018) with the analytical fit to the EoS shown in Fig. 2.7 (and Fig. 2.10). Though, given that our analytical fits produce an adiabatic index $\Gamma_\mathrm{AC}^\mathrm{Fit}$ that lies somewhere in the region between the accreted (Γ_AC) and ground-state (Γ_GC) crust, we note that the errors are still within bounds set by both the Gusakov and Chugunov (2020) and Fantina et al. (2022) models.

It would, in future, be worthwhile repeating all of the calculations which are to be presented in this thesis using the GC20 model (alongside the BSk19-21 models we are already considering). At the time of writing, however, the EoS for GC20 model is not readily available, as well as the compositional information having only recently been made available in Tables 1 and 2 of Potekhin et al. (2023)[13].

---

[13] We will, however, briefly make use of their composition tables when estimating the mass quadrupole moment generated from capture layer shifts for different equation of state models in Sec. 6.3.2.

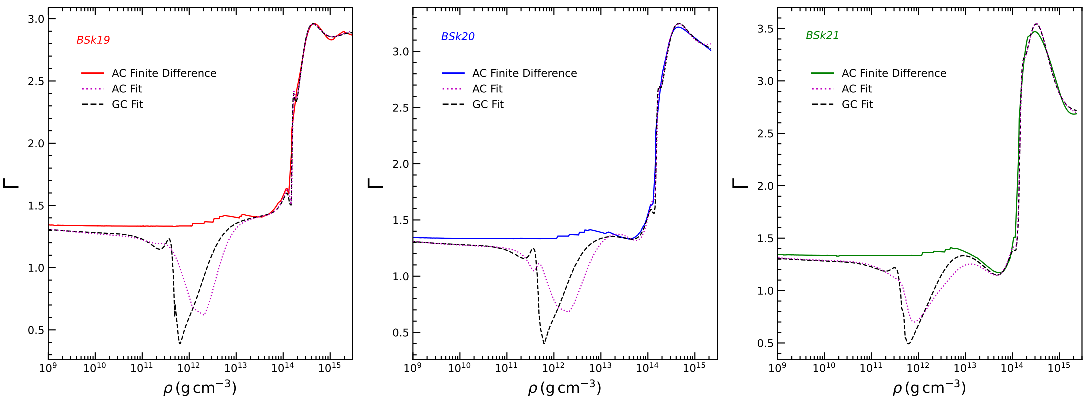

FIGURE 2.10: Adiabatic index $\Gamma = \partial \ln P / \partial \ln \rho$ corresponding to the pressure-density relations given in Fig. 2.7. Solid lines indicate Γ obtained via finite difference methods on tabulated data of the accreted equations of state BSk19 (*left*), BSk20 (*centre*), and BSk21 (*right*), while dotted and dashed lines were obtained via differentiation of Eq. (2.26) for the analytical representations of the accreted (AC) and ground-state (GC; non-accreted) equations of state respectively.

2.5.2.2 Shear modulus

The crust is usually assumed to be an isotropic, body-centered cubic Coulomb crystal with an effective shear modulus μ. To further complete the picture of our accreted crust, we use the result of Zdunik et al. (2008) (their Eq. (18)) obtained from the original calculation by Ogata and Ichimaru (1990), which we write as

$$\mu = 7.8 \times 10^{28} \left(\frac{\rho}{10^{13}\ \mathrm{g\ cm^{-3}}} \right)^{4/3} \left(\frac{10^3 (1 - X_\mathrm{n})}{A} \right)^{4/3} \left(\frac{Z}{40} \right)^2 \mathrm{dyne\ cm^{-2}}. \qquad (2.40)$$

We apply this formula to describe the shear modulus everywhere in the accreted crust. This choice is only an approximation, however, since Eq. (2.40) is (strictly speaking) only valid for point-like nuclei (Zdunik et al., 2008). Recall that the deepest layers of the crust likely contain the series of finite-sized ‘nuclear pastas’ discussed in Section 2.3.2 (recall Fig. 2.2) which, in principle, should be modelled differently (see e.g. Caplan et al., 2018 and references therein). We neglect the existence of pasta phases here, however, since the BSk19-21 EoSs assume purely spherical nuclei exist down to the crust-core transition (Pearson et al., 2012; Fantina et al., 2022).

The run of μ with pressure in the accreted crust is shown in the bottom panel of Fig. 2.11. It can be seen that the shear modulus is small relative to the pressure ($\mu/P \sim 10^{-3} - 10^{-2}$), which is indicative of how large a deformation can be supported by the crust (Ushomirsky et al., 2000). A series of (smoothed) discontinuities in the shear modulus are also observed at the location of each capture layer as $(A_1, Z_1) \to (A_2, Z_2)$ due to steps in both Z and A (as shown in the top two panels).

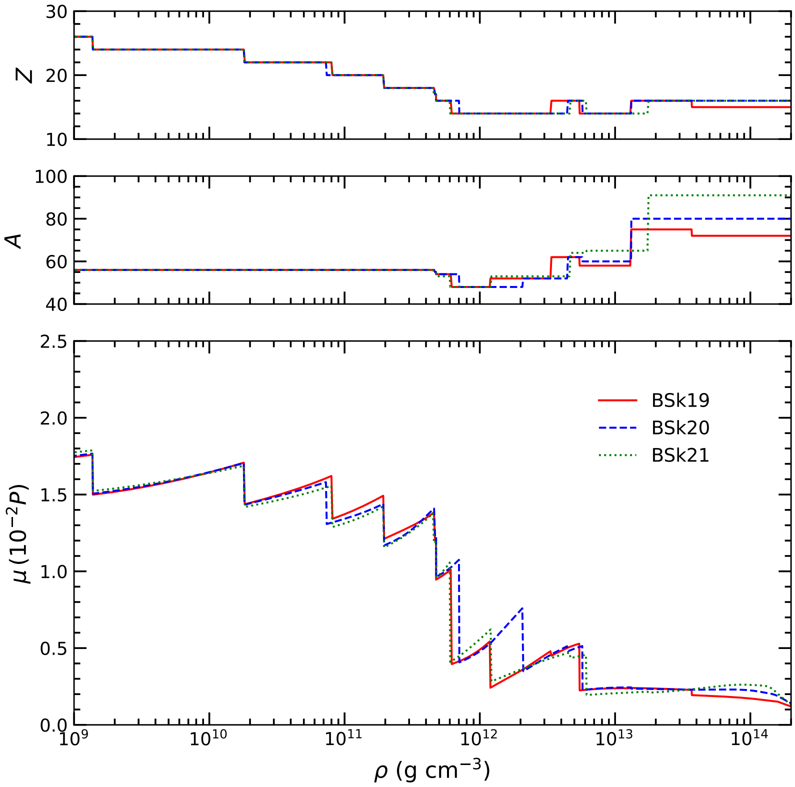

FIGURE 2.11: The run of atomic number Z (upper panel), mass number A (middle panel) and shear modulus μ/P (bottom panel) with depth in the crust of an accreted neutron star for the equations of state BSk19 (red solid line), BSk20 (blue dashed line) and BSk21 (green dotted line). Data is taken from Tables 1 and A1 - A3 of Fantina et al. (2018).

2.6 The stellar structure equations

In this section we derive both the Newtonian and relativistic equations of stellar structure for a non-rotating, spherically-symmetric body in static equilibrium. We will see how the EoS is the crucial ingredient for building spherical, fluid stars, and discuss the differences in the global structure of neutron stars composed of accreted and catalysed matter.

2.6.1 Newtonian stars

Neutron stars are often modelled as an ideal fluid. By definition, ideal (perfect) fluids have zero shear stresses, zero viscosity, and are isotropic in the sense that they exert pressure equally in all directions. In Newtonian theory, the fundamental equations of fluid dynamics (for a perfect fluid) are the *continuity equation*

$$\partial_t \rho + \nabla_i (\rho v^i) = 0 , \tag{2.41}$$

and the *Euler equation*

$$\rho(\partial_t + v^j \nabla_j) v_i = -\nabla_i P - \rho \nabla_i \Phi \,, \tag{2.42}$$

where ρ, P, v are the rest-mass, (isotropic) pressure, and velocity of the fluid respectively, and Φ is the gravitational potential, given by *Poisson's equation*

$$\nabla^2 \Phi \equiv \nabla_i (\nabla_i \Phi) = 4\pi G \rho \,, \tag{2.43}$$

where G is the gravitational constant. The continuity equation is a mathematical statement of mass conservation; the rate of change of mass in a fixed volume is equal to flux of mass through that volume. For a spherically-symmetric body, the total mass M is

$$M \equiv \int_0^R 4\pi r^2 \rho(r) dr \,, \tag{2.44}$$

where R is the radius of the body.

Similarly, the Euler equation is a mathematical statement of momentum conservation derived from Newton's second law; acceleration of the fluid (given by the time derivative of v on the LHS of Eq. (2.42)) is sourced by the presence of a pressure gradient and a gravitational field on the RHS of Eq. (2.42). The gravitational field itself is determined from Eq. (2.43), and is derived from Gauss's law for gravity which states that the gravitational flux through any closed surface is proportional to the enclosed mass.

Objects such as stars are self-gravitating bodies - the individual constituents of the star are held together by the combined gravity of the object as a whole. Stable stars are also assumed to be in equilibrium, as well as static. In this instance, the velocity in the fundamental equations (2.41) - (2.42) vanishes, leading to a trivial solution of the continuity equation (2.41) and the reduction of the Euler equation (2.42) to just

$$\nabla_i P = -\rho \nabla_i \Phi \,, \tag{2.45}$$

which is commonly referred to as the equation for *hydrostatic equilibrium* of a static, non-rotating fluid body. In this state, it is supported against gravitational collapse by just the fluid pressure gradient.

A static, non-rotating body that is perfectly spherical has a total mass given by Eq. (2.44). If we define $m(r)$ as the mass enclosed within some radius $r < R$, then it follows that

$$\frac{dm(r)}{dr} = 4\pi r^2 \rho(r) \,. \tag{2.46a}$$

Similarly, the equation for hydrostatic balance (2.45) for a spherically symmetric body (i.e. one that depends only on the radial coordinate) can be written

$$\frac{dP(r)}{dr} = -\rho \frac{d\Phi(r)}{dr} , \tag{2.46b}$$

where the latter term on the RHS may be obtained simply by integrating Poisson's equation to give

$$\frac{d\Phi(r)}{dr} = \frac{Gm(r)}{r^2} . \tag{2.46c}$$

The coupled equations (2.46) are the *Newtonian equations of stellar structure*. However, as they currently stand, these equations cannot be solved. In order to close this system, we need the equation of state; the pressure-density relation introduced in Section 2.2.

The Newtonian structure equations (2.46) are often used to model celestial objects such as main-sequence stars. The high-density regions of NSs, however, are not well described by these equations due to their compactness (an estimate of the significance of relativistic effects on a celestial object). A description of the core of a NS requires full general relativity in order to produce accurate results. This is not to say that Newtonian models are useless, however. Newtonian calculations are much easier to construct that those in general relativity, and may still be applicable in low-density regions like the crust.

Indeed, in this thesis we shall employ both a relativistic, as well as a Newtonian framework in order build thermal mountains. Specifically, we shall use the relativistic hydrostatic equations (which are to be discussed in the following section) in order to construct our background model, but make use of the Newtonian heat equations (Sec. 4.2) in order to compute our thermal model, as well as a modified form of the Newtonian Euler equation (2.42) (i.e. with the inclusion of a term involving the shear modulus μ) to compute the elastic response of the crust due to lateral temperature gradients (Sec. 6.2.1). We do this chiefly in order to make our calculations simpler, but so that we may still make use of realistic equations of state in our calculations, which would otherwise lead to grossly unphysical density profiles in Newtonian theory. Given the compactness of a typical neutron star is $M/R \sim 0.2$, however, we should expect fractional errors in the thermal structure and the elastic calculation when neglecting general relativity. Nonetheless, we shall proceed in this manner in order to simplify the overall problem and focus on prescribing a realistic source term (Sec. 6.2.1) that has, until now, been absent in the literature.

2.6.2 Relativistic stars

As we have now seen, the equilibrium structure of a fluid star results from the balance between the 'inwards pull' of gravity and the 'outwards push' of the fluid pressure. Deriving the hydrostatic structure equations in a relativistic framework is, in principle, not vastly different from that of the Newtonian procedure, except in one important regard.

The Euler equation (2.42) is, by construction, predicated on the fundamental premise of Newton's second law of motion. The existence of a gravitational acceleration $\nabla_i \Phi$ in Eq. (2.42) is necessarily associated with a 'force' that results in the acceleration of the fluid element. The term 'gravitational acceleration' under the description of general relativity, however, is a misnomer. In a Newtonian sense, gravitational acceleration is truly an acceleration of an object in free fall due to some gravitational force. In a relativistic description, though, such a force is fictitious.

Indeed, in general relativity, space and time are unified to into a single four-dimensional continuum. Whilst space in Newtonian gravity is necessarily flat, this is not the case in general relativity. The presence of matter results in a 'warping' of this so-called *spacetime*, with gravity manifesting as the geometric impression and objects in free fall traveling along geodesics in the spacetime. How exactly the matter shapes the geometry of the spacetime is dictated by the relativistic field equations[14]

$$G_{ab} \equiv R_{ab} - \frac{1}{2} R g_{ab} = \frac{8\pi G}{c^4} T_{ab} \,, \tag{2.47}$$

where G_{ab} is known as the Einstein tensor, R_{ab} is the Ricci tensor and R is the Ricci scalar; both of which are determined by the spacetime metric g_{ab}, which represents gravity. The energy-density and pressure within the system is then encoded in the energy-momentum tensor T_{ab}.

Solving Eq. (2.47) is, by any stretch of the imagination, a formidable task. Unabridged, the Einstein field equations are a system of ten, highly non-linear, coupled second-order partial differential equations. Indeed, finding *exact solutions* to Eq. (2.47) may only be achieved by exploiting various symmetries to simplify the problem.

One such symmetry we may seek to exploit is that of the (assumed) spherical symmetry of neutrons stars that we adopted in order to derive the Newtonian stellar structure equations (2.46a) - (2.46c).

In analogy with the previous section, we begin with the Bianchi identity, which tells us that

$$\nabla^a G_{ab} = 0 \,, \tag{2.48}$$

and therefore that the divergence of the stress-energy tensor (via Eq. (2.47)) also vanishes, such that

$$\nabla^a T_{ab} = 0 \,. \tag{2.49}$$

---

[14] Note that relativists often tend to use so-called *geometrized units*, where $G = c = 1$ in order to simplify the equations.

The above represents the law for conservation of both energy and momentum in GR, and may be loosely interpreted as the equations of motion for a *relativistic* fluid.

The energy-momentum tensor for an ideal fluid as given in Andersson and Comer (2021) is (their Eq. (5.11))

$$T_{ab} = (\epsilon + P)u_a u_b + P g_{ab} = \epsilon u_a u_b + P \perp_{ab} , \tag{2.50}$$

where ϵ is the total energy density (related to the rest-mass density ρ as $\epsilon = \rho c^2$ at $T = 0$ K) as measured - along with the isotropic pressure P - by an observer co-moving with the fluid with four-velocity u^a. In the final term on the RHS of Eq. (2.50), the projection operator $\perp_{ab} \equiv u_a u_b + g_{ab}$ is introduced in order to express the components of T_{ab} into the timelike and spacelike directions of an inertial observer.

Following Andersson and Comer (2021), contracting Eq. (2.49) along u^a yields

$$u^a \nabla_a \epsilon + (\epsilon + P)\nabla_a u^a = 0 . \tag{2.51}$$

This result, with ρ replaced with $(\epsilon + P)$ - i.e the inertial mass per unit volume - is the relativistic analogue of the continuity equation (2.41). Similarly, by projecting (2.49) along $\perp_{ab}$, one may obtain

$$(\epsilon + P)u^b \nabla_b u_a = - \perp_a^{\ b} \nabla_b P , \tag{2.52}$$

which may be identified as the relativistic analogue to the Euler equation (2.42).

2.6.2.1 The Tolman-Oppenheimer-Volkov equation

Having outlined the procedure for determining the equations of motion for a *relativistic* fluid (2.51) - (2.52), we now turn our attention back to the problem of hydrostatic equilibrium in general relativity[15].

Recall that we are considering the case of a static, non-rotating NS that is built of a perfect fluid. As a consequence, the only non-vanishing component of the fluid four-velocity u^a is the time component u^0. In much the same way as we proceeded in the Newtonian case, the static nature of the fluid means that the relativistic conservation equation (2.51) is trivially satisfied, and the relativistic Euler equation (2.52) is reduced to

---

[15] The interested reader may also want to consult a number of textbooks relating to the derivation of the general relativistic structure equations, including Maggiore (2007); Andersson (2019); Hartle (2021), to name a few.

$$\nabla_i P = -\frac{1}{2}(\epsilon + P)\nabla_i \nu \,, \tag{2.53}$$

where ν is now a function of the radial position r that is determined from the spacetime metric g_{ab}. The metric is a tool that encapsulates the geometric and causal structure of spacetime; akin to generalized Pythagorean theorem that also includes a temporal component. Birkhoff's theorem indicates that the *Schwarzschild solution* is the most general description of spacetime outside of a non-rotating, spherically symmetric star. Inside the star however, one need consider a more general metric, appropriate to that of a body with a static density and pressure profile. Distances in spacetime are measured by the line element, which for our spherically-symmetric NS (again in geometrized units $c = G = 1$; but will restore the dependence later on) is

$$ds^2 = g_{ab}dx^a dx^b = -e^\nu dt^2 + e^\lambda dr^2 + r^2(d\theta^2 + \sin^2\theta d\phi^2) \,, \tag{2.54}$$

where dx^a is the infinitesimal change in x^a. Like the function ν, λ is also a function of position, and both are often referred to appropriately as the *metric functions*. If one chooses the proper boundary conditions for this interior metric to match that of the Schwarzchild metric at the surface of the star (the empty space outside the star is exactly that described by the Schwarzschild metric), then ν and λ outside of the star are given by

$$e^\lambda \equiv \frac{1}{1 - 2M/r} \,, \tag{2.55}$$

$$e^\nu \equiv 1 - 2M/r \,. \tag{2.56}$$

By comparing the relativistic Euler equation (2.52) to that of its Newtonian counterpart (2.41), it can be inferred that the function $\nu(r)$ has the physical interpretation as the relativistic analogue to the Newtonian potential Φ. For our spherically symmetric NS, the equation for hydrostatic balance in relativity Eq. (2.51) can be written more explicitly as

$$\frac{dP}{dr} = -\frac{1}{2}(\epsilon + P)\frac{d\nu}{dr} \,. \tag{2.57}$$

In order to proceed, we require an expression analogous to (2.46c) obtained from Possion's equation. To do this, one must go back to the Einstein equations (2.47) for a perfect fluid (i.e. using Eq. (2.50)). The stress-energy tensor is diagonal (in a spherical coordinate system), with eigenvalues of energy density and pressure

$$T_t^t = \epsilon \,, \tag{2.58}$$

$$T_i^{\ j} = \delta_i^{\ j} P \,. \tag{2.59}$$

The only non-zero components of the Einstein tensor are therefore $G_t^{\ t}$ and $G_r^{\ r}$. Inserting Eqs (2.58) and (2.59) into the Einstein equation (2.47) yields

$$G_t^{\ t} = 8\pi T_t^{\ t} = 8\pi \epsilon e^{\nu} \quad \longrightarrow \quad \frac{dm}{dr} = 4\pi r^2 \epsilon \,, \tag{2.60}$$

$$G_r^{\ r} = 8\pi T_r^{\ r} = 8\pi P e^{-\nu} \quad \longrightarrow \quad \frac{d\nu}{dr} = \frac{2(m + 4\pi r^3 P)}{r(r-2m)} \,, \tag{2.61}$$

where, upon finally eliminating $d\nu/dr$ from Eqs. (2.57) and (2.61) (and restoring the values of G and c), one may obtain the relativistic equation for hydrostatic equilibrium as

$$\frac{dP}{dr} = -\frac{G\epsilon(r)m(r)}{c^2 r^2}\left[1 + \frac{P(r)}{\epsilon(r)}\right]\left[1 + \frac{4\pi r^3 P(r)}{m(r)c^2}\right]\left[1 - \frac{2Gm(r)}{c^2 r}\right]^{-1} \,. \tag{2.62}$$

Collectively, Eqs (2.60) - (2.62) are more famously referred to as the *Tolman-Oppenheimer-Volkoff equations* (TOV; Tolman, 1939; Oppenheimer and Volkoff, 1939).

2.6.3 Solutions to the Tolmann-Oppenheimer-Volkoff equations

The relativistic stellar structure equations (2.60) - (2.62), when appended with an appropriate barotropic equation of state, can be solved numerically for the quantities $P(r)$, $m(r)$ and $\nu(r)$ for a non-rotating, spherically symmetric neutron star. The system is a set of 2 coupled ordinary differential equations (ODEs) in (2.60) and (2.62) (one may see from Eqs (2.60) - (2.62) that the metric potential ν decouples from the other two equations), which constitutes a boundary value problem with a set of inner and outer boundary conditions:

Inner Boundary: At the centre of the star, the enclosed mass at $m(r_0)$ must vanish. Strictly speaking, the integration *should* begin at $r_0 = 0$, with suitable initial values $P_\mathrm{c} \equiv P(r_0) = P(\epsilon_\mathrm{c})$ and $\nu_\mathrm{c} \equiv \nu(r_0)$ specified[16]. However, the TOV equations in spherical coordinates are singular at the origin, and hence one must start at some small value $r \neq 0$ away from the origin. A leading-order series expansion of Eq. (2.60) at small radius yields

$$m(r) \approx 4/3\, \pi\, \epsilon_\mathrm{c}\, r_0^3 \,, \tag{2.63}$$

---

[16] The central pressure can be obtained simply via an interpolation of a chosen central density $\epsilon_\mathrm{c} = \rho_\mathrm{c} c^2$. As for the metric potential, since it decouples from (2.60) - (2.62), one is free to simply set $\nu(r = 0)$ with an arbitrary constant, and then correct it at the surface via a suitable outer boundary condition.

Table 2.5: Comparison of the maximum mass configurations for different equations of state listed in Haensel (2003) (*cf.* their Table 2) and those obtained using the `Python` ODE solver `solve_ivp`.

EoS	Maximum Mass Configurations (Haensel, 2003)		Maximum Mass Configurations (`solve_ivp`)	
	$M_{\max}$ ($M_{\odot}$)	R (km)	$M_{\max}$ ($M_{\odot}$)	R (km)
SLy	2.05	9.99	2.05	9.98
FPS	1.80	9.27	1.80	9.25
BPAL12	1.46	9.00	1.45	9.01
BGN1H1	1.64	9.38	1.63	9.34
BBB2	1.92	9.49	1.92	9.49

for an initial radius $0 < r_0 \ll R$ and central density $\rho_c \equiv \rho(r_0)$, which may be freely specified.

Outer Boundary: At the surface one must have $P(R) = 0$ as the pressure outside the star vanishes. One must also ensure consistency in matching the metric function $\nu(r)$ in the interior, to that of the exterior of the star given by the Schwarzchild solution (2.56) such that $e^{\nu(R)} = 1 - 2M/R$, with $M = M(R)$ the total mass-energy of the star.

In order to fix the hydrostatic structure, one may arbitrarily chose the central density ρ_c and integrate from the center of the star ($r \approx 0$) outward to where the pressure drops to zero. The TOV equations may be readily solved in this manner as an initial value problem using the `Python` programming language and the ODE solver `scipy.integrate.solve_IVP`, implementing an explicit Runge-Kutta method of order $O(h4)$ with error estimation of the order $O(h5)$. The fidelity of the integrator allows for automatic adjusting of the step size of the integration, which is advantageous since the domain of the integration is not known *a priori*. The solver returns an accurate value of r at which the condition $P(R) = 0$ is met, which is achieved via a root-finding algorithm to find the radial point corresponding to a sign change as $P(r) \to 0$.

For a given EoS, the solution of the TOV equations depends solely on the central density. Modifying the starting value of ϵ_c produces a corresponding one-parameter family of equilibrium configurations. The spectrum of masses and radii $[M(\epsilon_c), R(\epsilon_c)]$ for multiple equations of state may be depicted graphically to produce the famed *mass-radius (*M-R) diagrams. To test the suitability of the `scipy.integrate.solve_IVP` method, Fig. 2.12 gives the characteristic M-R curves solved in `Python` for a number of different EoSs listed in Haensel (2003).

It should be emphasised however that not all equilibrium solutions that may appear in the M-R diagram are stable solutions. Such unstable solutions are indicated by the dashed portions of the various curves in Fig. 2.12. In these regions, any density perturbations in the fluid would grow unabated (exponentially) in time, causing the NS to either expand, or collapse into a black hole. The maximum mass[17] (i.e. the largest stable solution, where $dM/dR = 0$) and corresponding radius for each EoS are listed of each in Table 2 of Haensel (2003), and therefore

---

[17] The existence of a 'maximum mass' is a relativistic phenomenon which manifests in the denominator of Eq. (2.61) which insists that $m < r/2$.

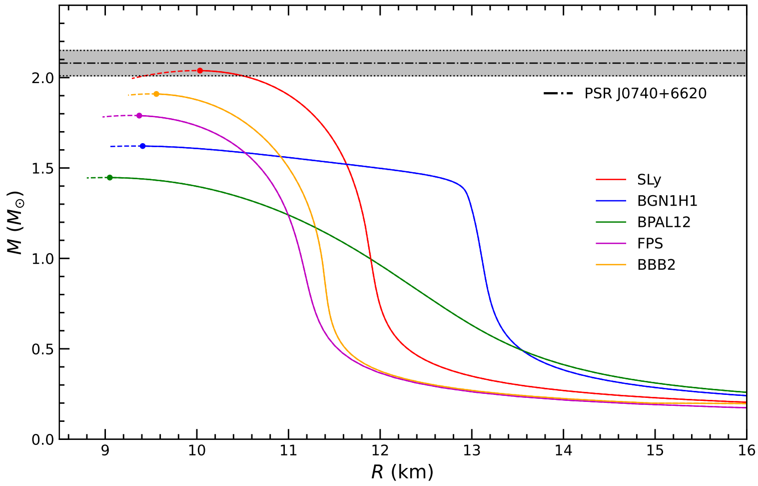

FIGURE 2.12: Gravitational mass M as function of the neutron star radius R for a number of different EoS models given in Haensel (2003). The maximum mass on each curve is indicated by a filled circle. Configurations to the left of the maximum (dashed lines) are unstable with respect to small radial perturbations. The shaded band corresponds to the measured mass of the millisecond pulsar PSR J0740+6620; $M^{68\%} = 2.08 \pm 0.07 M_\odot$ (Miller et al., 2021).

can be cross-referenced against `solve_IVP` to gauge its suitability for use in subsequent work. This comparison is summarised in Table 2.5, which shows good agreement across all candidates.

The uncertainty in the true nature of the interactions of matter beyond nuclear saturation leads to much speculation about the *exact* dependence of the pressure on density. The choice of EoS (such as those included in Figure 2.12) leads to differing predictions for the maximum mass that neutron stars may support. Since a plethora of different EoSs have been put forward, it is common to categorise them using a measure of so-called *stiffness*.

The stiffness qualitatively describes how quickly the pressure increases with density. The steeper this dependence, the 'stiffer' the EoS is said to be. Stiffness has the physical interpretation as follows: The stiffer the EoS, the more difficult it is to compress the constituent fluid, making it more stable against gravitational collapse. It is therefore the case that stiffer EoSs can support larger masses than their '*softer*' counterparts, which experience a greater amount of compression at an equivalent density.

Determining the true EoS of dense matter is certainly a candidate for the 'holy grail' of NS astrophysics. And though whilst many differing ideas have been put forward, there are couple of constraints that all realistic EoSs must satisfy. The two most notable restrictions are:

- i) the speed of sound c_s (in geometric units) at any point within the fluid must be less than 1 in order to respect causality,
- ii) that the speed of sound in the fluid be greater than zero, so that the fluid is thermodynamically stable.

TABLE 2.6: The baryon number density n_b, rest-mass density ρ, and pressure P at the crust-core transition predicted by the equations of state BSk19, BSk20, and BSk21. Adapted from Table II of Pearson et al. (2012).

EoS	$n_{\mathrm{crust-core}}$	$\rho_{\mathrm{crust-core}}$	$P_{\mathrm{crust-core}}$
BSk19	0.0885	1.497×10^{14}	6.850×10^{32}
BSk20	0.0854	1.444×10^{14}	5.844×10^{32}
BSk21	0.0809	1.367×10^{14}	4.302×10^{32}

These constraints are not particularly restrictive, however, and there is significant leeway in the regime $0 < c_s < 1$. In practise, narrowing down the true EoS comes down to a combination of both terrestrial experiments (e.g. measurements of the neutron skin thickness - PREX/CREX; Adhikari et al., 2021), as well as measurements of NS masses and radii through direct astrophysical (e.g. the *Neutron Star Interior Composition Explorer Mission* - NICER; Riley et al., 2021) and gravitational-wave observations (e.g. Abbott et al., 2018).

Indeed, the maximum mass may be inferred from astrophysical observations of both thermal and non-thermal emissions from the NS surface, which may then be cross referenced with a suitably large mass-radius diagram. Recent analysis of NICER XTI and XMM-Newton data on the millisecond pulsar PSR J0740+6620, for example, indicates the star has a gravitational mass $M^{68\%} = 2.08 \pm 0.07 M_{\odot}$ (Miller et al., 2021). Any EoS candidate that predicts a maximum mass of $M_{\max} \lesssim 2M_{\odot}$ is therefore likely too soft to be viable. In reference to Fig. 2.12, such a result indicates that only the SLy model is stiff enough to be viable amongst those sampled from Haensel (2003).

2.6.4 Hydrostatic structure of isolated and accreting neutron stars: BSk19, BSk20, and BSk21

The HZ90 model is the seminal description of the accreted crust, and has been used in many numerical simulations of accreting NSs since its original inception. One caveat to the model, however, is that the pressure-density table was only computed for the region of the crust where non-equilibrium reactions occur ($\sim 3 \times 10^7 - 2 \times 10^{13}$ g cm^{-3}). Therefore, to model an accreting NS as a whole, one is required to 'bolt on' this EoS to a separate one that describes the innermost part the crust; which itself must then be joined to a third EoS that describes the core. Constructing such a 'jury-rigged' pressure-density relation can, however, lead to systematic errors in the macroscopic structure of the star (e.g. the mass and radius) if the different pieces of the EoS are thermodynamically inconsistent (Fortin et al., 2016; Suleiman et al., 2021).

The EDFs BSk19, BSk20, and BSk21 on the other hand, are capable of modelling all of the outer crust, the neutron-rich clusters (together with the neutron liquid) of the inner crust, as well as homogeneous matter in the core in a thermodynamically consistent way. These EoSs are therefore said to provide a *unified* treatment of all regions of an accreted NS. Since unified EoSs for cold-catalysed matter can also be predicted by the BSk19-21 EDFs as well (Sec 2.5), this

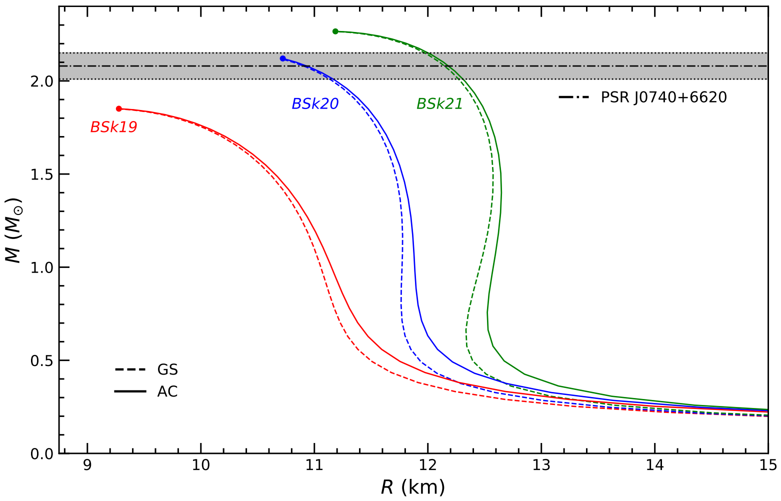

FIGURE 2.13: Mass-radius relations for accreted (AC) and non-accreted (GS) neutron stars for equations of state based on the energy-density functionals BSk19, BSk20, and BSk21. The maximum mass on each curve is indicated by a filled circle. The shaded band corresponds to the measured mass of the millisecond pulsar PSR J0740+6620; $M^{68\%} = 2.08 \pm 0.07 M_\odot$ (Miller et al., 2021).

allows for a direct comparison between the global properties of both accreting and non-accreting NSs (see also Fantina et al., 2022).

The accreted crust is noticeably stiffer than that of its ground-state counterpart, particularly in the region $10^{11} - 10^{13}$ g cm^{-3} (Figs 2.6 and 2.10). To further investigate the properties of the two types of crust, we solve the TOV equations for both the ground-state (Goriely et al., 2010) and accreted (Fantina et al., 2022) BSk19-21 EoSs, for a range of different central densities to create the familiar M-R curves. The result is shown in Fig. 2.13, where the difference in stiffness can be seen in the difference in radii between the two crusts. The largest masses in Fig. 2.13 are 1.86, 2.14, and 2.27 $M_\odot$ for the BSk19-21 EoSs respectively. For BSk19 and BSk21, these correspond to maximum TOV neutron star mass as calculated by Potekhin et al. (2015) (the maximum mass is effectively the same for both accreted and catalysed neutron stars). For BSk20, however, the largest mass is not the 'maximum' mass (i.e. where the star is hydrostatically stable), but rather the mass of the star at which the EoS becomes *superluminal* (i.e. where $dP/d\rho > c^2$). As noted in Potekhin et al. (2015), configurations with higher ρ_c (corresponding to 2.14 $M_\odot < M < 2.16 M_\odot$) should not be trusted as the innermost regions of the core will be superluminal. The publicly-available data tables have been truncated at the point whereby either the limit of hydrostatic stability is reached, or the EoS becomes superluminal, whichever occurs first (*cf.,* Fig. 8 of Potekhin et al. (2015) and surrounding text).

The softening of the ground-state EoS implies that its crust is thinner than that of a crust composed of processed material. To determine the actual thickness of the crust, one need know precisely the location of the crust-core transition (where the lattice structure disappears and the system

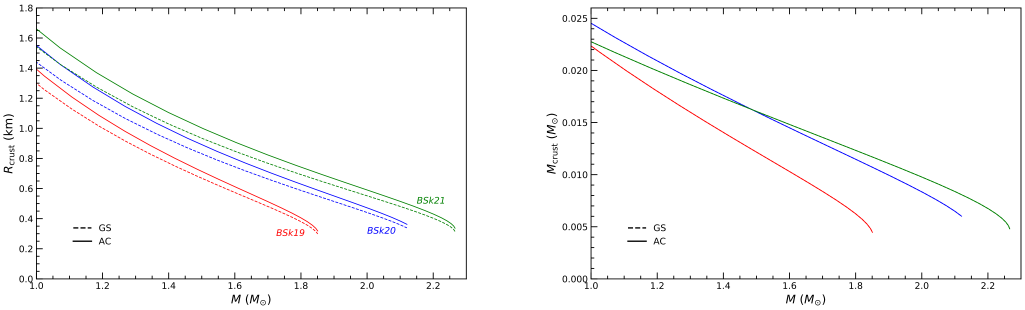

FIGURE 2.14: Thickness $R_{\rm crust}$ (*left panel*) and mass $M_{\rm crust}$ (*right panel*) of the crust of accreted (AC) and non-accreted (GS) neutron stars for equations of state based on the energy-density functionals BSk19, BSk20, and BSk21.

changes to a liquid phase of homogeneous matter), which can only be done accurately if the inner crust and the core are treated within the same physical framework. The location of the crust-core transition for the BSk19-21 EoSs - which is the same for both accreted and non-accreted crusts (Fantina et al., 2022) - are given in Table 2.6.

With the location of the crust-core transition known, one can determine the size of the core by integrating the TOV equations outwards from the chosen central density ρ_c, up to the core-crust transition (i.e. when the condition $P(R) = P_{\rm crust-core}$ is met) and computing the corresponding mass $M_{\rm core}$ and radius $R_{\rm core}$. The crust mass $M_{\rm crust}$ and crust thickness $R_{\rm crust}$ is then obtained by subtracting $M_{\rm core}$ and radius $R_{\rm core}$ from the result whereby $p(R) = 0$, corresponding to the surface of the star. In Fig. 2.14 we show the results of such a calculation, plotting the crustal thickness $R_{\rm crust}$ and crustal mass $M_{\rm crust}$ as a function of the total mass M. It is evident that whilst the respective masses of the two types of crust remain almost identical, the accreted crust is indeed thicker than its ground-state counterpart, at least within the Fantina et al. (2018, 2022) framework.

3

Gravitational-waves from Thermal Mountains

Having formally described the interior structure of spherically-symmetric neutron stars, in this chapter we shall discuss in greater detail one particular mechanism in which the neutron star may be driven away from this assumed perfect sphericity. We begin in Section 3.1 by summarising how exactly gravitational-waves emerge within the framework of general relativity, before moving on to discuss the rate at which energy is carried away by these waves from an arbitrary source.

In Section 3.2 we examine the rate at which GWs are radiated away specifically from a rigidly rotating neutron star with a sustained quadrupolar deformation. In Bildsten (1998) it was suggested that GW torques from a sufficiently large mountain could be limiting the spin period of accreting NSs; whereby angular momentum transferred from the accretion disk is balanced by the loss of angular momentum due to gravitational radiation. This equilibrium value has since been come to be known as the 'torque balance limit', and is discussed in greater detail in Section 3.2.1. We then conclude this chapter by describing the particular Bildsten (1998) mechanism to generate the required mountain - so-called 'wavy' electron capture layers - which form in the presence of an sufficiently anisotropic internal temperature distribution.

3.1 The Einstein equation revisited

As briefly mentioned at the top of Section 1.2, gravitational-waves are generated by any massive accelerating object. Akin to waves which ripple on the surface of a pond when disturbed, the motion of such objects creates ripples in the spacetime in which they inhabit.

The 'size' of these ripples is related to the amount of curvature of the spacetime. And, as we saw in Fig. 1.4, there is an abundance of astrophysical sources of gravitational radiation in the Universe. The strongest and most rapidly varying curvatures of spacetime occur in regions occupied by merging black holes and neutron stars. Though, even in this regime, predictions of the resulting gravitational radiation (such as the waveform in Fig. 1.2) may still only be achieved through full, computationally intensive *numerical* simulation of the Einstein Equation

$$G_{ab} \equiv R_{ab} - \frac{1}{2} R g_{ab} = \frac{8\pi G}{c^4} T_{ab}\,, \tag{3.1}$$

and in fact finding *exact* solutions may only be achieved in a number of idealised cases.

3.1.1 Gravitational-waves in linearised theory

A far more tractable problem is to consider the regime of weak spacetime curvature, such as the case for the motion of a pair of orbiting black holes or neutron stars *well-before* the point of merger. Any gravitational radiation from such a source may be idealised as a series of plane waves, originating as small perturbations on an otherwise flat spacetime which propagate away from the source at the speed of light.

Rather than solve the full Einstein equation, one assumes that the waves generated by the stress-energy tensor T_{ab} are sufficiently weak that the metric g_{ab} may be written as

$$g_{ab} = \eta_{ab} + h_{ab}\,, \tag{3.2}$$

where η_{ab} is the metric of flat spacetime (the Minkowski metric), given in Cartesian coordinates as

$$\eta_{ab} dx^a dx^b = -dt^2 + dx^2 + dy^2 + dz^2\,, \tag{3.3}$$

and h_{ab} is the metric perturbation (considered 'weak' in the sense that $|h_{ab}| \ll 1$ for all a and b).

The result obtained by evaluating the Einstein tensor G_{ab} to first order in the perturbed metric (3.2) is known as the *linearised theory of gravity*. Deeper insights into the theory of GWs may be found in a number of textbooks (Misner et al., 1973; Maggiore, 2007; Andersson, 2019; Hartle, 2021; to name a few), and so in this chapter will generally only summarise important results. In reproducing the linearised theory of gravity for our purposes, we start with the so-called *trace-reversed* metric perturbation

$$\bar{h}_{ab} = h_{ab} - \frac{1}{2} \eta_{ab} h\,. \tag{3.4}$$

The form of this perturbation is inspired by the form of the Einstein tensor itself (Eq. (3.1)), and reverses the sign of the trace as

$$\bar{h}^{a}{}_{a} = h^{a}{}_{a} - \frac{1}{2} h^{b}{}_{b} \delta^{a}{}_{a} = h^{a}{}_{a} - 2h^{b}{}_{b} = -h^{a}{}_{a} \, , \tag{3.5}$$

such that one may retrieve the original perturbation back as

$$\bar{\bar{h}}_{ab} = \bar{h}_{ab} - \frac{1}{2}\eta_{ab}\bar{h}^{c}{}_{c} = h_{ab} - \frac{1}{2}\eta_{ab}h^{c}{}_{c} + \frac{1}{2}\eta_{ab}h^{c}{}_{c} = h_{ab} \, . \tag{3.6}$$

Inserting the trace-reversed perturbation (3.4) into the Einstein tensor, after a little algebra one finds that

$$G_{ab} = -\frac{1}{2}(\Box\bar{h}_{ab} + \eta_{ab}\partial^{c}\partial^{d}\bar{h}_{cd} - \partial^{c}\partial_{b}\bar{h}_{ac} - \partial^{c}\partial_{a}\bar{h}_{bc}) \, , \tag{3.7}$$

where $\Box \equiv \partial^{a}\partial_{a}$ is the flat-space wave operator. Though, in its current form, this result remains rather daunting. General relativity is formulated in such a way however that ones choice of coordinates is, in some sense, arbitrary, and it is possible to simply choose a coordinate system in which the above may be simplified. The presence of the d'Alembert operator in the linearised Einstein tensor (3.7) leads one to seek a set of coordinates, or a *gauge*, which transforms (3.7) into that of a *wave equation*. Clearly, this could be achieved if the (trace-reversed) metric perturbation were to satisfy the condition

$$\eta_{ab}\partial^{c}\partial^{d}\bar{h}_{cd} - \partial^{c}\partial_{b}\bar{h}_{ac} - \partial^{c}\partial_{a}\bar{h}_{bc} = 0 \, . \tag{3.8}$$

One such condition is given by the requirement that

$$\partial^{b}\bar{h}_{ab} = 0 \, , \tag{3.9}$$

a set of four conditions which determine what is commonly known as the *Lorenz gauge*, due to its analogy with that of the equations of electromagnetism. In the Lorenz gauge, each of the 2nd, 3rd, and 4th terms in Eq. (3.7) immediately vanish, leaving us with the final result

$$G_{ab} = \Box\bar{h}_{ab} = -\frac{16\pi G}{c^{4}}T_{ab} \, . \tag{3.10}$$

3.1.2 Energy loss from gravitational-waves

Given the necessary conditions for their creation, GWs carry away energy from the system that produces them. Though, it is by no means a trivial task to *quantify* the energy associated with these waves. A central tenet of the theory of GR is the *equivalence principle*, which determines that gravitational effects 'vanish' in a local inertial frame. This is to say that one can always find a frame in which spacetime is flat in the neighbourhood of some other given point. The direct consequence of the equivalence principle is therefore that one cannot localise the effect of a passing GW, nor localise its energy.

It turns out that computing the rate of energy loss due to gravitational radiation (within the GR framework) requires going beyond that of the first-order perturbation of the Einstein tensor introduced in the previous section. The details of such a calculation are beyond what we require here, though the interested reader is directed to, for example, Andersson (2019) for a more concrete derivation.

If, for now, we remain in the regime of weak spacetime curvature, it is possible that one may find an approximate solution to Eq. (3.10) in terms of a formal expansion away from *Newtonian gravity*. This leads to the so-called *quadrupole formula*, which, in the absence of a strict derivation, can ultimately be anticipated from some more simple physics and a few dimensional arguments. What follows is based loosely on similar descriptions laid out in both Andersson (2019) and Hartle (2021).

To begin, recall that the (linearised) Einstein equation (3.10) is set of ten equations for each of the components of the (trace-reversed) metric perturbation $\bar{h}_{ab}$, with each component obeying a separate (sourced) flat-space wave equation of the form

$$-\frac{\partial^2 f(x)}{\partial t^2} + \vec{\nabla}^2 f(x) = j(x)\,. \tag{3.11}$$

The general solution to the above wave equation is obtained via a (retarded) Green's function[1]

$$f(\vec{x},\, t) = -\frac{1}{4\pi}\int \frac{[j(\vec{x}',\, t' = t - |\vec{x} - \vec{x}'|)]}{|\vec{x} - \vec{x}'|}\, d^3x'\,. \tag{3.12}$$

In keeping with the notion of 'weak' spacetime curvatures, it is natural to consider the form of the above solution at a distance far away from the (correspondingly weak) source. In this regime, one may assume that

$$t' = t - |\vec{x} - \vec{x}'| \approx t - r\ , \tag{3.13}$$

where r is the distance to the centre of the source; and so the general solution (3.12) is, asymptotically,

$$f(\vec{x}, t) \xrightarrow[r\to\infty]{} -\frac{1}{4\pi r}\int j(\vec{x}',\, t - r)\, d^3x'\,. \tag{3.14}$$

---

[1] Strictly speaking, the *most* general solution to Eq. (3.11) includes an *incoming* wave $O(\vec{x}',\, t + |\vec{x} - \vec{x}'|)$, as well as an outgoing wave $j(\vec{x}',\, t - |\vec{x} - \vec{x}'|)$. However, only the latter is physically relevant for the specific case of a gravitational-wave, and thus only the retarded, or casual, solution is required.

The asymptotic amplitude of a passing GW a large distance from a weak source (determined by the stress-energy tensor T_{ab}; Eq. (3.10)) is (in geometrized units), therefore

$$\bar{h}_{ab}(\vec{x},\, t) \xrightarrow[r\to\infty]{} \frac{4}{r}\int T_{ab}(\vec{x}',\, t-r)\, d^3x' \,. \tag{3.15}$$

This result is essentially an affirmation of what we set out to prove at the beginning of Section 3.1.1; that the GWs Eq. (3.15) are *plane-waves* at sufficiently large distances away from their source. In order to proceed, we need a way of evaluating the integral (3.15). To do this, one need make use of the equations of motion (2.49) which determine the conservation laws for energy and momentum in general relativity (respectively) as

$$\begin{aligned} \partial_t T_{tt} + \partial_j T_{tj} &= 0\,, \\ \partial_t T_{jt} + \partial_k T_{jk} &= 0\,, \end{aligned} \tag{3.16}$$

in order to show (Andersson, 2019; Hartle, 2021)

$$\int T_{jk}\, d^3x = \frac{1}{2}\partial_t^2 \int T_{tt} x_j x_k\, d^3x \,. \tag{3.17}$$

In this ‘near-Newtonian’ scenario, the component of the stress-energy tensor T_{tt} will be dominated by the rest-mass density ρ of the source, and thus it is convenient to define the RHS of the above in terms of the *mass quadrupole moment* tensor

$$I_{jk} \equiv \int \rho(t,\vec{x})\, x_j x_k\, d^3x \,, \tag{3.18}$$

which allows us to write the asymptotic gravitational wave amplitude (3.15) more succinctly as

$$\bar{h}_{jk}(\vec{x},\, t) \xrightarrow[r\to\infty]{} \frac{2}{r}\ddot{I}_{jk}(t-r)\,. \tag{3.19}$$

With this result in hand, we now return to the issue of energy in gravitational-waves. Being a plane-wave, we should expect (as in the case of electromagnetism) that the energy density of the GW is proportional to the *square* of its amplitude. As it happens, Eq. (3.19) dictates that the GW amplitude far from its source is proportional to the second time derivative of the mass quadrupole moment I_{jk}. This tells us that the GW luminosity, i.e. the total power radiated from the source per unit time, should therefore be quadratic in the time derivatives of I_{jk}.

Exactly which time derivative of I_{jk} is required in order to compute the GW luminosity may then be inferred on dimensional grounds. Working in geometrized units, both mass and time have units of length. The mass quadrupole moment, through Eq. (3.18), therefore has units of (length)^3. The luminosity, on the other hand, is

$$L_{\mathrm{GW}} \equiv \left(\frac{dE}{dt}\right)_{\mathrm{GW}} \sim \left[\frac{ML^2}{T^2}\right]\frac{1}{T} \sim \frac{L}{L} \tag{3.20}$$

and thus dimensionless. It therefore follows that the luminosity must be a quadratic in $\dddot{I}^{jk}$, the *third* time-derivative of the mass quadrupole moment tensor.

It turns out that a full derivation of the GW luminosity, obtained by computing the GW stress-energy tensor to second order, follows our intuition and yields the result (with values of G and c reinstated)

$$L_{\mathrm{GW}} = \frac{1}{5}\frac{G}{c^5}\left\langle \dddot{\bar{I}}_{jk}\dddot{\bar{I}}^{jk}\right\rangle, \tag{3.21}$$

where the angled brackets $\langle ... \rangle$ denotes a time-average of one period of the new quantity $\dddot{\bar{I}}$, defined as

$$\dddot{\bar{I}}_{jk} \equiv I_{jk} - \frac{1}{3}\delta_{ij}I^k_k\,. \tag{3.22}$$

The final result is expressed in terms of this *trace reduced* mass quadrupole moment tensor (hence the bar notation, in corollary with the trace-reversed metric perturbation (3.4)) since it makes explicit the fact that the GW luminosity vanishes for spherically symmetric sources (in Cartesian coordinates x, y, and z will be identical). This is a general result in GR that is made explicit through *Birkoff's thereom*, which states that any spherically symmetric solution of the (vacuum) field equations must be both stationary (i.e. does not vary in time) and asymptotically flat (i.e. have vanishing curvature) and thus there can be no gravitational waves.

The result Eq. (3.21) will be required in the following section in order to determine the GW luminosity from the specific case of a rigidly rotating neutron star supporting a mountain, and in-turn understanding the role mountains could potentially play in dictating the spin-equilibrium of accreting neutron stars in LMXB systems.

3.2 Gravitational-waves from accreting neutron stars

Accreting neutron stars have long been considered to be possible sources of (continuous) gravitational-waves in order to solve a problem in the realm of observational astronomy. Prevailing theory suggests that the observed population of the most rapidly rotating (millisecond) pulsars stems from LMXB systems (Bhattacharya and van den Heuvel, 1991). A 'recycling' scenario posits angular momentum from an accretion disk is transferred to the neutron star (via external magnetic fields), leading to spin-up torques (Ghosh et al., 1977; Ghosh and Lamb, 1979a,b; Dai, H.-L. and Li, X.-D., 2006). Such a process occurs over extraordinarily long timescales, gradually spinning the NS up until it has accreted all the available matter from its sub-solar companion.

In principle, extended accretion should have no difficulty spinning up these NSs to that of the centrifugal break-up frequency ($\sim$ 1-2 kHz; Lattimer and Prakash, 2007). Yet, the fastest-observed millisecond pulsar to-date, PSR J1748-2446ad, rotates at just 716 Hz (Hessels, 2006). The lack of observations of *sub-millisecond* accreting millisecond pulsars within the galaxy are therefore indicative of some additional (as yet) *unknown* braking torque preventing the spin up of these stars to the centrifugal break-up limit. The natural problem to consider then is exactly what physical processes could be responsible for removing angular momentum from these stars and preventing them from reaching sub-millisecond periods.

In recent years, the interaction between the NS's external magnetic field and the accretion disk, as well as the emission of GWs, have been invoked to explain this observation puzzle. In favour of the former suggestion, it has been suggested by Patruno et al. (2012) that an external magnetic field strength of $\sim 10^8$ G could be enough to explain lack of observed spin-rates of AMXPs exceeding $\sim$ 700 Hz. However, a more recent study by Bhattacharyya and Chakrabarty (2017) implies that such a result may only be true of steadily accreting NSs. For systems which transiently accrete, evidence suggests that a field strength of 10^8 G might not sufficient to reproduce observation.

3.2.1 The torque-balance limit: Accretion in low-mass X-ray binaries

The various torques which act on the NS over the course of its lifetime dictate its spin evolution. In the case of an LMXB, this spin evolution is of course dominated by the process of matter accretion. If one recalls the schematic picture Fig. 2.3, mass transfer from the companion star occurs via Roche-lobe overflow. The Roche lobe itself is simply the region around a star within which orbiting material is gravitationally bound to it. Over an extended period of time, the surface of the companion star expands outwards and eventually beyond that of its Roche lobe. Any material from the companion star which lies outside of the Roche lobe may then be 'transferred' into the NS's own Roche lobe, through the inner Lagrange point (Fig. 3.1).

This transfer of mass between the two binary components leads to a transfer of angular momentum between the two stars as well. However, this angular momentum cannot be transferred directly to the NS, and instead an accretion disk forms around it. Exactly how matter is transported from the disk to the surface will be determined by the presence of a magnetic field. If magnetic field lines, which emanate from the crust, permeate into the accretion disk, then matter from the disk will likely be channelled onto the magnetic poles of the NS along the field lines. This is then the point at which then an accreted particle gives up its angular momentum upon arriving at the surface, spinning the star up. The material torque on the star from the accretion is usually approximated as (Ghosh and Lamb, 1979b)

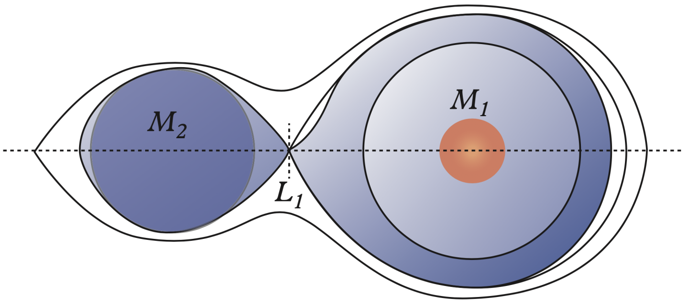

FIGURE 3.1: Schematic illustration of the process of mass transfer via Roche-lobe overflow. Mass is transferred from the lower-mass star M_2 to the higher-mass star M_1 through the inner Lagrangian point $L1$ and forms an accretion disk. Image credit: reproduced from Andersson (2019).

$$N_{\rm acc} = \dot{M}\sqrt{GMR_M}\,, \tag{3.23}$$

where R_M is the magnetosphere radius, defined at the point whereby the magnetic pressure begins to dominate the fluid pressure.

The picture is complicated, however, due to the fact there is likely some differential rotation between the NS and the accretion disk. This can cause the field lines to become twisted and misaligned. As a result, the coupling between the NS's rotation, its external magnetic field strength, and the mass accretion rate can lead to torques that actually either spin up or spin down the star. The possibility of accretion leading to spin-down torques means that the *net* torque on the star is the sum of these two contributions, leading to a modification of Eq. (3.23) as (Ho et al., 2013)

$$N_{\rm acc} = \dot{M}\sqrt{GMR_M}(1-\omega)\,. \tag{3.24}$$

The sign of the torque (i.e. whether the NS is spun up or down), is determined by ω, the so-called *fastness parameter*, defined by

$$\omega = \frac{\Omega_*}{\Omega_K(r)} = \left(\frac{R_M}{R_c}\right)^{3/2}\,, \tag{3.25}$$

where Ω_* is the angular frequency of the star and Ω_K is the angular velocity of a particle in a Keplerian orbit. For the most simple case whereby matter falls radially onto the star, the magnetospheric radius R_M is

$$R_M = \left(\frac{\mu_{\rm mag}^4}{2GM\dot{M}^2}\right)^{1/7} \approx 7.8\left(\frac{B}{10^8{\rm G}}\right)^{4/7}\left(\frac{R}{10^8{\rm km}}\right)^{12/7}\left(\frac{M}{1.4M_\odot}\right)^{-1/7}\left(\frac{\dot{M}}{\dot{M}_{\rm Edd}}\right)^{-2/7}{\rm km}\,, \tag{3.26}$$

where $\mu_{\text{mag}} \sim BR^3$ is the magnetic dipole moment and $\dot{M}_{\text{Edd}} = 2 \times 10^{-8} M_\odot \, \text{yr}^{-1}$ is the *Eddington mass accretion limit*, the point at which the outward radiation pressure is balanced by the inwards gravitational attraction of the in-falling matter. The final quantity R_c is known as the *co-rotation radius*

$$R_c \approx 17 \left(\frac{(2\pi/\Omega_*)}{1\text{ms}} \right)^{2/3} \left(\frac{M}{1.4 M_\odot} \right)^{1/3} \text{km} \,, \tag{3.27}$$

and is defined as the point at which matter inside the disk rotates at same velocity as the NS magnetosphere.

When $R_M < R_c$, matter in the disk enveloped by the magnetosphere spins faster than the NS. A particle that is funnelled onto the NS therefore has a greater specific angular momentum than the star itself, and so imparts some of the excess when it hits the surface. This results in a positive torque on the NS, spinning it up. On the other hand, if $R_M > R_c$, then the magnetic field lines will rotate faster than the local Keplerian speed of matter in the disk. This 'propeller regime' can cause the accretion flow to be centrifugally inhibited, resulting in accreted matter being expelled from the disk, and ultimately resulting in a negative torque on the NS, spinning it down.

An equilibrium between these two competing effects may be achieved at the point whereby $R_M = R_c$, at which point the *equilibrium spin frequency* will be

$$\nu_{\text{eq}} = \frac{\Omega_*^{\text{eq}}}{2\pi} \approx 530 \left(\frac{B}{10^8 \text{G}} \right)^{-6/7} \left(\frac{R}{10\text{km}} \right)^{-18/7} \left(\frac{M}{1.4 M_\odot} \right)^{5/7} \left(\frac{\dot{M}}{\dot{M}_{\text{Edd}}} \right)^{3/7} \text{Hz} \,, \tag{3.28}$$

and has since been come to be known as the '*torque balance limit*'.

A combination of a weak external magnetic field and high rate of mass accretion are required to generate spin frequencies typical of observed LMXBs (i.e a few hundreds of Hz). For a canonical 10 km, 1.4 $M_\odot$ neutron star, Andersson et al. (2005) showed that the inferred strengths of the magnetic fields for LMXBs accreting at $\lesssim 10^{-2} \dot{M}_{\text{Edd}}$ are consistent with those estimated for millisecond radio pulsars. This suggests that the magnetic-torque phenomenon can explain quite well the observed spin-rate of many LMXB systems. One caveat to this model however is that it does not predict sensible magnetic field strengths for NSs accreting close to the Eddington limit. It is possible that this could perhaps hint towards additional spin-down mechanisms in sufficiently rapidly accreting systems, though this is by no means certain.

One reason for this is that the exact nature of the interaction between the accretion disk and the NS is not clear. The description presented above may certainly be improved, but at the cost of introducing additional parameters characterised by poorly understood physics. One important piece that is missing from current models is an understanding of the viscosity of the disk, which determines how effectively energy and angular momentum may be dissipated.

3.2.2 Additional spin-down torques? Gravitational-waves from a quadrupolar deformation

All this is to say that current observations cannot uniquely attribute the observed spin-rates of accreting neutron stars to that of the magnetic spin equilibrium model *alone*. For example, statistical analysis by Patruno et al. (2017) of the spin-distribution of LMXBs suggests evidence for two distinct sub-populations. The majority of the NSs exhibit, on average, a ‘low’ spin frequency ($\bar{\nu}_s \approx 300$ Hz). There are a small minority of stars, however, which exhibit much higher spin frequencies ($\bar{\nu}_s \approx 575$ Hz). The curious nature of this observation is that *if* there is indeed an additional braking mechanism present in the system, then it must set in sharply once a star reaches a given spin rate.

It just so happens that, in the case of a deformed (rotating) NS, the rate of angular momentum lost via GW emission scales as a steep (fifth) power of the star’s spin frequency (see Eq. (3.35) below). The idea that GW torques from mountains may be dictating the spin-equilibrium period in LMXBs was popularised by Bildsten (1998). The idea echoed earlier discussions by Papaloizou and Pringle (1978) & Wagoner (1984), that equilibrium might be achieved via gravitational-wave emission from rotational instabilities. Encouragingly, recent timing observations of the pulsar PSR J1023+0038 has shown that the NS spins down ~ 27% faster during episodes of active accretion than in periods of quiescence (Haskell and Patruno, 2017). This result can, at least qualitatively, be explained by the presence of gravitational-wave torques from a transient ‘mountain’ inside the star that forms during phases of accretion.

Recall that the quadrupole moment tensor vanishes for a spherically symmetric system. Consider, therefore, a NS that has been perturbed away from sphericity by some density perturbation $\delta\rho \equiv \mathbb{R}\{\delta\rho_{\ell m}(r)Y_{\ell m}(\theta,\phi)\}$[2]. For our purposes, we are interested only in the $\ell = m = 2$ component, since this will give rise to quadrupolar gravitational radiation. This perturbation deforms the star, creating a mountain which will radiate GWs continuously at twice the spin frequency (i.e. $f_{\rm GW} = 2\nu_s$; Sec. 1.3.3). The rate at which angular momentum is radiated away by the deformed NS (rotating about the z-axis) is determined by the gravitational-wave luminosity Eq. (3.21) as

$$N_{\rm GW} = \frac{1}{\Omega_*}\frac{dE}{dt} = \frac{L_{\rm GW}}{\Omega_*} = \frac{1}{5\Omega_*}\frac{G}{c^5}\langle \delta\dddot{I}^2_{xx} + \delta\dddot{I}^2_{xy} + \delta\dddot{I}^2_{yx} + \delta\dddot{I}^2_{yy}\rangle \,, \tag{3.29}$$

where, in the case of our perturbed star, we have

$$\dddot{\text{Ɨ}}_{jk} \equiv \delta I_{jk} = \int \delta\rho \, x_j x_k \, d^3V \,. \tag{3.30}$$

---

[2] In general the spherical harmonics $Y_{\ell m}$ are complex. We need only consider the real part since all physical quantities must be real.

In spherical polar coordinates (Fig. 1), the quadrupolar density perturbation may be written more explicitly as

$$\begin{aligned}\delta\rho_{22} &= \mathbb{R}\{\delta\rho_{22}(r)Y_{22}[\theta,\phi(t)]\}\\ &= \frac{1}{4}\sqrt{\frac{15}{2\pi}}\,\delta\rho_{22}(r)\sin^2\theta\cos\left(2[\phi-\Omega_* t]\right),\end{aligned} \tag{3.31}$$

and thus the required components of the quadrupole moment tensor are

$$\delta I_{xx} \equiv -\delta I_{yy} = \frac{\sqrt{30}\sqrt{\pi}}{15}\cos(2\Omega_* t)\int \delta\rho_{22}(r)r^4 dr\,, \tag{3.32}$$

$$\delta I_{xy} \equiv \delta I_{yx} = \frac{\sqrt{30}\sqrt{\pi}}{15}\sin(2\Omega_* t)\int \delta\rho_{22}(r)r^4 dr\,, \tag{3.33}$$

where the final quantity is the *mass quadrupole moment scalar*, defined in terms of the perturbation's multipole moments as (Ushomirsky et al., 2000)

$$Q_{\ell m} = \int \delta\rho_{\ell m}(r)r^{\ell+2}\,dr\,. \tag{3.34}$$

The nature of the density perturbation, and what physical processes within the star might generate it are the focus of Chapters 5 and 6 (and indeed the motivation behind this entire thesis!). For now, though, we shall just assume that this density perturbation exists and explore its consequences.

Through inserting Eqs (3.32) - (3.33) into the angular momentum equation (3.29), and using the definition (3.34), it may be shown that a rigidly rotating deformed NS has

$$N_{\mathrm{GW}} = \frac{L_{\mathrm{GW}}}{\Omega_*} = \frac{256\pi}{75}\frac{G}{c^5}\Omega_*^5 Q_{22}^2 = \frac{512\pi^2}{75}\frac{G}{c^5}\nu_s^5 Q_{22}^2\,, \tag{3.35}$$

and that the GW torque on the star is parameterised by both the spin frequency ν_s of the star as well as the size of the quadrupole moment Q_{22}.

The next logical step is attempt to ascertain exactly how large a mass-quadrupole is required in order for GW emission to play a significant role in determining the spin-evolution. If one assumes, for simplicity, that GW emission is responsible for *100%* of the spin down torques acting on the star, then the quadrupole moment required such that GW emission balances the accretion torque (3.23) is (Bildsten, 1998; Ushomirsky et al., 2000)

$$\tilde{Q}_{\rm eq} \approx 3.5 \times 10^{37} \text{ g cm}^{-3} \left(\frac{M}{1.4M_\odot}\right)^{1/4} \left(\frac{R}{10\,\text{km}}\right)^{1/4} \left(\frac{\dot{M}}{10^{-9}M_\odot\text{yr}^{-1}}\right)^{1/2} \left(\frac{300\text{Hz}}{\nu_s}\right)^{5/2} . \tag{3.36}$$

Mass accretion rates of LMXBs are typically in the region $10^{-11} \lesssim \dot{M} \lesssim 10^{-8}$ $\text{M}_\odot$ yr^{-1}, with many of the NSs rotating with frequencies $300 < \nu_s < 700$ Hz. Such considerations imply that $\tilde{Q}_{\rm eq} \approx 10^{37-39}$ g cm^2 is required in order to attain torque balance (assuming gravitational radiation is the only source of spin-down energy loss).

Though, whilst we now have a tangible number on which to work with, the mass quadrupole itself is not a particularly intuitive measure of how big a deformation (or mountain) is required in order to dictate the spin-equilibrium of the star. Instead, the non-sphericity is more normally associated with the neutron star *ellipticity*, and is related to the size of Q_{22} as

$$\varepsilon = \frac{(\delta I_{xx} - \delta I_{yy})}{I_{zz}} = \sqrt{\frac{8\pi}{15}} \frac{Q_{22}}{I_{zz}} . \tag{3.37}$$

For the sake of simplicity, we can assume that $I_{zz} = {}^2/_5 MR^2 \sim 10^{45}$ g cm^{-3} (i.e. the moment of inertia of a spherically symmetric, constant density canonical NS)[3]. Using Eq. (3.36), the required ellipticity for torque balance at the critical frequency $\nu_s = 300$ Hz is

$$\varepsilon \approx 5 \times 10^{-8} \left(\frac{\dot{M}}{10^{-9}M_\odot\text{yr}^{-1}}\right)^{1/2} \left(\frac{300\text{Hz}}{\nu_s}\right)^{5/2} , \tag{3.38}$$

for a star with $M = 1.4M_\odot$ and $R = 10$ km. Such a result indicates that in order to balance the accretion torque, one requires an ellipticity $\varepsilon \sim 10^{-8} - 10^{-9}$. For context, the most recent search for continuous GWs (at the time of writing), targeting directly 20 AMXP, has constrained the upper limit of the ellipticity of IGR J00291 + 5934 to be $\varepsilon^{95\%} = 3.1 \times 10^{-7}$ (Abbott et al., 2022a). It is also much smaller (two or three orders of magnitude) than the theoretically-predicted *maximum* (elastic) mountain that the star could possibly sustain ($\varepsilon \sim 10^{-6}$; Sec. 1.3.3.2), and similar in magnitude to the predictions of a recent population-based analysis by Woan et al. (2018), which suggests that the *minimum* ellipticity of millisecond pulsars is of the order 10^{-9}.

Additionally, in the more realistic scenario of an accreting NS with an external magnetic field, recall that this may affect the net torque acting on the system. The required mass quadrupole $\tilde{Q}_{\rm eq}$ would be proportionately larger or smaller than the value given in (3.36) depending on the sign of the fastness parameter ω in Eq. (3.24), and whether the magnetic field is providing spin-up or spin-down torques to the star. Depending on ones point of view, this fact can be either a blessing or curse. On the one hand, additional spin-down torques supplied by the magnetic field reduces the minimum size of the mass quadrupole (and hence the size of the mountain) one needs to

---

[3] In principle, though, this value may vary by a factor of a few for different real stars - see e.g. Fig. 4 of Fantina et al. (2022) for calculations of I assuming the BSk19, BSk20, and BSk21 EoSs.

achieve torque balance, which alleviates the dependence on nature being able to facilitate the construction of sufficiently large mountains. Yet, on the other hand, by this same token such smaller mountains are inherently harder to detect, and require GW interferometers with greater sensitivities beyond current (and possibly near-future) capabilities.

3.2.2.1 The ‘wavy capture layer’

In coming this far, the pertinent question that remains to be addressed is that, assuming neutron stars do emit gravitational-waves to some degree, what possible physical processes might be causing it? We saw briefly in Section 1.3 that a host of phenomena could potentially generate gravitational radiation. But, in the context of accreting NSs (which provide the most encouraging *qualitative* evidence for their existence), the story of how large-scale deformations in the form of the conventional ‘thermal mountain’ might develop begins with the seminal paper of Bildsten (1998) and the formation of the so-called ‘wavy capture layers’.

To understand how this phenomenon may occur, we return to the discussion in Section 2.4.2, restricting ourselves to the outer crust[4]. The Fermi energy of free electrons increases as accreted matter is compressed into the crust. Once the Fermi energy equals that of the binding energy E_d of a particular nuclear species at a given depth, electron capture becomes energetically favourable leading to the transformation

$$(A, Z) + e^- \longrightarrow (A, Z-1) + \nu_e\,. \tag{3.39}$$

From the Fermi energy distribution, Bildsten (1998) estimated that the pressure in the outer crust generated by the relativistic degenerate electrons was

$$P(E_\mathrm{F}) = 1.42 \times 10^{30} \mathrm{erg\ cm^{-3}} \left(\frac{E_\mathrm{F}}{30\mathrm{MeV}}\right)^4 . \tag{3.40}$$

In these low density regions, the mass of a shell above a given capture layer can be approximated by the condition for (Newtonian) hydrostatic equilibrium (2.46a) - (2.46b) and Eq. (3.40) as

$$M_\mathrm{crust}(E_\mathrm{F}) = \frac{4\pi R^2 P}{g} \approx 5 \times 10^{-5}\, M_\odot \frac{R_6^4}{M_{1.4}} \left(\frac{E_\mathrm{F}}{30\ \mathrm{MeV}}\right)^4 , \tag{3.41}$$

where $g = GM/R^2$.

In Section 2.4.2, it was assumed that electron captures occur instantaneously once $E_\mathrm{F} > E_d$ making the process solely density dependent. However it had been previously shown by Bildsten

---

[4] Bildsten (1998) did not consider capture layers in the inner crust in his original work, but did later extend the idea to deeper regions in Ushomirsky et al. (2000).

and Cumming (1998) that actually this is only true of cold, weakly accreting NSs. For those that strongly accrete, and with temperatures exceeding $\sim 10^8$ K, the capture rates are in fact sensitive to the local temperature, with captures permitted out on the thermal tail of the Fermi distribution at physical points in the crust where $E_{\mathrm{F}} \lesssim E_d$. Consequently, in the regions of the crust that are hotter on average, electron-capture events can take place at lower density (closer to the star's surface) than colder regions (recall Fig. 1.10).

Such a phenomenon led Bildsten (1998) to conclude that the presence of a transverse temperature gradient in the outer regions of the crust would therefore lead to density asymmetries with an associated mass quadrupole $\Delta M \approx 4\pi R^2 \Delta\rho \Delta s_c$, where Δs_c is the difference in physical depth of the capture layer. Through perturbing the Fermi energy in Eq. (3.41) and introducing a non-zero temperature such that electrons with a Fermi energy $\Delta E_{\mathrm{F}} \approx 10 k_B \Delta T$ may still be captured, Bildsten (1998) estimated that the mass quadrupole generated within a single capture layer is

$$\Delta M \approx 5.8 \times 10^{-7} M_{\odot}\, \Delta T_8\, \frac{R_6^4}{M_{1.4}} \left(\frac{E_{\mathrm{F}}}{30\,\mathrm{MeV}} \right)^3 . \tag{3.42}$$

It is worth noting that the prefactor 5.8×10^{-7} is an order of magnitude larger than the value given in Eq. (3) of Bildsten (1998), and likely a typo in the original manuscript.

To better understand this result, one can make a back-of-the-envelope approximation of the induced ellipticity as a result of a single capture layer as

$$\varepsilon \approx \frac{Q}{I} \approx \frac{\Delta M}{M} \sim 10^{-8} . \tag{3.43}$$

Given that there are many electron capture layers in the outer crust (Tables A.1 - A.3), such a result suggests that, at least in this simple analysis, the GWs generated in the outer crust should be sufficient to counteract the spin-up torques provided by accretion.

3.2.2.1.1 Sourcing a temperature gradient

One *crucial* caveat to the Bildsten (1998) estimate however is that a lateral temperature gradient of 10^8 K is *assumed* to be present in Eq. (3.42). A description for the origin of the required temperature gradients themselves were not given, and thus the true extent of the mass quadrupole generated by these wavy-capture layers is uncertain.

In a follow-up paper, Ushomirsky et al. (2000) (hereafter UCB) sought to further substantiate the Bildsten (1998) mechanism by considering two possibilities to source the necessary temperature gradients. They argued that lateral variations in the crustal composition of the accreted crust due to asymmetric burning could (i) lead to asymmetries in heat energy released in the crust, and (ii) lead to anisotropies in the thermal conductivity due to varying charge-to-mass (Z^2/A) ratios. UCB found that temperature asymmetries of the percent level (i.e. $\delta T/T \sim 1\%$) could lead to the formation of mass quadrupoles large enough to balance accretion torques. However, UCB were also unable to justify the origin of either the compositional or nuclear heating asymmetries, instead simply assuming their existence *a priori* at the level of 10%.

More recently, Singh et al. (2020) also took the UCB argument one step further and explored the possibility of asymmetric accretion leading to quadrupolar deformations of the crust. The authors used the likely presence of (weak) magnetic fields of accreting neutron stars to model the flow of accreted matter onto the polar caps. They computed the temperature perturbations in the crust as a result of the build up of accreted matter, and calculated the corresponding mass quadrupole as per the results of UCB for the physical shifts of the capture layers. Their results focused on the particular pulsar PSR J1023+0038, since an observed increase in its spin-down rate during active episodes of accretion ($\sim 27\%$) is well documented (Sec. 3.2.2). Unfortunately however, the mass quadrupoles generated from such a mechanism were, in general, too small to explain the spin-down rate of PSR J1023+0038, unless significant amounts of shallow crustal heating (Sec. 4.3.2) is present in the outermost layers of the crust.

Additionally, Osborne and Jones (2020) also sought to try and help complete the picture originally laid out by Bildsten (1998) (and UCB) by providing a first-principles calculation for sourcing large-scale temperature asymmetry in the accreted crust. They also exploited the presence of weak magnetic fields ($\sim 10^9$ G) of NSs in LMXBs to compute temperature asymmetries, but via a different mechanism. They modelled the anisotropic heat conduction of relativistic electrons in the accreted crust as a result of *internal* crustal magnetic fields. They concluded that the 1% asymmetry required by UCB to attain torque balance was unlikely to be produced from this mechanism, though, finding that asymmetries of the order $\sim 10^{-5}\%$ could be produced in the deep crust by a 10^9 G field.

Over the course of the next two chapters, we will seek to revisit and improve various aspects of the Osborne and Jones (2020) mechanism for building a temperature asymmetry in the crust. Namely, we will also assume the star to be threaded with an internal magnetic field, but extend the computational domain to include a self-consistent calculation of the thermal structure of the core. In doing so, we shall allow for the possibility of the magnetic field to penetrate the core, with the expectation that non-vanishing temperature perturbations at the crust-core transition will lead to greater asymmetries in the deep crust.

4

Thermal Structure of Accreting Neutron Stars

In this chapter we shall construct the steady-state background thermal profile of a non-rotating, spherically symmetric and steadily accreting neutron star. We begin in Section 4.1 by discussing recent observations of accreting NSs within our galaxy, before presenting both the Newtonian and general relativistic heat equations which describe the thermal evolution in Section 4.2. Solving these equations requires accurate descriptions of the different components that comprise the heat equation, each of which are discussed in turn. The relevant contributions to crustal heating (Sec. 4.3), thermal conductivity (Sec. 4.4), neutrino cooling (Sec. 4.5), and effects of baryon superfluidity (superconductivity; Sec. 4.6) shown in this chapter are a collation of many results of a large number of other published works in the literature. The purpose is to give the reader an intuitive sense of how the many different components combine in order to be able to solve the heat equations and accurately predict the thermal structure.

In Section 4.7 we describe how the heat equations that determine the *steady-state* thermal profile are solved, and discuss the relevant boundary conditions. In Section 4.8 we then present results of our model for steadily accreting NSs, taking into account a range of different input parameters that reflect observations of different LMXBs. We then compare the results of our model with other works in the literature (Sec. 4.9), and discuss any differences between models.

4.1 Observations of accreting neutron stars

The first source of X-rays to be identified from outside the Solar System was the neutron star LMXB Scorpius X-1, discovered as far back as 1962 (Giacconi et al., 1962). Among all previous and current space-borne observatories, approximately 350 X-ray sources from within the galaxy have either been confirmed, or are suspected to be, LMXBs (Avakyan, A. et al., 2023).

Observational inferences suggest that many of these systems contain a neutron star, whilst others accommodate a more compact black hole.

A small percentage of these NS-LMXBs belong to the class of rapidly rotating accreting millisecond X-ray pulsars described in Section 3.2.1 (see Table 1 of Salvo and Sanna, 2022 for the full list). In general, AMXPs fall into two categories: (i) those that are almost always accreting (*persistent* systems), and (ii) those that accrete periodically (*transient* systems). In the latter case, transient systems may exhibit frequent swings in their X-ray luminosity, whereby outbursts of active accretion are separated by - in some cases quite long - periods of quiescence, where there is little to no accretion.

Indeed, transient systems typically present a low luminosity, in the region 10^{31-34} erg s^{-1}, but occasionally exhibit a sudden rise of their luminosity to that of 10^{36-39} erg s^{-1} for brief periods of time. The steady flow of gas from the companion star during quiescence leads to an enlargement of the NS's accretion disk. Once the disk reaches a critical mass, it can trigger instabilities in the disk that results in an abrupt increase in the accretion rate from the disk to the surface of the star by many orders of magnitude, leading to an '*outburst*'. The duration of these outbursts may last anywhere from days to years, but cease once the accretion disk has donated a sufficient amount of material. At this point the system returns to pre-outburst levels, where the process of accumulating matter in the accretion disk can begin again.

It is worth bearing in mind however that there is no hard-and-fast rule as to what delineates between a persistent and transient AMXP. Rather, they are simply 'considered' transient if their X-ray luminosity changes by a factor of ~ 1000 over a short period (Bahramian and Degenaar, 2023). As such, it not surprising that there a number of systems that fall somewhere between a transient and persistent system. If an AMXP exhibits extended outburst episodes that last on the time-scale of years, but still switch between active and inactive periods of accretion, then they may be referred to as *quasi-persistent* systems. The light curves (i.e. the brightness over a period of time) for three different LMXBs obtained by the *Rossi X-ray Timing Explorer* is shown in Figure 4.1.

Some AMXPs also exhibit phenomenon referred to commonly as *type I X-ray bursts* during their accretion phases. These bursts manifest as sharp, rapid rises in the luminosity followed by a slow and gradual decrease. They produce distinctive light curves, which in general are split into three distinct phases:

- ***the rise*** ($\sim 1-10$ s): A thermonuclear flash caused by the ignition of accumulated helium spreads across the surface.
- ***the peak***: The ocean ignites and explosive thermonuclear burning takes place.
- ***the decay*** ($\sim 20-200$ s): The flux begins to decrease once the helium fuel is spent and burning ceases.

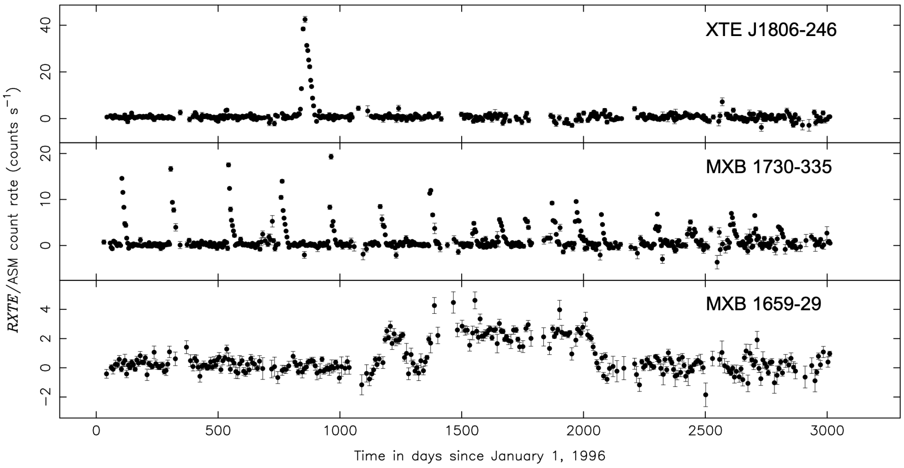

FIGURE 4.1: Observed light curves obtained from the *Rossi X-ray Timing Explorer* for three different X-ray transients indicated near the curves. Image credit: reproduced from Wijnands (2004).

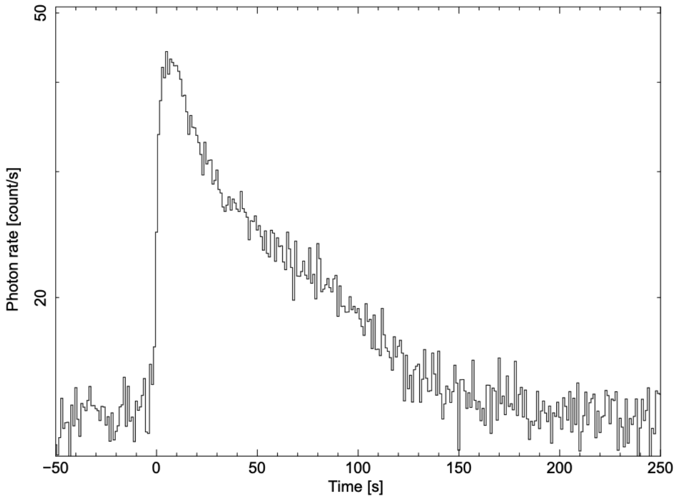

FIGURE 4.2: The average light curve of 20 type-I X-ray bursts from the '*rapid burster*' system MXB 1730-335. Image credit: reproduced from in't Zand et al. (2017).

The 'average light curve' of 20 type-I X-ray bursts from the so-called *rapid burster* system MXB 1730-335 can be seen in Figure 4.2.

The absence of accretion in periods of quiescence implies that the observed emission from these systems (10^{32-34} erg s^{-1}) cannot be sourced from thermonuclear burning in the ocean. Instead, prevailing theory suggests that low-level quiescent emission originates from thermal radiation generated *inside* the neutron star, which is then radiated away from its surface later on. The thermal state of accreting NSs has been studied by many authors, with the first works on thermal emission from NSs dating back to as early as the initial detection of Scorpius X-1 in the 1960's (e.g. Chiu and Salpeter, 1964; Morton, 1964). The relation between the surface and internal temperature was first identified by Tsuruta and Cameron (1966), who are credited with laying out the foundations for so-called *cooling theory*, allowing one to track the thermal evolution over successive outburst and quiescent cycles.

Cooling theory remains an active area of research today, with the expected crust cooling being observed from seven systems (Wijnands et al., 2017). Observing runs of these systems over several years has provided a wealth of data, allowing for the construction of the so-called *cooling curves* for these systems. This information has subsequently led to the development of a number of theoretical models that can track (and predict) the thermal evolution. These codes assume a variety of different heating and cooling processes, which can be adjusted in order to match the observations of cooling crusts, which in turn provide useful opportunities to constrain various crustal properties. Indeed, how the thermal evolution of transiently accreting NSs changes over successive outbursts depends on a range of factors; including how efficiently heat is stored, on the temperature of the core, as well as on a number of other crustal properties such as its thickness, the thermal conductivity, as well as the composition (see e.g. Potekhin et al., 2023 for a very recent calculation, as well as any references therein).

4.2 The heat equation

The thermal evolution of a spherically symmetric star is determined by (without GR correction terms) the energy balance equation

$$\rho C_P \frac{\partial T}{\partial t} + \nabla \cdot \boldsymbol{F} = Q \,, \tag{4.1}$$

where ρ is the mass density, C_P is the specific heat capacity (at constant pressure), T is temperature, $\boldsymbol{F}$ is the heat flux and, Q is the net rate of production of heat per unit time, given by

$$Q = Q_{\mathrm{h}} - Q_{\nu} \,, \tag{4.2}$$

where Q_{h} is the local heat energy deposited (per unit volume per unit time) inside the star, and Q_{ν} is energy loss due to neutrino emission.

In Section 2.6 we calculated the hydrostatic structure of a non-rotating, spherically-symmetric NS in static equilibrium. If one further assumes that the NS-LMXB is *steadily accreting*, then the temperature of the star can be presumed to be (to a reasonable approximation) unchanging in time (as well being spherically symmetric). A steady-state solution to the heat equation (4.1) results in the vanishing of the time derivative, and therefore the heat flux is related to the amount of heat energy generation as

$$\nabla \cdot \boldsymbol{F} = Q \,, \tag{4.3}$$

with the heat flux being related to the temperature T via *Fourier's law* as

$$\boldsymbol{F} = -\kappa \cdot \nabla T \,, \tag{4.4}$$

where κ is the thermal conductivity. For a spherically symmetric system (as is the case for a NS built from the TOV equations; recall Sec. 2.6.2), the luminosity L is related to the heat flux via $L = 4\pi r^2 F$, with $F = |\boldsymbol{F}|$. From this, one can derive a system of two coupled ODEs for L and T, with respect to the radial coordinate r, as

$$\frac{dL}{dr} = 4\pi r^2 Q \,, \tag{4.5}$$

$$\frac{dT}{dr} = -\frac{1}{\kappa}\frac{L}{4\pi r^2} \,. \tag{4.6}$$

To compute the temperature inside the NS requires integrating the heat transport equations (4.5) - (4.6) over the entire star. Such a calculation requires an accurate description of the heating term Q_h, neutrino cooling Q_ν, and thermal conductivity κ in the different regions of the star (recall Fig. 2.1), as well as a set of inner and outer boundary conditions at each end of the integration. These are to be discussed in detail in the following sections.

It is worth pointing out, however, that the intense gravitational fields associated with ultra-dense NSs, in principle, modifies the heat flow. The *relativistic* heat equation (applicable to neutron stars and black-holes) was derived by Thorne (1967) (and later reformulated in Thorne, 1977) and reads

$$C_P e^{\nu/2}\frac{\partial T}{\partial t} + \nabla \cdot (e^{\nu}\boldsymbol{F}) = e^{\nu} Q \,, \tag{4.7}$$

with the relativistic form of Fourier's law being written as

$$F = -e^{-\nu/2}\kappa \cdot \nabla (e^{\nu/2} T) \,. \tag{4.8}$$

Modelling of the thermal evolution of accreting NSs is done using general relativistic cooling codes such as `NSCool` (Page and Reddy, 2013); a one-dimensional code (i.e. one which assumes perfect spherical symmetry) that solves Eqs (4.7) - (4.8) once supplied with the relevant micro-physical inputs.

In the rest of this thesis however, we shall employ just the Newtonian formulation (4.5) - (4.6) to compute the thermal structure. We make this choice since we aim to connect our temperature perturbations (Chap. 5) with the calculations of the NS ellipticity obtained by Ushomirsky et al. (2000) and Osborne and Jones (2020), who worked in an entirely Newtonian framework.

TABLE 4.1: Heat per accreted nucleon (in MeV) deposited in the outer and inner crust of an accreting neutron star predicted by the energy-density functionals BSk19, BSk20, and BSk21 of Fantina et al. (2018) and the 'liquid drop' model of Haensel and Zdunik (1990a).

EoS	Outer crust	Inner crust	Total
BSk19	0.152	1.499	1.651
BSk20	0.144	1.471	1.615
BSk21	0.125	1.410	1.535
HZ90	0.09	1.36	1.45

4.3 Sources of crustal heating

As accreted material falls onto the surface, large amounts of gravitational binding energy (~ 200 MeV per accreted nucleon) is released. Only a fraction of the heat generated by gravitational energy release (or thermonuclear burning at the base of the ocean; ~ 5 MeV per accreted nucleon) will flow inwards towards the core, and it is therefore unlikely that these mechanisms are responsible for heating up the core to temperatures high enough to reproduce the quiescent X-ray spectra. This suggests there must be additional sources of heating *within* the interior of the star itself.

4.3.1 Deep crustal heating

Heat energy equivalent to the change in Gibbs-free energy is released each time the threshold for non-equilibrium electron-capture and pycnonuclear reactions is reached in the crust (recall Sec. 2.4.2). This 'deep crustal heating' (DCH), which begins during outburst as accreted material is compressed into the crust, propagates around the interior, including the core, heating it up. This mechanism, in principle, explains how the star is able to stay warm even after the outburst has ended, as heat at late times is transported from the cooling core back up to the surface, producing the thermal emission observed during quiescence.

The total amount of heat released per accreted nucleon in each of the F+18 and HZ90 models is shown in Table 4.1. How much of this heat is deposited in each of the capture layers with increasing density is shown in Fig. 4.3. The amount of heat generated is largely similar across each model, with most of the heat being generated within the inner crust at densities $\rho \sim 10^{12} - 10^{13}$ g cm^{-3}. Notably however, almost twice the amount of heat is produced in the BSk models (~ 1.4 MeV) due to pycnonuclear fusion than in the HZ90 model (0.86 MeV), indicating that individual electron-captures do not play a significant role in heating the crust when nuclear shell effects are taken into account (Sec. 2.4.2).

The role that DCH reactions play in determining the thermal evolution of the star depends on the type of LMXB system:

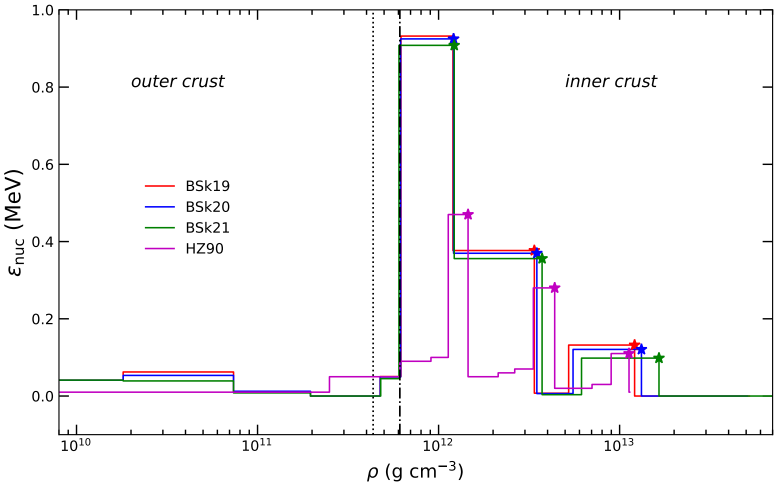

FIGURE 4.3: Heat deposited (per accreted nucleon) in the crust of an accreted neutron star as a function of the density for BSk19-21 (F+18; Tables A.1 - A.3) and HZ90 (Tables 1 and 2 of Haensel and Zdunik, 1990a). The step-like features represent our choice to smear the heat released at each transition over shells of constant (A, Z). Locations of pycnonuclear reactions are marked by stars, and the vertical dotted and dash-dotted lines refer to the outer to inner crust transition (neutron drip) for F+18 and HZ90 respectively.

Transient systems: in transient systems, DCH reactions occurring over the course of the accretion outburst will be conducted down through the crust and into the core. This heat is then later transported back up through the crust during periods of quiescence where it is released from the surface.

Quasi-persistent systems: in quasi-persistent systems (such as the AMXP KS 1731-260; Rutledge et al., 2002), the large amount of heat generated from DCH reactions can lead the crust to become much hotter than the equilibrium core temperature. If the length of the outburst exceeds the thermal diffusion time, then the quiescent luminosity after the outburst has ended will be dominated by the crust cooling rather than the core.

Persistent systems: if the accretion remains constant over a period years, then a steady-state can be reached in the crust. In this scenario, the amount of heat generated from DCH reactions is sufficiently large to compensate the heat loss via neutrinos from the core (Page and Reddy, 2013).

4.3.2 Shallow crustal heating

Though the DCH scenario explains very well the quiescent X-ray spectra of many transients, several NS-LMXB sources have been observed to be far hotter than what is theoretically predicted for the first 100 days or so of quiescence (Ootes et al., 2018). These light curves show a significant difference in the initial temperature of the crust at the end of outburst compared to that of the temperature at late times, when the crust and core of the star are brought back into thermal equilibrium. Such a phenomenon indicates the presence of some as-yet unknown *additional* heat sources in the outer layer ($\rho \leq 10^{10}$ g cm^{-3}) of the crust (e.g. Chamel et al., 2020).

The *average* amount of additional heating required by cooling simulations to replicate the observational data is around $1-2$ MeV per accreted nucleon (Ootes et al., 2018), roughly the same amount of heat released from DCH (Table. 4.1). Proposed explanations of this 'shallow crustal heating' (SCH) vary, including uncertainties in both the accretion rate (Ootes et al., 2016) and envelope constitution (Ootes et al., 2018), convection in the liquid ocean (Medin and Cumming, 2015), and differential rotation between the ocean and solid crust (Inogamov and Sunyaev, 2011).

In this work we shall follow the prescription of Osborne and Jones (2020) and smear the heat deposited in each capture layer over shells of constant (A, Z), with the width of the shell being defined by the density region between two consecutive capture layers (see Fig. 4.3). The amount of heat deposited in each layer (per unit volume per unit time) is a function of the accretion rate $\dot{M}$ only. By smearing the deposited heat over whole shells, the local energy deposited in each shell is

$$Q_{\rm h} = Q_{\rm nuc} + Q_{\rm S} = \frac{\dot{M}\epsilon_{\rm nuc}}{\frac{4}{3}\pi(r_i^3 - r_{i+1}^3)} + Q_{\rm S}\,, \tag{4.9}$$

where $\epsilon_{\rm nuc}$ is the heat deposited from DCH reactions per nucleon in a given capture shell (Eq. (2.17); and see the 7th columns in Tables A.1 - A.3), and r_i, r_{i+1} are the radii at the $i^{\rm th}$ capture layer. In Eq. (4.9), $Q_{\rm S}$ is the shallow heating term which affects only the lowest-density regions of the crust ($\rho_{\rm S} \leq 10^{10}$ g cm^{-3}). At densities $\rho < \rho_{\rm S}$, we add an extra 0.5 MeV per nucleon in each of three compositional shells defined by the densities $\rho = 1.00 \times 10^7$ g cm^{-3} (the approximate location of the base of the H/He layer), and $\rho = 1.38 \times 10^9$ g cm^{-3}, $\rho = 1.81 \times 10^{10}$ g cm^{-3}, $\rho = 7.37 \times 10^{10}$ g cm^{-3} (corresponding to the lowest-density compositional shells, which are the same across each of the BSk models; Tables A.1 - A.3) to give a total of 1.5 MeV per accreted nucleon of SCH. Accordingly, at densities whereby $\rho > \rho_{\rm S}$, we set $Q_{\rm S} = 0$, and the heat deposited into the crust is then supplied solely by the relevant DCH reactions.

4.4 Thermal conductivity

How efficiently the heat produced from SCH and DCH processes propagates around the star is determined by the thermal conductivity κ of the constituent matter. The primary carriers of heat inside NS crusts are relativistic electrons. In the core, the heat can be transported by electrons, muons (if available), as well as neutrons[1]. The thermal conductivity is temperature dependent, where, assuming the *relaxation-time approximation*, is given by (Yakovlev and Urpin, 1980)

---

[1] Protons also contribute to heat conduction in the core, though their contribution is negligible compared to neutrons and the leptons, since they are much fewer in number; Fig. 2.9.

$$\kappa_{\mathrm{x}} = \frac{\pi^2 k_{\mathrm{B}}\, n_{\mathrm{x}}}{3m_{\mathrm{x}}^*} T\tau_{\mathrm{x}}\,, \tag{4.10}$$

where n_{x} is the number density of the heat carrier (denoted by the subscript x, i.e. x = e, μ, n), m_{x}^* is its effective mass, and τ_{x} is the *effective* collision relaxation time. The total thermal conductivity is then a linear sum of the individual contributions from each carrier, i.e.

$$\kappa = \sum_{\mathrm{x}} \kappa_{\mathrm{x}} = \kappa_{\mathrm{e}} + \kappa_{\mu} + \kappa_{\mathrm{n}}\,. \tag{4.11}$$

4.4.1 Heat conduction in the accreted crust

There is a lack of definitive agreement within the literature concerning the prevalent scattering processes (i.e. the conduction mechanisms) in the accreted crust. In the context of thermal mountains, in the seminal paper by Bildsten (1998), it was assumed that electron-phonon interactions are the dominant scattering mechanism. In the later model developed by Ushomirsky et al. (2000), it was assumed that (following Brown, 2000) a combination of both electron-ion and electron-electron interactions are responsible for the majority of the heat conduction. More recent publications modelling the thermal structure, however (e.g. Geppert et al., 2004; Page et al., 2007; Aguilera et al., 2008; Osborne and Jones, 2020) all follow the formalism originally described in Yakovlev and Urpin (1980): the outer crust of the star dominated by electron-phonon interactions, and the inner crust dominated by electron-impurity scattering.

The effective relaxation time in the crust is simply the inverse of the sum of the collision frequencies of the individual scattering mechanisms. In regions where the crust is liquefied ($\Gamma_{\mathrm{Coul}} < 175$; Eq. (2.9)),

$$\tau = \frac{1}{\nu} = \frac{1}{\nu_{\mathrm{eQ}}}\,, \tag{4.12}$$

and in regions where the crust is solid ($\Gamma_{\mathrm{Coul}} \geq 175$),

$$\tau = \frac{1}{\nu} = \frac{1}{\nu_{\mathrm{ep}} + \nu_{\mathrm{eQ}}}, \tag{4.13}$$

where ν_{ep} and ν_{eQ} are the scattering frequencies from electron-phonon and electron-impurity collisions respectively (see the appendix of Brown and Cumming, 2009). Strictly speaking, there is also a contribution to τ from electron-electron (ν_{ee}) collisions. However, strong degeneracy of the (relativistic) electrons in the crust restricts the available phase space, and therefore has a negligible contribution to the overall thermal conductivity (Brown, 2000; Brown and Cumming, 2009).

At temperatures $T < T_m$ (i.e. $\Gamma > 175$) the crust is expected to form a solid, body-centred cubic lattice of bare nuclei (we shall discuss this in greater detail later in Section 6.1.1). Free electrons in the crust frequently collide with this lattice, transferring energy and momentum with each interaction. Such collisions create excitations in the lattice, corresponding to the creation and absorption of *phonons* (i.e. vibrations of the lattice), which in turn scatter the electrons.

When the temperature is above that of the Debye temperature[2], the scattering frequency is approximately (Brown and Cumming, 2009)

$$\nu_{\rm ep} = \frac{13e^2 k_B T}{\hbar^2 c}\,. \tag{4.14}$$

In the description of the accreted crust in Section 2.4.2, it was assumed that each layer of the crust is a shell of constant (A, Z), as depicted in Fig. 2.5. Both the BSk19-21 (F+18) and HZ90 models assume the ashes of X-ray bursts at the bottom of the envelope consist of pure ^{56}Fe only, and also go on to make the one-component plasma approximation. In reality however, nuclei far beyond the iron group with masses A $\sim 60 - 100$ are expected to be formed during hydrogen/helium burning as a result of rapid proton captures via the rp-process (Schatz et al., 1999). It is therefore possible that the layers of the crust will be to some degree an admixture of different nuclei as the heavier elements sink into the crust (e.g. Chamel et al., 2020). The exact distribution of these nuclei in the different crustal layers however is largely unknown.

Instead, the likely presence of other nuclear species is usually incorporated into simulations via the so called 'impurity factor' $\mathrm{Q}_{\rm imp}$, defined as (e.g. Brown and Cumming 2009)

$$Q_{\rm imp} \equiv \frac{1}{n_{\rm ion}} \sum_i n_i (Z_i - \langle Z \rangle)^2\,, \tag{4.15}$$

where the sum i is over all the different species of ions, with atomic number Z_i and mean atomic number $\langle Z \rangle$. If the crust is impure, then the thermal conductivity will be dominated by this electron-impurity scattering. The scattering is a function of the impurity parameter, with $Q_{\rm imp} \ll 1$ indicating the crust is very pure and $Q_{\rm imp} \gg 1$ suggesting the crust is very disordered.

For simplicity reasons it is common to assume that the transition between capture layers in the accreted crust occurs in an infinitely thin layer (Sec. 2.4.2). However, in real NSs they will have some finite thickness (Ushomirsky et al., 2000). Thermal broadening of the Fermi surface can cause electron captures to occur before their respective threshold densities (note that this is the motivation behind the 'wavy capture layer' model discussed in Sec. 3.2.2.1), in some cases even causing the layers to be thickened to sizes of the order of the width between separate layers. This fact is of particular significance in the inner crust where the number of capture layers per unit depth increases significantly. There is a possibility that, in the deep crust, thermal

---

[2] Below this temperature, scattering must be treated in a quantum manner (rather than classically) due to the absorption and emission of individual phonons (Baiko and Yakovlev, 1996), and Eq. (4.14) breaks down.

broadening effects can actually lead to the capture layers overlapping with one another (Brown, 2000; Ushomirsky et al., 2000). If the capture layers do overlap, then the mixing of the layers will produce a $Q_{\rm imp}$ value greater than unity and lead to significant disorder. For simplicity, since the zero-temperature BSk equations of state (i.e. the F+18 model) assume capture layers to be infinitely thin, we shall follow Osborne and Jones (2020) and ignore the thermal broadening effects, so as to avoid the mixing of the capture layers and assume the transition layers to be infinitely sharp.

It is important to point out that this assumption should not lead to any major issues further down the line. The method we shall explore in order to compute thermal mountain sizes in Chapter 6 will not explicitly rely on the capture layers themselves[3], and will not follow the ‘wavy capture layer’ mechanism proposed by Bildsten (1998). In any case, even if we were to follow the same method, Ushomirsky et al. (2000) also showed that the individual quadrupole moments due to the different capture layers add linearly, and so in principle any overlapping layers can be dealt with via superposition.

In the absence of thermal broadening effects, the electron-impurity scattering frequency is given by (Brown and Cumming, 2009)

$$\nu_{\rm eQ} = \frac{4\pi Q_{\rm imp} e^4 n_{\rm ion}}{p_{\rm F}^2 \nu_{\rm F}} \Lambda_{\rm imp} \,, \tag{4.16}$$

where $\Lambda_{\rm imp}$ is known as the logarithmic Coulomb factor, with a value ≈ 2 (Brown and Cumming, 2009) and $p_{\rm F}^2$, ν_F are the (electron) Fermi momentum (2.35) and Fermi velocity respectively.

Initially, it was believed that rapid proton captures at the base of the ocean would lead to an almost amorphous accreted crust (i.e. $Q_{\rm imp} \gg 1$). However, analysis of light curves from transient systems indicate that actually the crust of accreted NSs should be relatively well ordered. Specifically, many of these stars have been observed to cool down rather quickly during the first ~ 100 days after outburst (Wijnands, 2004). Such rapid cooling can only be explained by an accreted crust with high conductivity, since large amounts of heat must have been conducted downwards through the crust in a relatively short amount of time. This suggests that the crustal lattice actually contains very few impurities, contrary to the notion that nuclei far beyond the iron group are formed as a result of thermonuclear burning. In fact, modelling of these transiently accreting LMXBs suggests that $\mathrm{Q_{imp}}$ is likely of the order ~ 1 - 10 for most systems, but can sometimes reach as high as $\mathrm{Q_{imp}} \sim 100$ in regions of the deep crust where pasta phases occur (see e.g. Ootes et al., 2018 and references therein).

If the impurity parameter is sufficiently small, then the electron-phonon scattering will determine the thermal conductivity in the crust. If, however, the non-equilibrium reactions which take place in the crust do not reduce $Q_{\rm imp}$ from its large value at the base of the ocean (i.e. in the

---

[3] We will instead be exploring density perturbations sourced via a contribution to the total pressure in the crust from the crystal lattice itself (Sec. 6.1.1).

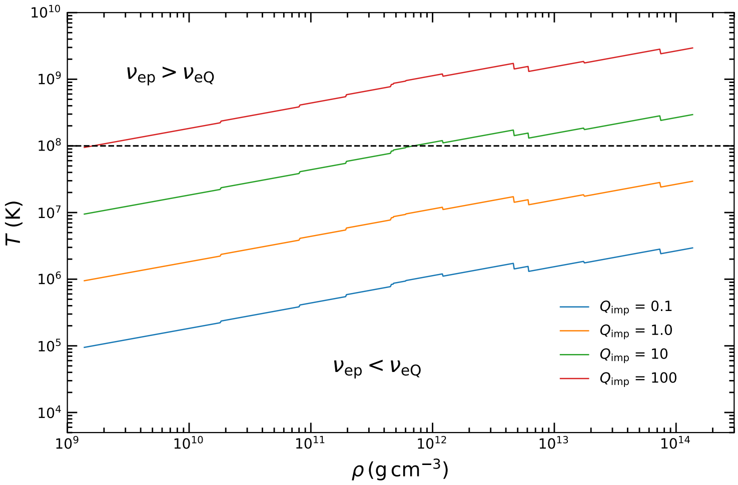

FIGURE 4.4: Phase-space diagram for electron-phonon $\nu_{\rm ep}$ and electron-impurity $\nu_{\rm eQ}$ scattering in the accreted crust assuming BSk21. The curves indicate the temperature Eq. (4.17) at which $\nu_{\rm ep} = \nu_{\rm eQ}$, as a function of density for different values of the impurity parameter $Q_{\rm imp}$ indicated in the legend. Temperatures above the curves indicate electron-phonon dominance, whilst temperatures below the curve indicate electron-impurity dominance. The dashed horizontal line at $T = 3 \times 10^8$ K indicates a fiducial temperature of a typical crust.

hydrogen/helium burning shell; Fig. 2.4), then heat transport will instead be dictated by the electron-impurity scattering (Brown, 2000).

By equating the electron-impurity (4.16) and electron-phonon scattering (4.14) frequencies, one may derive a parameterised formula for how the temperature relates to the divide in dominance between electron-phonon and electron-impurity scattering within the crust as

$$T_\nu = \frac{4\pi\,\hbar^2\,e^2\,n_{\rm N}\,Q_{\rm imp}}{13k_{\rm B}\,p_{\rm F}\,v_{\rm F}}\,{\rm K}\,. \tag{4.17}$$

In Figure 4.4 we show a phase-space diagram for the crust scattering frequencies $\nu_{\rm ep}$ and $\nu_{\rm eQ}$. The temperatures at which $\nu_{\rm ep} \equiv \nu_{\rm eQ}$ (Eq. (4.17)) are given as a function of density (assuming the EoS BSk21) in the crust for different values of the impurity parameter $Q_{\rm imp}$. Crustal temperatures above that of a given curve (i.e a crust with a given $Q_{\rm imp}$) indicate electron-phonon scattering is the dominant process, whilst crustal temperatures below that curve indicate electron-impurity scattering is dominant. For temperatures $T = 3 \times 10^8$ K, typical of that of accreting NSs, electron-phonon scattering is the dominant process in ordered ($Q_{\rm imp} \sim 1$) crusts.

Also note that if the value of $Q_{\rm imp}$ happens to be very large (i.e. of the order Z^2), then the impurity relaxation may be approximated by the so-called *electron-ion relaxation time*, whereby the heat conduction is then mediated by the scattering of electrons on bare nuclei. The electron-ion scattering frequency is (Yakovlev and Urpin, 1980)

$$\nu_{\mathrm{ei}} = \frac{4\pi Z^2 e^4 n_{\mathrm{N}}}{p_F^2 v_F} \Lambda_{\mathrm{ei}} \, , \tag{4.18}$$

where $\Lambda_{\mathrm{ei}} = \ln\left[(2\pi Z/3)^{1/3}(1.5 + 3/\Gamma_{\mathrm{Coul}})^{1/2}\right] - 1$.

4.4.2 Heat conduction in the core

Matter in the outer core typically consists of a sea of neutrons, with a small number of protons and electrons present. Deeper in the core, other particles, including muons, hyperons, pion condensates, and even deconfined quarks may then appear. What particles may or may not appear in the inner core are EoS dependent. Since we are assuming the BSk19-21 family of EoSs, we shall restrict ourselves to the fairly standard model of npeμ composition. Inside the core, the electrons are assumed to form a free, ultra-relativistic gas. Muons are also assumed to be free, however are assumed to be non-relativistic where they first appear, becoming more relativistic with increasing density. The baryons, on the other hand, are assumed to exist in a strongly coupled non-relativistic fluid.

We include in our model the contributions to the thermal conductivity from the electrons, muons and neutrons. Interactions between electrons and muons are mediated by Coulomb forces between themselves and other charged particles, whilst the strength of interactions involving neutrons is determined by the strong interaction. The following two Sections 4.4.2.1 and 4.4.2.2 are a collation (*i.e. not derived*) of the fundamental information and relevant equations obtained by Gnedin and Yakovlev (1995) and Baiko et al. (2001) respectively, which are required in order to solve the Newtonian heat equations (4.5) - (4.6) in the core.

4.4.2.1 Lepton conduction

The relationship between relaxation times and scattering frequencies is more complex in the core than it is in the crust (recall Eqs (4.12) - (4.13)). For the leptons, the total effective electron and muon scattering frequencies are

$$\nu_{\mathrm{e}} = \sum_i \nu_{\mathrm{e}i} = \nu_{\mathrm{ep}} + \nu_{\mathrm{ee}} + \nu_{\mathrm{e}\mu} \, , \tag{4.19}$$

$$\nu_{\mu} = \sum_i \nu_{\mu i} = \nu_{\mu\mathrm{p}} + \nu_{\mu\mu} + \nu_{\mu\mathrm{e}} \, , \tag{4.20}$$

respectively, where i is a particular charged particle (i.e. for leptons $i = e, \mu$ and for baryons $i = p$). The exact relationship between the scattering frequency ν and the effective relaxation time τ in the core has been shown to be (c.f. Eq. (17) of Gnedin and Yakovlev, 1995)

$$\tau_{\mathrm{e}} = \frac{\nu_{\mu} - \nu'_{\mathrm{e}\mu}}{\nu_{\mathrm{e}}\nu_{\mu} - \nu'_{\mathrm{e}\mu}\nu'_{\mu\mathrm{e}}} \,, \qquad \tau_{\mu} = \frac{\nu_{\mathrm{e}} - \nu'_{\mu\mathrm{e}}}{\nu_{\mathrm{e}}\nu_{\mu} - \nu'_{\mathrm{e}\mu}\nu'_{\mu\mathrm{e}}} \,. \tag{4.21}$$

The additional collision frequencies $\nu'_{\mathrm{e}\mu}$ and $\nu'_{\mu\mathrm{e}}$ in Eq. (4.21) are known as *partial effective cross-collision frequencies*, and couple the heat transport between the electrons and the muons. The complete calculations which determine the different scattering frequencies derive from a system of Boltzmann kinetic equations which demand multi-dimensional integrals over the momenta of the colliding particles.

The exact nature of these calculations are beyond the scope of this work. As mentioned previously, the full detailed evaluation of the collision integrals can be found in Gnedin and Yakovlev (1995) (and references therein). In this thesis we shall just include the final results of these detailed calculations, and present the relevant formulae in forms which are suitable for numerical calculation.

Firstly, the approximate collision frequencies of the leptons with charged baryons (i.e. protons; ν_{ep} and $\nu_{\mu\mathrm{p}}$) are

$$\nu_{\mathrm{ep}} \approx 1.15 \times 10^{12} \left(\frac{p_{\mathrm{F_e}}}{q_0}\right)^3 \left(\frac{m^*_{\mathrm{p}}}{m_{\mathrm{p}}}\right)^2 \left(\frac{n_0}{n_{\mathrm{e}}}\right) T_8^2 \mathcal{R}_{\mathrm{p}} \, \mathrm{s}^{-1} \,, \tag{4.22}$$

$$\nu_{\mu\mathrm{p}} = \nu_{\mathrm{ep}} \left(\frac{n_{\mathrm{e}}}{n_{\mu}}\right)^{1/3} \,, \tag{4.23}$$

where $\mathcal{R}_{\mathrm{p}}$ is a quantity which takes into account the possibility that the protons are *superconducting* and describes an associated reduction in the collision rate[4], and

$$q_0^2 = \frac{4e^2}{\pi\hbar} \sum_i m_i^* p_{\mathrm{F}_i} \,, \tag{4.24}$$

is known as the *squared static screening momentum*, and arises due to the fact interactions (via Coulomb forces) between individual charged particles in a system of many particles are damped by the presence of other charge carriers. It is usually assumed that the effect of this screening is weak in most situations, leading to the so called ‘weak-screening’ approximation, in which Eq. (4.24) may be approximated as

$$\frac{q_0^2}{p_{\mathrm{F}_e}^2} \approx 0.00929 \left[1 + \left(\frac{n_{\mu}}{n_{\mathrm{e}}}\right)^{1/3} + 2.83 \left(\frac{m^*_{\mathrm{p}}}{m_{\mathrm{p}}}\right) \left(\frac{n_{\mathrm{p}} n_0}{n_{\mathrm{e}}^2}\right)^{1/3} \mathcal{Z}_{\mathrm{p}} \right] , \tag{4.25}$$

---

[4] One may think of $\mathcal{R}_{\mathrm{p}}$ as a suppression factor. If the protons are superconducting, then $\mathcal{R}_{\mathrm{p}} < 1$. The superfluid/superconducting nature of NSs will be explored in greater detail in Section 4.6; and we shall consider the specific form of $\mathcal{R}_{\mathrm{p}}$ in Section 4.6.4.1.

where $\mathcal{Z}_{\rm p}$ is an additional suppression factor which describes the reduction of the screening momentum when the protons are in a superconducting state (again see Sec. 4.6.4.1).

Next, we shall consider the effective collision frequencies for electron-muon and muon-electron interactions. Again in the weak-screening approximation, these collision frequencies may be approximated as

$$\nu_{{\rm e}\mu} = 1.43\times10^{11}\left(\frac{p_{\rm F_e}}{q_0}\right)^3\left(\frac{n_0}{n_{\rm e}}\right)^{1/3}\left[1+\frac{1}{2}\left(\frac{n_\mu}{n_{\rm e}}\right)^{2/3}\right]T_8^2\ {\rm s}^{-1}\,, \tag{4.26}$$

$$\nu_{\mu{\rm e}} = \nu_{{\rm e}\mu}\left(\frac{n_{\rm e}}{n_\mu}\right)^{1/3}\,, \tag{4.27}$$

along with the associated cross-scattering frequencies $\nu'_{{\rm e}\mu}$ and $\nu'_{\mu{\rm e}}$ expressed as

$$\nu'_{{\rm e}\mu} \approx 1.43\times10^{11}\left(\frac{p_{\rm F_e}}{q_0}\right)^3\left(\frac{n_0}{n_{\rm e}}\right)^{1/3}\left(\frac{n_\mu}{n_{\rm e}}\right)^{2/3}T_8^2\ {\rm s}^{-1}\,, \tag{4.28}$$

$$\nu'_{\mu{\rm e}} = \nu'_{{\rm e}\mu}\left(\frac{n_{\rm e}}{n_\mu}\right)\,. \tag{4.29}$$

Finally, the electron-electron and muon-muon collision frequencies $\nu_{\rm ee}$ and $\nu_{\mu\mu}$ are approximated as

$$\nu_{\rm ee} = 3.58\times10^{11}\left(\frac{p_{\rm F_e}}{q_0}\right)^3\left(\frac{n_0}{n_{\rm e}}\right)^{1/3}T_8^2\ {\rm s}^{-1}\,, \tag{4.30}$$

$$\nu_{\mu\mu} = \nu_{\rm ee}\left(\frac{n_\mu}{n_{\rm e}}\right)\left[1+\frac{6}{5}\left(\frac{m_\mu c}{p_{\rm F_\mu}}\right)^{2/3}+\frac{2}{5}\left(\frac{m_\mu c}{p_{\rm F_\mu}}\right)^{4/3}\right]\,, \tag{4.31}$$

where $m_\mu = 1.88\times10^{25}$ g $\approx 206\,m_e$ is the muon rest-mass.

The left-hand panel of Fig. 4.5 shows the relative frequencies of the different Coulomb scattering interactions (as a function of the density) in the core assuming the BSk21 EoS model a constant temperature 3×10^8 K. When the effects of proton superconductivity are ignored, as is shown in Fig. 2.9, the lepton-proton interactions $\nu_{\rm ep}, \nu_{\mu\rm p}$ have the largest scattering frequencies, and therefore dominate the thermal conductivity. If any regions of the core are superconducting however, then this will suppress $\nu_{\rm ep}, \nu_{\mu\rm p}$, and the lepton-lepton collisions will dominate the conductivity (this will be explored in Sec. 4.6.4.1).

The right-hand panel of Fig. 4.5 then shows the density dependence of the electron, muon, and total lepton thermal conductivities (κ_e, κ_μ, and $\kappa_{e+\mu}$ respectively) in the core (this time for

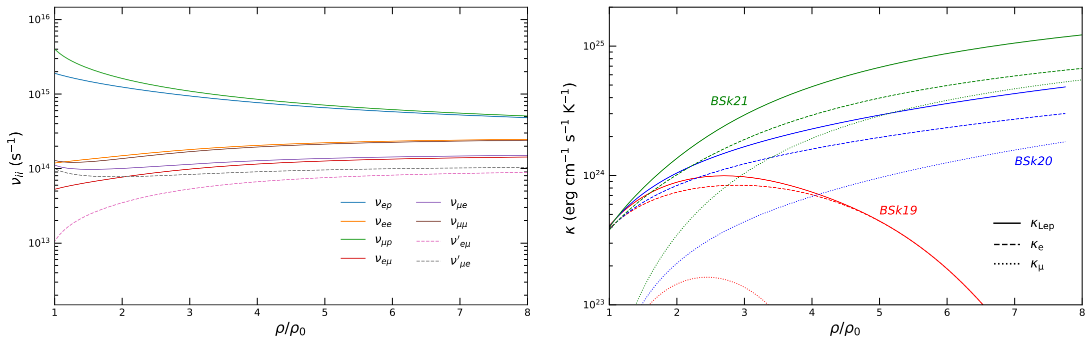

FIGURE 4.5: *Left panel:* Magnitude of the Coulomb scattering frequencies ν_{ij} as a function of density ($\rho_0 = 2.8 \times 10^{14}$ g cm^{-3}) in the core of a non-superconducting neutron star, assuming the equation of state BSk21 at a constant temperature $T = 3 \times 10^8$ K. *Right panel:* Corresponding thermal conductivity contributions κ_e, κ_μ, and $\kappa_{\rm Lep} = \kappa_e + \kappa_\mu$ for BSk21. Also included are the thermal conductivity contributions from the BSk19 and BSk20 equations of state, as indicated near the curves.

each of the BSk19-21 equations of state) assuming a constant core temperature 3×10^8 K and ignoring the effects of proton superconductivity. The shapes of the curves are determined by the number densities of electrons and muons (recall Fig. 2.9), which explains the drop of κ at high density in the BSk19 model. In any region of the core where muons are absent (i.e where the muon chemical potential exceeds than of the electron chemical potential; $\mu_\mu > \mu_{\rm e}$), then only the electron contribution to the lepton thermal conductivity remains, and Eq. (4.21) reduces to just $\tau_{\rm e} = 1/\nu_{\rm e}$, with $\tau_\mu = 0$.

4.4.2.2 Baryon conduction

In contrast to the leptons, the heat conduction via neutrons is mediated by the strong interaction. The heat transport via neutrons is effectively independent from the Coulomb-scattering leptons, and the relationship between the relaxation time and the effective nucleon-nucleon scattering frequencies is

$$\tau_{\rm n} = \frac{1}{\nu_{\rm nn} + \nu_{\rm np}}, \tag{4.32}$$

where $\nu_{\rm nn}$ and $\nu_{\rm np}$ correspond to the frequency of neutron-neutron and neutron-proton interactions respectively.

Much like the calculations performed by Gnedin and Yakovlev (1995), the full evaluation of the collision integrals between the neutrons and protons is beyond the scope of this thesis. Instead, we shall simply present here the results of Baiko et al. (2001) so that they may be used to compute the background thermal profile. The approximate collision frequencies $\nu_{\rm nn}$ and $\nu_{\rm np}$ in the core are

$$\nu_{\mathrm{nn}} \approx 3.48 \times 10^{15} \left(\frac{m_{\mathrm{n}}^{*}}{m_{\mathrm{n}}}\right)^{3} T_8^2 \left\{\mathcal{S}_{\mathrm{n2}}^{(0)} K_{\mathrm{n2}} \mathcal{R}_{\mathrm{n2}} + 3\mathcal{S}_{\mathrm{n1}}^{(0)} K_{\mathrm{n1}} [\mathcal{R}_{\mathrm{n1}} - \mathcal{R}_{\mathrm{n2}}]\right\} \mathrm{s}^{-1}, \tag{4.33}$$

$$\nu_{\mathrm{np}} \approx 3.48 \times 10^{15} \left(\frac{m_{\mathrm{n}}^{*}}{m_{\mathrm{n}}}\right) \left(\frac{m_{\mathrm{p}}^{*}}{m_{\mathrm{p}}}\right)^{2} T_8^2 \left\{\mathcal{S}_{\mathrm{p2}}^{(0)} K_{\mathrm{p2}} \mathcal{R}_{\mathrm{p2}} + 0.5 K_{\mathrm{p1}} \mathcal{S}_{\mathrm{p1}} [3\mathcal{R}_{\mathrm{p1}} - \mathcal{R}_{\mathrm{p2}}]\right\} \mathrm{s}^{-1}. \tag{4.34}$$

The quantities $\mathcal{S}_{\alpha}^{(0)} (\alpha = \mathrm{n1}, \mathrm{n2}, \mathrm{p1}, \mathrm{p2})$ are scattering cross sections[5], the quantities $\mathcal{R}_{\alpha}$ are superfluid reduction factors (Sec. 4.6.4.2) and K_{α} are terms that account for in-medium effects (see below). Analytical fits for the in-vacuum integrals $\mathcal{S}_{\alpha}^{(0)}$ may be shown to be (Baiko et al., 2001)

$$\mathcal{S}_{\mathrm{n1}}^{(0)} = \frac{14.57}{k_{\mathrm{F_n}}^{1.5}} \left[\frac{1 - 0.0788\, k_{\mathrm{F_n}} + 0.0883\, k_{\mathrm{F_n}}^2}{1 - 0.1114\, k_{\mathrm{F_n}}}\right], \tag{4.35a}$$

$$\mathcal{S}_{\mathrm{n2}}^{(0)} = \frac{7.880}{k_{\mathrm{F_n}}^{2}} \left[\frac{1 - 0.2241\, k_{\mathrm{F_n}} + 0.2006\, k_{\mathrm{F_n}}^2}{1 - 0.1742\, k_{\mathrm{F_n}}}\right], \tag{4.35b}$$

$$\mathcal{S}_{\mathrm{p1}}^{(0)} = \frac{0.8007\, k_{\mathrm{F_p}}}{k_{\mathrm{F_n}}^{2}} \Big[(1 + 31.28\, k_{\mathrm{F_n}} - 0.0004285\, k_{\mathrm{F_n}}^2 + 26.85\, k_{\mathrm{F_n}} + 0.08012\, k_{\mathrm{F_n}}^2) \cdot (1 - 0.5898\, k_{\mathrm{F_n}} + 0.2368\, k_{\mathrm{F_n}}^2 + 0.5838\, k_{\mathrm{F_p}}^2 + 0.884\, k_{\mathrm{F_n}} k_{\mathrm{F_p}})^{-1}\Big], \tag{4.35c}$$

$$\mathcal{S}_{\mathrm{p2}}^{(0)} = \frac{0.3830\, k_{\mathrm{F_p}}^4}{k_{\mathrm{F_n}}^{5.5}} \Big[(1 + 102.0\, k_{\mathrm{F_p}} - 53.91) \cdot (1 - 0.7087\, k_{\mathrm{F_n}} + 0.2537\, k_{\mathrm{F_n}}^2 + 9.404\, k_{\mathrm{F_p}}^2 + 1.589\, k_{\mathrm{F_n}} k_{\mathrm{F_p}})^{-1}\Big], \tag{4.35d}$$

where $k_{\mathrm{F_n}}, k_{\mathrm{F_p}} = (3\pi^2 n_{\mathrm{n,p}})^{1/3}$ are the Fermi wave-vectors of the protons and neutrons respectively, computed from the number fractions (2.32) - (2.34) ($n_{\mathrm{n,p}} = Y_{\mathrm{n,p}}\, n_{\mathrm{b}}$) as described in Section 2.5.1.

In addition to considering the nucleon-nucleon interactions in vacuum, Baiko et al. (2001) also considered the form of scattering cross sections *in medium*. They found that many-body effects can be rather significant, reducing the scattering cross sections by up to 100 – 500%. The quantities K_{α} in Eqs (4.33) - (4.34) describe these in-medium effects, with analytical fits expressed as[6]

---

[5] Strictly speaking these quantities are evaluated as multi-dimensional integrals over the momenta of colliding bare particles *in vacuum*.

[6] These equations, are, however, quite rudimentary and are strictly only valid in the regime whereby $m_{\mathrm{n}}^{*} = m_{\mathrm{p}}^{*} \equiv 0.8 m_{\mathrm{b}}$.

$$K_{\rm n1} = \left(\frac{m_{\rm b}}{m_{\rm n}^*}\right)^2 \Big[0.4583 + 0.892\,u_{\rm n1}^2 - 0.5487\,u_{\rm n1}^3 - 0.06205\,k_{\rm F_n} + 0.04022\,k_{\rm F_n}^2 + 0.2122\,u_{\rm n1}\,k_{\rm F_n}\Big]\,, \tag{4.36a}$$

$$K_{\rm n2} = \left(\frac{m_{\rm b}}{m_{\rm n}^*}\right)^2 \Big[0.4891 + 1.111\,u_{\rm n2}^2 - 0.2283\,u_{\rm n2}^3 + 0.01589\,k_{\rm F_n} - 0.02099\,k_{\rm F_n}^2 + 0.2773\,u_{\rm n2}\,k_{\rm F_n}\Big]\,, \tag{4.36b}$$

$$K_{\rm p1} = \left(\frac{m_{\rm b}}{m_{\rm p}^*}\right)^2 \Big[0.04377 + 1.100\,u_{\rm p1}^2 + 0.1180\,u_{\rm p1}^3 + 0.1626\,k_{\rm F_p} + 0.3871\,u_{\rm p1}\,k_{\rm F_p} - 0.2990\,u_{\rm p1}^4\Big]\,, \tag{4.36c}$$

$$K_{\rm p2} = \left(\frac{m_{\rm b}}{m_{\rm p}^*}\right)^2 \Big[0.0001313 + 1.248\,u_{\rm p2}^2 + 0.2403\,u_{\rm p2}^3 + 0.3257\,k_{\rm F_p} + 0.5536\,u_{\rm p2}\,k_{\rm F_p} - 0.3237\,u_{\rm p2}^4 + 0.09786\,u_{\rm p2}^2\,k_{\rm F_p}\Big]\,, \tag{4.36d}$$

where

$$u_{\rm n1} = k_{\rm F_n} - 1.665\,, \tag{4.37a}$$

$$u_{\rm n2} = k_{\rm F_n} - 1.556\,, \tag{4.37b}$$

$$u_{\rm p1} = k_{\rm F_p} - 2.126\,, \tag{4.37c}$$

$$u_{\rm p2} = k_{\rm F_p} - 2.116\,. \tag{4.37d}$$

To determine the relative effectiveness of the heat conduction via the different carriers, Fig. 4.6 shows the density dependence of the lepton (dashed lines), baryon (dotted lines), and total (solid lines) thermal conductivities ($\kappa_{e+\mu}$, κ_n, and $\kappa_{\rm tot} = \kappa_{e+\mu+n}$ respectively) in the *non-superfluid* core for each of the EoSs BSk19-21, assuming a constant $T = 3 \times 10^8$ K. The BSk20 and BSk21 models predict that the thermal conductivity from the leptons is always the dominant source of heat conduction in the core. In the BSk19 model however, the vanishing of the electrons and muons at high density (Fig. 2.9) means that the neutrons can become the dominant source of heat conduction in the innermost regions.

4.5 Sources of neutrino emission

Heat that is generated in the crust via DCH and SCH processes is conducted around the star through the variety of interactions discussed in the previous section. This propagation of heat

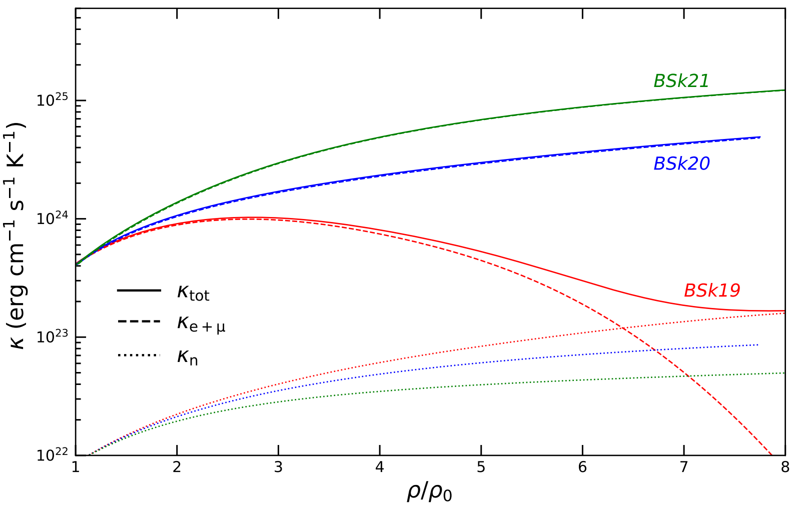

FIGURE 4.6: Thermal conductivity contributions from leptons $\kappa_{e+\mu}$, baryons $\kappa_{\rm n}$, and the *total* thermal conductivity $\kappa_{\rm tot} = \kappa_{\rm e} + \kappa_{\mu} + \kappa_{\rm n}$ assuming each of the BSk19, BSk20, and BSk21 equations of state. The core is assumed to be non-superconducting, at constant temperature $T = 3 \times 10^8$ K.

around the star drives another wide variety of interactions that result in the generation of neutrinos, which carrying away energy and cool down the star.

This neutrino luminosity is, in most cases, vastly dominated by interactions that take place inside the core. This should not be too surprising, given the core compromises $\sim 99\%$ of the star's total mass (recall the right-hand panel of Fig. 2.14). Reactions involving free neutrons and protons, are, however, significantly influenced by the presence of baryon superfluidity; suppressing the neutrino emissivities (as well as actually giving rise to a unique neutrino emission mechanism in the form of Cooper pair breaking and formation; Sec. 4.6.2.4) in a manner similar to that of thermal conduction involving baryons.

The principle neutrino emission mechanisms in the crusts and cores of NSs were famously reviewed by Yakovlev (2001). Convenient fitting formulae for the neutrino emissivity for each interaction as a function of density and temperature were collated (see their Sections 2 and 3), allowing for easy integration of many different neutrino processes into codes that compute the thermal structure of accreting and non-accreting NSs. In the rest of this section, we shall briefly describe these processes, presenting the fitting formulas necessary to compute the total neutrino luminosity Q_ν required to solve the heat equations (4.5) - (4.6) and compute the background thermal profile.

4.5.1 Neutrino emission in the accreted crust

In weakly-magnetised NSs ($B \lesssim 10^{13}$ G), the principle neutrino mechanisms in the crust are the decay of *plasmons* (quanta of the electromagnetic field within a plasma) into a neutrino-antineutrino pair

$$\gamma \longrightarrow \nu + \bar{\nu}\,, \tag{4.38}$$

and neutrino *bremsstrahlung* from the collisions of electrons with atomic nuclei

$$e(A,Z) \longrightarrow e(A,Z) + \nu + \bar{\nu}\,. \tag{4.39}$$

The efficiency of electron-ion bremsstrahlung is determined by the state of the ions in the crust. In regions of the crust where the ions are crystallised ($\Gamma_{\rm Coul} \geq 175$; Eq. 2.9), the neutrino emmisivity is suppressed due to separation of electron energy bands (Yakovlev and Kaminker, 1996). However, if significant heat is deposited into the crust via DCH and SCH processes, then in regions of the crust which melt and the ions are liquefied ($\Gamma_{\rm Coul} < 175$), collisions of relativistic degenerate electrons with atomic nuclei in the Coulomb liquid allow for more efficient neutrino emission (Haensel et al., 1996).

The neutrino luminosity (per unit volume per unit time) due to electron-ion bremsstrahlung was calculated in the solid and liquid phases by Yakovlev and Kaminker (1996) & Haensel et al. (1996) respectively, and may be written

$$Q_{\rm br} = 3.229 \times 10^{11}\,\frac{Z^2}{A}(1 - X_{\rm N})\,\rho_{12}\,T_8^6\,L\,{\rm erg\ s^{-1}\ cm^{-3}}\,, \tag{4.40}$$

where L is a dimensionless parameter known as the *Coulomb parameter* which distinguishes between the two possible states of the crust. Loosely speaking, when the ions are crystallised, then $L \sim 0.2$, whilst in regions of the crust that are liquefied, one has $L \sim 1$[7].

If significant portions of the crust were to be melted, then it is likely the crust will be at temperatures close to, or exceeding 10^9 K. At these temperatures, the interactions of free electrons with plasma microfields can also become a significant source of neutrinos. Several types of plasmons are thought to exist in NS matter, and they can, in theory, emit neutrinos of any flavor. The neutrino luminosity generated by the decay of plasmons is given by Yakovlev (2001) as

---

[7] Strictly speaking, L is a slowly-varying function of density, temperature, and composition. An analytic fit for the Coulomb parameter was proposed by Haensel et al. (1996) (their Eq. (25)), but it does not change appreciably in the context of the parameter space explored here.

$$Q_{\rm pl} \approx \frac{G_{\rm F}^2}{96\pi^4\hbar\alpha_{\rm f}}\left(\frac{m_e c}{\hbar}\right)^9 (I_{\rm l}+I_{\rm t})\sum_\nu C_V^2\,, \tag{4.41}$$

where $G_{\rm F} = 1.496\times10^{49}$ erg cm^3 is known as the Fermi weak interaction constant, $\alpha_{\rm f} \equiv e^2/(\hbar c) \approx 1/137$ is the fine structure constant, and C_V are normalized vector constants which account for the fact that the decay process can produce neutrino pairs of any flavor (i.e. $\nu_{\rm e}\bar{\nu}_e$, $\nu_\mu\bar{\nu}_\mu$, $\nu_\tau\bar{\nu}_\tau$).

The final quantities $I_{\rm l}$, $I_{\rm t}$ are dimensionless functions which describe the contributions of both longitudinal and transverse plasmons (recall that they are essentially quanta of the electromagnetic field), respectively. Reliable analytic fits to these dimensionless functions were obtained by Yakovlev (2001), given as

$$I_{\rm l}+I_{\rm t} = I_{\rm pl} \approx t_{\rm r}^9(16.23 f_{\rm p}^6 + 4.604 f_{\rm p}^{15/2})\exp(-f_{\rm p})\,, \tag{4.42}$$

where $t_r \equiv k_{\rm B}T/(m_e c^2)$ is a dimensionless relativistic temperature, and $f_{\rm p}$ is referred to as the 'dimensionless plasma parameter', given by

$$f_{\rm p} = \frac{\hbar\omega_{\rm pe}}{k_{\rm B}T} = \frac{1}{t_{\rm r}}\left[\frac{4\alpha_{\rm f}x_{\rm r}^3}{3\pi\sqrt{1+x_{\rm r}^2}}\right]^{1/2}, \tag{4.43}$$

where $x_{\rm r}$ is the relativity parameter (2.36).

Figure 4.7 shows a phase-space diagram for the neutrino luminosity Q_ν due to plasmon decay and electron-ion bremsstrahlung processes in the crust. There is an enormous variation in the values of Q_ν ($\sim$ 14 orders of magnitude) that are covered in the $\rho - T$ space, ranging from $T = 10^7 - 5\times10^9$ K, and $\rho \sim 10^9 - 10^{14}$ g cm^{-3}. Such variations result as a consequence of the strong temperature dependence of the different processes. The coloured regions indicate where the plasma (green) and bremsstrahlung (crystalline [light red] or liquefied [dark red]) processes dominate. Electron-ion bremsstrahlung in the solid phase can be seen to be the dominating the emissivity over the majority of the crust for most temperatures typical of that of accreting NSs due to its high melting temperature (the dotted line).

4.5.2 Neutrino emission in the core

Neutrino emission in the core is determined by numerous different nuclear reactions that often scale with density, as well as (to a steep power) the temperature. Loosely speaking, these mechanisms can be subdivided into two categories: *fast* and *slow* processes. In general, the fast processes are much more efficient neutrino emitters than the slow processes, but have density thresholds that restricts their presence to only the innermost region of the most massive NSs. In

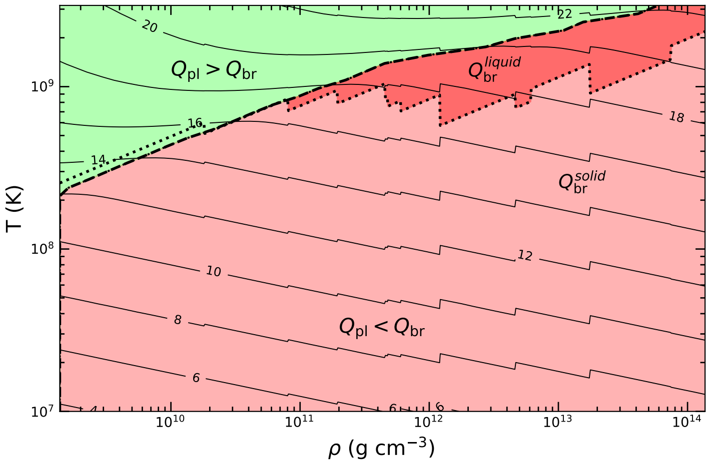

FIGURE 4.7: Phase-space diagram showing the neutrino luminosity Q_ν in the accreted crust of a weakly-magnetized neutron star due to plasmon decay and electron-ion bremsstrahlung processes. The assumed equation of state model is BSk21. Contour lines are the magnitude of the *total* neutrino luminosity $Q_\nu + Q_{\rm pl}$, and are labelled by the value of $\log_{10}[Q_\nu\ ({\rm erg\ cm^{-3}\ s^{-1}})]$. The coloured regions indicate where the plasma, or bremsstrahlung (either crystalline or liquefied) processes dominate. The dashed line indicates the position in the phase-space diagram whereby the processes are equal in magnitude, and the dotted line corresponds to the melting temperature $T_{\rm m}$, whereby $\Gamma_{\rm Coul}(\rho) = 175$; Eq. (2.9).

the next few sections we will discuss the strongest of these reactions; direct URCA, modified URCA, and nucleon-nucleon bremsstrahlung.

The total neutrino emissivity from the sum of these processes is illustrated in the left- (assuming the EoS BSk20) and right-hand panels (assuming BSk21) of Fig. 4.8. One may immediately notice the huge range in Q_ν between the different processes (spanning $\sim$ 22 orders of magnitude in the right-hand panel) as a consequence their strong temperature dependence. Over the course of the next few sections we shall take the time to discuss each of these processes in turn.

4.5.2.1 Direct URCA processes

By far the most powerful emission mechanism is the direct URCA (Durca) process. In simple npe matter the process is simple, and consists of successive reactions of beta decay and electron capture:

$$\rm n \longrightarrow p + e^- + \bar{\nu}_e\,, \qquad p + e^- \longrightarrow n + \nu_e\,. \tag{4.44}$$

These reactions ensure that nucleons in the core remain in a state of beta-equilibrium, whereby the chemical potentials of the matter satisfies the equality $\mu_{\rm n} = \mu_{\rm p} + \mu_{\rm e}$. In equilibrium, both reactions proceed at equivalent rates, and the composition of core remains constant. Equally, if the system is brought out of equilibrium for whatever reason, one of the two reactions is

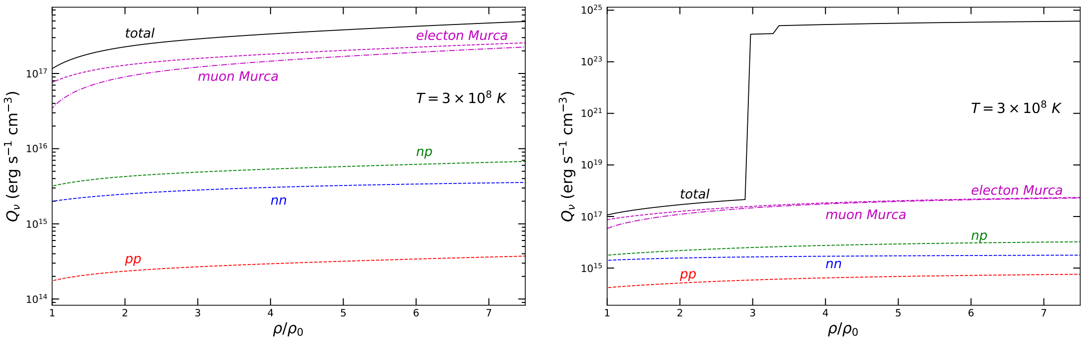

FIGURE 4.8: *Left panel:* Density dependence of the neutrino luminosity Q_ν of modified URCA (Sec. 4.5.2.2) and nucleon-nucleon bremsstrahlung (Sec. 4.5.2.3) in the core of a non-superfluid neutron star assuming the BSk20 equation of state at $T = 3 \times 10^8$ K (note direct URCA processes are forbidden; Sec. 4.5.2.1). *Right panel:* Same as left panel but assuming the BSk21 equation of state (whereby direct URCA processes are permitted). Direct URCA processes are so dominant that its luminosity curve lies beneath the black curve denoting the total neutrino luminosity.

enhanced/suppressed such that the proton/neutron fractions once again return to their respective equilibrium values. The neutrino emissivity due to Durca processes in the core of NSs was obtained by Lattimer et al. (1991), and may be approximated as

$$Q_\nu^{(\mathrm{Durca})} = 4.00 \times 10^{27} \left(\frac{n_e}{n_0}\right)^{1/3} \frac{m_n^* m_p^*}{m_n^2} T_9^6\, \Theta_{\mathrm{npe}} \ \ \mathrm{erg\ cm^{-3}\ s^{-1}}\,, \tag{4.45}$$

where Θ_{npe} is a step function such that $\Theta_{\mathrm{npe}} = 1$ if the Fermi momenta p_{F_n}, p_{F_p} and p_{F_e} satisfies the so-called *triangle condition* (see below) and $\Theta_{\mathrm{npe}} = 0$ otherwise.

The reactions (4.44) may proceed only when the energies of the reacting particles (electrons, protons, and neutrons) are approximately equal to that of their respective Fermi energies (Potekhin et al., 2015). The triangle inequality is a statement of momentum conservation that the Fermi momenta of each particle must be smaller than the sum of the other two. Neutrons are by far the most abundant particle in the core (Fig. 2.9), and so p_{F_n} is much larger than both p_{F_p} and p_{F_e}. The Durca triangle condition implies $p_{F_n} \leq p_{F_p} + p_{F_e}$ (or equivalently $n_n^{1/3} \leq n_p^{1/3} + n_e^{1/3}$). Charge neutrality in the core also requires that $n_e = n_p$, which implies that $n_n \leq (2n_p^{1/3})^3 \leq 8n_p$. Defining the proton fraction to be $Y_p = n_p/(n_n + n_p)$, one finds that the critical proton fraction must be $Y_{cp} \geq 1/9 \sim 11\%$. The quantity Θ_{npe} therefore acts as a threshold, whereby Durca reactions may only proceed at a given density if the proton fraction there exceeds $\sim 11\%$. Given that the number densities of each particle is EoS dependent, so too is the Durca threshold.

If permitted by the EoS, then the Durca process includes contributions from muons as well, via the interactions

$$\mathrm{n} \longrightarrow \mathrm{p} + \mu + \bar{\nu}_\mu, \qquad \mathrm{p} + \mu \longrightarrow \mathrm{n} + \nu_\mu\,. \tag{4.46}$$

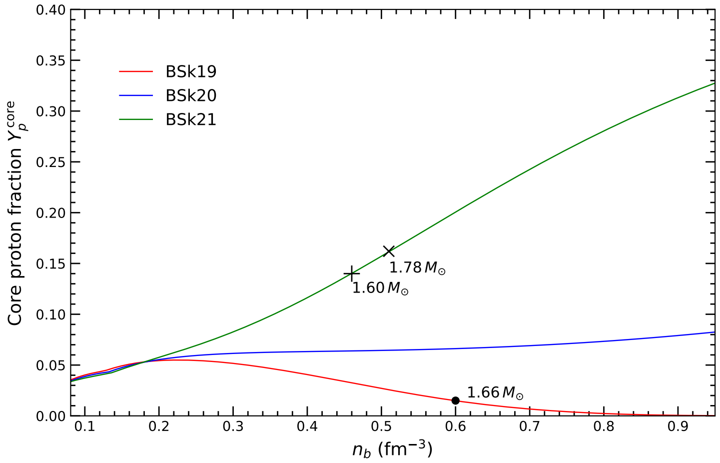

FIGURE 4.9: Proton fractions inside the core as a function of the density for each of the BSk19-21 equations of state. The BSk19 model forbids direct URCA processes to take place at any density, but permits modified URCA processes to proceed at densities exceeding $1.66\,M_\odot$ as indicated by the filled circle (see Sec. 4.5.2.2) . The BSk20 equation of state also forbids direct URCA processes from taking place, but does allow for modified URCA processes at all densities. The BSk21 model also permits modified URCA processes at all densities, but has minimum threshold densities at which electron and muon direct URCA may proceed as indicated by the + and × markers respectively.

In regions of the core where electrons and muons coexist, the processes occur in parallel, with the emissivity of the muon contribution being identical to Eq. (4.45) if $m^*_\mu = m^*_\mathrm{e}$. Given the condition of beta equilibrium implies $\mu_\mu = \mu_\mathrm{e}$, this is a reasonable assumption. The only difference is the condition on the step function Θ_{npe}, which need be replaced by $\Theta_{\mathrm{np}\mu}$. The presence of muons will increase the threshold by several percent (Potekhin et al., 2015), and muon Durca will open at a slightly higher density, determined by the number density of muons predicted by the EoS.

In figure 4.9 we re-plot the number fractions of protons Y_p in the core for each of BSk19-21 (recall Fig. 2.9). The triangle condition is satisfied only for the accreting EoS BSk21, with the electron $n_{\mathrm{Durca,\,e}}$ and muon $n_{\mathrm{Durca},\,\mu}$ thresholds being (to 2 s.f.) 0.46 fm^{-3} and 0.51 fm^{-3} respectively, and are marked by a × and + in Fig. 4.9. These densities equate to electron and muon Durca becoming a contributory (or even dominant) cooling mechanism in stars (assuming the EoS BSk21) with masses greater than 1.60 and 1.78 $M_\odot$ respectively.

4.5.2.2 Modified URCA processes

If Durca processes are forbidden, then the next most efficient neutrino processes in NS cores are the modified URCA (Murca) reactions:

$$\mathrm{n} + \mathrm{N} \longrightarrow \mathrm{p} + \mathrm{e}^- + \bar{\nu}_\mathrm{e} + \mathrm{N}, \tag{4.47}$$

where N is a ‘spectator’ nucleon that ensures that momentum conservation is always satisfied. This additional nucleon implies the reaction may go through two ‘channels’, either

$$\mathrm{n} + \mathrm{n} \longrightarrow \mathrm{p} + \mathrm{n} + \mathrm{e}^{-} + \bar{\nu}_{\mathrm{e}}, \quad \mathrm{p} + \mathrm{n} + \mathrm{e}^{-} \longrightarrow \mathrm{n} + \mathrm{n} + \nu_{\mathrm{e}} \tag{4.48}$$

or

$$\mathrm{n} + \mathrm{p} \longrightarrow \mathrm{p} + \mathrm{p} + \mathrm{e}^{-} + \bar{\nu}_{\mathrm{e}}, \quad \mathrm{p} + \mathrm{p} + \mathrm{e}^{-} \longrightarrow \mathrm{n} + \mathrm{p} + \nu_{\mathrm{e}}, \tag{4.49}$$

which are referred to as the neutron and proton ‘branches’ respectively. In standard CGS units, the neutrino emissivity of the neutron branch can be approximated as (Yakovlev, 2001)

$$Q_{\mathrm{e}}^{(\text{Murca; n-branch})} = 8.1 \times 10^{21} \left(\frac{m_{\mathrm{n}}^{*}}{m_{\mathrm{n}}}\right)^{3} \frac{m_{\mathrm{p}}^{*}}{m_{\mathrm{p}}} \left(\frac{n_{\mathrm{p}}}{n_{0}}\right)^{1/3} T_{9}^{8} \alpha_{\mathrm{n}} \beta_{\mathrm{n}} \ \ \mathrm{erg\ cm^{-3}\ s^{-1}}, \tag{4.50}$$

where α_{n} is a quantity that describes momentum transfer in the Born approximation, and β_{n} includes non-Born corrections. It was assumed by Yakovlev and Levenfish (1995) that $\beta_{\mathrm{n}} = 0.68$, and that α_{n} is (taken from results obtained by Friman and Maxwell, 1979)

$$\alpha_{\mathrm{n}} = 1.76 - 0.63 \left(\frac{n_{0}}{n_{\mathrm{n}}}\right)^{2/3}. \tag{4.51}$$

Similarly, the neutrino emissivity of the proton branch of the Murca process was given by Yakovlev (2001) as

$$Q_{\mathrm{e}}^{(\text{Murca; p-branch})} = Q_{\mathrm{e}}^{(M_{\mathrm{n}})} \left(\frac{m_{\mathrm{p}}^{*}}{m_{\mathrm{n}}^{*}}\right)^{2} \left(\frac{(p_{\mathrm{F_e}} + 3p_{\mathrm{F_p}} - p_{\mathrm{F_n}})^{2}}{8 p_{\mathrm{F_e}} p_{\mathrm{F_p}}}\right) \Theta_{\mathrm{e}}^{(\text{Murca; p-branch})} \ \ \mathrm{erg\ cm^{-3}\ s^{-1}}. \tag{4.52}$$

Unlike the neutron branch, the proton branch contains the threshold factor $\Theta_{\mathrm{e}}^{(\text{Murca; p-branch})}$. In ordinary npe matter, the triangle condition for the proton Murca branch requires $p_{\mathrm{F_n}} < 3p_{\mathrm{F_p}} + p_{\mathrm{F_e}}$, indicating that the proton fraction must exceed $Y_p \sim 0.015$ in order for the proton branch to proceed (Yakovlev, 2001). In reference to Fig. 2.9, the triangle condition for Murca is satisfied at every point in the core of the star in the BSk20 and BSk21 models, but $Q_{\mathrm{e}}^{(\text{Murca; p-branch})}$ is forbidden by the BSk19 model at number densities $n_b > 0.6$, as indicated in Fig. 4.9.

Much like the Durca process, if muons are present then there will also be muon Murca processes occurring in parallel. The emissivities of both the neutron and proton branches are analogous to that of their electron counterparts and are given, respectively, by

$$Q_{\mu}^{(\text{Murca; n-branch})} = 8.1 \times 10^{21} \left(\frac{m_{\text{n}}^{*}}{m_{\text{n}}} \right)^{3} \frac{m_{\text{p}}^{*}}{m_{\text{p}}} \left(\frac{n_{\mu}}{n_{0}} \right)^{1/3} \left(\frac{n_{\text{p}}}{n_{\text{e}}} \right)^{1/3} T_{9}^{8} \alpha_{\text{n}} \beta_{\text{n}} \ \text{erg cm}^{-3}\ \text{s}^{-1} \tag{4.53}$$

and

$$\begin{aligned} Q_{\mu}^{(\text{Murca; p-branch})} = Q_{\text{e}}^{(\text{Murca; n-branch})} & \left(\frac{n_{\mu}}{n_{\text{e}}} \right)^{1/3} \left(\frac{m_{\text{p}}^{*}}{m_{\text{p}}^{*}} \right)^{2} \\ & \times \left(\frac{(p_{\text{F}_{\mu}} + 3p_{\text{F}_{\text{p}}} - p_{\text{F}_{\text{n}}})^{2}}{8 p_{\text{F}_{\mu}} p_{\text{F}_{\text{p}}}} \right) \Theta_{(\text{Murca; p-branch})_{\mu}} \ \text{erg cm}^{-3}\ \text{s}^{-1}, \end{aligned} \tag{4.54}$$

where we have made the substitutions $\Theta_{\text{e}}^{(\text{Murca; p-branch})} \longrightarrow \Theta_{\mu}^{(\text{Murca; p-branch})}$ and $p_{\text{F}_{\text{e}}} \longrightarrow p_{\text{F}_{\mu}}$. Also note the additional factor $(n_{\mu}/n_{\text{e}})^{1/3}$ added for both the neutron and proton branches.

The involvement of 5 degenerate Fermions (compared to the three involved in the Durca process) means the phase space is relatively limited. Specifically, it is reduced by a factor of the order T^{2}. It is this addition of the spectator nucleon that gives the observed temperature dependence $Q^{(\text{Durca})} \propto T^{6}$ in the Direct case and $Q^{(\text{Murca})} \propto T^{8}$ in the modified process. Under typical NS core conditions, the neutrino production rate is ~ 6 orders of magnitude for Durca than Murca (Fig. 4.8). And so whilst the Durca process is far more efficient than Murca, the fact the threshold for the latter process is much lower (Fig. 4.9), it is the case that Murca is often the dominant cooling mechanism in a non-superfluid core, except in the highest density regions of the heaviest stars.

4.5.2.3 Neutrino bremsstrahlung

Whilst the Murca process is ubiquitous within the cores of most NSs, there are certain circumstances, such as in extreme superfluidity, whereby the process can be significantly suppressed Yakovlev (2001). In the absence of both Durca and Murca processes, the neutrino luminosity inside the core is determined by neutrino bremsstrahlung radiation that arises from the set of nucleon-nucleon interactions

$$\text{n} + \text{n} \longrightarrow \text{n} + \text{n} + \nu + \bar{\nu}, \tag{4.55}$$

$$\text{n} + \text{p} \longrightarrow \text{n} + \text{p} + \nu + \bar{\nu}, \tag{4.56}$$

$$\text{p} + \text{p} \longrightarrow \text{p} + \text{p} + \nu + \bar{\nu}. \tag{4.57}$$

The most important characteristic of these interactions is that, contrary to both the URCA processes, nucleon-nucleon bremsstrahlung interactions do not involve a change in composition.

Consequently, these processes operate at all densities, and there are no thresholds associated with momentum conservation.

The presence of muons in the core has no influence on nucleon-nucleon interactions, and the neutrino emissivities of the bremsstrahlung interactions (4.55) - (4.57) may be approximated as (Yakovlev, 2001)

$$Q^{(\mathrm{nn})} = 7.5\times10^{19}\left(\frac{m_\mathrm{n}^*}{m_\mathrm{n}}\right)^4\left(\frac{n_\mathrm{n}}{n_0}\right)^{1/3} T_9^8\alpha_{\mathrm{nn}}\beta_{\mathrm{nn}}\mathcal{N}_\nu \ \ \mathrm{erg\ cm^{-3}\ s^{-1}}\,, \tag{4.58}$$

$$Q^{(\mathrm{np})} = 1.5\times10^{20}\left(\frac{m_\mathrm{n}^*}{m_\mathrm{n}}\right)^2\left(\frac{m_\mathrm{p}^*}{m_\mathrm{p}}\right)^2\left(\frac{n_\mathrm{p}}{n_0}\right)^{1/3} T_9^8\alpha_{\mathrm{np}}\beta_{\mathrm{np}}\mathcal{N}_\nu \ \ \mathrm{erg\ cm^{-3}\ s^{-1}}\,, \tag{4.59}$$

$$Q^{(\mathrm{pp})} = 7.5\times10^{19}\left(\frac{m_\mathrm{p}^*}{m_\mathrm{p}}\right)^4\left(\frac{n_\mathrm{n}}{n_0}\right)^{1/3} T_9^8\alpha_{\mathrm{pp}}\beta_{\mathrm{pp}}\mathcal{N}_\nu \ \ \mathrm{erg\ cm^{-3}\ s^{-1}}\,, \tag{4.60}$$

respectively, where $\mathcal{N}_\nu$ accounts for the fact that the interactions are permitted to produce neutrinos of any flavour ($\nu_\mathrm{e}\bar{\nu}_\mathrm{e}$, $\nu_\mu\bar{\nu}_\mu$, $\nu_\tau\bar{\nu}_\tau$; and so $\mathcal{N}_\nu = 3$). The quantities α_{NN} and β_{NN} are analogous to their Murca counterparts, and have values $\alpha_{\mathrm{nn}} = 0.59$, $\alpha_{\mathrm{np}} = 1.06$, $\alpha_{\mathrm{pp}} = 0.11$; $\beta_{\mathrm{nn}} = 0.56$, $\beta_{\mathrm{np}} = 0.66$, $\beta_{\mathrm{pp}} \approx 0.7$.

The general structure of these expressions are markedly similar to that of Murca. Most notably, the temperature dependence is the same. Notice, however, that the numerical coefficients are approx. two orders of magnitude smaller for the bremsstrahlung processes than for the Murca. As we shall, whilst in *non-superfluid* matter the bremsstrahlung emmisivity is relatively inconsequential (Fig. 4.8), it turns out that nucleon-nucleon interactions can actually dominate the Murca if the superfluidity it strong enough.

4.6 Superfluidity in neutron stars

Despite the numerous advancements in both experimental and theoretical techniques for probing the interiors of neutron stars, it is no secret that the properties of the ultra-dense core remain very much uncertain. At a minimum, the core can be described as a mixture of interacting neutrons, protons, and electrons (plus muons). With the separations between particles being so small, it is possible that at a particular temperature, the attractive part of the nuclear potential can lead to the formation of 'correlated pairs' of nucleons. This can lead to a gap in the energy spectrum of these nucleons, and the transition to a state of so-called *superfluidity* (or *superconductivity*).

The idea that superfluids may be present in the interiors of NSs was first proposed by Migdal (1959), soon after the development of the microscopic theory of superconductivity by Bardeen et al. (1957). As a result, the influence of neutron superfluidity/proton superconductivity on heat conduction and neutrino processes (and therefore on the thermal evolution) quickly became an active area of research. For all of the fervent excitement surrounding NS superfluids, *evidence* for such a phenomenon might only come in the form of cooling observations.

Indeed, the supernova remnant Cassiopeia A is thought to contain a young ($\sim$ 330 year old) neutron star, which has recently showed a noticeable, unexpected decline of $\sim 4\%$ in its effective surface temperature over a 10 year period (Heinke and Ho, 2010). It so happens that this decline could, in theory, be explained by additional neutrino emission due to the breaking/formation of so-called *Cooper pairs* (see below, and more specifically Sec. 4.6.2.4), accelerating the cooling if (at least some of) the neutrons are indeed superfluid (Shternin et al., 2011).

The temperature at which nucleons transition to at superfluid/superconducting state is relatively unknown (Sec. 4.6.1), as well as the effects these states of matter have on the relevant heat conduction and neutrino emission mechanisms. The analysis of cooling curves, however, can allow for the constraining of both of these phenomena, which would otherwise be left to speculation. In the particular case of Cassiopeia A, Shternin et al. (2011) were able to draw the following conclusions from the observations:

- The maximum critical temperature for neutron pairing in the core must be $T_{\mathrm{cn,\,max}} \approx (7-9)\times 10^8$ K.
- The range of densities in which the neutrons are superfluid (see Fig. 4.10) must be quite large in order for the neutrino emissivity from the formation and breaking of Cooper pairs to be sufficiently strong.
- The neutrino emission from the core of Cassiopeia A before the decline in surface temperature must have been suppressed by a factor 30 – 100 than that of standard Murca processes in ordinary matter (i.e. the emissivity of Murca presented in Sec. 4.5.2.2).

In the following sections, we shall discuss theoretical attempts to predict the amount of suppression of the various neutrino processes involving baryons that operate in the core. We shall present formulae for the reduction factors $\mathcal{R}$ of each mechanism, so that they may be applied to our numerical code for computing the thermal background of our steadily-accreting NS. In the interest of transparency, the formulae presented are (mostly) a collation of the results originally reviewed in Section 4 of Yakovlev (2001), rather than derived.

4.6.1 The superfluid energy gap and critical transition temperature

The phenomenon of superfluidity occurs as a result of *Cooper pairing* of nucleons, whereby the attractive piece of the interaction between particles can lead to the formation of ‘pairs’ of bound nuclei[8]. These Cooper pairs may form once the temperature of the system falls below the

---

[8] For a more technical description of the pairing phenomenon (specific to applications relating to neutron stars), see the recent review by Haskell and Sedrakian (2018).

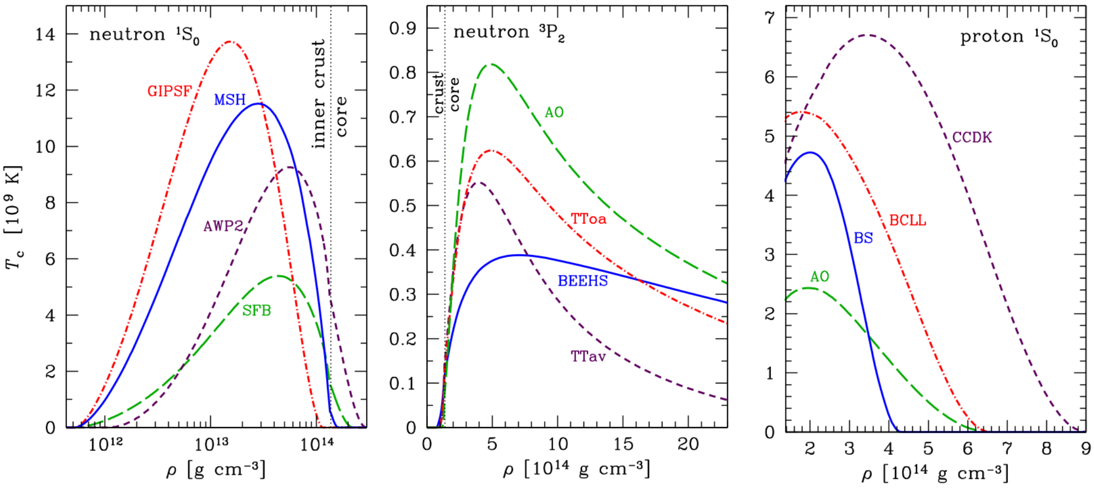

FIGURE 4.10: Critical temperatures of singlet neutron (left panel), triplet neutron (middle panel), and singlet proton (right panel) pairing in the inner crust and core of a neutron star, for different superfluidity models marked near the curves: AO (Amundsen and Østgaard, 1985a,b), AWP2 (Ainsworth et al., 1989), BCLL (Baldo et al., 1992), BEEHS (Baldo et al., 1998), BS (Baldo and Schulze, 2007), CCDK (Chen et al., 1993), GIPSF (Gandolfi et al., 2008), MSH (Margueron et al., 2008), SFB (Schwenk et al., 2003), TTav and TToa (Takatsuka and Tamagaki, 2004). Image credit: reproduced from Potekhin et al. (2015).

so-called '*critical temperature*', T_c, which denotes the transition from the normal to superfluid state. In the normal state, the dispersion relation of Fermions is continuous. In the superfluid state however, a discontinuity develops, resulting in an energy gap $\Delta_{\text{gap}}(T)$[9] .

In standard npeμ matter, superfluidity is typically thought to manifest in terms of the pairing of protons, and the pairing of neutrons. Neutrons in the inner crust and protons in the core are thought to pair in the singlet (${}^1S_0$) state (Wolf, 1966), while neutrons in the core, on the other hand, are expected to pair in a triplet (${}^3P_2$) state (Hoffberg et al., 1970; Tamagaki, 1970). The exact nature of the pairing gap inside NSs is still the subject of active research (e.g. Potekhin et al., 2015), and there remains a degree of uncertainty in both the exact range of densities for which the protons and neutrons can be superfluid, but also on their respective transition temperatures. The critical temperatures depend on the inclusion of in-medium effects, and rely heavily on the assumed model for the nuclear interactions. Many authors (e.g. Amundsen and Østgaard, 1985a,b; Ainsworth et al., 1989; Baldo et al., 1992, 1998; Baldo and Schulze, 2007; Chen et al., 1993; Gandolfi et al., 2008; Margueron et al., 2008; Schwenk et al., 2003; Takatsuka and Tamagaki, 2004) have all attempted to model the transition temperatures of either the singlet-state/triplet-state neutrons or singlet-state protons, each to differing results. The results of these calculations were summarised and plotted as a function of the mass density by Potekhin et al. (2015), which we show here in Figure 4.10.

Many of the calculations of the critical temperatures lack convenient fitting formulae in terms of the density. Therefore, in order to be able to introduce effects of superfluidity into this work,

---

[9] The subscript 'gap' serves to distinguish the energy gap from the Lagrangian perturbation Δ that we will encounter in Chapter 6.

TABLE 4.2: Parameters to calculate proton superconducting and neutron superfluid critical transition temperatures. Reproduced from Table 2 of Brown (2000).

Pairing type	T_{c0} [MeV]	k_0 [fm^{-3}]	Δ_k [fm^{-3}]
neutron $^1S_0$	0.802	0.7	1.2
proton $^1S_0$	0.345	0.7	1.0
neutron $^3P_2$	0.0076	2.0	1.6

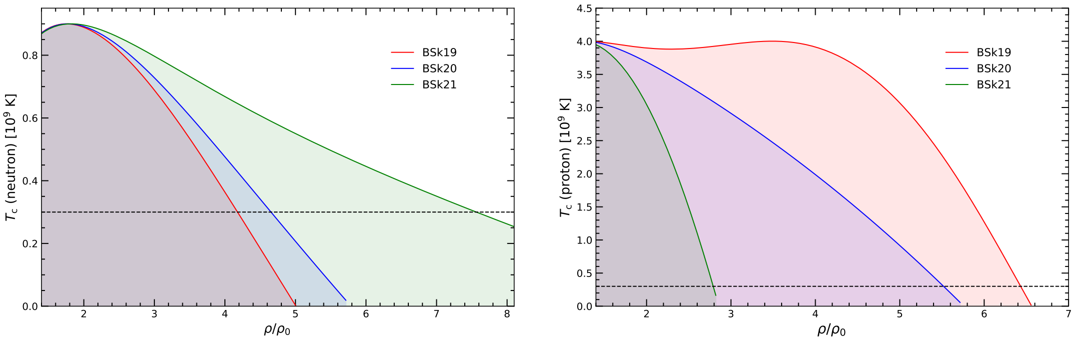

FIGURE 4.11: Superfluid transition temperatures T_c as a function of the density for the BSk19. BSk20, and BSk21 equations of state as obtained from Eq. (4.61) and Table 4.2. The left-hand and right-hand panels show neutron $^3P_2$ and proton $^1S_0$ pairing in the core respectively. The shaded region under each curve represents the range of temperatures whereby the nucleons will be superfluid/superconducting. The dashed horizontal line indicates a typical temperature of 3×10^8 K.

we follow the prescription of Brown (2000). It can be shown that the critical temperatures are (approximately) quadratic functions of the Fermi wavevector $k_{\mathrm{n,\,p}} = (3\pi^2 n_{\mathrm{n,p}})^{1/3}$, with $n_{\mathrm{n,p}}$ being the number density of neutrons and protons respectively (computed as per Sec. 2.5.1). Brown (2000) gives the functional form of T_c for each of the $^1S_0$ proton, $^1S_0$ neutron and $^3P_2$ neutron states as

$$T_{c\,(\mathrm{n,p})} = T_{c0}\left[1 - \frac{(k_{\mathrm{n,p}} - k_0)^2}{(\Delta_k/2)}\right], \tag{4.61}$$

where T_{c0}, k_0, and Δ_k are parameters chosen to reproduce the critical transition temperatures calculated by Amundsen and Østgaard (1985a,b) for the $^1S_0$ singlet and Amundsen and Østgaard (1985b) $^3P_2$ triplet states respectively[10]. The parameters $T_{c\,0}$, k_0, and $\Delta_{k_{n,p}}$ are listed in Table 4.2, and are valid for the regime whereby $k_{n,p} < \Delta_{k_{n,p}}$, with T_c vanishing outside this range.

The critical transition temperatures (in units of 10^9 K) for singlet-state $^1S_0$ proton and triplet-state $^3P_2$ neutron pairing in the core[11] (obtained via Eq. (4.61) and Table 4.2) as a function of the mass density can be seen in Figure 4.11. Note that the maximum critical temperatures for the

---

[10] Notice that in Fig. 4.10, only the critical transition temperature for triplet-state neutrons predicted by Amundsen and Østgaard (1985b) reproduces the maximum critical temperature for neutron pairing in the core ($7 - 9 \times 10^8$ K) inferred from cooling observations of Cassiopeia A (Sec. 4.6).

[11] The singlet-state $^1S_0$ neutron pairing in the crust will be discussed later in Section 4.6.2.4.

protons are an order of magnitude larger than for the neutrons, and that each EoS model predicts a cutoff whereby superfluidity/superconductivity is destroyed. This occurs when the condition $k_{n,p} < \Delta_{k_{n,p}}$ is no longer satisfied, determined by the number density of baryons n_b in the core, as per Fig. 2.9.

Typically, the energy gap $\Delta_\mathrm{gap}(T)$ is assumed to be much smaller than the chemical potential of the paired nuclei (Yakovlev, 2001). In this case the superfluid phenomenon only really affects processes involving nucleons which take place near the Fermi surface; such as heat transport and neutrino emission[12]. In order to understand the effects superfluidity may have on the microphysics, it is convenient to introduce the quantity

$$\nu_\mathrm{gap} = \frac{\Delta_\mathrm{gap}(T)}{k_\mathrm{B}T}\,, \tag{4.62}$$

known as the *dimensionless gap amplitude*. This parameter depends on the type of superfluidity (i.e. the type of pairing). For both the ${}^1S_0$ singlet state and the ${}^3P_2$ triplet states, Levenfish and Yakovlev (1994) proposed the analytical fits

$$\nu_1^\mathrm{gap} = \sqrt{1-\tau_\mathrm{gap}}\left[1.456 - \frac{0.157}{\sqrt{\tau_\mathrm{gap}}} + \frac{1.764}{\tau_\mathrm{gap}}\right], \tag{4.63}$$

$$\nu_2^\mathrm{gap} = \sqrt{1-\tau_\mathrm{gap}}\left[0.7893 + \frac{1.188}{\tau_\mathrm{gap}}\right], \tag{4.64}$$

with the subscripts 1 and 2 referring to ${}^1S_0$ and ${}^3P_2$ pairing respectively, and where τ_gap is a dimensionless temperature

$$\tau_\mathrm{gap} = \frac{T}{T_\mathrm{c}}\,, \tag{4.65}$$

with T_c being the superfluid critical temperature Eq. (4.61).

In Fig. 4.12 the dimensionless gap parameter Eq. (4.62) for both singlet-state (4.63) and triplet-state (4.64) pairing is plotted as a function of the density. It may be seen that $\nu_1^\mathrm{gap} > \nu_2^\mathrm{gap}$ over most of the core, since the critical temperatures for protons in the (${}^1S_0$) state are much higher than those of the neutrons in the (${}^3P_2$) state (Fig. 4.11). Such a result has implications for the structure of the expressions of the superfluid reductions factors that describe the suppression of the various neutrino mechanisms, which we shall now discuss.

---

[12] The superfluid phenomenon likely also affects the heat capacity as well. We do not consider such effects here, however, since we are only interested interest in the steady-state thermal structure of accreting neutrons stars, in which case the time derivative (which includes the specific heat capacity C_P) in the heat equation (4.1) vanishes.

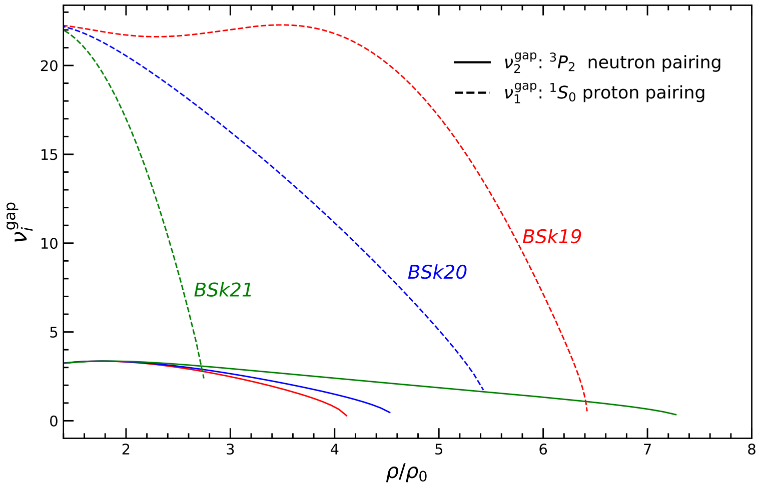

FIGURE 4.12: The dimensionless gap parameter Eq. (4.62) as a function of the density ($\rho_0 = 2.8 \times 10^{14}$ g cm^{-3}) for each of the BSk19, BSk20, and BSk21 equations of state, for both singlet-state (4.63) and triplet-state (4.64) pairing. A constant core temperature $T = 3 \times 10^8$ K is assumed.

4.6.2 Superfluid suppression of neutrino processes

We are now in a position to evaluate how the presence of an energy gap in the baryon energy spectrum affects the neutrino emission from accreting NSs. Most generally, the neutrino emissivity Q_ν of any *baryonic* process in the presence of superfluidity can be written as

$$Q_\nu^{(\text{process})} = Q_{\nu_0}^{(\text{process})} \mathcal{R}_{(\text{pairing type})}^{(\text{process})}, \tag{4.66}$$

where $Q_{\nu_0}^{(\text{process})}$ is the emissivity of the particular neutrino mechanism (be it Durca, Murca, ect.) in *non-superfluid matter* (Sec. 4.5) and $R_{(\text{pairing type})}^{(\text{process})}$ is the corresponding appropriate superfluid reduction factor[13], with the subscript referring to which of the particles involved in a given interaction are superfluid/superconducting (Table 4.2).

Indeed, in order to assess how the neutrino emissivity (4.66) is affected for each neutrino mechanism, one need consider the reduction coefficient $\mathcal{R}$ in four different scenarios, when:

- i) the protons are superconducting and the neutrons are normal,
- ii) the neutrons are superfluid and the protons are normal,
- iii) the protons *and* neutrons are both superconducting/superfluid,
- iv) *neither* of the protons or neutrons are superconducting/superfluid.

---

[13] In general $\mathcal{R} \leq 1$, with $\mathcal{R} \equiv 1$ being, by definition, the reduction factor in non-superfluid matter.

In each of these cases, we shall be in a regime whereby the superfluidity is not too strong (i.e. $v_{\rm gap} \lesssim 20$; Fig. 4.12). This is because in accreting NSs the internal temperature is $T \sim 10^8 - 10^9$ K, and often not as cold as isolated NSs. In the following sections, we shall, in turn, discuss the appropriate reduction factors associated with the different core neutrino mechanisms (Durca, Murca, and nucleon-nucleon bremsstrahlung) considered in Section 4.5.2 in each of the scenarios outlined above.

4.6.2.1 Superfluid suppression: Superconducting protons and normal neutrons

Direct URCA:

Assuming an npeμ composition in the core, the electron and muon Durca processes Eqs (4.44) & (4.46) are suppressed identically, and $\mathcal{R}^{(\rm Durca;\, e)} \equiv \mathcal{R}^{(\rm Durca;\, \mu)}$.

When only the protons are superconducting (scenario i), the reduction factor is determined by Eq. (4.63) since they pair in the singlet ${}^1S_0$ state, and may be approximated as (Yakovlev and Levenfish, 1995)

$$\begin{aligned}\mathcal{R}_{\rm p}^{(\rm Durca)} = & \left[0.2312 + \sqrt{(0.7688)^2 + \left(0.1438\, v_1^{\rm gap}\right)^2}\right]^{5.5} \\ & \times \exp\left[3.427 - \sqrt{(3.427)^2 + \left(v_1^{\rm gap}\right)^2}\right],\end{aligned} \tag{4.67}$$

where $v_1^{\rm gap}$ is the singlet-state pairing gap (4.63).

Modified URCA:

For Murca processes, the problem is treated in much the same as the Durca mechanism, with the reduction factors derived in a similar fashion (Yakovlev and Levenfish, 1995; Yakovlev, 2001). The only difference to consider in the modified case is that we have two separate sequences of reactions; the neutron and proton branches. Just as in the Durca case, the suppression factors apply equally to Murca processes mediated by muons as they do electrons, since the superfluidity phenomenon only affects baryons.

For the first case whereby the protons are superconducting and the neutrons are normal (scenario i), for intermediate values of $v_{\rm gap}$, the suppression factors for the neutron and proton branches are, respectively

$$\mathcal{R}_{\rm p}^{(\rm Murca;\, n\text{-}branch)} = \frac{a^{7.5} + b^{5.5}}{2} \exp\left[3.4370 - \sqrt{(3.4370)^2 + \left(v_1^{\rm gap}\right)^2}\right], \tag{4.68}$$

$$a = 0.1477 + \sqrt{(0.8523)^2 + \left(0.1175\, v_1^{\rm gap}\right)^2}, \tag{4.69}$$

$$b = 0.1477 + \sqrt{(0.8523)^2 + \left(0.1297\, v_1^{\mathrm{gap}}\right)^2}, \tag{4.70}$$

and

$$\mathcal{R}_{\mathrm{p}}^{(\text{Murca; p-branch})} = c^7 \exp\left[5.339 - \sqrt{(5.339)^2 + \left(2v_1^{\mathrm{gap}}\right)^2}\right], \tag{4.71}$$

$$c = 0.2414 + \sqrt{(0.7586)^2 + \left(0.1318\, v_1^{\mathrm{gap}}\right)^2}. \tag{4.72}$$

Nucleon-nucleon bremsstralung:

The relevant suppression factors for the neutrino-pair emission via baryon bremsstrahlung processes were also collated by Yakovlev (2001). In analogy with Durca and Murca reactions, formulae for the case of singlet-state proton superconductivity alone were obtained by Yakovlev and Levenfish (1995). The suppression factors for the np, pp, and nn interactions (4.55) at intermediate values of v_{gap} are

$$\begin{aligned}\mathcal{R}_{\mathrm{p}}^{(\mathrm{np})} = \frac{1}{2.732}\Bigg\{& a \exp\left[1.306 - \sqrt{(1.306)^2 + \left(v_1^{\mathrm{gap}}\right)^2}\right] \\ &+ 1.7372\, b^7 \exp\left[3.303 - \sqrt{(3.303)^2 + 4\left(v_1^{\mathrm{gap}}\right)^2}\right]\Bigg\},\end{aligned} \tag{4.73}$$

$$a = 0.9982 + \sqrt{(0.0018)^2 + \left(0.3815\, v_1^{\mathrm{gap}}\right)^2}, \tag{4.74}$$

$$b = 0.3949 + \sqrt{(0.6051)^2 + \left(2.666\, v_1^{\mathrm{gap}}\right)^2}, \tag{4.75}$$

$$\begin{aligned}\mathcal{R}_{\mathrm{p}}^{(\mathrm{pp})} = \frac{1}{2}\Bigg\{& a^2 \exp\left[4.228 - \sqrt{(4.228)^2 + 4\left(v_1^{\mathrm{gap}}\right)^2}\right] \\ &+ b^{7.5} \exp\left[7.762 - \sqrt{(7.762)^2 + 9\left(v_1^{\mathrm{gap}}\right)^2}\right]\Bigg\},\end{aligned} \tag{4.76}$$

$$a = 0.1747 + \sqrt{(0.8253)^2 + \left(0.07933\, v_1^{\mathrm{gap}}\right)^2}, \tag{4.77}$$

$$b = 0.7333 + \sqrt{(0.2667)^2 + \left(0.1678\, v_1^{\mathrm{gap}}\right)^2}, \tag{4.78}$$

with

$$\mathcal{R}_{\rm p}^{(\rm nn)} = 1.0 \tag{4.79}$$

since the neutron-neutron interactions (4.55) will not be affected by proton superconductivity.

4.6.2.2 Superfluid Suppression: Superfluid neutrons and normal protons

Direct URCA:

When only the neutrons are superfluid (scenario ii), the reduction factor for the Durca process is determined by Eq. (4.64) since they pair in the triplet ${}^3P_2$ state, and is given by (Yakovlev and Levenfish, 1995)

$$\mathcal{R}_{\rm n}^{(\rm Durca)} = \left[0.2546 + \sqrt{(0.7454)^2 + \left(0.1284\, v_2^{\rm gap}\right)^2}\right]^5 \exp\left[2.701 - \sqrt{(3.427)^2 + \left(v_2^{\rm gap}\right)^2}\right]. \tag{4.80}$$

Modified URCA:

In scenario ii, the reduction factor specific to the Murca *proton branch* is (Yakovlev and Levenfish, 1995)

$$\mathcal{R}_{\rm n}^{(\rm Murca;\ p\text{-}branch)} = \frac{a^7 + b^5}{2} \exp\left[2.399 - \sqrt{(2.398)^2 + \left(v_2^{\rm gap}\right)^2}\right], \tag{4.81}$$

$$a = 0.1612 + \sqrt{(0.8388)^2 + \left(0.1177\, v_2^{\rm gap}\right)^2}, \tag{4.82}$$

$$b = 0.1612 + \sqrt{(0.8388)^2 + \left(0.1274\, v_2^{\rm gap}\right)^2}. \tag{4.83}$$

The reduction factor at intermediate values of the dimensionless energy gap parameter were not, however, given by Yakovlev and Levenfish (1995) for the Murca *neutron branch*. Instead, the authors calculated only the asymptote of the reduction factor $\mathcal{R}_{\rm n}^{(\rm Murca;\ n\text{-}branch)}$ in the limit $\tau_{\rm gap} \ll 1$ (i.e. when $T \ll T_c$).

This is a problem, since the critical temperatures of the ${}^3P_2$ triple-state neutrons predicted by Amundsen and Østgaard (1985b) (Fig. 4.10) indicate it is unlikely that one will enter the regime $T \ll T_c$ for a typical accreting NS (whereby $T \sim 10^8 - 10^9$) K. This issue was later addressed in Yakovlev (2001), suggesting that, in cases of moderate superfluidity (i.e. $v_{\rm gap} \sim 10$), the suppression factor of the *neutron branch* of the modified Urca process due to neutron superfluidity should not deviate strongly from the suppression factor of the *proton branch due to proton superfluidity*, and so

$$\mathcal{R}_{\rm n}^{\rm (Murca;\ n\text{-}branch)} \approx R_{\rm p}^{\rm (Murca;\ p\text{-}branch)}\,(\nu_2^{\rm gap})\,, \tag{4.84}$$

whereby one simply makes the substitution $\nu_1^{\rm gap} \rightarrow \nu_2^{\rm gap}$ in Eq. (4.71).

This issue is something that has featured in other codes seeking to solve the full time-dependent heat equation such as `NSCool`, used in other published works on NS cooling (e.g. Page, 1997; Page and Reddy, 2006; Page et al., 2006). Indeed, within the source code of `NSCool`, the suppression factor of the neutron branch is approximated as[14]

$$\mathcal{R}_{\rm n}^{\rm (Murca;\ n\text{-}branch)} = R_{\rm p}^{\rm (Murca;\ p\text{-}branch)}\left[39.1\,\tau_{\rm gap}\exp\left(-\frac{1.188}{\tau_{\rm gap}}\right)\right], \tag{4.85}$$

where the exponential term has been added such that $R_{\rm n}^{\rm (Murca;\ n\text{-}branch)} \approx R_{\rm n}^{\rm (Murca;\ p\text{-}branch)}$ in the limit $\tau \ll 1$.

Nucleon-nucleon bremsstralung:

A further complication arises from the fact that Yakovlev and Levenfish (1995) also restricted themselves to considering only the single-state ($^1S_0$) pairing of protons for bremsstrahlung interactions. Therefore, for the case of the triplet-state pairing of the neutrons, we again follow Yakovlev (2001), as well as what can be inferred from `NSCool`, who take the suppression factors for neutron superfluidity alone (scenario ii) at intermediate values of $\nu_{\rm gap}$ to be

$$\mathcal{R}_{\rm n}^{\rm (nn)} \approx R_{\rm p}^{\rm pp}(\nu_2^{\rm gap}), \tag{4.86}$$

$$R_{\rm n}^{\rm (np)} \approx R_{\rm p}^{\rm np}(\nu_2^{\rm gap}), \tag{4.87}$$

with

$$\mathcal{R}_{\rm n}^{\rm (pp)} = 1.0, \tag{4.88}$$

since this time any proton-proton interactions will not affected by neutron superfluidity.

4.6.2.3 Superfluid suppression: Superconducting protons and superfluid neutrons

Direct URCA:

Lastly, in the presence of *simultaneous* proton superconductivity and neutron superfluidity (scenario iii), the reduction factor for Durca processes takes the form (Yakovlev, 2001)

---

[14] The source code is freely available at http://www.astroscu.unam.mx/neutrones/NSCool/.

$$\mathcal{R}^{(\mathrm{Durca})}_{\mathrm{pn,\,np}} = \frac{10^4 - 2.839\left(\nu_2^{\mathrm{gap}}\right)^4 - 5.022\left(\nu_1^{\mathrm{gap}}\right)^4}{10^4 + 757.0\left(\nu_2^{\mathrm{gap}}\right)^2 + 1494\left(\nu_1^{\mathrm{gap}}\right)^2 + 211.1\left(\nu_1^{\mathrm{gap}}\nu_2^{\mathrm{gap}}\right)^2 + 0.4832\left(\nu_1^{\mathrm{gap}}\nu_2^{\mathrm{gap}}\right)^4} \,. \quad (4.89)$$

The above formula is strictly valid only in the regime of intermediate superfluidity whereby $\sqrt{\nu_1^2 + \nu_2^2} \lesssim 5$). In reference to Fig. 4.12, it may be seen that this condition is far exceeded in the lowest density regions of the core, pushing the boundaries of the applicability of Eq. (4.89) in most regions of the core. In regions of the core where both superfluidities are strong, it was estimated by Levenfish and Yakovlev (1994) that the reduction factor may be approximated as

$$\mathcal{R}^{(\mathrm{Durca})}_{\mathrm{pn,\,np}} \sim \min\left(\mathcal{R}^{(\mathrm{Durca})}_{\mathrm{p}},\, R^{(\mathrm{Durca})}_{\mathrm{n}}\right), \quad (4.90)$$

where $\mathcal{R}^{(\mathrm{Durca})}_{\mathrm{p}}$ and $\mathcal{R}^{(\mathrm{Durca})}_{\mathrm{n}}$ are of course the respective reduction factors (4.67) and (4.80) for either type of superfluidity acting alone.

Modified URCA:

The corresponding case (scenario iii) for Murca processes were also not considered in Yakovlev and Levenfish (1995). However, in a subsequent publication by the same authors (Levenfish and Yakovlev, 1996), it was argued that the expression for the reduction factor of both the neutron and proton branches of Murca in the presence of proton superconductivity *and* neutron superfluidity would not differ significantly from the equivalent expression for the Durca process Eq. (4.89). These expressions are, as given in Yakovlev (2001),

$$\mathcal{R}^{(\mathrm{Murca;\ p\text{-}branch})}_{\mathrm{pn,\,np}}\left(\nu_2^{\mathrm{gap}},\, \nu_1^{\mathrm{gap}}\right) \approx \left[\frac{R^{(\mathrm{Durca})}_{\mathrm{pn,\,np}}\left(\nu_2^{\mathrm{gap}},\, 2\nu_1^{\mathrm{gap}}\right)}{R^{(\mathrm{Durca})}_{\mathrm{n}}}\right] R^{(\mathrm{Murca;\ p\text{-}branch})}_{\mathrm{n}} \,, \quad (4.91)$$

$$\mathcal{R}^{(\mathrm{Murca;\ n\text{-}branch})}_{\mathrm{pn,\,np}}\left(\nu_2^{\mathrm{gap}},\, \nu_1^{\mathrm{gap}}\right) \approx \left[\frac{R^{(\mathrm{Durca})}_{\mathrm{pn,\,np}}\left(2\nu_2^{\mathrm{gap}},\, \nu_1^{\mathrm{gap}}\right)}{R^{(\mathrm{Durca})}_{\mathrm{p}}}\right] R^{(\mathrm{Murca;\ n\text{-}branch})}_{\mathrm{p}} \,. \quad (4.92)$$

Nucleon-nucleon bremsstralung:

The final case we must consider is then scenario iii for the bremsstrahlung interactions. This formulae, as obtained by Yakovlev (2001), is

$$\mathcal{R}^{(\mathrm{np})}_{\mathrm{pn}} \approx \left[\frac{R^{(\mathrm{Durca})}_{\mathrm{pn,\,np}}\left(\nu_2^{\mathrm{gap}},\, \nu_1^{\mathrm{gap}}\right)}{R^{(\mathrm{Durca})}_{\mathrm{p}}}\right] R^{(\mathrm{np})}_{\mathrm{p}} \,. \quad (4.93)$$

4.6.2.4 Cooper pair breaking and formation

So far, we have discussed the influence of baryon superfluidity in the context of suppression of the neutrino emissivity of Durca, Murca and bremsstrahlung processes that would *already* be present in the core of a non-superfluid accreting NSs. Yet, at the onset of superfluidity (i.e. when a NS becomes sufficiently cool), the baryon dispersion relation near the Fermi surface is sufficiently distorted that the following reaction

$$\mathrm{N} \rightarrow \mathrm{N} + \nu_{\mathrm{x}} + \bar{\nu}_{\mathrm{x}} \,, \tag{4.94}$$

where x = e, μ, τ, may be opened up, and is associated with the formation of the Cooper pairs themselves (Cooper pair breaking and formation; CPBF). An expression for the total neutrino emissivity of this process was obtained by Yakovlev et al. (1999), and may be written as (Yakovlev, 2001)

$$Q^{(\mathrm{CPBF})} = 1.170 \times 10^{21} \left(\frac{m_{\mathrm{n}}^{*}}{m_{\mathrm{n}}}\right)\left(\frac{p_{\mathrm{F_N}}}{m_{\mathrm{N}} c}\right) \mathcal{N}\, a\, F(\nu_{\mathrm{gap}})\, T_9^7 \ \mathrm{erg\ cm^{-3}\ s^{-1}} \,, \tag{4.95}$$

where the quantity a is a numerical factor which depends on the type of superfluidity as

$$\begin{aligned} a_{\mathrm{p}} &= 0.0064 \\ a_{\mathrm{n}_{\nu_1}} &= 1 \\ a_{\mathrm{n}_{\nu_2}} &= 4.17 \,. \end{aligned} \tag{4.96}$$

The quantity $F(\nu_{\mathrm{gap}})$ is a function that also depends on the type of superfluidity, with convenient fitting formulas obtained by Yakovlev et al. (1999) in the regime of moderate superfluidity as

$$\begin{aligned} F_1(\nu_1^{\mathrm{gap}}) = &\left(0.602\,(\nu_1^{\mathrm{gap}})^2 + 0.5942\,(\nu_1^{\mathrm{gap}})^4 + 0.288\,(\nu_1^{\mathrm{gap}})^6\right) \\ &\times \left(0.5547 + \sqrt{(0.4453)^2 + 0.0113\,(\nu_1^{\mathrm{gap}})^2}\right)^{1/2} \\ &\times \exp\left[-\sqrt{4\,(\nu_1^{\mathrm{gap}})^2 + (2.245)^2} + 2.245\right] \end{aligned} \tag{4.97}$$

and

$$\begin{aligned} F_2(v_2^{\mathrm{gap}}) = & \frac{\left(1.204\left(v_1^{\mathrm{gap}}\right)^2 + 3.733\left(v_1^{\mathrm{gap}}\right)^4 + 0.3191\left(v_1^{\mathrm{gap}}\right)^6\right)}{1 + 0.3511\left(v_1^{\mathrm{gap}}\right)^2} \\ & \times\left(0.7591 + \sqrt{(0.2409)^2 + 0.3145\left(v_1^{\mathrm{gap}}\right)^2}\right)^{1/2} \\ & \times\exp\left[-\sqrt{4\left(v_1^{\mathrm{gap}}\right)^2 + (0.4616)^2} + 0.4616\right]. \end{aligned} \tag{4.98}$$

Unlike the suppression behaviour of the other neutrino interactions, the strength of the Cooper pairing emissivity sharply increases as the temperature falls below that of T_c – reaching some maximum at $T \sim T_c/5$ before decreasing again (Yakovlev, 2001). Under certain circumstances, it is possible for the neutrino emission from the formation of Cooper pairs to be comparable in magnitude to that of Murca processes (Sec. 4.6.3). Even more interesting, such a mechanism is not confined to just the core of the star, with Cooper pair formation of neutrons in the inner crust taking place under the right conditions.

The density dependence of the neutrino emissivities in the accreted crust of a weakly-magnetized NS (assuming the BSk21 EoS) in the presence of singlet-state $^1S_0$ neutron superfluidity is shown in the right-hand panel of Fig. 4.13. The critical temperature of the neutrons as a function of the density are also shown in the left-hand panel.

The CPBF process appears after the onset of neutron-drip ($\rho \sim 4 \times 10^{11}$ g cm^{-3}), and is competitive with the emissivity due to plasmon decay in the density range $10^{12} - 10^{13}$ g cm^{-3}. Even at $T = 10^9$ K, however, electron bremsstrahlung remains the dominant neutrino process over the majority of the crust. It can also be seen that there are two peaks in the Cooper-pair spectrum; one near the neutron drip point, and a second much narrower peak just before the core-crust transition ($\rho \sim 1.4 \times 10^{14}$ g cm^{-3}) where the CPBF mechanism briefly dominates over the electron bremsstrahlung.

4.6.3 Leading reactions in superfluid neutron star cores

In Fig. 4.14, the superfluid reduction factors of Durca, Murca, and nucleon-nucleon bremsstrahlung processes due to superfluidity of neutrons and/or protons is plotted as a function of the density. We assume two models, one with the BSk20 EoS (whereby Durca processes are *forbidden*; Fig. 4.9), and the other with BSk21 (whereby Durca processes are *permitted*), both at a constant core temperature $T = 3 \times 10^8$ K. For the BSk20 model, it can be seen that neutrino emission via neutron-neutron bremsstrahlung is largely unaffected by the neutron superfluidity, whilst the proton-proton bremsstrahlung is heavily suppressed over much of the core. The cause of this behavior may be identified through a combination of Figs 4.11 & 4.12. The stronger superfluidity associated with the protons (due to having a much higher critical temperature than the neutrons) correspondingly leads to greater suppression.

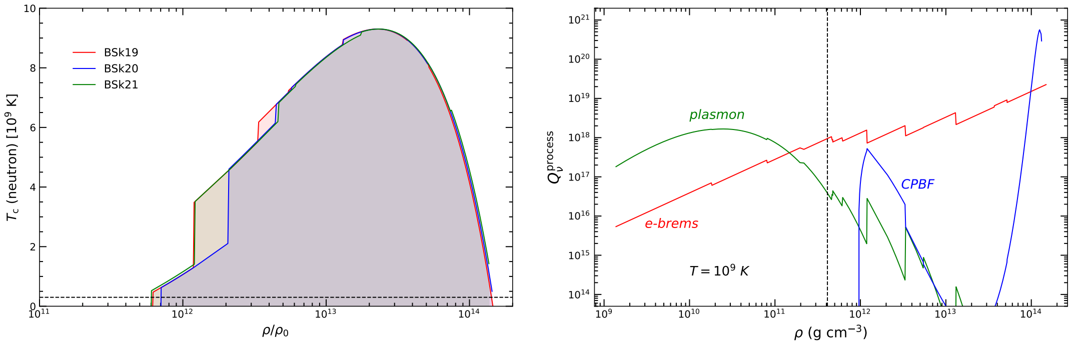

FIGURE 4.13: *Left panel*: Superfluid transition temperatures T_c as a function of the density for singlet state ($^1S_0$) pairing of neutrons in the inner crust. *Right panel*: Density dependence of the neutrino luminosity Q_ν in a weakly-magnetized accreted *superfluid* crust (assuming the BSk21 equation of state at constant $T = 10^9$ K.). Neutrino mechanisms present are indicated near the curves.

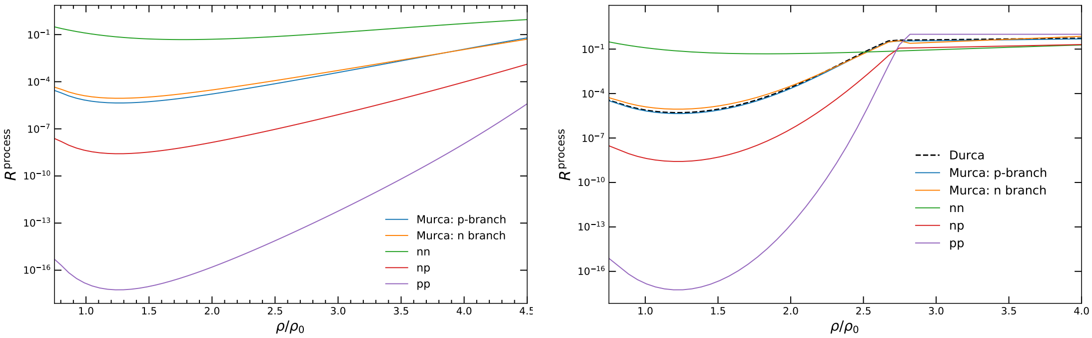

FIGURE 4.14: *Left panel*: Superfluid reduction factors of modified URCA and nucleon-nucleon bremsstrahlung processes due to superfluidity of neutrons and/or protons, assuming BSk20 and a constant core temperature $T = 3 \times 10^8$ K. *Right panel*: Same as left, but instead assuming the BSk21 equation of state where direct URCA processes are permitted.

In the BSk21 model, the behavior is largely similar. Though, again in reference to Fig. 4.11, it may be seen that proton superconductivity is destroyed in the core at densities $\sim 4\rho_0$. Beyond these densities, only the neutrons are (weakly) superfluid (Fig. 4.12), and so the reduction factors begin to converge towards their non-superfluid limits at $\mathcal{R} = 1$, where the neutron superfluidity is also destroyed at $\sim 10\rho_0$.

Of course however, the magnitude of the reduction factors alone does not tell the full story as to how the neutrino emission is affected by baryon superfluidity. As an illustration of how the presence of baryon superfluidity affects the *total neutrino luminosity* in the core, in Fig. 4.15 we re-plot Fig. 4.8, this time showing the density dependence of the neutrino luminosity Q_ν in superfluid matter (dashed lines), as well as when superfluid effects are ignored (solid lines). The shaded regions labelled i - iv indicate the particular superfluidity scenario at that point in the core (recall the discussion at the beginning of this section). For example, the light grey regions (scenario iii) are where the both neutrons are superfluid *and* protons are superconducting.

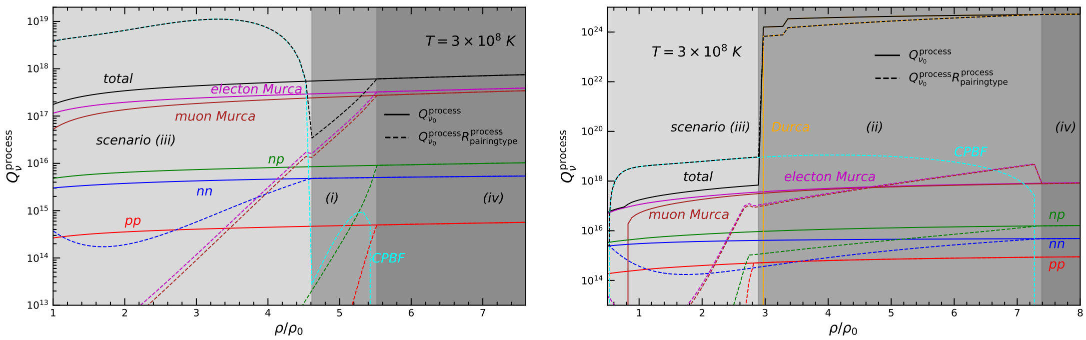

FIGURE 4.15: Density dependence of the neutrino luminosity Q_ν in superfluid (dashed lines) and non-superfluid (solid lines) matter in the core of a neutron star. The left panel assumes the BSk20 equation of state (where Durca processes are forbidden), and the right panel assumes the BSk21 equation of state where direct URCA processes are permitted. Both panels assume a constant core temperature $T = 3 \times 10^8$ K. The shaded regions labelled (i) - (iv) indicate the particular superfluidity scenario at that point in the core (Recall the discussion at the beginning of this section).

In the non-superfluid case, Murca processes dominate in the BSk20 model over the full density range, and dominate in the BSk21 model in the outer core until Durca reactions kick-in. However, when correcting for the possibility for superfluidity/superconductivity in the core, both electron and muon Murca processes are heavily suppressed in the low-density regions. In fact, the dominant source of neutrinos in the outer regions of the core in both the BSk20 and BSk21 models is the formation and breaking of the Cooper pairs. In the BSk20 model, CPBF dominates until the point whereby the neutron superfluidity is destroyed (notice the transition from scenario iii to scenario i), at which point Murca processes once again become the dominant source of neutrino emission. A similar scenario persists in the BSk21 model also, with CPBF dominating in the outer regions of the core until the threshold density for Durca processes is reached ($\sim 4\rho_0$), at which point Durca then supplies the majority of neutrinos emitted from the star.

4.6.4 Superfluid suppression of the thermal conductivity

4.6.4.1 Superfluid suppression of the lepton conductivity

Baryon superfluidity also affects how efficiently heat may be transported around the star. Recall that the heat conduction via leptons may be mediated in a variety of ways (Fig. 4.5). Two of these pertain to that of the interactions between electrons/muons and the protons. The effects of superfluidity/superconductivity (in this section we shall use the two interchangeably) on heat conduction involving protons are two-fold: (i) a reduction in the collision frequency of interactions between protons and charged leptons, and (ii) a reduction in screening momentum (recall the additional reduction factor $\mathcal{Z}_\text{p}$ in Eq. (4.25)).

Much like the neutrino emissivity of any baryonic process in the presence of superfluidity, the collision frequencies between leptons and charged baryons (protons in npeμ matter) including superfluidity effects can be written as

$$\nu_{i\mathrm{p}} = \nu_{i\mathrm{p}}^{(0)} \mathcal{R}_\mathrm{p}, \tag{4.99}$$

where $\nu_{i\mathrm{p}}^{(0)}$ is the electron/muon-proton scattering frequency in non-superfluid matter (Eqs (4.22) and (4.23)) and $\mathcal{R}_\mathrm{p}$ is the superfluidity suppression factor. For protons in the $^1S_0$ state, the suppression factor for intermediate values of ν^gap is given by (Gnedin and Yakovlev, 1995)

$$\begin{aligned}
\mathcal{R}_\mathrm{p} =& \Bigg\{ 0.7694 + \sqrt{(0.2306)^2 + \left(0.07207\, \nu_1^\mathrm{gap}\right)^2} \\
&+ \left(27.00 \left(\nu_1^\mathrm{gap}\right)^2 + 0.1476 \left(\nu_1^\mathrm{gap}\right)^4\right) \exp\left(-\sqrt{(4.273)^2 + \left(\nu_1^\mathrm{gap}\right)^2}\right) \\
&+ 0.5051 \left[\exp\left(4.273 - \sqrt{4.273^2 + \left(\nu_1^\mathrm{gap}\right)^2}\right) - 1\right]\Bigg\} \\
&\times \exp\left(1.187 - \sqrt{(1.187)^2 + \left(\nu_1^\mathrm{gap}\right)^2}\right).
\end{aligned} \tag{4.100}$$

Recall also that the squared static screening momentum (4.24) is written as

$$q_0^2 = \frac{4e^2}{\pi\hbar}\left(m_\mathrm{e}^* p_{\mathrm{F_e}} + m_\mu^* p_{\mathrm{F}_\mu} + \sum_\mathrm{b} m_\mathrm{b}^* p_{\mathrm{F_b}} \mathcal{Z}_\mathrm{b}\right), \tag{4.101}$$

where $\mathcal{Z}_\mathrm{b}$ is the suppression factor, in this case associated specifically with the proton screening momentum (i.e. b = p). Gnedin and Yakovlev (1995) proposed a fit for $\mathcal{Z}_\mathrm{p}$ for intermediate values of ν^gap as

$$\begin{aligned}
\mathcal{Z}_\mathrm{p} =& \left[0.9443 + \sqrt{(0.0557)^2 + \left(0.1886\, \nu_1^\mathrm{gap}\right)^2}\right]^{1/2} \\
&\times \exp\left(1.753 - \sqrt{(1.753)^2 + \left(\nu_1^\mathrm{gap}\right)^2}\right).
\end{aligned} \tag{4.102}$$

At temperatures $T < T_\mathrm{cp}$ (Fig. 4.11), the formation of proton-proton pairs leads to a decrease in the density of available heat carriers. At the same time, this leads to a reduction in the proton screening, as other charged particles effectively ‘see’ fewer protons since they are paired-up and can no longer interact with other particles. How these two effects impact the overall thermal conductivity can be understood from Fig. 4.16, which shows the density dependence of the scattering frequencies of the various Coulomb interactions (left-panel) and the total lepton contribution to the thermal conductivity (right-hand panel), assuming both superfluid matter (dashed lines) and normal matter whereby superfluid effects are ignored (solid lines).

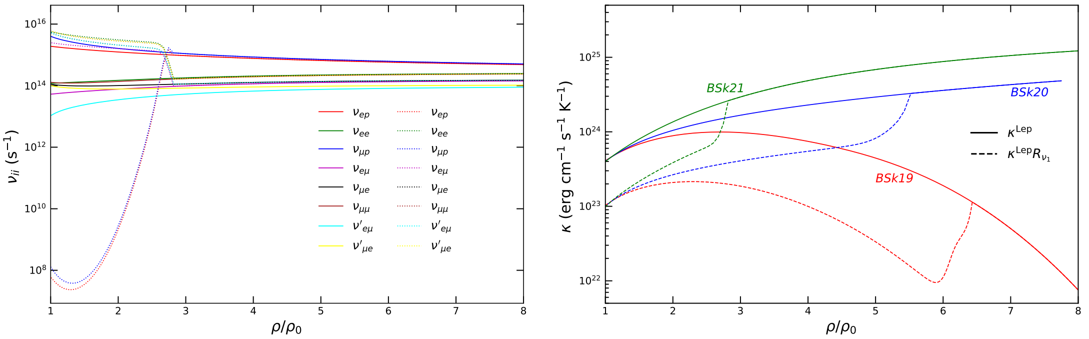

Figure 4.16: *Left panel:* Magnitude of the Coulomb scattering frequencies ν_{ij} in superconducting matter (dashed lines) and normal non-superconducting matter (solid lines), assuming the BSk21 equation of state at a constant temperature $T = 3 \times 10^8$ K. *Right panel:* Thermal conductivity from electrons and muons in normal and superconducting matter for each of BSk19, BSk20, and BSk21.

In regimes of moderate to strong superfluidity ($\nu_{\rm gap} \gtrsim 10$), the proton screening is suppressed, and the total screening momentum (4.101) is just

$$q_0^2 \approx \frac{4e^2}{\pi\hbar}\left(m_e^* p_{{\rm F}_e} + m_\mu^* p_{{\rm F}_\mu}\right). \tag{4.103}$$

This is an important result, since *all* of the different scattering frequencies scale as $\nu_{ij} \propto q_0^{-3}$ (Sec. 4.4.2.1). As $\mathcal{Z}_{\rm p} \rightarrow 0$, the reduction in the total screening momentum ultimately *enhances* the scattering frequencies of all interactions. For the two specific interactions involving protons, however, the scattering frequencies scale as $\nu_{i{\rm p}} \propto q_0^{-3}\mathcal{R}_{\rm p}$, and account for the additional 'direct' consequence of the reduction in available heat carriers. Therefore, although $\nu_{i{\rm p}}$ is enhanced as $\mathcal{Z}_{\rm p} \rightarrow 0$, at the same time it is decreased 'faster' as $\mathcal{R}_{\rm p} \rightarrow 0$. The overall effect is to enhance the scattering frequency of interactions involving just leptons (i.e. $\nu_{\rm ee}$, $\nu_{\mu\mu}$, etc.), but decrease the scattering frequencies of both $\nu_{\rm ep}$ and $\nu_{\mu{\rm p}}$.

This behavior may be observed directly in the left-hand panel of 4.16. Note the increase in $\nu_{\rm ee}$, $\nu_{\mu\mu}$, etc. (the dotted lines) and the decrease in $\nu_{i{\rm p}}$ (at low density), relative to the solid lines which ignore superfluid effects. The total thermal conductivity due to electrons and muons is then plotted in the right-hand panel of Fig. 4.16 (the dotted lines also represent κ in superfluid matter, whilst the solid lines ignore superfluid effects). The thermal conductivity is suppressed at low density relative to non-superfluid matter, as κ is dominated almost entirely by the enhanced collisions between electrons and muons (since $\kappa \propto 1/\nu$, where $\nu = \nu_{\rm e} + \nu_\mu$ are given in Eqs (4.19) - (4.20)). At high density, once the superconductivity is destroyed[15], the dashed and solid curves merge as $\mathcal{Z}_{\rm p} \rightarrow 1$ and $\mathcal{R}_{\rm p} \rightarrow 1$.

---

[15] The exact density at which the superconductivity is destroyed is of course EoS dependent; see Fig. 4.11

4.6.4.2 Superfluid suppression of the baryon conductivity

Heat conduction via neutrons is mediated by the strong interaction, and is also sensitive to the state of the matter in the core and whether or not the nucleons are superfluid/superconducting. The overall effect of baryon superfluidity on the collision integrals (and thus the scattering frequencies introduced in Sec. 4.4.2.2) was also calculated by Baiko et al. (2001).

Recall that the approximate scattering frequencies for $\nu_{\rm nn}$ and $\nu_{\rm pp}$ collisions are (Eqs (4.33) - (4.34))

$$\nu_{\rm nn} \approx 3.48 \times 10^{15} \left(\frac{m_{\rm n}^*}{m_{\rm n}}\right)^3 T_8^2 \left\{\mathcal{S}_{\rm n2}^{(0)} K_{\rm n2}\mathcal{R}_{\rm n2} + 3\mathcal{S}_{\rm n1}^{(0)} K_{\rm n1} [\mathcal{R}_{\rm n1} - \mathcal{R}_{\rm n2}]\right\} {\rm s}^{-1}, \tag{4.104}$$

$$\nu_{\rm np} \approx 3.48 \times 10^{15} \left(\frac{m*_{\rm n}}{m_{\rm n}}\right)\left(\frac{m_{\rm p}^*}{m_{\rm p}}\right)^2 T_8^2 \left\{\mathcal{S}_{\rm p2}^{(0)} K_{\rm p2}\mathcal{R}_{\rm p2} + 0.5 K_{\rm p1}\mathcal{S}_{\rm p1} [3\mathcal{R}_{\rm p1} - \mathcal{R}_{\rm p2}]\right\} {\rm s}^{-1}, \tag{4.105}$$

where $S_\alpha^{(0)}$ ($\alpha = {\rm n1, n2, p1, p2}$) are the scattering cross sections, K_α are coefficients which describe in-medium effects, and $\mathcal{R}_\alpha$ are the suppression factors. Unlike the effect of baryon superfluidity on lepton conduction, the nature of the suppression of the neutron conductivity, much like the neutrino emission, depends on different combinations of superfluid/normal particles. The possible scenarios to be considered are (Sec. 4.6.2).

- i) the protons are superconducting and the neutrons are normal,
- ii) the neutrons are superfluid and the protons are normal,
- iii) the protons *and* neutrons are both superconducting/superfluid,
- iv) *neither* of the protons or neutrons are superconducting/superfluid.

In the latter case, one of course simply has $\mathcal{R}_\alpha \equiv 1$ and the thermal conductivity is as described in Section 4.4.2.2.

Superfluid Suppression: Superfluid neutrons and normal protons

Consider first the effects of superfluidity on the scattering frequency between just neutrons ($\nu_{\rm nn}$). The relevant reductions factors that appear in Eq. (4.104) are $\mathcal{R}_{\rm n1}$ and $\mathcal{R}_{\rm n2}$. Analytical representations of these reduction factors fitted to numerical results were obtained by Baiko et al. (2001) as

$$\begin{aligned}\mathcal{R}_{\mathrm{n1}}(v_2^{\mathrm{gap}}) = \frac{2}{3}&\left[0.9468 + \sqrt{(0.0532)^2 + 0.5346\,(v_2^{\mathrm{gap}})^2}\right]^3 \exp\left[0.377 - \sqrt{(0.377)^2 + 4\,(v_2^{\mathrm{gap}})^2}\right]\\ &+ \frac{1}{3}\left(1 + 1.351\,(v_2^{\mathrm{gap}})^2\right)^2 \exp\left[0.169 - \sqrt{(0.169)^2 + 9\,(v_2^{\mathrm{gap}})^2}\right]\end{aligned} \tag{4.106}$$

and

$$\begin{aligned}\mathcal{R}_{\mathrm{n2}}(v_2^{\mathrm{gap}}) = \frac{1}{2}&\left[0.6242 + \sqrt{(0.3758)^2 + 0.07198\,(v_2^{\mathrm{gap}})^2}\right]^3 \exp\left[3.6724 - \sqrt{(3.6724)^2 + 4\,(v_2^{\mathrm{gap}})^2}\right]\\ &+ \frac{1}{2}\left(1 + 0.01211\,(v_2^{\mathrm{gap}})^2\right)^9 \exp\left[7.5351 - \sqrt{(7.5351)^2 + 9\,(v_2^{\mathrm{gap}})^2}\right].\end{aligned} \tag{4.107}$$

Similarly, for the effects on the scattering frequency between the protons and neutrons (ν_{np}) when only the neutrons are superfluid, the relevant reductions factors from Eq. (4.105) are $\mathcal{R}_{\mathrm{p1}}$ and $\mathcal{R}_{\mathrm{p2}}$. Analytic fits for these reduction factors may be approximated as

$$\begin{aligned}\mathcal{R}_{\mathrm{p1}}(v_2^{\mathrm{gap}}, 0) = &\left[0.4459 + \sqrt{(0.5541)^2 + 0.03016\,(v_2^{\mathrm{gap}})^2}\right]^2\\ &\times \exp\left[2.1178 - \sqrt{(2.1178)^2 + (v_2^{\mathrm{gap}})^2}\right],\end{aligned} \tag{4.108}$$

$$\begin{aligned}\mathcal{R}_{\mathrm{p2}}(v_2^{\mathrm{gap}}, 0) = &\left[0.801 + \sqrt{(0.199)^2 + 0.04645\,(v_2^{\mathrm{gap}})^2}\right]^2\\ &\times \exp\left[2.3569 - \sqrt{(2.3569)^2 + (v_2^{\mathrm{gap}})^2}\right].\end{aligned} \tag{4.109}$$

Superfluid suppression: Superconducting protons and normal neutrons

When only the protons are superconducting, the only branch of the neutron conductivity that is affected is of course the interactions between the protons and the neutrons. In this case, the appropriate forms of the reductions factors $\mathcal{R}_{\mathrm{p1}}$ and $\mathcal{R}_{\mathrm{p2}}$ are

$$\mathcal{R}_{\mathrm{p1}}(0,\, \nu_1^{\mathrm{gap}}) = \frac{1}{2}\left[0.3695 + \sqrt{(0.6305)^2 + 0.01064\,(\nu_1^{\mathrm{gap}})^2}\right]^3 \exp\left[2.4451 - \sqrt{(2.4451)^2 + (\nu_1^{\mathrm{gap}})^2}\right] + \frac{1}{2}\left(1 + 0.1917\,(\nu_1^{\mathrm{gap}})^2\right)^{1.4} \exp\left[4.6627 - \sqrt{(4.6627)^2 + 4\,(\nu_1^{\mathrm{gap}})^2}\right], \tag{4.110}$$

$$\begin{aligned}\mathcal{R}_{\mathrm{p2}}(0,\, \nu_1^{\mathrm{gap}}) = 0.0436 &\left[\sqrt{(4.345)^2 + 19.55\,(\nu_1^{\mathrm{gap}})^2} - 3.345\right] \\ &\times \exp\left[2.0247 - \sqrt{(2.0247)^2 + 4\,(\nu_1^{\mathrm{gap}})^2}\right] \\ &+ 0.0654 \exp\left[8.8992 - \sqrt{(8.8992)^2 + 1.5\,(\nu_1^{\mathrm{gap}})^2}\right] \\ &+ 0.891 \exp\left[9.627 - \sqrt{(9.627)^2 + 9\,(\nu_1^{\mathrm{gap}})^2}\right].\end{aligned} \tag{4.111}$$

Superfluid Suppression: Superfluid neutrons and superconducting protons

The final case we need then consider is the affects on the scattering between collisions of protons and neutrons when *both* the particles are superfluid/superconducting. Unlike the cases whereby only one of the particles are superfluid/superconducting, the fits which determine $\mathcal{R}_{\mathrm{p1}}$ and $\mathcal{R}_{\mathrm{p2}}$ in which neutrons and protons are superfluid were only fitted to numerical results in regimes of moderate superfluidity whereby $\nu_1^{\mathrm{gap}} \equiv \nu_2^{\mathrm{gap}} \leq 12$. The fit to $\mathcal{R}_{\mathrm{p1}}$ reads (Baiko et al., 2001)

$$\begin{aligned}\mathcal{R}_{\mathrm{p1}}(\nu_2^{\mathrm{gap}},\, \nu_1^{\mathrm{gap}}) = {} & (0.7751 + 0.4823\,u_{\mathrm{n}} + 0.1124\,u_{\mathrm{p}} + 0.04991\,u_{\mathrm{n}}^2 + 0.08513\,u_{\mathrm{n}}u_{\mathrm{p}} \\ & + 0.01284\,u_{\mathrm{n}}^2 u_{\mathrm{p}}) \exp\left(-u_+ - u_-\right) + (0.2249 + 0.3539\,u_+ \\ & - 0.2189\,u_- - 0.6069\,u_{\mathrm{n}}u_- + 0.7362\,u_{\mathrm{p}}u_+) \exp\left(-2u_+\right),\end{aligned} \tag{4.112}$$

where

$$u_\alpha = \sqrt{\left(\nu_\alpha^{\mathrm{gap}}\right)^2 + (1.485)^2} - 1.485 \qquad \alpha = +,\, -,\, \mathrm{n},\, \mathrm{p}, \tag{4.113}$$

with

$$\nu_-^{\mathrm{gap}} = \min(\nu_2^{\mathrm{gap}},\, \nu_1^{\mathrm{gap}}), \quad \nu_+^{\mathrm{gap}} = \max(\nu_2^{\mathrm{gap}},\, \nu_1^{\mathrm{gap}}). \tag{4.114}$$

The fit to $\mathcal{R}_{\mathrm{p2}}$, on the other hand, is given by

$$\begin{aligned}\mathcal{R}_{\mathrm{p2}}(\nu_2^{\mathrm{gap}},\, \nu_1^{\mathrm{gap}}) = {} & (1.1032 + 0.8645\, u_{\mathrm{n}} + 0.2042\, u_{\mathrm{p}} + 0.07937\, u_{\mathrm{n}}^2 + 0.1451\, u_{\mathrm{n}} u_{\mathrm{p}} \\ & + 0.01333\, u_{\mathrm{n}}^2 u_{\mathrm{p}}) \exp\left(-u_+ - u_-\right) + (-0.1032 + 0.2340\, u_+ \\ & + 0.06152\, u_{\mathrm{n}} u_+ + 0.7533\, u_{\mathrm{n}} u_- + 1.007\, u_{\mathrm{p}} u_+) \exp\left(-2u_+\right),\end{aligned} \tag{4.115}$$

where

$$u_\alpha = \sqrt{\left(\nu_\alpha^{\mathrm{gap}}\right)^2 + (1.761)^2} - 1.761 \qquad \alpha = +,\, -,\, \mathrm{n},\, \mathrm{p}\,, \tag{4.116}$$

with

$$\nu_-^{\mathrm{gap}} = \min(\nu_2^{\mathrm{gap}},\, \nu_1^{\mathrm{gap}}), \quad \nu_+^{\mathrm{gap}} = \max(\nu_2^{\mathrm{gap}},\, \nu_1^{\mathrm{gap}})\,. \tag{4.117}$$

It is the case, however, that $\nu_1^{\mathrm{gap}} \sim 20$ in the low density regions of the core when $T = 3 \times 10^8$ K (Fig. 4.12). The maximum error in both $\mathcal{R}_{\mathrm{p1}}$ and $\mathcal{R}_{\mathrm{p2}}$ obtained by Baiko et al. (2001) are said to be 14%, occurring at the maximum value of $\nu_1^{\mathrm{gap}} = 12$ sampled from the numerical data. It is therefore worth bearing in mind that the neutron-proton scattering is possibly over-suppressed in our model when $\nu_1^{\mathrm{gap}} \sim 20$. However, even when $\nu_1^{\mathrm{gap}} = 12$, $\mathcal{R}_{\mathrm{p1}}$ $\mathcal{R}_{\mathrm{p2}}$ are said by Baiko et al. (2001) to be exponentially small. Therefore, since the contribution to the total thermal conductivity from the leptons is typically greater than that of the neutron contribution at low density regions in non-superfluid matter anyway (Fig. 4.6), it is unlikely this will have a significant impact on the overall picture.

In addition, the expression which determines the thermal conductivity itself (4.10) (due to strong interactions) is modified in the presence of neutron superfluidity as

$$\kappa_n = \frac{\pi^2 k_{\mathrm{B}}\, n_{\mathrm{n}}\, {\mathcal{R}_C}^2}{3m_{\mathrm{n}}^*} T\tau_{\mathrm{n}}\,, \tag{4.118}$$

and contains an additional factor ${\mathcal{R}_C}^2$, which accounts for the fact that the presence of neutron superfluidity also affects the neutron heat flux directly. Baiko et al. (2001) provide another convenient fitting formula for this additional reduction factor, given as

$$\begin{aligned}\mathcal{R}_C(\nu_2^{\mathrm{gap}}) = {} & \left[0.647 + \sqrt{(0.353)^2 + 0.109\,\left(\nu_2^{\mathrm{gap}}\right)^2}\right]^{1.5} \\ & \times \exp\left[1.39 - \sqrt{(1.39)^2 + \left(\nu_2^{\mathrm{gap}}\right)^2}\right],\end{aligned} \tag{4.119}$$

and is valid in regimes of both weak and strong superfluidity.

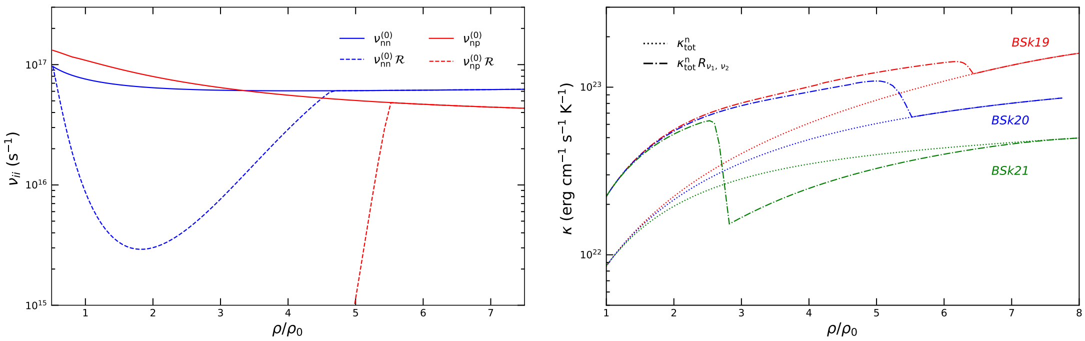

FIGURE 4.17: *Left panel:* Magnitude of the nucleon scattering frequencies ν_{ij} in superconducting matter (dashed lines) and normal non-superconducting matter (solid lines), assuming the BSk21 equation of state at a constant temperature $T = 3 \times 10^8$ K. *Right panel:* Thermal conductivity from neutrons in normal (dotted) and superconducting (dash-dotted) matter for each of BSk19, BSk20, and BSk21.

In Fig. 4.17, the left-hand panel shows the density dependence (at $T = 3 \times 10^8$ K) of the $\nu_{\rm nn}$ and $\nu_{\rm np}$ scattering frequencies in both normal (i.e when superfluid effects are ignored) and superfluid matter (solid and dashed lines respectively). The right-hand panel also shows the neutron thermal conductivity in both normal and superfluid matter (dotted and dash-dotted lines respectively). In the previous section, the overall effect of proton superconductivity was to *suppress* the thermal conductivity contribution from the *leptons*, due to a reduction in the proton screening momentum, which enhances the scattering frequencies of collisions involving just electrons and muons (Sec. 4.6.4.1).

The opposite effect is now observed in Fig. 4.17, however, with proton superconductivity *enhancing* the thermal conductivity contribution from the *neutrons*. This seemingly strange behavior can be explained in the following way: In the low density regions where $T_{\rm cp} > T_{\rm cn}$ the np collisions are necessarily suppressed as $\mathcal{R}_{\rm p1} \longrightarrow 0$ and $\mathcal{R}_{\rm p2} \longrightarrow 0$, which directly enhances $\kappa_{\rm n}$. However, once the proton superconductivity is destroyed, then one enters the regime whereby $T_{\rm cn} > T_{\rm cp}$ and the thermal conductivity starts to fall due to the decrease in the density of available heat carriers. As the density continues to increase, $\kappa_{\rm n}$ continues to decrease as $T \longrightarrow T_{\rm cn}$, until the point whereby neutron superfluidity is also destroyed and $\kappa_{\rm n}$ approaches that of the thermal conductivity in non-superfluid matter.

Finally, in Fig. 4.18, we plot for comparison in the left-hand panel the neutron thermal conductivity in both normal and superfluid matter (dotted and dash-dotted lines respectively), *as well as* the lepton thermal conductivity in both normal and superfluid matter (solid and dash-dotted lines respectively). Once again, it can be seen that the lepton conductivity is the dominant source of heat conduction in BSk20 and BSk21 over all densities. However, neutrons can again become the dominant source of heat conduction in the innermost regions of NS cores assuming the BSk19 EoS (recall Fig. 4.6). For completeness, the right-hand panel of Fig. 4.18 then shows the sum of these two contributions, giving the *total thermal conductivity* in the core of both superfluid and non-superfluid NSs.

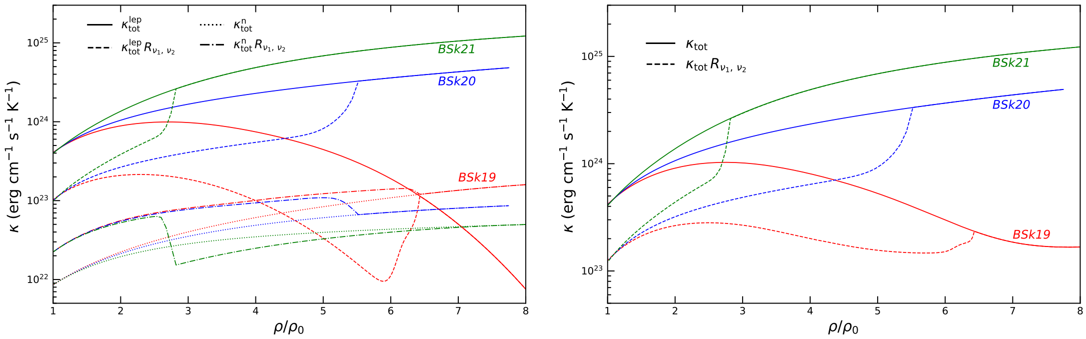

FIGURE 4.18: *Left panel:* Thermal conductivity via neutrons ($\kappa_{\rm n}$) in normal and superfluid matter (solid and dashed lines respectively), as well as leptons ($\kappa_{\rm lep}$; dotted and dash-dotted lines respectively) for each of the BSk19, BSk20, and BSk21 equations of state. *Right panel:* Total thermal conductivity $\kappa_{\rm tot} = \kappa_{\rm lep} + \kappa_{\rm n}$ for each of BSk19, BSk20, and BSk21 in normal (solid lines) and superfluid matter (dashed lines). Both panels assume a core temperature $T = 3 \times 10^8$ K.

4.7 Solving the heat equation

Supplied with the relevant microphysics detailed in the preceding sections, we are now in a position to compute the background thermal structure of an accreting NS. As we have already seen, both theoretical, as well as observational considerations, imply that the neutrino luminosity, thermal conductivity, etc. are extremely large. To ensure the numerical computation is both as accurate and efficient as possible, is it therefore convenient for Eqs (4.5) - (4.6) to be non-dimensionalised. The simplest method of non-dimensionalisation is to simply divide all quantities that appear in the heat equations by some 'characteristic value' appropriate to that of the interior.

Therefore, in order to non-dimensionalise Eqs (4.5) - (4.6), we start by defining the following relations

$$\begin{aligned} \hat{T} &= \frac{T}{T_{\rm typ}} , \\ \hat{\kappa} &= \frac{\kappa}{\kappa_{\rm typ}} , \\ \hat{R} &= \frac{R}{R_{\rm typ}} , \end{aligned} \tag{4.120}$$

where '^' is the non-dimensionalised parameter.

The value of the 'typical' parameter is largely arbitrary. The easiest choice to make is that of $R_{\rm typ}$, the typical NS radius, which can be specified to be the edge of the star (computed from the TOV solution; Sec. 2.6.2.1), such that if $R_{\rm typ} = R_{\rm OB}$, then $\hat{r} \leq 1$ within star. Another simple choice to make is that of $T_{\rm typ}$, the typical NS temperature. Most observational evidence indicates their temperatures to be of the order $10^8 - 10^9$ K, and thus $T_{\rm typ} = 10^9$ K is an acceptable choice.

The choice for $\kappa_{\rm typ}$, the typical NS thermal conductivity, however, is a little more arbitrary. As we have seen over the course of this chapter, the thermal conductivity can vary upwards of 10 orders of magnitude between the crust and core of the star. We shall therefore choose a value that is approximately half-way (logarithmically) between the lowest value of the crust and highest value in the core; and assume $\kappa_{\rm typ} = 10^{21}$ erg s^{-1} K^{-1} in the remainder of this thesis.

From Fourier's law and the relations (4.120), an expression for a typical flux, $F_{\rm typ}$, can be defined as

$$F_{\rm typ} = \frac{\kappa_{\rm typ} T_{\rm typ}}{R_{\rm typ}} \,, \tag{4.121}$$

from which a typical luminosity, $L_{\rm typ}$ is then defined as

$$L_{\rm typ} = F_{\rm typ} R_{\rm typ}^2 = \kappa_{\rm typ} T_{\rm typ} R_{\rm typ} \,. \tag{4.122}$$

With these relations, the pair of ODEs (4.5) - (4.6) may be expressed in dimensionless form as

$$\frac{d\hat{L}}{d\hat{r}} = 4\pi \hat{r}^2 Q \frac{R_{\rm typ}^3}{L_{\rm typ}} \,, \tag{4.123}$$

$$\frac{d\hat{T}}{d\hat{r}} = -\frac{1}{\kappa} \frac{\hat{L}}{4\pi \hat{r}^2} \kappa_{\rm typ} \,. \tag{4.124}$$

and will be the form of the ODEs solved in the following sections.

4.7.1 Boundary conditions and method of solution

The system of ODEs (4.123) - (4.124) is a boundary value problem with a set of outer and inner boundary conditions. The outer boundary is set by the interface whereby the crust meets the accreted material falling onto the star. For simplicity, we set the interface at the approximate location of the bottom of the hydrogen/helium burning layer at $\rho = 10^7$ g cm^{-3} (see, for example, Fig. 19 in Chamel and Haensel, 2008). When thermonuclear burning in the envelope is stable, we follow the prescription of Ushomirsky et al. (2000) and assume that the outer boundary condition is fixed by the temperature at the base of this layer. This temperature at the base of the ocean was computed by Schatz et al. (1999), and is given by

$$T_{\rm OB} = 5.3 \times 10^8 {\rm K} \left(\frac{\dot{m}}{\dot{m}_{\rm Edd}} \right)^{2/7} , \tag{4.125}$$

where $\dot{m}$ is the *local* accretion rate and $\dot{m}_{\rm Edd}$ is the local Eddington limit. In the calculations that follow, we will henceforth assume uniform accretion over the surface of the star, and therefore parameterise our results in terms of $\dot{M}$, the *global* rate of mass accretion.

Burning is assumed to stable when the NS is accreting at a level $\dot{M} = 0.1 - 1\dot{M}_{\rm Edd}$ ($\dot{M}_{\rm Edd} = 2 \times 10^8 \, M_\odot \, {\rm yr}^{-1}$; Schatz et al., 1999). If the accretion rate is much lower, however, then burning in the upper atmosphere can lead to type I X-ray bursts (Sec. 4.1). These bursts produce a rapid increase in the observed luminosity as burning of the accreted material quickly breaks out into thermonuclear runaway (Fig. 4.2).

Since we seek only a steady-state solution to our background thermal equations, we will also interpret $\dot{M}$ as a *time-averaged* accretion rate. On a timescale much larger than that of an individual burst, we can average over all of the bursts in a given accretion episode. Such a choice allows us to apply Eq. (4.125) even at low accretion rates, as we can effectively assume a constant $T_{\rm OB}$ even if burning in the upper atmosphere is unstable.

To obtain the boundary condition at the centre of the star, initially one might naively set $L|_{r=0} = 0$ for the centre of the star. However, much like the TOV equations, the heat equations are also singular at the origin due to the use of spherical coordinates. We therefore expand all variables via Taylor series about the center in order to obtain an approximate solution of the coupled ODEs at small radii. Our variables for the thermal background are T, L, κ, and Q. For each of these quantities we shall use an expansion of the form

$$q(r) = q_0 + q_1 r + \frac{1}{2} q_2 r^2 + O(r^3), \tag{4.126}$$

where the subscripts on q denote the order of the coefficient within the Taylor expansion. These expressions lead to polynomial expressions in r on both sides of the heat equations. The condition for each coefficient is found simply by equating coefficients of the same power in r on both sides. Strictly speaking, both the net rate of production of heat Q and thermal conductivity κ are functions of both density and pressure, and thus

$$\begin{aligned} Q &= Q(\rho, T)\,, \\ \kappa &= \kappa(\rho, T)\,. \end{aligned} \tag{4.127}$$

As such, we additionally require an expansion on the background quantity $\rho(r)$ as well. Formally, this involves Taylor expanding the TOV equations about the origin as well. However, this would require the use of the Taylor expansion on the exponential metric factors. This is unnecessary here since Eqs (4.123) - (4.124) are the Newtonian forms of the heat equation. We will therefore treat $\rho(r)$ in terms of the Newtonian form of hydrostatic balance. The background density $\rho(r)$ can be expanded in exactly the same way as in Eq. (4.126), given by

$$\rho(r) = \rho_0 + \frac{1}{2}\rho_2 r^2 , \tag{4.128}$$

with the zeroth-order coefficient simply being the value of the density at the centre of the star (i.e. $\rho_0 \equiv \rho_{\rm cent}$), which is a known quantity (Tab. 2.6). Using this result, the first and second-order coefficients of Q and κ are given by

$$Q_1 = \frac{\partial Q_0}{\partial T} T_1 , \tag{4.129a}$$

$$\kappa_1 = \frac{\partial \kappa_0}{\partial T} T_1 , \tag{4.129b}$$

$$Q_2 = \frac{\partial Q_0}{\partial \rho}\rho_2 + \frac{\partial^2 Q_0}{\partial T^2} T_1^2 + \frac{\partial Q_0}{\partial T} T_2 , \tag{4.129c}$$

$$\kappa_2 = \frac{\partial \kappa_0}{\partial \rho}\rho_2 + \frac{\partial^2 \kappa_0}{\partial T^2} T_1^2 + \frac{\partial \kappa_0}{\partial T} T_2 . \tag{4.129d}$$

Substituting these quantities into the Taylor expanded ODEs, we find that

$$\begin{aligned} L(r) &= \frac{4}{3}\pi Q_0(\rho_0, T_0) r^3 + O(r^4) , \\ T(r) &= T_0 - \frac{1}{6}\frac{Q_0(\rho_0, T_0)}{\kappa_0(\rho_0, T_0)} r^2 + O(r^3) . \end{aligned} \tag{4.130}$$

Both Q and κ are functions of ρ and T only. Given that ρ_0 is just the central density, the result Eq. (4.130) for both the luminosity and temperature at the origin is therefore a one-parameter family of solutions, parameterised by the central temperature $T_0 \equiv T_{\rm cent} = T(\rho_{\rm cent})$.

To obtain the unknown value of $T_{\rm cent}$, we use the Python ODE solver `solve_BVP`, which implements a 4th order collocation algorithm as outlined by Kierzenka and Shampine (2001) to obtain the value of $T_{\rm cent}$ that satisfies the outer boundary condition Eq. (4.125). An initial guess for the integration is constructed by fixing the temperature throughout the entire star to that of $T_{\rm OB}$, which is a function of the predetermined accretion rate only.

4.8 Thermal structure of accreting neutron stars

In this section we present results for the computation of the thermal structure of non-rotating, spherically symmetric and steadily accreting neutron stars. The hydrostatic properties of the stars that we shall consider are listed in Table 4.3, whereby the mass and radii were obtained by integrating the TOV equations (2.60) - (2.62), from the central density listed in column 2, outward to where the pressure drops to zero (as per the prescription laid out in Sec. 2.6.3).

TABLE 4.3: Central density ρ_c, total mass M, crustal mass $M_{\rm crust}$, radius R, crust thickness $R_{\rm crust}$ and total heat released per accreted nucleon $Q_{\rm tot}$, for four different neutron star models: three low mass (LM) BSk19-21 models and one high mass (HM) BSk21 model.

Model	ρ_c [10^{15} g cm^{-3}]	M [$M_\odot$]	$M_{\rm crust}$ [$M_\odot$]	R [km]	$R_{\rm crust}$ [km]	$Q_{\rm tot}$ [MeV]
BSk19 (LM)	1.321	1.40	0.014	10.80	0.83	1.535
BSk20 (LM)	0.924	1.40	0.018	11.81	1.00	1.615
BSk21 (LM)	0.732	1.40	0.018	12.64	1.11	1.651
BSk21 (HM)	1.284	2.10	0.009	12.16	0.52	1.651

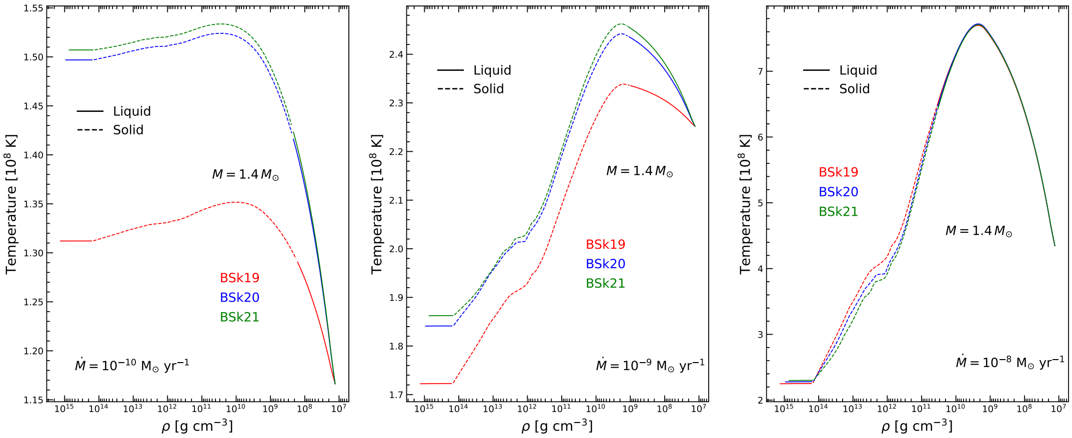

FIGURE 4.19: Temperature profiles (in units of 10^8 K) of the low-mass neutron star models listed in Table 4.3 as a function of density, accreting at $\dot{M} = 10^{-10}$ M$_\odot$ yr^{-1} (*Left*), $\dot{M} = 10^{-9}$ M$_\odot$ yr^{-1} (*center*), and $\dot{M} = 10^{-8}$ M$_\odot$ yr^{-1} (*Right*). In all cases we assume $Q_{\rm imp} = 1$, $Q_{\rm S} = 1.5$ MeV. The solid lines indicate fluid regions of the star, whilst dashed lines indicate regions where the star forms a solid Coulomb lattice. The crust begins at the point where the Coulomb parameter $\Gamma_{\rm Coul} = 175$ (assuming a one component plasma; Eq. 2.9), and ends at the crust-core transition (Table. 2.6).

There are four different BSk19-21 models listed in Table 4.3: three low-mass (LM) 1.4 $M_\odot$ stars, and one high-mass (HM) 2.1 $M_\odot$ star, such that we may determine the effects of Durca emission on the thermal structure. In Fig. 4.19, we show the temperature profiles of each of the LM models as a function of the density, for three different accretion rates (10^{-10}, 10^{-9}, and 10^{-8} $M_\odot$ yr^{-1}), as indicated in each panel. In this figure we are assuming an impurity parameter $Q_{\rm imp} = 1$, and shallow heating term $Q_{\rm S} = 1.5$ MeV, taken as averages from experimental observations (e.g. Ootes et al., 2016).

For all considered accretion rates, the radial temperature gradient (dT/dr) may be observed to change from positive in the inner crust to negative in the outer crust, becoming steeper as $\dot{M}$ increases. The temperature gradient is negative when heat flows to the surface, and positive when the heat is conducted down into the core. Over the majority of the crust, heat is mostly conducted into the core where it is then radiated away as neutrinos.

In Fig. 4.20, we plot the temperature profiles for the HM model as a function of the density, for the same three accretion rates considered in Fig. 4.19. In contrast to the LM stars, the temperature gradient is positive over the entire crust, whereby heat is overwhelmingly conducted down through the crust into the core. Clearly, the HM model produces a much cooler star than

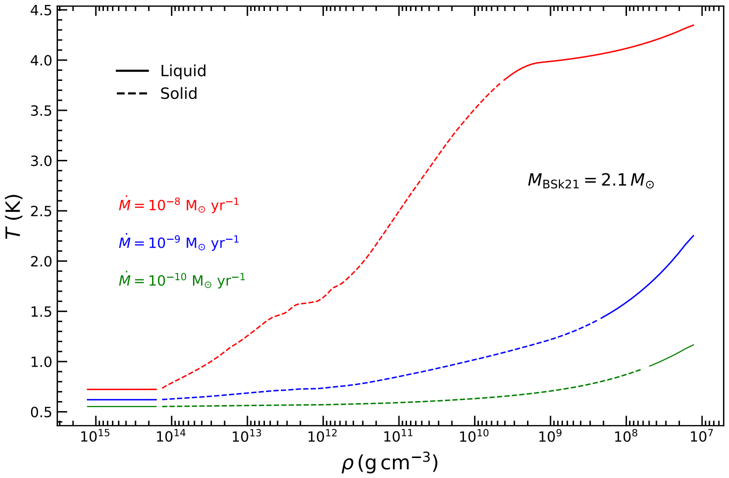

FIGURE 4.20: Temperature profiles (in units of 10^8 K) of the high-mass neutron star model listed in Table 4.3 as a function of density, accreting at $\dot{M} = 10^{-10}$ $\mathrm{M_\odot}$ $\mathrm{yr^{-1}}$ (green), $\dot{M} = 10^{-9}$ $\mathrm{M_\odot}$ $\mathrm{yr^{-1}}$ (blue), and $\dot{M} = 10^{-8}$ $\mathrm{M_\odot}$ $\mathrm{yr^{-1}}$ (red). The solid lines indicate fluid regions of the star, whilst dashed lines indicate regions where the star forms a solid Coulomb lattice. The crust begins at the point where the Coulomb parameter $\Gamma_{\rm Coul} = 175$ (assuming a one component plasma; Eq. 2.9), and ends at the crust-core transition (Table. 2.6).

any of the LM models. This is due to the presence of Durca emission, which more effectively radiates away heat conducted down into the core (recall Fig. 4.15).

The accretion of matter onto the NS may cause parts of the crust to melt (Brown, 2000). Any such molten regions will not be able to contribute to building an elastic mountain (thermal or otherwise) due to the vanishing of any existent shear stresses. The solid regions of the crust (i.e. whereby $\Gamma_{\rm Coul} \geq 175$) are indicated by the dashed regions of each of the curves in Figs. 4.19 - 4.20. When Durca reactions are active, the cooler crust is entirely solid ($\Gamma_{\rm Coul} \geq 175$) over the heat producing region ($10^9 \lesssim \rho \lesssim 10^{14}$ g cm^{-3}) for all considered accretion rates. In the hotter LM stars, the inner crust is also solid for each model at each accretion rate, but can become liquid at densities $\rho \lesssim 10^{11}$ g cm^{-3} in the outer crust. In all cases, the very outer-most layers ($10^7 - 10^8$ g cm^{-3}) just below the envelope are liquid.

In the analysis of their own deformation producing mechanism, Ushomirsky et al. (2000) found that it is the deeper capture layers that contribute the most to the formation of the mass quadrupole. The increased density, together with a greater shear modulus in the inner crust allow this portion of the crust to support greater stresses than the outer layers. Therefore, as long as the heat producing region of our crust is solid, then we are likely in a regime whereby the crust can sustain a mountain developed from a non-axisymmetric temperature distribution.

Before determining how exactly the temperature asymmetry may be introduced, though, we shall first consider the implications of some of the background parameters, namely the impurity parameter $\mathrm{Q_{imp}}$ and shallow heating term $\mathrm{Q_S}$, on the star's thermal structure.

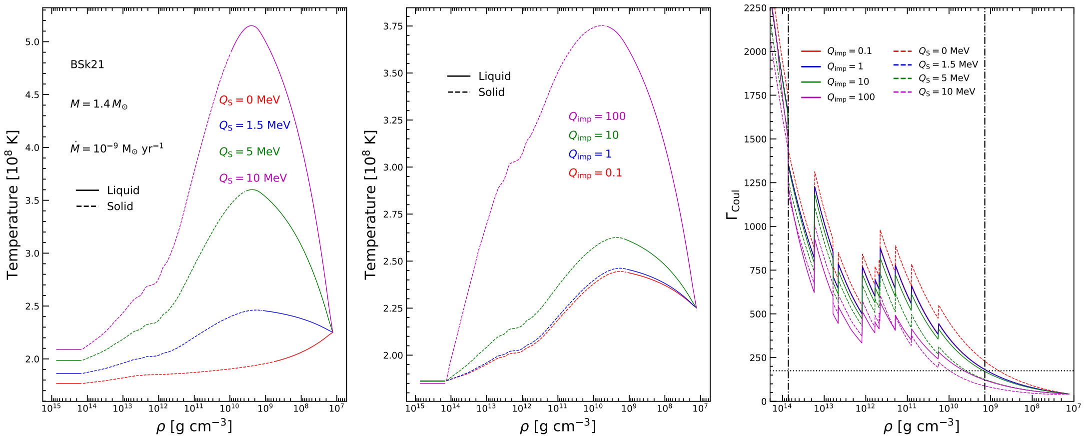

FIGURE 4.21: Temperature profiles for the low-mass BSk21 model in Table 4.3, for different values of shallow heating Q_S (*left panel*) and impurity parameter $Q_{\rm imp}$ (*right panel*) indicated in the legend. In the left panel, a fixed value $Q_{\rm imp} = 1$ is assumed. In the middle panel a fixed value $Q_S = 1.5$ MeV is assumed. The solid lines indicate fluid regions of the star, whilst dashed lines indicate regions where the star forms a solid Coulomb lattice, as per the right-hand panel which shows the corresponding values of the Coulomb parameter computed via Eq. (2.9).

In producing Figs 4.19 - 4.20, $Q_{\rm imp}$ and Q_S were assumed to be 1.0, and 1.5 MeV respectively, taken as averages from observational constraints. However, these quantities can, in principle, be much larger. For example, $Q_{\rm imp}$ may exceed 100 at the end of stable burning (Schatz et al., 1999), and Q_S may be required to be as much as 17 MeV per accreted nucleon to fit observational data from some soft X-ray transients (see e.g. Table 1 of Chamel et al., 2020). In the left-hand and centre panels of Fig. 4.21, we show how the background temperature profile depends upon the value of Q_S and $Q_{\rm imp}$ respectively, for the low-mass BSk21 model, assuming a fixed accretion rate of $\dot{M} = 10^{-9} M_\odot$ yr^{-1}.

In the left-hand panel of Fig. 4.21 we vary the shallow crustal heating parameter Q_S from $0 - 10$ MeV per accreted nucleon, with the impurity parameter fixed at $Q_{\rm imp} = 1.0$. The increased levels of heat deposited in the outer layers of the star naturally leads to a hotter crust. This introduces steeper temperature gradients, as the outer boundary condition at the base of the H/He layer is fixed by that of the accretion rate, and independent of Q_S.

In the centre panel, we vary the impurity parameter over three orders of magnitude, noting that the temperature profile is largely insensitive to the impurity parameter when $Q_{\rm imp} \lesssim 1$, but see large differences when $Q_{\rm imp} = 100$. Such a result is interpreted as follows. As the impurity parameter increases, the thermal conductivity in the crust decreases, with $\kappa_e \propto 1/Q_{\rm imp}$ in the regime where electron-impurity scattering dominates over electron-phonon scattering. This leads to less conduction of heat from the crust into the core, raising the crust temperature, with increased cooling from crustal neutrino emission.

For completeness, we have also plotted in the right-hand panel of Fig. 4.21 the corresponding values of the Coulomb parameter, to check whether increased amounts of electron-impurity scattering or shallow crustal heating can melt the crust. Increasing the value of $Q_{\rm imp}$ does not make an appreciable difference to the state of the ions in the crust, and even an additional 10 MeV per nucleon of SCH does not melt the inner crust of the star, melting only the outer crust at densities $\rho \sim 10^{10}$ g cm^{-3}.

4.9 Comparison with the literature

To place these results into context, we take the time to compare these results with that of previous authors who have sought to model the thermal structure of an accreted NS crust in order to generate thermal mountains; namely Ushomirsky et al. (2000) (UCB) and Osborne and Jones (2020) (OJ20). We shall take a step-by-step approach to consider the similarities and differences between the models, beginning with the background hydrostatic structure used by both UCB and OJ20:

Ushomirsky et al. (2000): The accreted crust was constructed using the Newtonian equations of mass conservation and hydrostatic balance (2.46a) - (2.46b), supplemented with an EoS in the inner crust obtained by Negele and Vautherin (1973), and composition taken from Haensel and Zdunik (1990a). The crust obtained from these conditions was 1.1 km thick, with a mass $M_{\rm crust} = 0.06\,M_\odot$.

Osborne and Jones (2020): The authors here adopted the same approach as Ushomirsky et al. (2000), constructed using the Newtonian formulation with the EoS and composition taken from Haensel and Zdunik (1990a,b). This time, the crust was found to be 1.45 km thick, with a mass $M_{\rm crust} = 0.09\,M_\odot$.

Both these models adopt a similar approach to what has been attempted here, save for the method to compute the hydrostatic background structure of the star. As a reminder, the NSs we have considered thus far have the properties listed in Table 4.3, obtained by solving the fully *general-relativistic* TOV equations (2.60) - (2.62), supplemented with the more modern accreted EoSs obtained by Fantina et al. (2022). The discussion that follows in this section is therefore not a *direct* comparison with previous results, but will still give a good indication of how these new results place with other well received pieces in the literature, for reasons which we shall now discuss.

Both UCB and OJ20 computed the thermal structure of the accreted crust in a Newtonian setting (the same approach taken in this thesis), solving the heat equations[16] (4.5) - (4.6), rather than the general relativistic structure equation (2.49). Since the EoS is usually calculated at zero temperature, it may be assumed to be temperature independent[17]. The calculation of the star's hydrostatic structure is therefore often separated from the thermal calculation, allowing for a

---

[16] Strictly speaking these authors solved the Newtonian heat equations for the flux rather than the luminosity, but the two are trivially related as $L = 4\pi r^2 F$.

[17] We will, however, in Chap. 6, consider some finite temperature corrections to the EoS using perturbation theory.

more meaningful comparison between the results obtained here and those obtained by UCB and OJ20.

Before looking at the structure of the background thermal profiles, it is also worth looking at some of the intricacies of the UCB and OJ20 models, and in particular at some of the assumptions made about the microphysics of the heat conduction and neutrino emissivity:

Ushomirsky et al. (2000): The crustal microphysics implemented in this model follows, for the most part, from Brown (2000) (except for the treatment of the deep crustal heating reactions, which will be discussed in greater depth shortly). Most significantly, UCB assumed the accreted crust to be *very impure*; and as such assumed neutrino emission to be largely dominate by *liquid-phase* electron-ion bremsstrahlung (Eq. (4.40); and recall the discussion in Sec. 4.5.2.3), and the thermal conductivity to be dominated by electron-ion scattering (Eq. (4.18); i.e. Eq. (4.16) when $Q_{\text{imp}} \sim Z^2$).

Osborne and Jones (2020): The crustal microphysics implemented in this model differs from UCB in some important regards. Namely, OJ20 assumed the opposite to be true, that the accreted crust was actually relatively *pure*. It was assumed that the neutrino emissivity is dominated by *solid-phase* (crystallised) electron-ion bremsstrahlung Eq. (4.40), and that the thermal conductivity is determined by a mixture of electron-phonon and electron-impurity scattering (recall the phase-space diagram Fig. 4.4 for where each mechanism dominates).

In this thesis we have expanded greatly upon the crustal microphysics used by either UCB or OJ20, and have included elements of both models in order to build a more realistic crust. The real difference between the models of UCB and OJ20 and the one constructed here, however, is the treatment of the core. Indeed, both UCB and OJ20 modelled only the crust of the NS. As such, there was no self-consistent calculation of the neutrino emissivity in the core, nor was there any description of the heat conduction, either.

Instead, the inner boundary condition at the base of the crust was obtained by equating the flux flowing into the core to the neutrino luminosity of the core as

$$-4\pi R_{\text{IB}}^2 F_{\text{IB}} = L_{\text{core}}(T_{\text{IB}})\,, \tag{4.131}$$

where the core neutrino luminosity L_{core} was assumed to be provided solely by Murca processes, following a formula given in Shapiro and Teukolsky (1983) as

$$L = 5.31 \times 10^{39}\,\text{erg s}^{-1}\,\frac{M}{M_\odot}\left(\frac{\rho_0}{\rho}\right) T_8^9 \exp\left[\frac{-\Delta_{\text{gap}}}{k_{\text{B}}T}\right]. \tag{4.132}$$

This formula led both UCB and OJ20 to consider two possibilities; one where the core was strongly superfluid, and one where the core was ‘normal’. In the case of the former, the

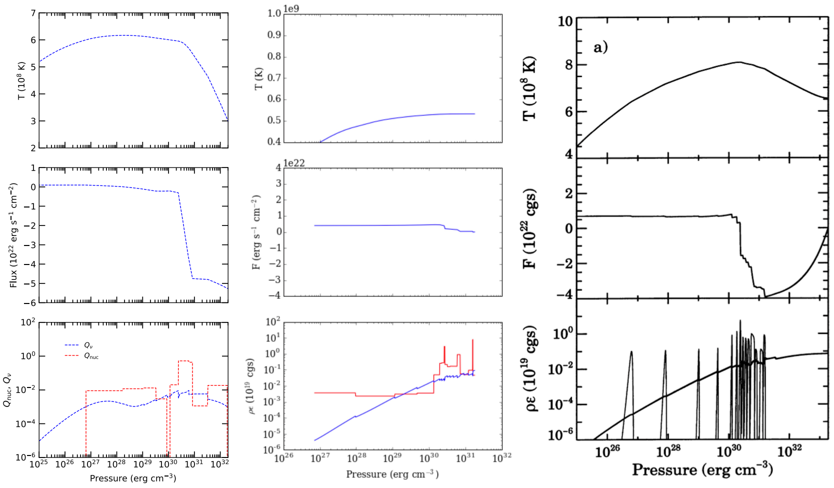

FIGURE 4.22: Background temperature (top row panels), heat flux (middle row panels), neutrino luminosity and nuclear heating profiles (bottom row panels) in the crust of an accreting neutron star as obtained by the model presented in this thesis (left column panels), as well as the models of Osborne and Jones (2020) (middle column panels) and Ushomirsky et al. (2000) (right column panels). The latter two models do not include a self-consistent model of the core, and instead use Eq. (4.132) to model neutrino emission. Both Osborne and Jones (2020) and Ushomirsky et al. (2000) assume a superfluid core in this figure, with $\Delta_{\rm gap} = 1$ MeV. The accretion rate is $10^{-8} M_\odot$ yr^{-1} in all models, with an assumed impurity parameter $Q_{\rm imp} = 100$ and shallow heating term $Q_{\rm S} = 0$ MeV in our model and the model of Osborne and Jones (2020), in order to reproduce the microphysics of Ushomirsky et al. (2000) (see surrounding text).

suppression of the Murca processes is accounted for by the factor $\exp(-\Delta_{\rm gap}/k_{\rm B}T)$ (notice this is the definition of the dimensionless gap amplitude $\nu_{\rm gap}$ (4.62)). For practical purposes, it was assumed that $\Delta_{\rm gap} \equiv 0$ if the core was composed of only normal matter, or $\Delta_{\rm gap} \equiv 1$ MeV if it was superfluid.

The background temperature and flux profiles, as well as the heat generation from DCH reactions and total crustal neutrino emissivity for a star with a *superfluid core* for the models of UCB (right-hand panel), OJ20 (centre panel) and the model presented in this thesis (left-hand panel; assuming the BSk21 EoS) is shown in Fig. 4.22. In all models it is assumed that the crust is very impure ($Q_{\rm imp} = 100$ in ours and the OJ20 model), that the accretion rate is $\dot{M} = 10^{-8}\ M_\odot$ yr^{-1}, and that there are no shallow heating sources present.

The first thing to notice in these plots is the difference in the form of the curves describing the heat generation $Q_{\rm h}$. The differences arise from the choice in which we (and OJ20) have made in depositing the heat into each of the capture layers. In our model, recall that capture layers are assumed to be infinitely thin, and thus it was chosen to smear the heat over each capture 'shell' of constant A and Z (Sec. 4.3). In the UCB model, however, the finite width of each individual capture layer was calculated, leading to heat release over narrow pressure/density ranges.

The second significant point to make is that ours and the UCB models show a steep decline in the heat flux (i.e. becoming large and negative) at $P \sim 10^{30}$ erg s^{-1} cm^{-3}, as a result of increased neutrino emission in the inner crust where most of the heat is produced via DCH reactions (Table

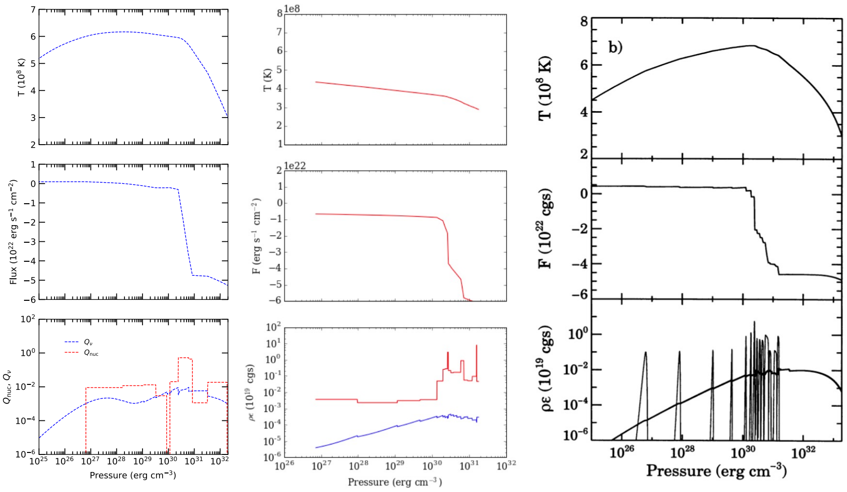

FIGURE 4.23: Same as Fig. 4.22, but showing the results of Osborne and Jones (2020) and Ushomirsky et al. (2000) when assuming the core to be normal (i.e. no superfluidity), with $\Delta_{\text{gap}} = 0$ MeV in Eq. (4.132), The left panel (i.e the model presented in this thesis) is the same as in Fig. 4.22, since the superfluidity is computed self-consistently.

4.1). Specifically, in our model the flux drops rapidly at 2.5×10^{30} erg s^{-1} cm^{-3}, corresponding to the location of a pycnonuclear reaction in the inner crust where 908 keV of heat energy is released (which actually is the largest single release of heat from any capture layer in the BSk models; Tables A.1 - A.3). In the UCB model on the other hand, rather than a smooth drop in the flux profile, a series of step-like features are observed. These steps arise from the choice of implementing the Haensel and Zdunik (1990b) EoS, which predicts a more stratified inner crust than the BSk models (Fig. 2.5), and where heat is deposited into the crust more evenly across the individual capture layers (Fig. 4.3).

One difference in the UCB model however is that the flux begins to rise (i.e. becomes less negative, approaching zero) at high pressure beyond the heat-producing region, whereas in the OJ20 model and our own the flux simply plateaus. This rise in the UCB model is a consequence of the (assumed) strong superfluidity in the core. When $\Delta_{\text{gap}} = 1$ in Eq. (4.132), one effectively has $F_{\text{IB}} = 0$ in Eq. (4.131) and the neutrino luminosity is suppressed at the crust-core boundary. Hopefully, however, it is clear from the lengthy discussion in Section 4.6.2 that the formula (4.132) is a gross simplification of the influence of superfluidity on the core microphysics. Not only is the superfluid energy gap Δ_{gap} itself a function of the temperature, but Murca processes are not the only neutrino process taking place in the core. In fact, in regimes of strong superfluidity, although Murca processes are indeed suppressed, the enhancement of neutrino emission by the formation of Cooper pairs (CPBF) can actually result in greater neutrino emission from the core (Fig. 4.15) when it is superfluid.

Finally, we shall compare our model with that of the UCB and OJ20 models in the crust of an accreting NS when the core is assumed to be composed of *normal matter*. These results are summarised in Fig. 4.23, assuming the same parameters as in Fig. 4.22. When the core is assumed to be non-superfluid (in their models), it can be seen that the OJ20 model now also predicts a dramatic fall in the heat flux in the deep crust, similar to our own model. Equally interesting is the UCB model, which while exhibiting the familiar drop in the heat flux at $P \sim 10^{30}$ erg s^{-1} cm^{-3}, does not recover like it did in the superfluid case, instead plateauing at pressures beyond the heat producing region. The reason for this behavior is clear, with more efficient neutrino emission in the normal core case leading the shallower temperature gradients in the deep crust.

The take-away message from this comparison is to highlight the need for an accurate description of the core in order to produce accurate models of the crust. By approximating the neutrino emission from the core solely by Murca processes (as per Eq. (4.132)), one can grossly overestimate the effects of superfluidity on the thermal profile of the star. The inclusion of superfluid effects in the UCB and OJ20 models leads to temperatures in the deep crust that are 1.5 – 2x larger than those produced from the model presented in this thesis. This is significant, since (as we shall see later on) that it is the denser regions of the crust that contribute most to the formation of the mass quadrupole. And, given that it is the perturbations of the background thermal profile which source the *thermal* mountains to begin with (which we shall go on to discuss now), it is of the utmost importance to have an accurate description of the background temperature profile in these regions.

5

Temperature Asymmetry in Accreting Neutron Stars

In this chapter we outline how large-scale temperature variations deviating from the spherically-symmetric thermal background computed in Chap. 4 might be introduced via the addition of an internal magnetic field. We begin in Section 5.1 by discussing how the presence of a magnetic field can influence heat conduction within neutron stars. This phenomenon has been studied by a number of authors, including Yakovlev and Urpin (1980); Geppert et al. (2004); Pons and Geppert (2007); Page et al. (2007); Aguilera et al. (2008), who have shown that the temperature distribution of highly magnetised neutron stars ($B \sim 10^{15}$ G) is *anisotropic*.

Due to external inferences placing limits on the magnetic field of neutron stars in LMXBs to just $10^8 - 10^9$ G, however, in Section 5.2, we outline how the presence of such weak magnetic fields may generate small perturbations in the heat flow, and derive a set of first-order coupled ODEs which describes the perturbed thermal structure. The functional form of the magnetic field is then described in Section 5.3, where we shall discuss how one may model fields that are confined to the crust of the star, as well as those that may extend into the core.

We continue in Section 5.4 by discussing how the perturbation equations may then be solved, and critique the boundary conditions used by Ushomirsky et al. (2000) and Osborne and Jones (2020) in previous calculations of the perturbed thermal structure. The discussed methods are then followed up in Section 5.5 where we present results for the level of temperature asymmetry ($\delta T/T$) introduced by the magnetic field on the unperturbed background (recall Sec. 4.8). In Section 5.6 we then place these results into the context of wider continuous GW searches, discussing how the expected level of temperature asymmetry calculated here can be used to make simple estimates of NS ellipticity based on the results of UCB[1].

---

[1] We will, however, of course go on to compute the ellipticity self-consistently afterwards in Chapter 6.

5.1 Thermal conductivity in the presence of a magnetic field

Free electrons are responsible for most of the heat conduction in the crust. In the presence of a magnetic field, the classical Larmor rotation of the electrons would act to convert the thermal conductivity (which has been treated thus far as a scalar quantity) into a directional-dependent tensor, and lead to anisotropic heat flow (Page et al., 2007).

5.1.1 The thermal conductivity tensor

Fourier's law (including contributions from each of the heat carriers) in tensorial form is written as

$$F^i = -\sum_{\mathrm{x}} \kappa_{\mathrm{x}}^{ij} \nabla_j T \, , \tag{5.1}$$

where κ_{x}^{ij} is the thermal conductivity tensor, and x denotes the heat carrier involved (x = e, μ, n). The heat flux including contributions from the magnetic field were derived by Yakovlev and Urpin (1980). For a magnetic field $\mathbf{B} = B\mathbf{b}$, the heat flux carried by species x can be written in vectorial form as

$$\mathbf{F}_{\mathrm{x}} = -\kappa_{\mathrm{x}}^{\perp} \left[\nabla T + (\omega_B^{\mathrm{x}} \tau_{\mathrm{x}})^2 (\mathbf{b} \cdot \nabla T) \cdot \mathbf{b} + \omega_B^{\mathrm{x}} \tau_{\mathrm{x}} (\mathbf{b} \times \nabla T) \right] , \tag{5.2}$$

where $\kappa_{\mathrm{x}}^{\perp}$ is the component of the thermal conductivity tensor perpendicular to the magnetic field, $\mathbf{b}$ is the unit vector of the magnetic field (pointing in the direction of the magnetic field) and $\omega_B^{\mathrm{x}} \tau_{\mathrm{x}}$ is known as the '*magnetisation parameter*'. The magnetisation parameter is the product of the (already familiar; Eqs (4.12) - (4.13) and (4.21)) effective relaxation time τ_{x}, with the electron/muon gyrofrequency ω_B^{x} (which determines the angular frequency of the motion of an electron perpendicular to the magnetic field), and is defined as

$$\omega_B^{\mathrm{x}} = \frac{eB}{m_{\mathrm{x}}^* c} \, . \tag{5.3}$$

For the neutrons in the core, their contribution to the heat flux is unaffected by the addition of the magnetic field (since they are electrically neutral; $\omega_B^{\mathrm{x}} = 0$ when x = n) and Eq. (5.2) is simply

$$\mathbf{F}_{\mathrm{n}} = -\kappa_{\mathrm{n}}^{0} \nabla T \, , \tag{5.4}$$

where κ_{n}^{0} is the neutron part of the *scalar* conductivity (given by Eq. (4.10) when x = n).

In the core, nuclear equilibrium considerations imply the equality of the electron and muon chemical potentials, and therefore that the gyrofrequency of the two charge carriers are the same (i.e. $m_e^* = \mu_e/c^2 = \mu_\mu/c^2 \equiv m_\mu^*$). In the calculations that follow, we therefore assume the same ω_B for both muons and electrons.

The addition of the magnetic field deflects a piece of the heat flux in the direction orthogonal to both the temperature gradients and the local magnetic field (a thermal analogue of the Hall effect), as can be seen from the final term in Eq. (5.2). In spherical polar coordinates, specifying that the polar axis coincides with the magnetic field's symmetry axis, the electron/muon contribution to the thermal conductivity can be written as

$$\kappa_{ij}^{\mathrm{x}} = \kappa_\perp \left[\hat{I}_{ij} + (\omega_B \tau_{\mathrm{x}})^2 \begin{pmatrix} b_{rr} & b_{r\theta} & b_{r\phi} \\ b_{r\theta} & b_{\theta\theta} & b_{\theta\phi} \\ b_{r\phi} & b_{\theta\phi} & b_{\phi\phi} \end{pmatrix} + \omega_B \tau_{\mathrm{x}} \begin{pmatrix} 0 & -b_\phi & b_\theta \\ b_\phi & 0 & -b_r \\ -b_\theta & b_r & 0 \end{pmatrix} \right], \tag{5.5}$$

where $\hat{I}_{ij}$ is the identity matrix, b_r, b_θ, and b_ϕ are the components of the unit vector of the magnetic field **b** in the direction of the magnetic field, and $b_{ij} = b_i b_j$, for $i, j = r, \theta, \phi$ [2].

The influence of the magnetic field may perhaps be more intuitively understood however by switching to Cartesian coordinates. Substituting $r \longrightarrow x$, $\theta \longrightarrow y$, $\phi \longrightarrow z$, it follows that for a magnetic field orientated along the z-axis (such that $b_{\mathrm{x}} = b_y = 0$), then[3]

$$\kappa = \begin{pmatrix} \kappa^\perp & -\kappa^\wedge & 0 \\ \kappa^\wedge & \kappa^\perp & 0 \\ 0 & 0 & \kappa^\parallel \end{pmatrix}, \tag{5.6}$$

where $\kappa^\parallel$ is the component of the thermal conductivity parallel to the magnetic field and $\kappa^\wedge$ is the so-called Hall component. These components of the thermal conductivity tensor are related to the scalar conductivity (κ^0 in Eq. (5.4)) as

$$\kappa_{\mathrm{x}}^\parallel = \kappa_{\mathrm{x}}^0, \qquad \kappa_{\mathrm{x}}^\perp = \frac{\kappa_{\mathrm{x}}^0}{(1 + (\omega_B^{\mathrm{x}} \tau_{\mathrm{x}})^2)}, \qquad \kappa_{\mathrm{x}}^\wedge = \omega_B^{\mathrm{x}} \tau_{\mathrm{x}}\, \kappa_{\mathrm{x}}^\perp\,. \tag{5.7}$$

In the direction perpendicular to the magnetic field, the thermal conductivity is suppressed, corresponding to a diminishing of the heat flow orthogonal to the magnetic field (Yakovlev and

---

[2] This formula appears in Aguilera et al. (2008), though there are two sign discrepancies in the final term in their expression which have been corrected.

[3] This formula is also incorrectly printed in Aguilera et al. (2008), containing a sign error in the two hall terms $\kappa^\wedge$ due to the misprint in Eq. (5.5).

Urpin, 1980). The ratio of the conductivities parallel and perpendicular to the magnetic field is then given in terms of the magnetisation parameter as

$$\frac{\kappa_{\rm x}^{\parallel}}{\kappa_{\rm x}^{\perp}} = 1 + (\omega_B^{\rm x}\tau_{\rm x}(T))^2\,, \tag{5.8}$$

where x in this instance denotes the *charged* carrier involved (i.e. x = e, μ). As noted above, the neutrons, whilst contributing to the thermal conductivity in the core, have no interaction with the magnetic field and therefore their contribution does not produce any anisotropy in the heat flow (Eq. (5.8) reduces to 1 when x = n). In regions where the electrons, muons, and neutrons coexist, the individual conductivity tensors $\kappa_{\rm x}$ simply add linearly (via Eq. (5.1)).

5.2 The thermal perturbation equations

In the previous section we saw that the magnetisation parameter is an indicator of the amount of suppression of the thermal conductivity. In order to proceed, it is convenient to express the heat flux equation (5.2) in terms of $\omega_B\tau_{\rm x}$. Substituting the expression for $\kappa_\perp$ (5.7) into Eq. (5.2) yields

$$\mathbf{F}_{\rm x} = -\frac{\kappa_{\rm x}^{\parallel}}{1+(\omega_B\tau_{\rm x})^2}\left[\boldsymbol{\nabla}T + (\omega_B\tau_{\rm x})^2(\mathbf{b}\cdot\boldsymbol{\nabla}T)\cdot\mathbf{b} + \omega_B\tau_{\rm x}(\mathbf{b}\times\boldsymbol{\nabla}T)\right]. \tag{5.9}$$

Strictly in the regime $\omega_B\tau_{\rm x} \ll 1$, one may treat the addition of the magnetic field as a perturbation of the heat flow from that of the non-magnetic, spherically symmetric background heat flux, and we may write

$$\begin{aligned}\mathbf{F}_{\rm x}^0 + \delta\mathbf{F}_{\rm x} = -\frac{(\kappa_{\rm x}^0 + \delta\kappa_{\rm x}^{\parallel})}{1+(\omega_B\tau_{\rm x})^2}\Bigg[&\boldsymbol{\nabla}(T_0+\delta T) + (\omega_B\tau_{\rm x})^2[\mathbf{b}\cdot\boldsymbol{\nabla}(T_0+\delta T)]\cdot\mathbf{b}\\ &+\omega_B\tau_{\rm x}[\mathbf{b}\times\boldsymbol{\nabla}(T_0+\delta T)]\Bigg],\end{aligned} \tag{5.10}$$

where we have written all perturbed quantities, $\mathbf{F}$, T, and $\kappa_\parallel$ as

$$\mathbf{F}_{\rm x} = \mathbf{F}_{\rm x}^0 + \delta\mathbf{F}_{\rm x}\,, \quad T = T_0 + \delta T\,, \quad \kappa_{\rm x}^{\parallel} = \kappa_{\rm x}^0 + \delta\kappa_{\rm x}^{\parallel}\,. \tag{5.11}$$

In the limit of $\omega_B\tau_{\rm x} \ll 1$, a Taylor series expansion of the perturbed heat flux (5.10) up to second order in $\omega_B\tau_{\rm x}$ yields

$$\begin{aligned}\mathbf{F}_{\mathrm{x}}^0 + \delta\mathbf{F}_{\mathrm{x}} = &- \left[(\kappa_{\mathrm{x}}^0 + \delta\kappa_{\mathrm{x}}^{\|}) + (\omega_B\tau_{\mathrm{x}})^2(\kappa_{\mathrm{x}}^0 + \delta\kappa_{\mathrm{x}}^{\|})\right]\cdot \\ &\left[\boldsymbol{\nabla}(T_0 + \delta T) + (\omega_B\tau_{\mathrm{x}})^2[\mathbf{b}\cdot\boldsymbol{\nabla}(T_0 + \delta T)]\cdot\mathbf{b} + \omega_B\tau_{\mathrm{x}}[\mathbf{b}\times\boldsymbol{\nabla}(T_0 + \delta T)]\right].\end{aligned} \tag{5.12}$$

From here, linearising in both $\omega_B\tau_{\mathrm{x}}$ and δT leads to

$$\begin{aligned}\mathbf{F}_{\mathrm{x}}^0 + \delta\mathbf{F}_{\mathrm{x}} = &- \kappa_{\mathrm{x}}^0\left[\nabla(T_0 + \delta T) + \omega_B\tau_{\mathrm{x}}[\mathbf{b}\times\boldsymbol{\nabla}(T_0 + \delta T)]\right] \\ &- \delta\kappa_{\mathrm{x}}^{\|}\left[\boldsymbol{\nabla}(T_0 + \delta T) + \omega_B\tau_{\mathrm{x}}[\mathbf{b}\times\boldsymbol{\nabla}(T_0 + \delta T)]\right].\end{aligned} \tag{5.13}$$

Upon further simplifying, one is simply left with

$$\delta\mathbf{F}_{\mathrm{x}} = -\kappa_{\mathrm{x}}^0\left[\nabla\delta T + \omega_B\tau_{\mathrm{x}}[\mathbf{b}\times\boldsymbol{\nabla}T_0]\right] - \delta\kappa_{\mathrm{x}}^{\|}\boldsymbol{\nabla}T_0\,, \tag{5.14}$$

which determines the thermal flux perturbation within a (weakly) magnetised NS to leading order. Finally, following OJ20, we introduce (for convenience) the quantity

$$\tilde{\omega} = \frac{e}{m_{\mathrm{x}}^* c}\,, \tag{5.15}$$

which may be referred to as the gyromagnetic frequency *per unit magnetic field strength*. This, along with the fact that the magnetic field strength is related the unit vector of the magnetic field as $\mathbf{B} = B\mathbf{b}$, allows the perturbed thermal heat flux to be written in a more intuitive form as

$$\begin{aligned}\delta\mathbf{F} &= \sum_{\mathrm{x}} -\kappa_{\mathrm{x}}^0\left[\nabla\delta T + \tilde{\omega}\tau_{\mathrm{x}}[\mathbf{B}\times\boldsymbol{\nabla}T_0]\right] - \delta\kappa_{\mathrm{x}}^{\|}\boldsymbol{\nabla}T_0 \\ &= -\kappa_e^0\left[\boldsymbol{\nabla}\delta T + \tilde{\omega}\tau_e[\mathbf{B}\times\boldsymbol{\nabla}T_0]\right] - \delta\kappa_e^0\boldsymbol{\nabla}T_0 \\ &\quad - \kappa_\mu^0\left[\boldsymbol{\nabla}\delta T + \tilde{\omega}\tau_\mu[\mathbf{B}\times\boldsymbol{\nabla}T_0]\right] - \delta\kappa_\mu^0\boldsymbol{\nabla}T_0 \\ &\quad - \kappa_{\mathrm{n}}^0\boldsymbol{\nabla}\delta T - \delta\kappa_{\mathrm{n}}^0\boldsymbol{\nabla}T_0\,.\end{aligned} \tag{5.16}$$

We have now an expression for the perturbed thermal heat flux due to the presence of a magnetic field. Since the perturbed flux is calculated relative to some non-magnetic spherically symmetric background heat flux, it is natural to decompose all of the perturbed quantities in terms of spherical harmonics. Starting with the perturbed heat flux, given a scalar spherical harmonic $Y_{\ell m}(\theta,\phi)$ this quantity will admit a vector harmonic expansion (VSH) of the form

$$\delta\mathbf{F} = \sum_{\ell=0}^{\infty}\sum_{m=-l}^{l}\left[U_{\ell m}(r)\,Y_{\ell m}\hat{\mathbf{r}} + V_{\ell m}(r)\,r\boldsymbol{\nabla}Y_{\ell m} + W_{\ell m}(r)\,(\mathbf{r}\times\boldsymbol{\nabla}Y_{\ell m})\right], \tag{5.17}$$

where $\hat{\mathbf{r}}$ is the radial unit vector. Since our expansion of the perturbed heat flux implies both polar and axial perturbations, it is useful to also decompose the magnetic field into its constituent poloidal and toroidal components as (Rädler et al., 2001)

$$\mathbf{B} = \mathbf{B}_{\rm pol} + \mathbf{B}_{\rm tor}\,, \tag{5.18}$$

with the two pieces themselves expressed in terms of two scalar functions $\Phi(r,\theta,\phi)$ and $\Psi(r,\theta,\phi)$ such that

$$\mathbf{B}_{\rm pol} = -\boldsymbol{\nabla}\times(\mathbf{r}\times\boldsymbol{\nabla}\Phi)\,, \quad \mathbf{B}_{\rm tor} = -\mathbf{r}\times\boldsymbol{\nabla}\Psi\,. \tag{5.19}$$

These scalar functions, along with the temperature perturbation δT, can then also be decomposed in terms of spherical harmonics as

$$\delta T = \delta T_{\ell m}(r) Y_{\ell m}(\theta,\phi), \tag{5.20}$$

$$\Phi = \Phi_{\ell m}(r) Y_{\ell m}(\theta,\phi), \tag{5.21}$$

$$\Psi = \Psi_{\ell m}(r) Y_{\ell m}(\theta,\phi). \tag{5.22}$$

Note that in writing down Eqs. (5.20) - (5.22) we have neglected to include the relevant double sum over ℓ and m, and will continue to do so unless otherwise stated. This is largely for reasons of brevity, but also because ultimately we will consider only the component of the magnetic field (and associated temperature perturbation) that gives rise to leading-order gravitational radiation from a rotating neutron star: perturbations with $\ell = m = 2$. Substituting both the magnetic field components and decomposed temperature perturbation into the RHS of equation (5.16) gives

$$\begin{aligned}\delta\mathbf{F}_{\rm x} = -\kappa_{\rm x}^0\left[\frac{d\delta T_{\ell m}}{dr}\hat{\mathbf{r}}Y_{\ell m} + \delta T_{\ell m}\boldsymbol{\nabla}Y_{\ell m}\right] - \frac{d\kappa_{\rm x}^0}{dT}\frac{dT}{dr}\delta T_{\ell m}\hat{\mathbf{r}}Y_{\ell m} \\ - \kappa_{\rm x}^0\tilde{\omega}\tau_{\rm x}\left[(B_{\rm pol} + B_{\rm tor})\times\boldsymbol{\nabla}T_0\right]\,.\end{aligned} \tag{5.23}$$

We seek to compare the RHS of the above result (5.23) with that of the VSH decomposition of $\delta\mathbf{F}_{\rm x}$ in Eq. (5.17). To do so, we must first write down the components of the magnetic field in Eq. (5.23) (specifically the final term $[B_{\rm pol} + B_{\rm tor}]\times\boldsymbol{\nabla}T_0$) in terms of the two scalar functions $\Phi(r,\theta,\phi)$ and $\Psi(r,\theta,\phi)$. For clarity, we shall consider each component independently:

Firstly, for the *toroidal* component, we have,

$$
\begin{aligned}
&-\kappa_{\mathrm{x}}^{0}\tilde{\omega}\tau_{\mathrm{x}}\left[B_{\mathrm{tor}}\times\boldsymbol{\nabla}T_0\right]\\
&=-\kappa_{\mathrm{x}}^{0}\tilde{\omega}\tau_{\mathrm{x}}\left[(-\mathbf{r}\times\boldsymbol{\nabla}\Psi)\times\boldsymbol{\nabla}T_0\right]\\
&=-\kappa_{\mathrm{x}}^{0}\tilde{\omega}\tau_{\mathrm{x}}\left[-\mathbf{r}\times(\boldsymbol{\nabla}\Psi\times\boldsymbol{\nabla}T_0)-\boldsymbol{\nabla}\Psi\times(\mathbf{r}\times\boldsymbol{\nabla}T_0)\right]\\
&=-\kappa_{\mathrm{x}}^{0}\tilde{\omega}\tau_{\mathrm{x}}\left[(-\mathbf{r}\cdot\boldsymbol{\nabla}T_0)\boldsymbol{\nabla}\Psi-(-\mathbf{r}\cdot\boldsymbol{\nabla}\Psi)\boldsymbol{\nabla}T_0\right]\\
&=-\kappa_{\mathrm{x}}^{0}\tilde{\omega}\tau_{\mathrm{x}}\left[\hat{\mathbf{r}}r\frac{dT_0}{dr}\hat{\mathbf{r}}\frac{d\Psi_{\ell m}}{dr}Y_{\ell m}+\hat{\mathbf{r}}r\frac{dT_0}{dr}\hat{\mathbf{r}}\Psi_{\ell m}\boldsymbol{\nabla}Y_{\ell m}-\hat{\mathbf{r}}r\frac{d\Psi_{\ell m}}{dr}\frac{dT_0}{dr}\hat{\mathbf{r}}Y_{\ell m}\right]\\
&=\left[-\kappa_{\mathrm{x}}^{0}\tilde{\omega}\tau_{\mathrm{x}}r\frac{dT_0}{dr}\Psi_{\ell m}\right]\boldsymbol{\nabla}Y_{\ell m}\,. \qquad (5.24)
\end{aligned}
$$

And similarly, for the *poloidal* part, we have

$$
\begin{aligned}
&-\kappa_{\mathrm{x}}^{0}\tilde{\omega}\tau_{\mathrm{x}}\left[B_{\mathrm{pol}}\times\boldsymbol{\nabla}T_0\right]\\
&=-\kappa_{\mathrm{x}}^{0}\tilde{\omega}\tau_{\mathrm{x}}\left[\left[\boldsymbol{\nabla}\times(-\mathbf{r}\times\boldsymbol{\nabla}\Phi)\right]\times\boldsymbol{\nabla}T_0\right]\\
&=-\kappa_{\mathrm{x}}^{0}\tilde{\omega}\tau_{\mathrm{x}}\left\{\boldsymbol{\nabla}\times\left[-\mathbf{r}\times\left(\frac{d\Phi_{\ell m}}{dr}\hat{\mathbf{r}}Y_{\ell m}+\Phi_{\ell m}\boldsymbol{\nabla}Y_{\ell m}\right)\right]\times\boldsymbol{\nabla}T_0\right\}\\
&=-\kappa_{\mathrm{x}}^{0}\tilde{\omega}\tau_{\mathrm{x}}\left[\left[\boldsymbol{\nabla}\times(-\Phi_{\ell m}\mathbf{r}\times\boldsymbol{\nabla}Y_{\ell m})\right]\times\boldsymbol{\nabla}T_0\right], \qquad (5.25)
\end{aligned}
$$

where, using the standard result

$$
\boldsymbol{\nabla}\times\left[\Phi_{\ell m}\mathbf{r}\times\boldsymbol{\nabla}Y_{\ell m}\right]=-\frac{1}{r}l(l+1)\Phi_{\ell m}Y_{\ell m}\hat{\mathbf{r}}-\left(\frac{d\Phi_{\ell m}}{dr}+\frac{1}{r}\Phi_{\ell m}\right)r\boldsymbol{\nabla}Y_{\ell m}\,, \qquad (5.26)
$$

the poloidal component becomes

$$
\begin{aligned}
&-\kappa_{\mathrm{x}}^{0}\tilde{\omega}\tau_{\mathrm{x}}\left[\left[\boldsymbol{\nabla}\times(-\Phi_{\ell m}\mathbf{r}\times\boldsymbol{\nabla}Y_{\ell m})\right]\times\boldsymbol{\nabla}T_0\right]\\
&=\kappa_{\mathrm{x}}^{0}\tilde{\omega}\tau_{\mathrm{x}}\left\{\left[\left(\frac{1}{r}l(l+1)\Phi_{\ell m}Y_{\ell m}\hat{\mathbf{r}}\right)\times\boldsymbol{\nabla}T_0\right]\right.\\
&\qquad\left.+\left[\left(\frac{d\Phi_{\ell m}}{dr}r\boldsymbol{\nabla}Y_{\ell m}\right)\times\boldsymbol{\nabla}T_0\right]+\left[\left(\Phi_{\ell m}\boldsymbol{\nabla}Y_{\ell m}\right)\times\boldsymbol{\nabla}T_0\right]\right\}\\
&=\left[\kappa_{\mathrm{x}}^{0}\tilde{\omega}\tau_{\mathrm{x}}\left(\frac{1}{r}\Phi_{\ell m}\frac{dT_0}{dr}+\frac{d\Phi_{\ell m}}{dr}\frac{dT_0}{dr}\right)\right]\mathbf{r}\times\boldsymbol{\nabla}Y_{\ell m}\,. \qquad (5.27)
\end{aligned}
$$

Taking the final results Eqs (5.24) and (5.27) for the toroidal and poloidal parts of the field respectively, we find

$$
\begin{aligned}
\delta \mathbf{F}_{\mathrm{x}} = -\left[\frac{d\kappa_{\mathrm{x}}^0}{dT}\frac{dT_0}{dr}\delta T_{\ell m} - \kappa_{\mathrm{x}}^0\frac{d\delta T_{\ell m}}{dr}\right] Y_{\ell m}\,\hat{\mathbf{r}} - \left[\frac{1}{r}\left(\delta T_{\ell m} - \tilde{\omega}\tau_{\mathrm{x}}\Psi_{\ell m} r\frac{dT_0}{dr}\right)\kappa_{\mathrm{x}}^0\right] r\nabla Y_{\ell m} \\
- \left[\kappa_{\mathrm{x}}^0\tilde{\omega}\tau_{\mathrm{x}}\left(\frac{1}{r}\Phi_{\ell m}\frac{dT_0}{dr} + \frac{d\Phi_{\ell m}}{dr}\frac{dT_0}{dr}\right)\right]\mathbf{r}\times\nabla Y_{\ell m}\,. \quad (5.28)
\end{aligned}
$$

The first of the coupled first-order ODEs is then obtained by comparing the coefficients of Eq. (5.28) with the general expression (5.17), giving

$$
\begin{aligned}
\frac{d\delta T_{\ell m}}{dr} &= -\sum_{\mathrm{x}}\frac{1}{\kappa_{\mathrm{x}}^0}\left[\frac{d\kappa_{\mathrm{x}}^0}{dT}\frac{dT}{dr}\delta T_{\ell m} + U_{\ell m}\right] \\
&= -\frac{1}{\kappa}\left[\left(\frac{d\kappa_e^0}{dT} + \frac{d\kappa_\mu^0}{dT} + \frac{d\kappa_{\mathrm{n}}^0}{dT}\right)\frac{dT}{dr}\delta T_{lm} + U_{lm}\right],
\end{aligned}
\tag{5.29}
$$

where $\kappa = \kappa_e^0 + \kappa_\mu^0 + \kappa_{\mathrm{n}}^0$ (Eq. (4.11)). The transverse components of the field $V_{\ell m}$ and $W_{\ell m}$ (with respect to $\mathbf{r}$), are also obtained through the definition (5.17), given by

$$
\begin{aligned}
V_{\ell m} &= \sum_{\mathrm{x}}\frac{1}{r}\left(\tilde{\omega}\tau_{\mathrm{x}}\Psi_{\ell m} r\frac{dT}{dr} - \delta T_{\ell m},\right)\kappa_{\mathrm{x}}^0 \\
&= \frac{1}{r}\left\{\left[\left(\kappa_e^0\tilde{\omega}\,\tau_e + \kappa_\mu^0\tilde{\omega}\,\tau_\mu\right)\Psi_{lm} r\frac{dT}{dr}\right] - \kappa\delta T_{lm}\right\},
\end{aligned}
\tag{5.30}
$$

$$
\begin{aligned}
W_{\ell m} &= -\sum_{\mathrm{x}}\kappa_{\mathrm{x}}^0\tilde{\omega}\tau_{\mathrm{x}}(T)\left(\frac{1}{r}\Phi_{\ell m}\frac{dT_0}{dr} + \frac{d\Phi_{\ell m}}{dr}\frac{dT_0}{dr}\right) \\
&= -\left(\kappa_e^0\tilde{\omega}\,\tau_e + \kappa_\mu^0\tilde{\omega}\,\tau_\mu\right)\left[\frac{1}{r}\Phi_{lm}\frac{dT_0}{dr} + \frac{d\Phi_{lm}}{dr}\frac{dT_0}{dr}\right].
\end{aligned}
\tag{5.31}
$$

The expressions for $V_{\ell m}$ and $W_{\ell m}$ indicate that a toroidal field gives rise to a polar perturbation of the heat flux $\delta\boldsymbol{F}$, and likewise a polar field gives rise to a toroidal perturbation of the heat flux.

To obtain the second ODE, we begin by considering the energy conservation equation (4.3). As a reminder, the heat flux (in Newtonian theory) is related to the net rate of heat energy generated per unit volume (per unit time) as

$$
\boldsymbol{\nabla}\cdot\mathbf{F} = Q, \tag{5.32}
$$

where $Q = Q_\mathrm{h} - Q_\nu$, and Q_h, Q_ν are the amounts of heat generated via DCH & SCH processes (Sec. 4.3), and heat lost via neutrino emission (Sec. 4.5) respectively. The perturbed form of the energy conservation equation is simply

$$\boldsymbol{\nabla} \cdot \delta\mathbf{F} = \delta Q. \tag{5.33}$$

Then, decomposing δQ in terms of the spherical harmonics, leads to

$$\boldsymbol{\nabla} \cdot \delta\mathbf{F} = \frac{dQ}{dT} \delta T_{\ell m} Y_{\ell m} \,. \tag{5.34}$$

For simplicity, we will assume that the nuclear heating term Q_h is independent of the temperature (and magnetic field strength). This is justified since the heat release calculated by Fantina et al. (2018) neglects thermal contributions to thermodynamic potentials and considers only ground-state transitions to compute the composition of the accreted crust[4]. The presence of the magnetic field therefore influences the net heat generated Q within the star only via the dependence of the neutrino cooling Q_ν on the temperature (via the expressions presented in Sec. 4.4). We may therefore rewrite Eq. (5.33) as

$$\boldsymbol{\nabla} \cdot \delta\mathbf{F} = -\frac{dQ_\nu}{dT} \delta T_{\ell m} Y_{\ell m} \,. \tag{5.35}$$

Taking the divergence of Eq. (5.17) is the standard result (neglecting the sum over ℓ and m)

$$\boldsymbol{\nabla} \cdot \delta\mathbf{F} = \left[\frac{dU_{\ell m}}{dr} + \frac{2}{r} U_{\ell m} - \frac{1}{r} \ell(\ell+1) V_{\ell m} \right] Y_{\ell m} \,, \tag{5.36}$$

where the final term in Eq. (5.17) has now vanished since

$$\boldsymbol{\nabla} \cdot \left(W_{lm} \mathbf{r} \times \boldsymbol{\nabla} Y_{lm} \right) = 0 \,. \tag{5.37}$$

By comparing Eq. (5.36) with the RHS of Eq. (5.35) we obtain the second ODE describing the perturbed thermal structure as

$$\frac{dU_{\ell m}}{dr} = \frac{dQ_\nu}{dT} \delta T_{\ell m} - \frac{2}{r} U_{\ell m} + \frac{1}{r} \ell(\ell+1) V_{\ell m}. \tag{5.38}$$

We now have a set of four equations (5.29), (5.30), (5.31) and (5.38) in the four unknowns $\delta T_{\ell m}$, $V_{\ell m}$, $W_{\ell m}$, and $U_{\ell m}$, with the magnetic stream functions ($\Phi_{\ell m}$ and $\Psi_{\ell m}$, assumed known; Sec.

---

[4] For highly magnetised stars ($B \gtrsim 10^{13}$ G) however, significant amounts of so-called *Joule heating* can arise due to dissipation of the magnetic field in the solid crust (e.g. Miralles et al., 1998). Though, as we shall see, our perturbation equations are only valid for magnetic field strengths $B \lesssim 10^{12} - 10^{13}$, in which case the heating rate due to dissipation of the magnetic field is negligible compared to that of the heating rate due to DCH reactions.

5.3) playing the role of source terms. Note, however, that Eq. (5.31) (giving $W_{\ell m}$ in terms of $\Phi_{\ell m}$) decouples from the other three equations. Physically, we can say that the poloidal part of the magnetic field $\Phi_{\ell m}$ induces a *purely toroidal* perturbation in the heat flux $W_{\ell m}$, and therefore produces no perturbation in the temperature (i.e. does not couple to $\delta T_{\ell m}$). Given that we are interested specifically in temperature perturbations, we will *not* consider poloidal magnetic fields in the following analysis, *only toroidal ones*. This leaves us with Eqs (5.29), (5.30) and (5.38) in the three unknowns $\delta T_{\ell m}$, $V_{\ell m}$, and $U_{\ell m}$. Such a result stands in contrast to the mass quadrupole more normally associated with magnetic NSs built directly from magnetic stresses (via Lorentz forces - i.e. the magnetic mountain; Sec. 1.3.3.1), whereby it is both the toroidal *as well as* the poloidal component of the magnetic field that can generate the mountain (Sec. 1.3.3.1).

A rigidly and steadily rotating triaxial star will emit mainly quadrupolar gravitational radiation. If we set the spin axis to be along Oz, this corresponds to emission via only the $\ell = m = 2$ mass quadrupole moment, generating GWs at twice the spin frequency (Sec. 3.1.2). The corresponding temperature perturbation that sources this (via the 'wavy capture layers'; Sec. 3.2.2.1) will also be $\ell = m = 2$, as described in Ushomirsky et al. (2000).

5.3 The internal magnetic field

To solve the thermal perturbation equations, we first need to specify the form of the internal magnetic field. Despite compelling evidence for a dipolar configuration of the external magnetic field around NSs, the internal field structure remains largely unknown. As such, we have (within reason) relative freedom in prescribing the internal field. We have shown that for small magnetic fields (such that $\omega_B \tau_\mathrm{x} \ll 1$), the poloidal component of an internal magnetic field is inconsequential in building our thermal mountain, and therefore consider a *purely toroidal* magnetic field.

We are also interested only in the component of this toroidal magnetic field that gives rise to quadrupolar gravitational-wave radiation, and therefore again specialise to the $l = m = 2$ spherical harmonic. From our definition of the toroidal component of the magnetic field (Eq. (5.19)), we write down the functional form of the toroidal field as[5]

$$\begin{aligned} \boldsymbol{B}_{\mathrm{tor}} &= -\mathbf{r}\times\boldsymbol{\nabla}\left[\Psi(r)\, Y_{22}(\theta,\phi)\right] \\ &= -\frac{1}{2}\sqrt{\frac{15}{2\pi}}\,\Psi(r)\,\left[\sin\theta\,\sin 2\phi\,\boldsymbol{e}_\theta + \sin\theta\cos\theta\cos 2\phi\,\boldsymbol{e}_\phi\right]. \end{aligned} \tag{5.39}$$

---

[5] We find that the magnitude of Eq. (5.39) is a factor two larger than given in Eq. (34) of OJ20, as well as a sign discrepancy in the final term containing $\boldsymbol{e}_\phi$.

The magnitude of $\boldsymbol{B}_{\rm tor}$ is a function of position. We follow OJ20 and parameterise our magnetic field configurations in terms of the *maximum* value of $|\mathbf{B}_{\rm tor}|$ within the star. This will occur at the point where $\Psi(r)$ attains its maximum value, along the line $\theta = \pi/2$, $\phi = \pi/4$.

For any value of the magnetic stream function $\Psi_{22}(r)$, we define the form of the toroidal magnetic field on the domain

$$\boldsymbol{B}_{\rm tor} = \begin{cases} 0 & \text{if } r \leq R_{\rm B,\,min} \\ \text{Eq. (5.39)} & \text{if } R_{\rm B,\,min} < r < R_{\rm B,\,max} \\ 0 & \text{if } r \geq R_{\rm B,\,max}\,, \end{cases} \tag{5.40}$$

such that the magnetic field vanishes outside of the region of the star defined by the inner and outer radii $R_{\rm B,\,min}$ and $R_{\rm B,\,max}$, respectively. We make a distinction between this region of the star that the magnetic field permeates and the computational domain of the background and perturbed calculation ($R_{\rm IB}$ and $R_{\rm OB}$), since the two are not necessarily one and the same (and is something that will be explored in Sec. 5.5).

In modelling the thermal profile of the whole star, we seek to allow for the possibility of the magnetic field to permeate the core (unlike OJ20 who confined the magnetic field to just the crust), with the expectation that non-vanishing temperature perturbations at the crust-core transition lead to greater asymmetries in the deep crust. One potential caveat to this procedure, however, is the feasibility of having a magnetic field in the core of a NS that is almost certainly superconducting over some density range (recall Fig. 4.11). Minimum energy considerations of superconducting matter implies any magnetic flux within the medium should be expelled due to the Meissner–Ochsenfeld effect (e.g. Khan, 2003).

This, however, is not the whole story. In the seminal description of the properties of a proton superconductor in NS matter by Baym et al. (1969), it was argued that the conductivity of regular conducting matter is sufficiently large that the characteristic timescale for the expulsion of magnetic flux is comparable with that of the age of the Universe. In a more recent analysis of this phenomenon by Ho et al. (2017), the authors suggest that actually the magnetic field may persist in the bulk of the core for at least $\gtrsim 10^7$ years after the star's birth, as a result of disparities in the cooling timescale and the associated diffusion timescale of magnetic field itself. One caveat to this, however, is that NS-LMXBs are expected to be much older than this, at $\sim 10^9$ yr. Despite this, Ho et al. (2017) also estimated that even after 10^7 years, the field is likely only expelled from the innermost ≤ 100 m of the core (assuming a 10^{11} G field). It is therefore possible that the field may not have been completely expelled from the core, even after 10^9 years.

To this end, we consider two functional forms for the magnetic stream function $\Psi(r)$. In the first instance, we take the form of the toroidal field to be

$$\Psi(r) = C[(r - R_{\rm B,\,min})(r - R_{\rm B,\,max})]^2\,, \tag{5.41}$$

where C is a constant, such that the magnetic field vanishes outside of the region defined in Eq. (5.40), and is a maximum at the midpoint of the domain where $r = (R_{\mathrm{B,\,max}} - R_{\mathrm{B,\,min}})/2$. This form of $\Psi(r)$ allows us to consider two possibilities, where: (i) the magnetic field permeates the entire star, extending over the full computational domain where $R_{\mathrm{B,\,min}} = R_{\mathrm{IB}}$ and $R_{\mathrm{B,\,max}} = R_{\mathrm{OB}}$, or (ii), the magnetic field is confined to only the *crust* of the star, such that $R_{\mathrm{B,\,min}} = R_{\text{crust-core}}$ and $R_{\mathrm{B,\,max}} = R_{\mathrm{OB}}$, where $R_{\mathrm{crust-core}}$ is the radial location of the crust-core interface obtained from our TOV solution (Tab. 2.6). The second case is equivalent to the form of the toroidal field used by OJ20, following the prescription of one particular field configuration originally considered by Pons and Geppert (2007) (*cf.* their Eq. (35)).

The second functional form for the magnetic stream function we consider is derived from Eq. (12) of Aguilera et al. (2008), which we have modified to be

$$\Psi(r) = \Psi_0\, x \left(1 - x\right)^2 \left(x - \frac{R_{\mathrm{B,\,min}}}{R_{\mathrm{B,\,max}}}\right)^{65}, \tag{5.42}$$

where $x = r/R_{\mathrm{B,\,max}}$ with $R_{\mathrm{B,\,min}} = R_{\mathrm{IB}}$ and $R_{\mathrm{B,max}} = R_{\mathrm{OB}}$ and Ψ_0 is a constant chosen such that magnetic field has a maximum value $B = 10^9$ G. The value of the exponent in Eq. (5.42) was chosen (somewhat) arbitrarily, in order to capture the possibility of a magnetic field that extends beyond the crust-core transition, but drops rapidly before reaching the centre of the star. This choice will allow us to explore whether non-vanishing temperature perturbations at the crust-core transition lead to greater asymmetries in the deep crust, whilst still remaining consistent with the results of Ho et al. (2017) that the magnetic field is expelled from the innermost region of the star due to proton superconductivity, but not from the core entirely.

In Fig. 5.1 we plot the magnitude of the internal toroidal magnetic field as a function of the density for the LM BSk20 model in Table 4.3, for the three different configurations of $\Psi(r)$ discussed above. The prescription of our magnetic field requires that the field vanishes outside of the region defined by $R_{\mathrm{B,\,min}}$ and $R_{\mathrm{B,\,max}}$ (Eq. (5.40)). The red and blue lines denote the functional form of the magnetic field as described by Eq. (5.41) when $R_{\mathrm{B,min}}$ is set to R_{IB} and $R_{\mathrm{crust-core}}$ respectively, whilst the green line denotes the functional form of the magnetic field as described by Eq. (5.42). The green curve acts as an intermediary case between the two extremes whereby the field extends over the entire computational domain (the red line), and where it is confined to just the crust (the blue line).

5.3.1 Remaining in the perturbative regime

In order to treat the presence of a magnetic field as a perturbation on the heat flow, one must be in the regime whereby $\omega_B \tau(T) \ll 1$. For temperatures typical of NS-LMXBs ($T \sim 10^8 - 10^9$ K), OJ20 found this procedure is safe for internal *crustal* magnetic fields strengths $B \lesssim 10^{12}$ G. Given that we are now extending our computational domain, we need to take care to remain in the perturbative regime in the core as well as the crust.

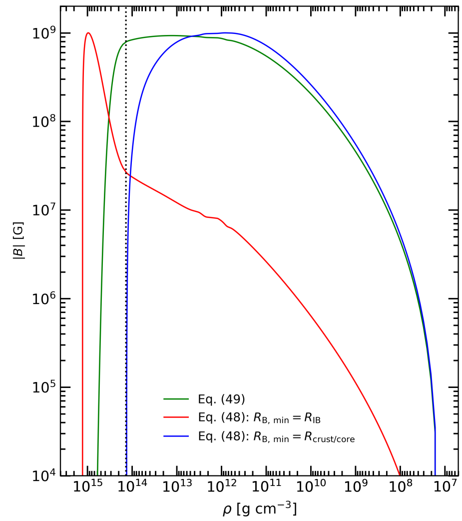

FIGURE 5.1: Magnitude of the internal toroidal magnetic field $B_{\rm tor}$ as a function of the density for three different field configurations. The blue curve shows a toroidal field that is confined to the crust only - Eq. (5.41) with $R_{\rm B,\,min} = R_{\rm crust-core}$. The red curve shows the magnitude of the toroidal field that permeates the entire star - Eq. (5.41) with $R_{\rm B,\,min} = R_{\rm IB}$. The green curve shows a toroidal magnetic field that penetrates only the outer core of the neutron star - Eq. (5.42). All are normalised to have the same maximum strength $B = 10^9$ G. The vertical dotted line indicates the location of the crust-core transition of the BSk20 equation of state (Table 2.6).

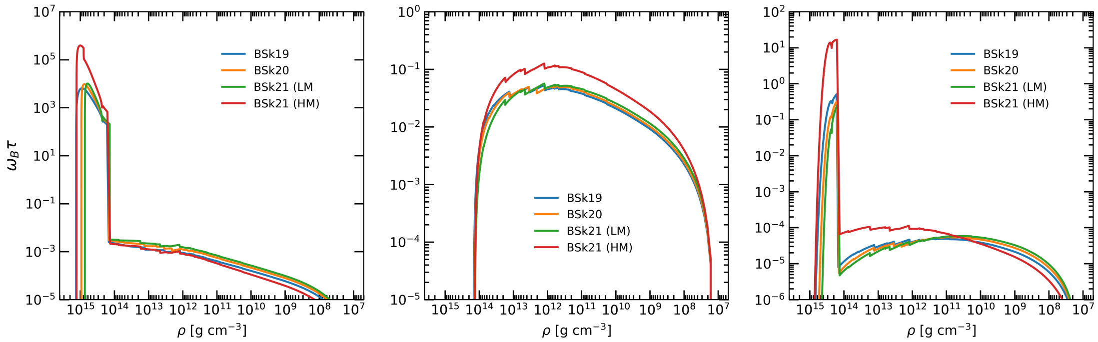

FIGURE 5.2: The Magnetization parameter $\omega_B\tau$ inside an accreting neutron star due to an internal toroidal magnetic field ($B = 10^{12}$ G) assuming each of Eq. (5.41) with $R_{\rm B,\,min} = R_{\rm IB}$ (*left*); Eq. (5.41) with $R_{\rm B,\,min} = R_{\rm crust-core}$ (*centre*); and Eq. (5.42) (*right*). Here $Q_{\rm imp} = 1.0$, $Q_{\rm S} = 1.5$ MeV and $\dot{M} = 0.05\dot{M}_{\rm Edd}$.

The thermal conductivity (which is proportional to τ; Eq. (4.10)) is a few orders of magnitude larger in the core than in the crust (Compare Figs 4.4 and 4.5). Before calculating the perturbed thermal structure, we therefore plot in Fig. 5.2 the magnetisation parameter $\omega_B\tau$ for each of the three different magnetic field configurations discussed in the previous section, for the four different BSk19-21 EoS models listed in Table 4.3.

We choose the maximum value of the magnetic field to be $B = 10^{12}$ G in all cases in order to compare with OJ20. For the case where the magnetic field extends over the entire star (the left panel of Fig. 5.2, assuming the red curve in Fig. 5.1) the magnitude of the magnetisation parameter in the *core* is clearly in the regime $\omega_B\tau(T) \gg 1$, far exceeding the condition in which our perturbation equations are valid. Notably, $\omega_B\tau(T)$ is greatest in the HM BSk21 model (where Durca processes are permitted), being an order of magnitude larger than any of the LM models. This is a result of the squared-temperature dependence of the scattering frequency ν in the core ($\tau \propto 1/\nu \propto 1/T^2$; Sections 4.4.2.1 and 4.4.2.2) and the enhanced cooling associated with Durca processes. The right panel of Fig. 5.2 (with B described by the green curve in Fig. 5.1) tells a similar story, where $\omega_B\tau \gg 1$ when Durca is active.

We shall therefore omit the HM BSk21 result from our subsequent calculations involving a *core* magnetic field. Additionally, in order to remain perturbative and recover the condition whereby $\omega_B\tau \ll 1$ *everywhere* in the star, we restrict ourselves to magnetic field strengths $B \sim 10^8$ G when using Eq. (5.41) (when $R_{\mathrm{B,min}} = R_{\mathrm{IB}}$), and $B \sim 10^9$ G when using Eq. (5.42). These choices remain reasonable assumptions, given inferences of the external magnetic field strength are $10^8 - 10^9$ G for LMXBs.

Note however that when the magnetic field is confined to just the crust, (the middle panel in Fig 5.2), we remain perturbative even when the magnetic field is assumed to be 10^{12} G, in agreement with OJ20. The largest magnetic field strengths we shall consider as ‘safe’ for the crust-only configuration are $B \sim 10^{12}$ G when Durca is active, and $B \sim 10^{13}$ G when Durca is forbidden.

These maximum values of the magnetic field to be considered ‘safe’ in our calculations should be regarded as approximations, since the exact value of the magnetisation parameter within the star depends not just on the assumed magnetic field strength, but also on the interior temperature profile (since $\tau \propto 1/T^2$; Sec. 4.4.2.1) which is a property of the background calculation. The results for $\omega_B\tau(T)$ shown in Fig. 5.2 are specific to the choice $Q_{\mathrm{imp}} = 1.0$, $Q_{\mathrm{S}} = 1.5$ MeV and $\dot{M} = 0.05\dot{M}_{\mathrm{Edd}}$ in the non-magnetised thermal background. The exact maximum allowed value of B for any given thermal background will therefore vary slightly if one changes any of these quantities. This fact is accounted for in all subsequent calculations, and those few results we present that are out of the perturbative regime will be appropriately highlighted, such that any conclusions drawn from these results may be treated with correspondingly appropriate discretion. In Section 5.5, for example, we shall briefly consider results outside of the perturbative regime in order to discuss a potential proof-of-concept method to place upper limits on the strength of the magnetic field in the NS interior, which currently is poorly understood.

5.4 Solving the perturbation equations

5.4.1 boundary conditions and method of solution

The equations (5.29) and (5.38) (together with the algebraic expression Eq. (5.30)) are a set of coupled first-order ODEs which describe the perturbed thermal structure of accreting neutron stars with an interior magnetic field. They are to be solved numerically using a set of (inner and outer) boundary conditions. In their analysis, OJ20 adopted the boundary conditions derived by UCB, who also modelled just the crust of the star. The temperature perturbation at both the inner and outer boundaries (the crust-core interface and the base of the ocean respectively) were set to be zero, i.e. $\delta T_{\text{IB}} = \delta T_{\text{OB}} = 0$. UCB argued that this is a good approximation if the thermal conductivity is significantly higher in both the ocean and the core of the star.

Indeed, the core thermal conductivity *is* a few orders of magnitude greater than in the crust (compare Figs 4.4 and 4.17). However, consider our source term (the first term in Eq. (5.30)),

$$\begin{aligned} S &\equiv \tilde{\omega}\,\frac{dT}{dr}\,\Psi_{\ell m}\,\sum_{\text{x}}\kappa_{\text{x}}\,\tau_{\text{x}} \\ &= -\tilde{\omega}\,\frac{F}{\kappa}\,\Psi_{\ell m}\,\kappa\,\tau \\ &= -\tilde{\omega}\,F\,\Psi_{\ell m}\,\tau\,. \end{aligned} \tag{5.43}$$

If one writes the radial temperature gradient as $dT/dr = -F/\kappa$ (through Eq. (4.4)), then it can be seen that the source term is independent of the thermal conductivity - instead depending on the strength of the toroidal magnetic field $\Psi_{\ell m}$. The magnetic field can therefore provide a non-zero temperature perturbation in the core even if the thermal conductivity there is very large. This possibility was not explored in OJ20, and thus the extension of the computational domain into the core allows us to explore the possibility of a core magnetic field's influence on the magnitude of the temperature perturbation in the deep crust, with the condition $\delta T_{\text{IB}} = 0$ removed.

In extending the computational domain of the calculation, we instead obtain our inner boundary condition by means of a regularity condition at the centre of the star (so as to avoid a singularity at $r = 0$ in spherical coodinates). We expand all variables in Eqs. (5.29), (5.30) and (5.38) via Taylor series near the origin to obtain an approximate solution at small radii. To leading order in r, the temperature perturbation δT and the radial flux perturbation U depend on the second radial derivative of δT (evaluated at the centre of the star) as

$$U_{IB} \approx -\,\kappa(\rho_c, T_{\text{cent}})\,\delta T''_{\text{cent}}\,r_{IB}\,, \tag{5.44}$$

$$\delta T_{IB} \approx \frac{1}{2}\,\delta T''_{\text{cent}}\,r_{IB}^2\,. \tag{5.45}$$

The inner boundary condition is then found by obtaining a solution for the second radial derivative $\delta T''$ that satisfies the outer boundary condition, which we shall now discuss.

Contrary to the situation in the core, and the claim made by UCB, both Fig. 5 of Potekhin et al. (1999) and Fig. 3 of Chugunov and Haensel (2007) suggest that the thermal conductivity in the ocean is actually lower than that of the crust (as well as the core). This naturally leads one to question the legitimacy of the $\delta T_{\text{OB}} = 0$ boundary condition at the top of the crust, as clearly the ocean cannot be assumed to be perfectly conducting if the conductivity is low there.

However, consider again the outer boundary condition in our unperturbed thermal background (Eq. (4.125)). The temperature at the base of the ocean is determined solely by the accretion rate, which we assume to be spherically symmetric. Therefore, if we assume there is no perturbation in the local accretion rate at the base of the ocean when we introduce the magnetic field, then there can be no perturbation in the temperature at the base of the ocean as well. In this case, this allows us to recover the $\delta T_{\mathrm{OB}} = 0$ boundary condition even if the ocean is not acting as a perfect conductor.

It is possible that a more accurate outer boundary condition for δT could be derived by matching the crustal thermal calculation to a flux-temperature relation in the ocean (Ushomirsky et al., 2000). In this case, the thermal profile would be then determined by not just the fraction of heat that is conducted up through the crust from the DCH/SCH processes, but also by the amount heat that is released due to compression of accreted material as it arrives at the NS surface (Bildsten and Cutler, 1995; Brown and Bildsten, 1998).

Rather than attempting such a large expansion of our computations, we have instead examined two other possible choices, in addition to the $\delta T_{\ell m} = 0$ condition motivated above. We wish to test to what extent the value of the temperature perturbation in the deep crust, where most of the quadrupole is generated (Ushomirsky et al., 2000), is sensitive to which outer boundary condition we use.

Specifically, we consider the following three outer boundary conditions:

- i) keeping the same $\delta T_{\mathrm{OB}} = 0$ as did OJ20 (and UCB),
- ii) assume a perfectly insulating condition for the perturbed heat flux: $U_{\mathrm{OB}} = 0$,
- iii) assume perfect blackbody emission from the surface, making use of the Stefan-Boltzmann Law.

In the latter case, the perturbed flux would simply be

$$U_{\mathrm{OB}} = 4\sigma T^3 \delta T_{\mathrm{OB}}\,. \tag{5.46}$$

It is worth bearing in mind, however, that whilst blackbody emission would be applicable to isolated NSs emitting into vacuum, it is less clearly relevant for an accreting NS, whose surface is blanketed in accreting material[6]. As we shall soon see, it turns out that the temperature perturbations in the deep crust *are* in fact insensitive to the choice of outer boundary condition (see Fig. 5.7), at least for densities $\rho \gtrsim 10^{13}$ g cm^{-3}.

---

[6] Note however that equation (5.46) would be well motivated for an accreting NS during periods of quiescence, and so may still be relevant in a time-averaged sense.

5.5 Perturbed thermal structure of accreting neutron stars

In this section we shall present results for the temperature perturbations induced by the magnetic field in terms of the fractional temperature perturbation $\delta T/T$. We do this for convenience (since it is dimensionless), in order to make a more straightforward comparison between the asymmetry and the ellipticity ε (i.e. the size of the mountain; Sec. 3.2.2). Strictly speaking however, it is the magnitude of the perturbation δT itself which is important. For example, a NS that is cold (10^7 K), or hot (10^9 K), would imply that $\delta T = 1 \times 10^5$ K and $\delta T = 1 \times 10^7$ K respectively for the same 1% fractional asymmetry. Such a result could therefore be misleading, since only the latter would lead to significantly large thermal mountains. However, for the NS models that we consider here, the temperature in the crust is mostly $T \sim 10^8$ K, varying between models only by a factor of a few, even when the efficient Durca process is permitted (see Fig. 4.19).

In Fig. 5.3 we plot $\delta T/T$ (as a percentage) of an an accreting NS with an internal toroidal magnetic field (assuming Eq. (5.41) with $R_{\mathrm{B,\,min}} = R_{\mathrm{IB}}$ - the red curve in Fig. 5.1) for the three different BSk19-21 LM models listed in Table 4.3. The Python ODE solver `solve_BVP` was again used for the integration, with the initial guess for the integration constructed by fixing the value of the temperature perturbation throughout the entire star to that of the results obtained by OJ20 ($\delta T \sim 10^3$ K). We use the same background model parameters as in Section 4.8 (i.e. $Q_{\mathrm{imp}} = 1$, $Q_{\mathrm{S}} = 1.5$ MeV) assuming three different accretion rates 10^{-10}, 10^{-9}, and 10^{-8} $M_\odot$ yr^{-1}. The internal toroidal magnetic field was set to have a magnitude $B = 10^8$ G at the midpoint of the star, extending over the full computational domain. These calculations assume the outer boundary condition $\delta T_{\mathrm{OB}} = 0$ in order to compare with both UCB and OJ20. The fractional temperature perturbation can be seen to depend strongly on the mass accretion rate $\dot{M}$, with the largest asymmetries being built in the softer BSk19 model (and correspondingly the smallest asymmetries being built from the stiffer BSk21). In the inner crust ($10^{12} < \rho < 10^{14}$ g cm^{-3}), the fractional temperature perturbations can be seen to lie in the region $\delta T/T \sim 10^{-4} - 10^{-2}$%, and is always largest at the point $r = (R_{\mathrm{B,\,max}} - R_{\mathrm{B,\,min}})/2$), corresponding to the location where the magnetic field is strongest (Fig. 5.1).

In their analysis, OJ20 found typical values of the fractional temperature perturbation $\delta T/T$ to be a few times 10^{-5} % in the deep crust ($\rho \sim 10^{13}$ g cm^{-3}) with a $B = 10^9$ G *crustal* magnetic field, irrespective of the accretion rate[7]. Under this new analysis, we have modelled the crust and core of the star, allowing for the possibility of the magnetic field to permeate the whole star. In doing so, we have obtained values for the fractional temperature perturbation that are up to ~ 2 orders of magnitude greater in the deep crust than the estimates obtained by OJ20, even when the magnetic field is assumed to be an order of magnitude smaller.

Clearly, this is a substantial increase in the level of temperature asymmetry in the crust. To reconcile these findings, in Fig. 5.4 we modify our calculation. We use the same computational domain as the previous calculation (i.e. R_{IB} and R_{OB} are unchanged) and continue to use Eq.

---

[7] OJ20 considered the same mass accretion rates as those considered here; 10^{-10}, 10^{-9}, and 10^{-8} $M_\odot$ yr^{-1}.

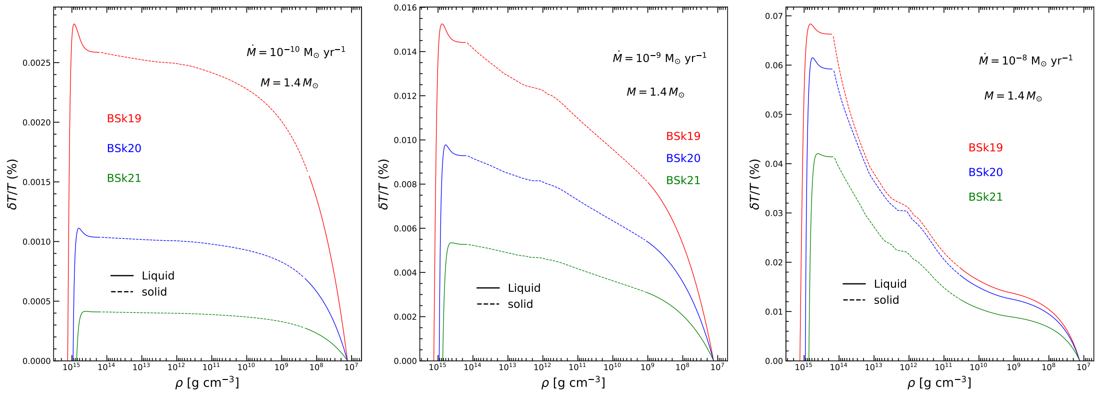

FIGURE 5.3: Magnitude of the fractional temperature perturbation $\delta T/T$ (as a percentage) inside an accreting neutron star due to a $B = 10^8$ G magnetic field - Eq. (5.41) with $R_{\rm B,\,min} = R_{\rm IB}$; Fig. 5.1. Here $Q_{\rm imp} = 1.0$, $Q_{\rm S} = 1.5$ MeV and $\dot{M} = 0.05$ are assumed, with time-averaged mass accretion rates $10^{-10} M_\odot$ yr^{-1} (*left*), $10^{-9} M_\odot$ yr^{-1} (*centre*), and $10^{-8} M_\odot$ yr^{-1} (*right*), as indicated in the panels.

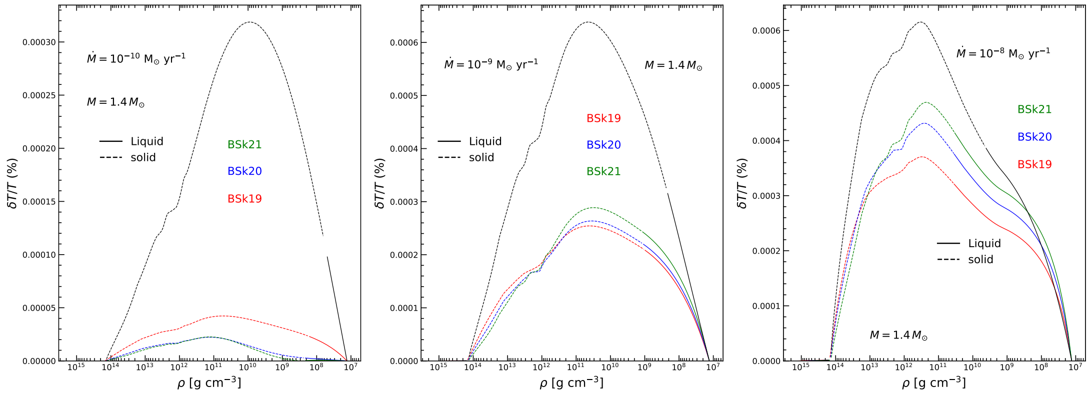

FIGURE 5.4: As for Fig. 5.3, but for a $B = 10^9$ G *crustal* magnetic field - Eq. (5.41) with $R_{\rm B,\,min} = R_{\rm crust-core}$; Fig. 5.1.

(5.41) for the functional form of B, but now confine the magnetic field to *only the crust* of the star. In this case, we have $R_{\rm B,min} = R_{\rm crust-core}$ and $R_{\rm B,max} = R_{\rm OB}$ (i.e. the blue curve in Fig. 5.1). The internal toroidal magnetic field was chosen to have a maximum magnitude this time at $B = 10^9$ G, consistent with the original calculation performed by OJ20. Additionally, since this calculation explores perturbations in only the crust, we also include the results for the HM BSk21 model, since $\omega_B \tau(T) = 0$ in the core (and therefore there is no source term) when the field is removed there.

Confining the magnetic field to the crust has a significant impact on both the magnitude of the temperature perturbation, as well as its distribution (as compared with Fig. 5.3). The shape of the curves in Fig. 5.4 match the results obtained by OJ20 markedly well (*cf.* their Fig. 4, reproduced for convenience in Fig. 5.5), also peaking at around $\rho \sim 10^{10}$ g cm^{-3}. Most interestingly, we see that the magnitude of the fractional temperature perturbation $\delta T/T$ is reduced to $\sim 10^{-4}\%$ when the core magnetic field is removed, and therefore also similar in magnitude to the results obtained by OJ20.

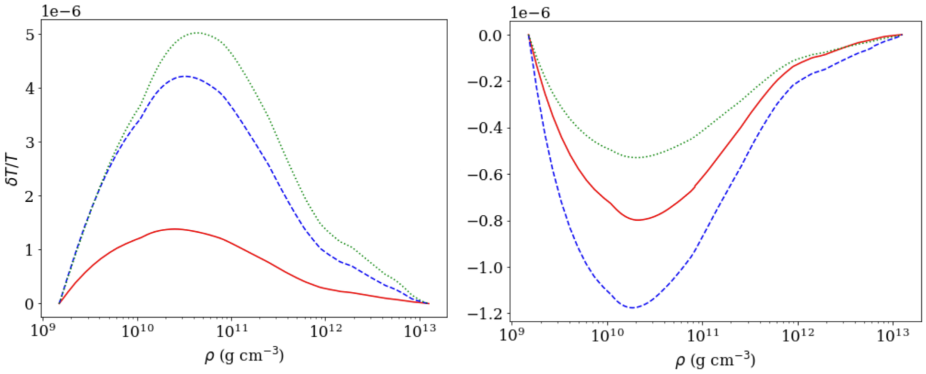

FIGURE 5.5: Perturbed thermal structure of a neutron crust with a weak crustal magnetic field obtained by Osborne and Jones (2020). Left: Fractional temperature perturbation $\delta T/T$ as a function of the density, for a neutron star with a non-superfluid core, a magnetic field strength $B = 10^9$ G, an impurity parameter $Q_{\rm imp} = 1$, and for the accretion rates of 10^{-8} $M_\odot$ yr^{-1} (green, dotted), 10^{-9} $M_\odot$ yr^{-1} (blue, dashed), and 10^{-8} $M_\odot$ yr^{-10} (red, solid). Right: same, but for a star with a superfluid core (recall Sec. 4.9). Reproduced from Figure 3 of Osborne and Jones (2020).

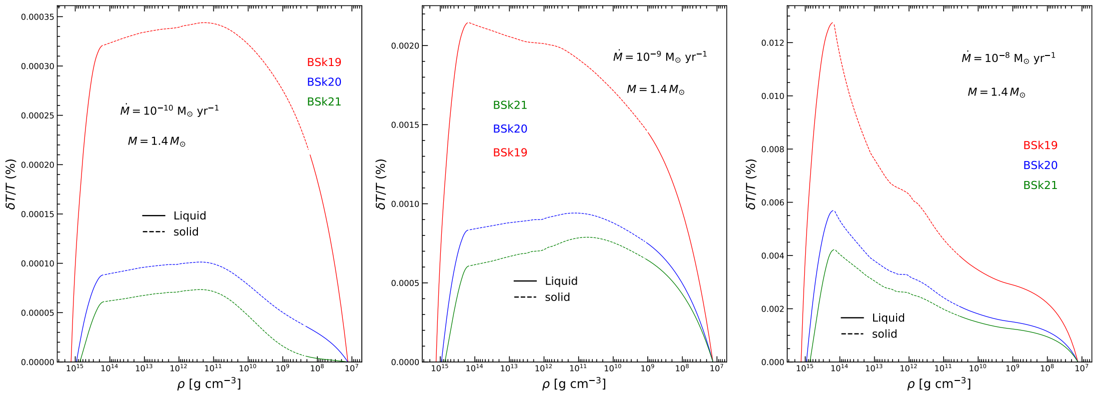

FIGURE 5.6: As for Fig. 5.3, but for a $B = 10^9$ G magnetic field that penetrates the outer core - Eq. (5.42).

To better understand this behavior, we refer back to Fig. 5.1. When the inner boundary of the internal field is set to be at the crust-core interface, the field does not penetrate the core of the star and the quartic nature of the field (see Eq. (5.41)) forces it to drop off by many orders of magnitude over very narrow density ranges in both the deep crust ($R_{\rm B,\,min}$) and the top of the crust ($R_{\rm B,\,max}$) - see the blue curve in Fig. 5.1. However, when the magnetic field *is* allowed to penetrate the core of the star, the gradient of the magnetic field strength varies much more slowly in the crust, particularly in the inner crust near the core/crust transition. Therefore, in the 'crust-only' scenario, it is likely the case that the sharp decline of the magnetic field strength over a narrow density region suppresses the perturbations, since the source term Eq. (5.43) (which is proportional to $\Psi_{\ell m}$) at each end of the integration is forced to become vanishingly small very quickly.

The last case we need consider is the intermediate one, where the magnetic field only partially penetrates into the core, as described by Eq. (5.42) (the green curve in Fig. 5.1). We give our

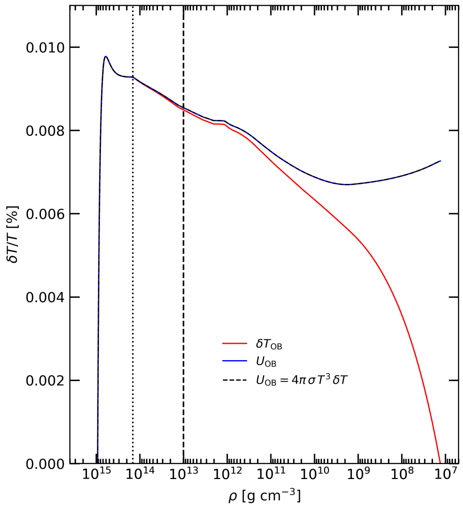

FIGURE 5.7: Magnitude of the fractional temperature perturbation $\delta T/T$ inside an accreting neutron star for the low-mass BSk20 model in Table 4.3, assuming each of the three different outer boundary conditions indicated near the curves. In all cases a $B = 10^8$ G core magnetic field is assumed - Eq. (5.41) with $R_{\rm B,\,min} = R_{\rm IB}$; Fig. 5.1. The black-dashed and blue curves are close in magnitude, and therefore lie almost on top of one another. The vertical dotted line is the location of the crust-core transition. The vertical dashed line indicates the fiducial density $\rho = 10^{13}$ g cm^{-3} deep in the inner crust. Here $Q_{\rm imp} = 1$, $Q_{\rm S} = 1.5$ MeV and $\dot{M} = 0.05\dot{M}_{\rm Edd}$.

results in Fig. 5.6, for the three LM models of Table 4.3. As one might perhaps expect, being the intermediary case between Figs. 5.3 and 5.4, the fractional temperature asymmetry $\delta T/T$ in this case is larger than when the field is confined the crust, but smaller than when the field is allowed to extend over the entire star.

As was discussed in Section 5.4.1, in addition to our $\delta T_{\rm OB} = 0$ outer boundary condition, we also consider two others, corresponding to zero flux $U_{\rm OB} = 0$ at the surface, and to the emission of blackbody radiation (Eq. (5.46)). We do this in order to gauge the sensitivity of δT in the inner crust to that of the choice of outer boundary condition.

The results are shown in Fig. 5.7. For the cases of zero surface flux and blackbody radiation (the blue and black-dashed curves respectively), we find that the magnitude of the temperature perturbations are very similar to each other over the entire computational domain (never differing by more than $\sim 0.1\%$). However, we see that allowing for a non-zero $\delta T_{\rm OB}$ causes δT to diverge quickly from the $\delta T_{\rm OB} = 0$ result at densities $\rho < 10^{12}$ g cm^{-3} as one approaches the base of the ocean. At densities $\rho > 10^{13}$ g cm^{-3}, though, the temperature perturbation is largely insensitive to the outer boundary condition, with all three outer boundary prescriptions giving essentially the same result. We will therefore continue to present results only for our preferred boundary condition of $\delta T_{\rm OB} = 0$, noting that other choices would have little impact on the temperature perturbation in the regions of the crust of importance for mountain building. We do stress, however, that this applies strictly to temperature perturbations. Other quantities could be affected by one's choice of boundary conditions. The surface flux emanating from the crust (which is potentially observable; Ushomirsky et al., 2000), for example, would be intimately tied to the outer boundary condition.

Additionally, an important aspect of the analysis done by OJ20 was to consider the effect of varying different properties of the background on the level of temperature asymmetry in the crust (*cf.* their Figs. 6 and 7). The thermal structure is a function of the many different components that enter the heat equation, some of which are properties of the EoS (e.g. the superfluid/superconducting critical temperatures), or constrained experimentally via observation (e.g. the shallow heating).

In Figs. 4.19 - 4.20 (and Figs. 5.3 - 5.6), we assumed values of the shallow heating and impurity parameter to be 1.5 MeV and 1.0 respectively, in line with the respective average values of these parameters from observational estimates. However, to determine how sensitive our results are to these quantities, we show in Fig. 5.8 how the temperature asymmetry $\delta T/T$ can vary with different values of $Q_{\rm imp}$ and $Q_{\rm S}$ respectively (recall Fig. 4.21 from Sec. 4.8).

The effects of altering these quantities are modest, but still noteworthy. When we vary the impurity parameter, much like the background temperature profile we find that the temperature perturbations are relatively insensitive to $Q_{\rm imp}$ when $Q_{\rm imp} \lesssim 1$, but are reduced noticeably when $Q_{\rm imp} = 100$. We interpret these findings in the following way, again considering the source term (5.43). Firstly, a larger $Q_{\rm imp}$ in the crust leads to steeper temperature gradients, as a larger thermal gradient is required to support the heat flux through the crust when the conductivity is reduced ($\kappa_{\rm eQ} \propto 1/Q_{\rm imp}$; see Eq. 4.10 and Fig. 4.21). But, when the conductivity is dominated by electron-impurity scattering ($Q_{\rm imp} \gg 1$), our source term is

$$S \propto \kappa \tau \frac{dT}{dr} \sim \tau^2 \frac{dT}{dr} \sim \frac{1}{Q_{\rm imp}^2} \frac{dT}{dr}, \tag{5.47}$$

since $\kappa \propto \tau$. Therefore, although steeper temperature gradients act to increase the strength of the source term, the inverse-squared dependence of S on the value of $Q_{\rm imp}$ means the source term (and therefore the magnitude of the perturbations) is in fact made smaller when electron-impurity scattering is the dominant scattering mechanism in the accreted crust.

For the shallow crustal heating term, the behavior of the temperature perturbations is more straightforward. As the amount of shallow heating is increased, so too is the magnitude of the perturbations in the inner crust. This is because of the source term's dependence on the radial temperature gradient, which is steeper for increased amounts of shallow heating (see Fig. 4.21).

Different LMXBs are observed to accrete at different (time-averaged) rates (see e.g. Table 2 of Galloway et al., 2017). A larger accretion rate naturally leads to a greater amount of heat being deposited into the inner crust (see Eq. (4.9)), resulting in a hotter crust with steeper temperature gradients, and therefore larger temperature perturbations (note the behavior of $\delta T/T$ with $\dot{M}$ in Figs 5.3, 5.4, and 5.6). In addition, as well as accreting at different rates, the masses of the NSs themselves also likely varies from system to system as well. As we have shown in Fig. 5.4, the mass of the star can be important when it comes to generating temperature perturbations, if the heavier star is able to support Durca processes.

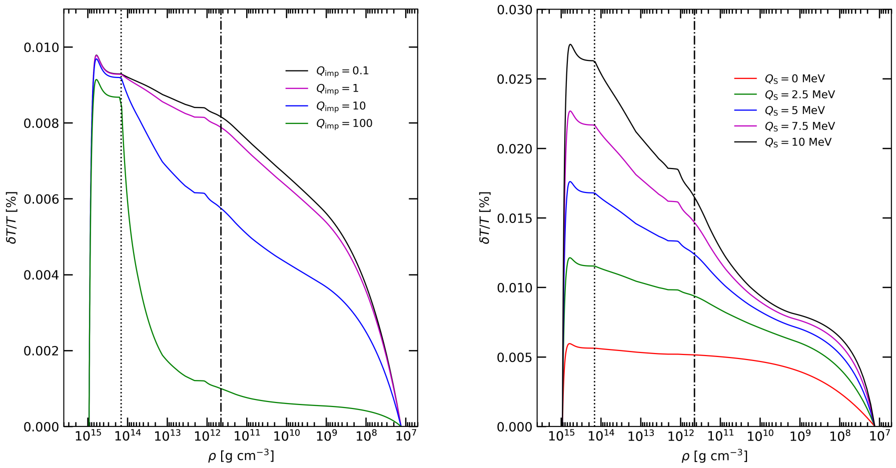

FIGURE 5.8: Magnitude of the fractional temperature perturbation $\delta T/T$ (as a percentage) inside an accreting neutron star for different values of the impurity parameter $Q_{\rm imp}$ (*left panel*) and shallow heating parameter $Q_{\rm S}$ (*right panel*). In all cases a $B = 10^8$ G core magnetic field is assumed - Eq. (5.41) with $R_{\rm B,\,min} = R_{\rm IB}$; Fig. 5.1. The vertical dotted line indicates the location of the crust-core transition, whilst the dash-dotted line is the location of neutron drip. Here $Q_{\rm S} = 1.5$ MeV and $\dot{M} = 0.05\dot{M}_{\rm Edd}$.

To explore this issue, and model a large range of different possible LMXB systems, Figs. 5.9 - 5.11 show the level of temperature asymmetry induced by the three different magnetic field configurations in Fig. 5.1 in the inner crust ($\delta T/T$ quoted at $\rho = 10^{13}$ g cm^{-3}) for a number of different NSs accreting in the interval $10^{-10} - 10^{-8}$ $M_\odot$ yr^{-1}, with varying masses. We present the results of these calculations as contour plots, with the magnitude of the temperature perturbation in the inner crust for a particular EoS/accretion rate/stellar mass combination being represented by colourbars. For the magnetic field configurations that extend into the core (the red and green curves in Fig. 5.1), we are limited to NS masses whereby Durca is prohibited, so as to not enter the regime whereby $\omega_B \tau \gg 1$ (recall the discussion from Sec. 5.3.1). Conversely, for the crust-only field, we consider masses varying between 1.4 M$_\odot$ and just below the TOV maximum of the particular BSk19-21 EoS model used (these being 1.86, 2.14, and 2.26 $M_\odot$ respectively; Section 2.6.4). As previously outlined, the maximum magnetic field strengths we consider in Fig. 5.9 is $B = 10^8$ G, and in Figs. 5.10 and 5.11 we set $B = 10^9$ G, in order to remain perturbative in all of our calculations.

Reminiscent of what we saw in Figs 5.3, 5.4, and 5.6, the size of the temperature perturbations are determined largely by the accretion rate, getting larger as $\dot{M}$ increases, but does also have a slight dependence on the stellar mass as well. For the softer BSk19 EoS, a less-massive NS leads to a greater magnitude of $\delta T/T$ for the two magnetic field configurations described by Eq. (5.41), whilst a more massive NS leads to greater temperature perturbations for the magnetic field configuration described by Eq. (5.42). For the stiffer BSK20 model, there appears to be no clear trend for how the mass affects the size of the perturbations, with each field configuration having different masses that lead to their respective largest perturbations.

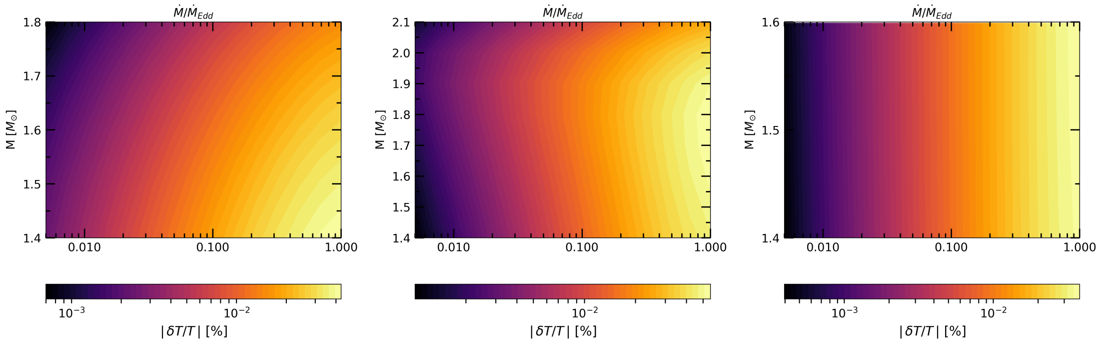

FIGURE 5.9: Magnitude of the fractional temperature perturbation $\delta T/T$ (as a percentage) as a function of both the accretion rate $\dot{M}$ and stellar mass M for the BSk19 (*left*), BSk20 (*centre*), and BSk21 (*right*) equations of state. All perturbations are quoted at the fiducial density 10^{13} g cm^{-3}, assuming a $B = 10^8$ G core magnetic field as described by Eq. (5.41) with $R_{\rm B,\,min} = R_{\rm IB}$. Here we set the impurity parameter $Q_{\rm imp} = 1$ and shallow heating term $Q_{\rm S} = 1.5$ MeV for all models.

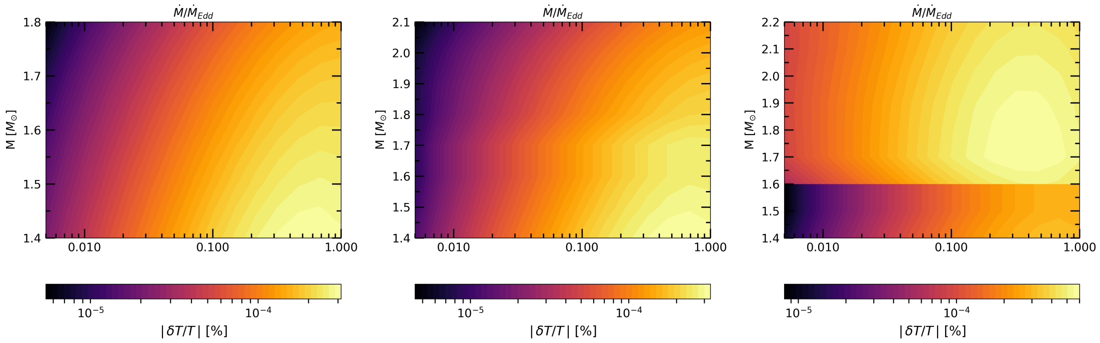

FIGURE 5.10: Same as Fig. 5.9, but instead assuming a $B = 10^9$ G crustal magnetic field described by Eq. (5.41) with $R_{\rm B,\,min} = R_{\rm crust-core}$.

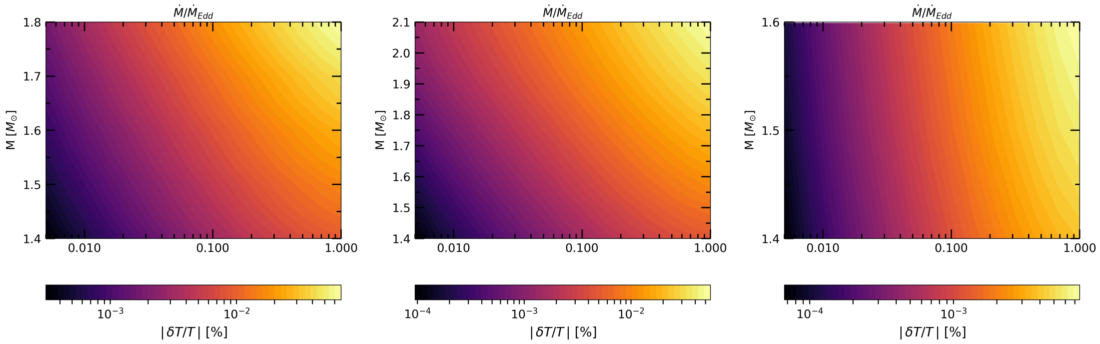

FIGURE 5.11: Same as Figs. 5.9 and 5.10, this time assuming a $B = 10^9$ G partially decayed magnetic field as described by Eq. (5.42).

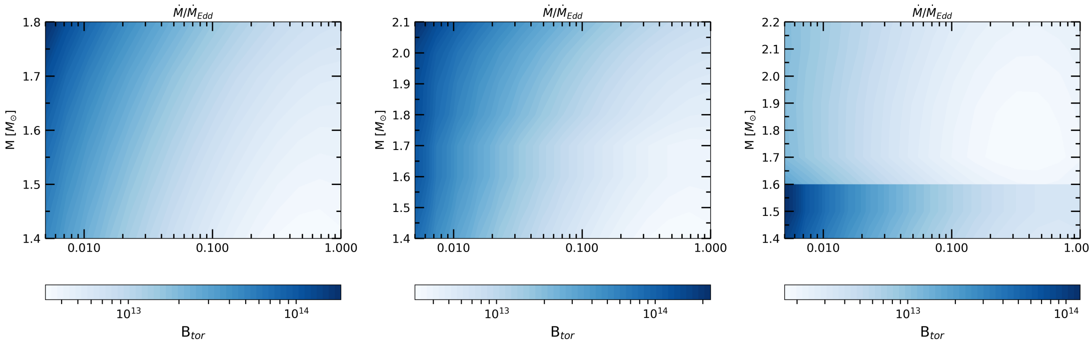

FIGURE 5.12: Magnitude of the *crustal* magnetic field strength - as described by Eq. (5.41), with $R_{\mathrm{B,\,min}} = R_{\mathrm{crust-core}}$ - required to achieve $\delta T/T \sim 1\%$ for each of the temperature perturbations considered in Fig. 5.10. Due to the requirement $\omega_B\tau \ll 1$, we only consider results whereby $B \leq 10^{13}$ G to be trustworthy (see Fig. 5.2).

Interestingly, for the stiffest BSk21 model, a darker band for masses $< 1.6\,M_\odot$ is clearly visible for the case whereby the magnetic field is confined to the crust, with large temperature perturbations (relatively speaking) being produced even at low accretion rates when $M > 1.6\,M_\odot$. The reason for this is the onset of Durca at $1.6\,M_\odot$, leading to steeper background temperature gradients in the accreted crust. The outer boundary temperature is fixed by the accretion rate (see Eq. (4.125)) and therefore the same for a given accretion rate, irrespective of the mass of the star. Consequently, a HM model whereby $M > 1.6\,M_\odot$ must have a steeper temperature gradient in the crust in order to still satisfy the outer boundary condition set by the accretion rate. If one again considers the source term in our problem, Eq. (5.43), recall that it is proportional to the radial background temperature gradient (dT/dr). Increased cooling of the star via Durca processes therefore increases the magnitude of the source term, in turn producing greater temperature asymmetries as compared to when Durca is forbidden.

For each of the calculations, the corresponding values of the Coulomb Parameter Γ_{Coul} (2.9) were also tracked to ascertain the physical state of the ions in the inner crust at each accretion rate. It was found that Γ_{Coul} never fell below 300, higher than the melting value of $\Gamma_{\mathrm{m}} \approx 175$, indicating the inner crust ($\rho > 10^{13}$ g cm^{-3}) remains solid even when approaching Eddington accretion limit. This suggests that our temperature perturbations could, at least in principle, lead to some kind of elastic deformation of the crust.

It is worth clarifying however that all of the calculations in Figs. 5.9 - 5.11 were made assuming $Q_{\mathrm{S}} = 1.5$ MeV. For completeness, an additional calculation of the LM BSk20 EoS model was performed with an assumed accretion rate $\dot{M} = 0.5\dot{M}_{\mathrm{Edd}} = 10^{-8}\,M_\odot$ yr^{-1} and accompanying shallow heating $Q_{\mathrm{S}} = 10$ MeV. This represents an extreme level of plausible crustal heating in the accreted crust, and serves to examine the state of the ions in the inner crust in this state of 'maximal' heating. The Coulomb parameter at the fiducial density $\rho = 10^{13}$ g cm^{-3} in this scenario was found to be $\Gamma_{\mathrm{Coul}} = 389$, and therefore we conclude that the crust remains solid even when the crust is - within observational constraints - maximally heated.

In the analysis done by UCB, it was calculated that a fractional temperature asymmetry $\delta T/T \sim 1\%$ was required to produce a mass quadrupole ($Q_{22} \approx 10^{37-38}$ g cm^{-2}) large enough to balance accretion torques from the NS companion. It is clear from Figs. 5.9 - 5.11, however, that even if the temperature asymmetry built from the magnetic field can translate into some kind of elastic deformation, none of our NS models produce perturbations large enough to create a mountain capable of generating GW emission at the required level.

In Figs. 5.9 and 5.11 we assumed magnetic fields strengths of 10^8 and 10^9 G respectively. These choices were made since they represent the largest magnetic fields strengths where our perturbation equations remain valid, and therefore the largest possible temperature asymmetries that may be achieved within the perturbative regime. However, magnetic fields in the core are probably larger than this value, even when taking account the inferences of the external field of LMXBs. It is therefore the case that temperature asymmetries formed in the deep crust as a result of a core magnetic field are also almost certainly larger than we have calculated here, but we cannot faithfully comment on their validity. In principle, this problem could be addressed with a non-perturbative calculation of the influence of a magnetic field on the heat conduction in the star, but this is beyond the scope of what we have derived here.

In Figure 5.10 however, we assumed a *crustal* magnetic field strength of just 10^9 G. Recall again the results of Fig. 5.2 (specifically the middle panel), where we showed that in principle the magnetic field could be as as strong as $\sim 10^{13}$ G until our perturbation equations begin to break down. Since the perturbation equations are linear in B (so long as one remains in the regime $\omega_B \tau \ll 1$), it is possible to simply re-scale our results to find the strength of the magnetic field that is required to produce a temperature asymmetry of $\sim 1\%$ for a given EoS/stellar mass and accretion rate combination. The result of such a calculation is shown in Fig. 5.12, which indicates that for *strongly* accreting NSs, the minimum field strengths required to generate $\sim 1\%$ temperature asymmetries are in the region a few $\times 10^{12}$ G. Fig. 5.12 therefore suggests we require magnetic fields approx. 3 orders of magnitude larger than external inferences to produce temperature perturbations at the level that UCB estimated are required for GW torque balance to occur.

Additionally, though the results of Fig. 5.12 also indicate that 1% asymmetry may be achieved in *weakly* accreting NSs as well, the required magnetic field strengths are of the order $B > 10^{13}$ G. Such results are outside of the perturbative regime however, and so must be taken with caution. Although, such strong *crustal* magnetic fields that far exceed 10^{12} G in accreting NSs are very unlikely to begin with, and therefore do not impact the overall picture regardless.

For comparison, OJ20 found that internal field strengths $\sim 10^{13}$ G (with slight variations depending on the choice of a normal or superfluid core and the presence of some additional shallow heating) were required to produce temperature asymmetries at the percent level for their ‘crust-only’ calculation. Due to their more simplistic model of the crust however, magnetic field strengths at this level were enough to push them out of the perturbative regime.

5.6 The resulting deformations

Before moving on to Chapter 6, we shall first take a moment to sum up the results from the previous section. We have shown that for the majority of our NS models, we are unable to reach the 1% temperature asymmetry in the deep crust that was required by UCB to generate significant GW emission. In most cases, we are limited by perturbative nature of our approach, whereby the condition $\omega_B\tau(T) \ll 1$ everywhere in the star must be satisfied in order for Eqs. (5.29) and (5.38) to be valid. We found that when the magnetic field is allowed to permeate the core, the level of asymmetry in the deep crust (10^{13} g cm^{-3}) is ~ 2 orders of magnitude larger than when the field is forced to be confined to the crust (compare Figs. 5.3 and 5.4). However, since the thermal conductivity is much larger in the core than in the crust, the condition $\omega_B\tau(T) \ll 1$ is broken for magnetic fields greater than $\sim 10^8$ G (Fig. 5.2).

In reality, if the magnetic field *is* able to permeate the core of the star (recall the discussion surrounding the Meissner-Ochsenfeld effect in Section 5.3), then it is highly likely it will be greater in magnitude than the 10^8 G we are limited to here. The picture is also further complicated by the fact that the Meissner effect is a property that extends to only Type I superconductors. Paired protons in the interior may also form a Type II superconductor (Baym et al., 1969), whereby rather than be expelled, the magnetic field is expected to be confined into isolated vortices. In fact, Akgün and Wasserman (2008) have even shown that quadrupolar distortions from axisymmetric toroidal magnetic fields in Type II superconducting matter are possible. It is worth bearing in mind, though, that such deformations are not a result of the same mechanism described here, but rather adds credence to the idea that a core magnetic field may be exploited to produce mountains. To this end, a reformulation of our mechanism in a non-perturbative regime could prove worthwhile. To reiterate, our perturbative approach can achieve asymmetries of the order 10^{-2} % when the magnitude of a core magnetic field is just 10^8 G.

Given the uncertainties surrounding the feasibility of a core magnetic field however, we should also stress the results obtained from the '*crust-only*' field configuration (Figs. 5.4 and 5.10). Although the expected asymmetry from a crust-confined $B = 10^9$ G magnetic field is of the order 10^{-4}%, the results of Fig. 5.12 show that if the strength of the magnetic field can exceed slightly above 10^{12} G, then the required asymmetry of 1% may still be achieved. This is an order of magnitude smaller than was required by OJ20 to achieve the same level of asymmetry, and, crucially, is still valid even in the perturbative regime (Fig. 5.2).

With this information in mind, it is time to begin to turn our attention towards how these perturbations in the star's internal temperature profile translate into deformations of the solid crust. Recall from Chapter 3 that the size of NS mountains are usually described in terms of the ellipticity, defined as (Eq. 3.37)

$$\varepsilon = \sqrt{\frac{8\pi}{15}}\frac{Q_{22}}{I}, \tag{5.48}$$

where I is the moment of inertia (usually taken to be 10^{45} g cm^2) and Q_{22} is the mass quadrupole moment.

In Chapter 6 we shall go on to to compute Eq. (5.48) *self-consistently* by exploiting a temperature-sensitive contribution to the pressure in the star's crust. However, as a first step towards this calculation, we shall first examine the size of the induced deformation by considering the calculation performed by UCB for the size of the mass quadrupole generated from temperature asymmetries in a single capture layer. Based on their results, OJ20 calculated a simple fitting formula for the NS ellipticity as (*cf.* their Eq. 2),

$$\varepsilon \sim 5 \times 10^{-8} \left[\frac{\delta T/T}{1\%} \right]. \tag{5.49}$$

Using this simple scaling (evaluated at our fiducial density $\rho = 10^{13}$ g cm^{-3}), one expects that a fractional temperature asymmetry at the percent level in the inner crust produces an ellipticity of $\sim 5 \times 10^{-8}$, irrespective of the assumed origin of the perturbations.

For the specific case of a magnetic field that is confined to the accreted crust (Eq. (5.41) with $R_{\mathrm{B,\,min}} = R_{\mathrm{crust-core}}$), the results of Fig. 5.12 represent the magnetic field strengths required to produce an ellipticity of this size, generating a mountain large enough to balance accretion torques with the emission of GWs.

To place these results in to context, reconsider the results from the recent continuous GW search by Abbott et al. (2022a), who constrained the ellipticity on the AMXP IGR J00291+5934 to be no more than $\varepsilon^{95\%} = 3.1 \times 10^{-7}$. In lieu of a continuous GW detection, the results obtained by Abbott et al. (2022a) are still useful. Namely, the upper limit on the ellipticity of IGR J00291+5934 can be combined with our results to tentatively place an upper limit on the strength of the internal magnetic field within the NS.

Since the temperature asymmetry (and therefore the ellipticity) has some dependence on the accretion rate $\dot{M}$, we can find an upper limit on the strength of the internal magnetic field by recalculating our temperature perturbations assuming an $\dot{M}$ specific to IGR J00291+5934. The star's mass, however, is not known, so we present results for both a 1.4 $M_\odot$ and 2.1 $M_\odot$ NS. As we have computed only steady-state solutions, we interpret our parameter $\dot{M}$ as the time-averaged accretion rate. This also ensures consistency in our use of Eq. (4.125) that requires burning at the base of the H/He layer to be stable. We estimate the average mass accretion rate in IGR J00291+5934 using data taken from Table 2 of Falco et al. (2017), for which the time-averaged X-ray flux $\langle F_{\mathrm{x}} \rangle$ is given for four independent outburst/quiescence cycles that occurred in the years 2004 - 2015. Using this information, we assume the mass accretion rate to then be of the form

$$\dot{M} = \langle F_{\mathrm{x}} \rangle \frac{4\pi R d^2}{GM}, \tag{5.50}$$

where d is the distance of IGR J00291+5934 from Earth. We averaged the results of Falco et al. (2017) to produce one value of $\langle F_{\rm x} \rangle$ over all four outburst/quiescence cycles. At a distance of 3 kpc, we estimate the accretion rates to be

$$\dot{M}_{1.4M_\odot} = 1.8 \times 10^{-12} M_\odot \, {\rm yr}^{-1} \approx 9 \times 10^{-5} \, \dot{M}_{\rm Edd} \,, \tag{5.51}$$

$$\dot{M}_{2.1M_\odot} = 1.2 \times 10^{-12} M_\odot \, {\rm yr}^{-1} \approx 5 \times 10^{-5} \, \dot{M}_{\rm Edd} \,. \tag{5.52}$$

for a 1.4 and 2.1 $M_\odot$ star respectively. These accretion rates are appreciably smaller than those we considered in Section 5.5, and therefore we re-calculate the size of the temperature perturbation $\delta T/T$, again quoting the result at the density $\rho = 10^{13}$ g cm^{-3} in the inner crust specific to these values of $\dot{M}$. In doing so, we find that

$$(\delta T/T)_{1.4M_\odot} \sim 3.3 \times 10^{-8} \, B_8 \;\Rightarrow\; \varepsilon_{1.4M_\odot} \approx 1.7 \,, \times 10^{-13} \, B_8 \,, \tag{5.53}$$

$$(\delta T/T)_{2.1M_\odot} \sim 4.3 \times 10^{-5} \, B_8 \;\Rightarrow\; \varepsilon_{2.1M_\odot} \approx 2.2 \times 10^{-10} \, B_8 \,, \tag{5.54}$$

assuming the BSk21 EoS and the field configuration given by Eq. (5.41) with $R_{\rm B,\,min} = R_{\rm IB}$. Using these results, it is possible to calculate the upper limit on the strength of the internal magnetic field required to produce the ellipticity constrained by Abbott et al. (2022a) as

$$B^{\varepsilon_{95\%}}_{1.4M_\odot} = \left[\frac{3.1 \times 10^{-7}}{1.7 \times 10^{-13}}\right] B_8 \approx 1.9 \times 10^{14} \, {\rm G} \,, \tag{5.55}$$

$$B^{\varepsilon_{95\%}}_{2.1M_\odot} = \left[\frac{3.1 \times 10^{-7}}{2.2 \times 10^{-10}}\right] B_8 \approx 1.4 \times 10^{11} \, {\rm G} \,. \tag{5.56}$$

We do stress however that these upper limits must be taken with caution. In reference to Eq. (5.16), it is the case that such large magnetic fields may predict the hall component $\kappa^{\wedge}$ of the field to be many orders of magnitude greater than the parallel component $\kappa^{\parallel}$. Such a result is clearly nonphysical (as can be seen by comparing $\kappa^{\wedge}$ and $\kappa^{\parallel}$ in Eq. (5.7)), and is a consequence of the fact that the condition $\omega_B \tau(T) \ll 1$ is broken for core magnetic fields greater than $\sim 10^8$ G (Fig. 5.2).

Though, given that methods to probe the structure of internal magnetic fields are so scarce, we present this method at least as a proof of concept to constrain the strength of the internal field. A calculation such as this is further motivation to return to a reformulation of this mechanism in the non-perturbative regime in the future, which would be able to explore magnetic fields in excess of the current limit of $\sim 10^8$ G.

Regardless, in the LM case where Durca is forbidden, the constraint on the upper limit of the magnetic field is not particularly informative: the upper limit is 5-6 orders of magnitude larger than externally inferred field strength. Our results for the HM star however, are more interesting: we obtain an upper limit on the internal toroidal magnetic field $\sim 10^{11}$ G. We must re-iterate that such magnetic fields push us far out of the perturbative regime however ($\sim$ 4 order of magnitude; Fig. 5.2), and therefore must be viewed cautiously.

Additionally, these results are also very much conditional on the accretion rate (and the star's mass; Figs. 5.9 - 5.11), and therefore the upper limits we present here are themselves limited by the low-level accretion of IGR J00291+5934. Analysis by Heinke et al. (2009) also indicates that quiescent spectrum of IGR J00291+5934 is in fact consistent with the *standard cooling model*, suggesting that it is a LM star (i.e. $M \lesssim 1.6 M_{\odot}$) and disfavouring the presence of Durca cooling. We would therefore benefit greatly from further targeted searches towards millisecond accreting pulsars, with the hope that the ellipticity can be accurately constrained for LMXBs that are accreting at greater rates (and exhibit evidence of enhanced cooling), as these systems would be more favourable for sustaining a thermal mountain.

6

Thermo-elastic Mountains on Accreting Neutron Stars

In this chapter we will now examine how deformations of the solid crust may form as a consequence of non-axisymmetric temperature variations, and compute their sizes. We begin in Section 6.1 by discussing how one may introduce (perturbatively) finite-temperature corrections onto the zero-temperature equation of state presented back in Section 2.2. Specifically, we describe a (new) method in which pressure perturbations may be generated in the solid crust through *thermal lattice pressures*, a small temperature-dependent contribution to the total pressure from the crust's ionic lattice.

In Section 6.2 we then derive the perturbation equations which describe the elastic response of the crust to existing temperature gradients, in a Newtonian framework. We outline the relevant boundary conditions specific to static perturbations of the crust, and present three methods in which one may compute the mass quadrupole moment from density perturbations associated with the thermal pressure perturbations described in Section 6.1.

We then present in Section 6.3 results for the ellipticity of accreting neutron stars generated through thermal perturbations in the lattice pressure, sourced from anisotropic heat conduction due to internal magnetic fields. The parameter space of both the mass accretion rate $\dot{M}$ and shallow heating parameter Q_{S} are explored. We shall then, in turn; assess the role that these mountains likely play in determining the spin-evolution of accreting neutron stars; compare the ellipticity generated via the crustal lattice pressures to those of the physical shifts of electron capture layers; contrast the ellipticity of thermal mountains with those of the more 'conventional' magnetic mountains.

6.1 Temperature dependence of the equation of state

In the previous chapter (Chap. 5) we explored whether lateral temperature gradients in accreting neutron stars could be generated from internal magnetic fields as a result of anisotropic heat conduction. In order to form the mountain, the asymmetry in the thermal structure (treated as a perturbation of the homogeneous background computed in Chap. 4) must lead to pressure imbalances which then lead to a physical displacement of the crustal matter. In practice, (and as we shall see in Sec. 6.2.1) such displacements are modelled in terms of a Lagrangian displacement field ξ^i, so that one may connect a given matter element in the perturbed configuration, to that of its position in the unperturbed background.

To source the thermal pressure perturbation, the equation of state (which thus far has been assumed to be zero-temperature; Sec. 2.2), must have some kind of temperature dependence. For an EoS of the form $P = P(\rho, T)$, the *Lagrangian* pressure perturbation ΔP is

$$\Delta P = \left.\frac{\partial P}{\partial \rho}\right|_T \Delta\rho + \left.\frac{\partial P}{\partial T}\right|_\rho \Delta T \,. \tag{6.1}$$

We first examined the size of the induced deformation from the temperature asymmetry using the simple scaling relation Eq. (5.49) in Section 5.6, fitted to the results of UCB, who evaluated the source terms and coefficients in Eq. (6.1) (as per their Appendix. A) through an equation of state parameterised as $P = P(\rho, \mu_e[\rho, T])$. This is the conventional picture of thermal mountains, where the dependence on temperature comes in through the electron chemical potential μ_e, which determines at what depth electron captures may take place (recall the description of the 'wavy capture layer' in Sec. 3.2.2.1).

In the following section we will consider a different (and simpler) source for temperature-dependence on the (crustal) equation of state. We shall instead consider a piece of the (thermal) crustal pressure that is necessarily tied to the ionic lattice itself. This is advantageous, at least in part, since the number of capture layers in the accreted crust varies significantly between different equation of state models[1] (Sec. 2.4.2). And, as we shall see in Section 6.3.2, this lack of definitive agreement in the composition of the crust can lead to wildly differing estimates (~ 4 orders of magnitude) for the *total* mass quadrupole (the Q_{22} generated within each individual capture layer add linearly) generated from the wavy capture layer scenario.

We term the deformations of the crust that arise from perturbations in the thermal lattice pressure as 'thermo-elastic mountains', rather than simply 'thermal mountains' since they do not require the resolution of individual capture layers. This serves to distinguish our work from that of the Bildsten (1998) and Ushomirsky et al. (2000) mechanism.

---

[1] It is also beneficial for us since our method to approximate the heat release from non-equilibrium reactions into 'shells' in the background model (recall Fig. 4.3) also does not resolve the true 'width' of the capture layers, where, strictly speaking, all of the heat would be released. In order to source the pressure perturbations by resolving individual capture layers, our method for calculating the heat release outlined in Section 4.3.1 would first need to be corrected, as per the procedure outlined in UCB.

6.1.1 The thermal lattice pressure

Within the crust of a neutron star, it is expected that relativistic electrons supply the majority of the pressure in the outer crust, while neutrons supply most of the pressure in the inner crust (Sec. 2.5.2.1).

The *total pressure* in the crust is, to a first approximation, determined by the zero-temperature EoS. It is the case, however, that there is likely to be some small thermal correction to both the electron and neutron pressures, particularly in accreting neutron stars where deep crustal heating processes (Sec. 4.3.1) can warm the crust to temperatures approaching 10^9 K (Fig. 4.19). Yet, these contributions are usually modelled in terms of a pressure associated with (Fermi) *gases* of electrons and neutrons (Sec. 2.3). Within the context of thermal mountains, which we are interested in here, we require a *sustained* deformation of the crust. Any such thermally-induced perturbations in these gases would likely be convected away far too quickly to be relevant for mountain building. Not only this, but in the specific context of the type of temperature perturbations that we are considering (i.e. those sourced from magnetic fields) there would actually likely be effectively no density perturbations at all in the deep crust (where most of the mass quadrupole would be formed, as this is where most of mass of the crust is contained) since the neutrons are electrically neutral[2].

There is, however, another component of the crustal pressure that *is* necessarily firmly tied to the elastic phase. Specifically, there is a non-negligible pressure that is generated directly by the ionic lattice itself; through (mainly) interactions of the ions with other ions, as well as with the background sea of electrons. Crucially, this *crustal lattice pressure* has a temperature-dependent piece, which will therefore also be sensitive to any existing temperature asymmetry in the crust (including those that arise from magnetic fields). As we shall see, it turns out that the crustal lattice pressure is small relative to the total (zero-temperature) pressure, and that the thermal correction is smaller still (Fig. 6.2). However, the fact that any perturbations in the pressure will be tied to the lattice itself makes it relevant for mountain building, since they will not be as easily convected away.

We have previously discussed (Sec. 2.5.2.2) that the crust is often assumed to be an isotropic, body-centered cubic Coulomb crystal. For such crystals, there are two important dimensionless quantities which describe their thermal properties. The first is the already-familiar Coulomb parameter Γ_{Coul}, defined in Eq. (2.9) as

$$\Gamma_{\text{Coul}} = \frac{Z^2 e^2}{k_B T}\left(\frac{4\pi n_{\text{b}}}{3}\right)^{1/3} . \tag{6.2}$$

---

[2] It is possible, however, that since the electrons are negatively charged, one could envisage a scenario whereby a large-scale internal magnetic field could generate 'stabilised' pressure perturbations in the electron gas. Such a '*thermo-magentic*' mountain however is not relevant to the current discussion.

Not only is this quantity useful in determining the crystallisation point of the crust (i.e. when the ratio of the ions' electrostatic potential energy to thermal energy exceeds 175; Sec. 2.3.1, and see Sec. 6.2.1.1), but it is also useful in order to quantify so-called *anharmonic corrections* to the low-temperature harmonic treatment of ionic oscillations[3] (Haensel et al., 2007). Generally speaking, the thermal properties of the crystal may be divided into a low temperature harmonic regime (when $\Gamma_{\mathrm{Coul}} \gg 1$), and a high temperature anharmonic regime (when $\Gamma_{\mathrm{Coul}} \ll 1$). From our description of the thermal background in Chapter 4, the results presented in Sec. 4.8 (specifically Fig. 4.21) indicate we are always in the harmonic regime ($\Gamma > 175$; i.e. at temperatures below the melting temperature T_{m} where the crust is solid) for all but the lowest density parts of the crust for the majority of the neutron star models that we will consider.

The second quantity is then the dimensionless ratio ${}^{T}/_{T_{\mathrm{pi}}}$, where T_{pi} is the *plasma ion temperature*, defined as (Haensel et al., 2007)

$$T_{\mathrm{pi}} = \frac{\hbar \omega_{\mathrm{pi}}}{k_B} , \tag{6.3}$$

and ω_{pi} is the plasma ion frequency (which describes the frequency at which the ions in the lattice naturally oscillate) given by

$$\omega_{\mathrm{pi}} = \left[4\pi e^2 n_{\mathrm{N}} \frac{Z^2}{m_i} \right]^{1/2} , \tag{6.4}$$

where n_{N} is the ion number density Eq. (2.27), and m_i is the ion mass $m_i = A m_{\mathrm{b}}$, such that

$$\frac{T}{T_{\mathrm{pi}}} = \frac{k_B T}{\hbar \omega_{\mathrm{pi}}} . \tag{6.5}$$

With this second relation, the thermal properties of the crustal lattice may be further divided into a low temperature *quantum* regime ($T \ll T_{\mathrm{pi}}$) and a high temperature *classical* regime ($T \gg T_{\mathrm{pi}}$). In order to gauge which of these two regimes a typical accreting neutron star presents itself, we plot in Fig. 6.1 the plasma ion temperature T_{pi} for the each of BSk19, BSk20, and BSk21, for an accreted crust. Given that our results for the thermal structure (Figs 4.19 - 4.20) indicate that the crustal temperature is typically $\sim 10^8 - 10^9$ K, this suggests that ${}^{T}/_{T_{\mathrm{pi}}} \lesssim 0.1$ over the majority of the crust ($\rho > 10^{11}$ g cm^{-3}), and therefore that is a typical accreting NS is within the quantum regime, but not deeply so.

For our purposes it is therefore not helpful to consider either limiting case where $T \ll T_{\mathrm{pi}}$ or $T \gg T_{\mathrm{pi}}$ to compute the thermal lattice pressure. Instead, we shall make use of results obtained by Baiko et al. (2001), who have previously calculated the thermodynamic functions of harmonic Coulomb crystals for arbitrary ${}^{T}/_{T_{\mathrm{pi}}}$. The Helmholtz Free energy F_{E} of a harmonic Coulomb

---

[3] When the temperature of the crystal is sufficiently high, then oscillations of the ions are large enough that a 'standard' quadratic form for the potential is no longer sufficient to describe the oscillations.

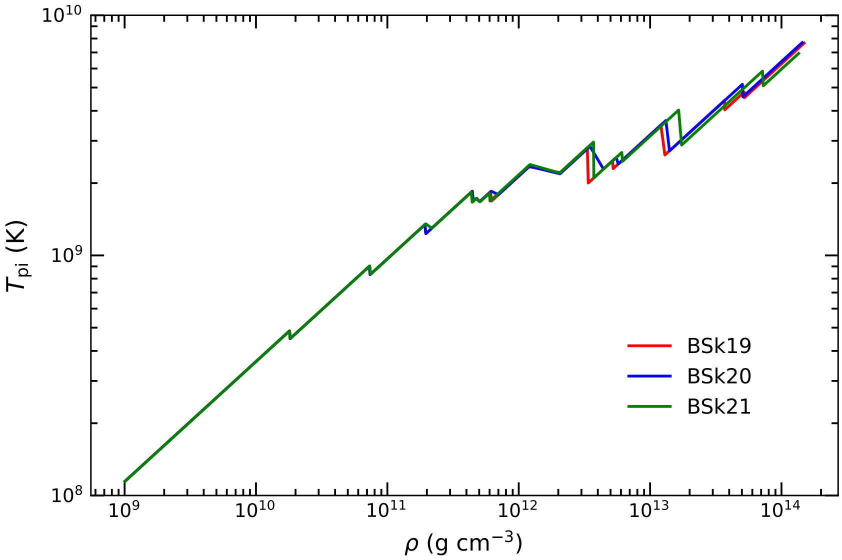

FIGURE 6.1: Plasma ion temperature T_{pi} for the accreted equations of state BSk19, BSk20 and BSk21.

crystal is determined by the energy of the static-lattice contribution, a contribution from zero-point vibrations, as well as a (finite temperature) thermal free energy. This thermal part of the free energy, which we will label F_{th}, is given in terms of a *reduced* thermal free energy f_{th} as

$$F_{\mathrm{th}} = f_{\mathrm{th}} N_{\mathrm{N}} k_B T \,. \tag{6.6}$$

A convenient fitting formula for the reduced thermal free energy of a harmonic Coulomb crystal was obtained by Baiko et al. (2001) as

$$f_{\mathrm{th}} = \sum_{n=0}^{3} \ln(1 - e^{-\alpha_n \theta}) - \frac{A(\theta)}{B(\theta)} \,, \tag{6.7}$$

with the quantities $A(\theta)$ and $B(\theta)$ given by

$$A(\theta) = \sum_{n=0}^{8} a_n \theta^n . \tag{6.8}$$

$$B(\theta) = \sum_{n=0}^{7} b_n \theta^n + \alpha_6 a_6 \theta^9 + \alpha_8 a_8 \theta^{11} \,, \tag{6.9}$$

where θ is a ‘quantum parameter’, defined in terms of the plasma ion frequency as (Eq. (6.5))

$$\theta \equiv \frac{\hbar \omega_{\mathrm{pi}}}{k_B T} = \frac{T_{\mathrm{pi}}}{T} \,, \tag{6.10}$$

Table 6.1: Parameters needed to calculate the reduced thermal free energy (Eqs (6.7) - (6.9)) of a body-centred cubic Coulomb lattice. This table is a reproduction of Table II of Baiko et al. (2001).

n	α_n	a_n	b_n
0	-	1	261.66
1	0.932446	0.1839	0.0
2	0.334547	0.593586	7.07997
3	0.265764	5.4814×10^{-3}	0.0
4	-	5.01813×10^{-4}	0.0409484
5	-	0.0	3.97355×10^{-4}
6	4.757014×10^{-3}	3.9247×10^{-7}	5.11148×10^{-5}
7	-	0.0	2.19749×10^{-6}
8	4.7770935×10^{-3}	5.8356×10^{-11}	-

and α_n, a_n and b_n are sets of constants with values given in Table 6.1, reproduced (for convenience) from Table II of Baiko et al. (2001) for the specific case of a *body-centered* cubic Coulomb lattice.

In corollary with the definition of the pressure in Section 2.2 (specifically Eq. (2.5)), the pressure of the Coulomb crystal can be obtained from the free energy using the thermodynamic relation

$$P = -\left.\frac{\partial F_{\mathrm{E}}}{\partial V}\right|_{N_{\mathrm{N}},T} . \tag{6.11}$$

In order to proceed, and obtain the pressure associated with the *thermal* piece of the free energy, one must make the V- dependence of F_{th} explicit. This dependence resides within the quantum parameter θ, through its dependence on the ion number density N_{N}, and we may write

$$P_{\mathrm{th}} = -N_{\mathrm{N}} k_B T \frac{df_{\mathrm{th}}}{d\theta} \left.\frac{\partial \theta}{\partial V}\right|_{N_{\mathrm{N}},T} . \tag{6.12}$$

The derivative of f_{th} is obtained directly by differentiating the fitting formulae (6.7) - (6.9) as (*cf.* Eq. (15) of Baiko et al., 2001)

$$\frac{df_{\mathrm{th}}}{d\theta} = \sum_{n=1}^{3} \frac{\alpha_n}{e^{\alpha_n \theta - 1}} - \frac{A'(\theta)B(\theta) - A'(\theta)B'(\theta)}{B^2(\theta)} , \tag{6.13}$$

while the derivative of θ is

$$\left.\frac{\partial \theta}{\partial V}\right|_{N_{\mathrm{N}},T} = \frac{\hbar}{k_B T} \left.\frac{\partial \omega_{\mathrm{pi}}}{\partial V}\right|_{N_{\mathrm{N}},T} = -\frac{\hbar}{2 k_B T} \frac{\omega_{\mathrm{pi}}}{V} , \tag{6.14}$$

since

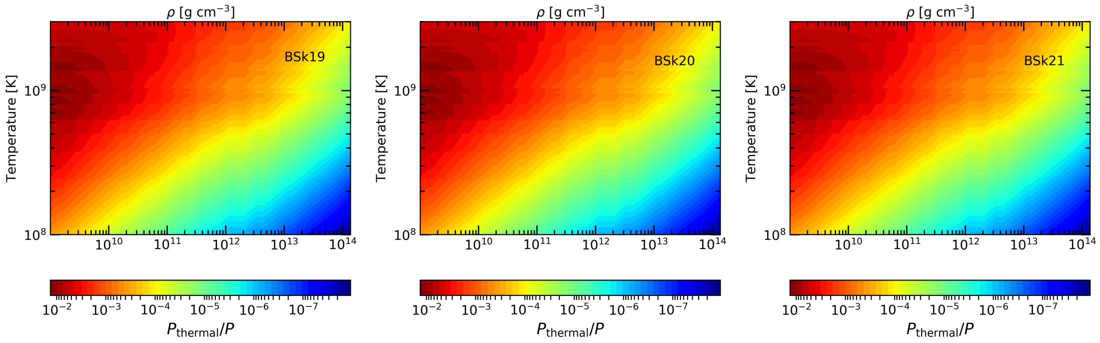

Figure 6.2: Ratios of the lattice thermal pressure to the total pressure as a function of both temperature and density for the accreted equations of state BSk19 (*left*), BSk20 (*centre*) and BSk21 (*right*).

$$\omega_{\mathrm{pi}}^2 = 4\pi e^2 n_{\mathrm{N}} \frac{Z^2}{M} = 4\pi e^2 \frac{N_{\mathrm{N}}}{V} \frac{Z^2}{M}\,, \tag{6.15}$$

and therefore

$$P_{\mathrm{th}} = \frac{1}{2}\hbar\omega_{\mathrm{pi}} n_{\mathrm{N}} \frac{df_{\mathrm{th}}(\theta)}{d\theta} = \frac{1}{2}\hbar\omega_{\mathrm{pi}} \left[\frac{\rho(1-X_{\mathrm{n}})}{m_{\mathrm{b}}A}\right] \frac{df_{\mathrm{th}}(\theta)}{d\theta}\,. \tag{6.16}$$

In Fig. 6.2 we plot the ratio of the thermal lattice pressure Eq. (6.16) relative to the zero-temperature pressure for each of the BSk19, BSk20, and BSk21 equations of state, as a function of both density and temperature. We plot the lattice pressure for a range of different temperatures in the region $10^8 - 3 \times 10^9$ K, in order to gauge the full parameter space of realistic LMXBs.

It can be seen that the lattice pressure is very much dependent on the temperature. In the deep crust ($\rho \sim 10^{13}$ g cm^{-3}), the fractional pressure perturbation can be as low as $\sim 10^{-7}$ when the crust is cold ($\sim 10^8$ K), and as large as $\sim 10^{-3}$ when it is hot ($\sim 10^9$ K). It is therefore clear that understanding the thermal structure of a *real* accreting neutron star is of the utmost importance in order to address the feasibility of generating large pressure perturbations, and subsequently build large mountains. This emphasises the need for an accurate description of the thermal structure, as presented in Chapter 4.

Though, within the specific context of building thermal mountains, it is, as we shall see in Section 6.2.1, more insightful to consider the *perturbation* in the thermal pressure, ΔP_{th}, rather than P_{th} itself. Indeed, thermal mountains themselves are of course sourced inherently by the presence of some temperature anisotropy inside the star. In practice, the *actual* fractional pressure perturbations of relevance to mountain building will be smaller.

In fact, the fractional change in the pressure caused by a fractional temperature perturbation $\Delta T/T$ will be

$$\frac{\Delta P_{\rm th}}{P} = \frac{T}{P}\frac{\partial P_{\rm th}}{\partial T}\bigg|_{\rho}\left(\frac{\Delta T}{T}\right), \tag{6.17}$$

where the derivative of the thermal pressure is

$$\frac{\partial P_{\rm th}}{\partial T}\bigg|_{\rho} = \frac{1}{2}\hbar\omega_{\rm pi}\frac{\theta}{T}\left[\frac{\rho(1-X_{\rm n})}{m_{\rm b}A}\right]\left[\frac{d^2 f_{\rm th}(\theta)}{d\theta^2}\right], \tag{6.18}$$

with the second derivative of the reduced thermal free energy $f''_{\rm th}$ following from Eq. (6.13), given by (*cf.* Eq. (16) of Baiko et al., 2001)

$$\begin{aligned}\frac{d^2 f_{\rm th}}{d\theta^2} = \sum_{n=1}^{3}\frac{\alpha_n^2 e^{\alpha_n\theta}}{e^{\alpha_n\theta-1}} + \frac{2A(\theta)(B'(\theta))^2}{B^3(\theta)} \\ - \frac{2A'(\theta)B'(\theta)+A(\theta)B''(\theta)}{B^2(\theta)} + \frac{A''(\theta)}{B(\theta)},\end{aligned} \tag{6.19}$$

where the prime in this instance denotes differentiation with respect to the quantum parameter θ.

6.2 Elastic deformations of the accreted crust

In this section we derive the set of perturbation equations (following closely the prescription originally outlined in UCB; inspired from earlier works by Alterman et al., 1959; Hansen and van Horn, 1979; McDermott et al., 1988) which quantify the elastic response of the accreted crust to lateral temperature gradients, and compute the quadrupole moment.

For reasons of simplicity, we wish to avoid solving the equations which determine the elastic readjustment of the crust in full general relativity. Instead, we would like to remain in a Newtonian setting so as to focus on implementing a *realistic* source term that has, until now, been absent in the literature[4] (recall Secs 1.3.3.2 and 3.2.2.1.1). Whilst in future we would seek to extend this formalism into a fully general relativistic framework (see Sec. 7.3.3), we note the results of Gittins and Andersson (2021); who found that the *maximum* mountain the crust could sustain due to an *unmodelled* thermal pressure perturbation $\delta P_{\rm th}$ (i.e. an artificial ‘forcing term’; see Eqs (57) - (59) in Gittins et al., 2021) changes by a factor ~ 2 when generalising the scheme to compute mountain sizes from a Newtonian framework into general relativity. Specifically, they found that $\varepsilon_{\rm max}^{\rm Newt} = 5.2\times10^{-7} \longrightarrow \varepsilon_{\rm max}^{\rm GR} \approx 1\times10^{-8}$ for a typical NS with $M = 1.4\,M_{\odot}$, $R = 10\,$km, indicating that Newtonian theory overestimates (thought not grossly) the size of the (maximum) deformation the crust can sustain.

---

[4] In this sense we also remain consistent in keeping with the Newtonian framework used to derive the thermal perturbation equations in Chapter 5, as well as determine the thermal structure of the unperturbed background in Chapter 4.

The thermal mountains we consider here, on the other hand, *are* modelled; sourced from thermal pressure perturbations in the crustal lattice (Sec. 6.1.1), generated as a result of anisotropic heat conduction via both crustal and core magnetic fields. In order to model the core, we have made use of the fully-relativistic TOV equations (Sec. 2.6.2.1) for the hydrostatic background such that we may make use of realistic equations of state; which, in Newtonian theory (Sec. 2.6.1), would have lead to grossly un-physical density profiles.

We shall consider deformations of the star to be static perturbations of an elastically un-strained background star[5] described by the Newtonian structure equations (2.41) - (2.43). In doing so, we shall simply map our solution from the relativistic TOV equations to a Newtonian star by reinterpreting the TOV radial coordinate, pressure and energy density as simply their Newtonian counterparts. In this sense, the Newtonian mass density is just the relativistic energy density divided by c^2.

Such a choice has two fundamental consequences. On the one hand, we preserve the original definition of the equation of state (specifically the pressure-density relation; Sec. 2.5), but on the other inevitably produce a neutron star whose local acceleration due to gravity does not quite satisfy Poisson's equation (2.43) for gravity, and thus does not match the value that Newtonian theory would prescribe.

In order to proceed we need confront the fact that there exists an inherent in-congruence between how the gravitational acceleration g (Where $g = \nabla_i \Phi$; Eqs (2.41) - (2.43)) is defined in relativistic and Newtonian gravity. Indeed, the term 'gravitational acceleration' in general relativity a misnomer. While in a Newtonian sense gravitational acceleration is truly an acceleration of an object in free fall due to some gravitational force; in a relativistic description, such a force is fictitious, with objects in free fall traveling along geodesics in a curved spacetime (Sec. 3.1).

As such, we instead choose to define g in the following way. In Newtonian gravity, the equation of hydrostatic balance (2.46b) may be rearranged to give

$$\frac{d\Phi(r)}{dr} \equiv g(r) = \frac{1}{\rho}\frac{dP(r)}{dr}. \tag{6.20}$$

Rather than call g the 'gravitational acceleration', defined by $g(r) = GM/r^2$ explicitly, we shall instead define it in terms of Eq. (6.20), where the quantity P' is given by the right-hand side of the TOV equation (2.62), which constrains the hydrostatic structure of the NS *as modelled by general relativity*. In practice, if one compares Eq. (6.20) with the right-hand side of Eq. (2.62), this 'pseudo-acceleration' is equivalent to assuming that

$$g(r) = \frac{Gm(r)}{r^2}\left(1 + \frac{P(r)}{\rho(r)c^2}\right)\left(1 + \frac{4\pi r^3 P(r)}{m(r)c^2}\right)\left(1 - \frac{2Gm(r)}{rc^2}\right)^{-1}. \tag{6.21}$$

---

[5] We shall also assume that the star is both spherically symmetric and non-rotating, and that the crust responds purely elastically to the temperature perturbations induced by the magnetic field.

Strictly speaking, this newly quantified g is *not* a gravitational acceleration, it is merely a relativistic analogue that we have created that will differ from the Newtonian g by a factor related to the compactness of the star[6].

This result may then be used to compute the radial derivative of g (see the next section; Eqs (6.41b) and (6.42)) as

$$\frac{dg}{dr} = \frac{\rho P'' + P'\rho'}{\rho^2}\,, \tag{6.22}$$

where P'' denotes the second radial derivative of the pressure P. We find that this procedure leads to discrepancies in the value of g obtained from Newtonian theory by $\approx 30\%$.

6.2.1 The elastic perturbation equations

In the following we use shall use Latin letters $i, j, k, ...$ etc. to denote spatial indices, and use primes to denote radial derivatives. We shall also refer to Eulerian and Lagrangian perturbations of the crust using δ and Δ respectively. Since the unperturbed background is assumed to be spherically symmetric (the hydrostatic structure is constructed from the TOV equations; Sec. 2.6.2.1), all perturbed scalar quantities, be they Eulerian or Lagrangian, may be decomposed into the familiar spherical harmonics. We write these as

$$\delta\Lambda = \sum_{\ell=0}^{\infty}\sum_{m=-\ell}^{\ell} \delta\Lambda_{\ell m}(r)\, Y_{\ell m}(\theta,\phi)\,, \tag{6.23}$$

$$\Delta\Lambda = \sum_{\ell=0}^{\infty}\sum_{m=-\ell}^{\ell} \Delta\Lambda_{\ell m}(r)\, Y_{\ell m}(\theta,\phi)\,, \tag{6.24}$$

where Λ is an arbitrary scalar, and the two types of perturbation are related as (Shapiro and Teukolsky, 1983)

$$\Delta\Lambda = \delta\Lambda + \xi^i \nabla_i \Lambda\,, \tag{6.25}$$

where ξ^i is the Lagrangian displacement vector. In this case, ξ^i represents the displacement of a piece of the crust from its unperturbed state (see Eq. (6.29) below).

We begin with the elastic Euler equation, which in Newtonian gravity, reads (recall Eq. (2.42) for a perfect fluid)

---

[6] Note, however, that in the limit $c \to \infty$ equation (6.21) reduces to just $g(r) = GM_r/r^2$, at which point one would recover the Newtonian gravitational acceleration.

$$0 = \rho \nabla_j \Phi - \nabla^i \tau_{ij} \,, \tag{6.26}$$

where τ_{ij} is the stress-energy tensor of the solid crust and Φ is the gravitational potential. The stress-energy tensor of the crust is described by

$$\tau_{ij} = -P g_{ij} + t_{ij}, \tag{6.27}$$

where g_{ij} is the flat 3-metric and t_{ij} is the (trace-free) shear stress tensor of the solid crust, defined by

$$t_{ij} = \mu \left(\nabla_i \xi_j + \nabla_j \xi_i - \frac{2}{3} g_{ij} \nabla^k \xi_k \right), \tag{6.28}$$

where μ is the shear modulus of the crust (Sec. 2.5.2.2).

Since the star is assumed to be non-rotating, we need only consider polar perturbations of the crust. The appropriate static displacement vector in this case is of the form (Ushomirsky et al., 2000)

$$\xi^i = \xi^r_{\ell m}(r)\, \hat{r}^i\, Y_{\ell m} + \xi^{\perp}_{\ell m}(r) \beta^{-1} r \nabla^i Y_{\ell m} \,, \tag{6.29}$$

where $\xi^r_{\ell m}$ and $\xi^{\perp}_{\ell m}$ are the radial and tangential components of the displacement respectively, and $\beta = \sqrt{\ell(\ell+1)}$.

Keeping to linear order, and treating the displacement vector ξ^i as a first-order quantity allows us to write down the equations which govern the perturbations of the crust due to some pressure perturbation δP as

$$0 = \delta\rho g \hat{r}_j - \nabla^i \delta\tau_{ij} \,, \tag{6.30}$$

where we have neglected perturbations in gravitational potential (the Cowling approximation) in order to simplify the problem, $\nabla_j \Phi = g$ is the acceleration due to gravity, and $\delta\rho$ is the Eulerian density perturbation given by

$$\delta\rho = -\nabla^i (\rho \xi_i) = -\left[\xi_r \rho' - \rho \left(\xi_r' + \frac{2}{r} \xi_r - \frac{\beta}{r} \xi_\perp \right) \right] Y_{\ell m} \,, \tag{6.31}$$

which follows from the perturbed form of the continuity equation (2.41).

The perturbed form of the stress-energy tensor Eq. (6.27) is given by[7] (Ushomirsky et al., 2000)

---

[7] Note in Eq. (6.34) we have corrected a typo from UCB for the last term containing ξ_r - *cf.* their Eq. (39b).

$$\begin{aligned}\delta\tau_{ij} =& g_{ij}Y_{\ell m}\delta\tau_{rr} + e_{ij}\left[2\mu\left(\frac{1}{r}\xi_r - \xi_r'\right)\right]Y_{\ell m} \\ &+ f_{ij}\delta\tau_{r\perp} + \Lambda_{ij}\frac{2\mu\beta}{r}\xi_\perp\,,\end{aligned} \tag{6.32}$$

where

$$\delta\tau_{rr} = -\delta P + \mu\left(\frac{4}{3}\xi_r' - \frac{4}{3r}\xi_r + \frac{2\beta}{3r}\xi_\perp\right), \tag{6.33}$$

$$\delta\tau_{r\perp} = \mu\left(\xi_\perp' - \frac{1}{r}\xi_\perp + \frac{\beta}{r}\xi_r\right), \tag{6.34}$$

$$e_{ab} = g_{ij} - \hat{r}_i\hat{r}_j\,, \tag{6.35}$$

$$f_{ij} = \beta^{-1}r\,(\hat{r}_i\,\nabla_j Y_{\ell m} + \hat{r}_j\,\nabla_i Y_{\ell m})\,, \tag{6.36}$$

$$\Lambda_{ij} = \beta^{-2}r^2\,\nabla_i\nabla_j Y_{\ell m} + \beta^{-1}f_{ij}\,. \tag{6.37}$$

Breaking down the perturbed Euler equation (6.30) along $\hat{r}^j$ (i.e. in the radial direction) and $\nabla^j Y_{\ell m}$ (the transverse direction) yields the following expressions

$$\delta\rho(r)g = \delta\tau_{rr}' - \frac{4\mu}{r}\left(\frac{1}{r}\xi_r - \xi_r'\right) - \frac{\beta}{r}\delta\tau_{r\perp} + \frac{2\mu\beta}{r^2}\xi_\perp\,, \tag{6.38}$$

and

$$\begin{aligned}0 =& \ \delta\tau_{rr} + 2\mu\left(\frac{1}{r}\xi_r - \xi_r'\right) \\ &+ \frac{1}{\beta}\left(3\delta\tau_{r\perp} + r\delta\tau_{r\perp}'\right) + \frac{2\mu\beta}{r}\left(\frac{1}{\beta^2} - 1\right)\xi_\perp\,,\end{aligned} \tag{6.39}$$

from which a set of coupled second-order ODEs for the components of the displacement vector ξ_r'' and $\xi_\perp''$ may then be obtained using Eqs (6.33) and (6.34) respectively, together with the perturbed continuity equation (6.31).

These ODEs however may be put into a more suitable form for numerical integration (as well as making the application of boundary conditions more straightforward) by making the following substitutions (McDermott et al., 1988; Ushomirsky et al., 2000)

$$\begin{aligned} z_1 &= \frac{1}{r}\xi_r\,, \qquad z_2 = \frac{\Delta\tau_{rr}}{P} = \frac{\delta\tau_{rr}}{P} - z_1\frac{d\ln P}{d\ln r}\,, \\ z_3 &= \frac{1}{\beta r}\xi_\perp\,, \quad z_4 = \frac{\Delta\tau_{r\perp}}{\beta P} = \frac{\delta\tau_{r\perp}}{\beta P}\,. \end{aligned} \tag{6.40}$$

This allows us to recast the second-order ODEs in ξ_r and $\xi_\perp$ in terms of a set of four coupled *first-order* ODEs for the variables z_{1-4}, given as (*cf.* Eqs (43a) - (43d) of UCB)

$$\begin{aligned} \frac{dz_1}{d\ln r} &= -\left(1+\frac{2\alpha_2}{\alpha_3}\right)z_1 + \frac{1}{\alpha_3}\left(z_2+\boldsymbol{\Delta S}\right) \\ &\quad + \frac{\ell(\ell+1)\alpha_2}{\alpha_3}z_3\,, \qquad (6.41a) \\ \frac{dz_2}{d\ln r} &= \left(UV - 4V + \frac{12\Gamma\alpha_1}{\alpha_3}\right)z_1 \\ &\quad + \left(V - \frac{4\alpha_1}{\alpha_3}\right)z_2 + \ell(\ell+1)z_4 - \frac{4\alpha_1}{\alpha_3}\boldsymbol{\Delta S} \\ &\quad + \left(\ell(\ell+1)V - \frac{6\ell(\ell+1)\Gamma\alpha_1}{\alpha_3}\right)z_3 \qquad (6.41b) \\ \frac{dz_3}{d\ln r} &= \frac{1}{\alpha_1}z_4 - z_1\,, \qquad (6.41c) \\ \frac{dz_4}{d\ln r} &= \left(V - \frac{6\Gamma\alpha_1}{\alpha_3}\right)z_1 - \frac{\alpha_2}{\alpha_3}z_2 + (V-3)z_4 + \frac{2\alpha_1}{\alpha_3}\boldsymbol{\Delta S} \\ &\quad + \frac{2}{\alpha_3}\{[2\ell(\ell+1)-1]\alpha_1\alpha_2 + 2[\ell(\ell+1)-1]\alpha_1^2\}z_3\,, \qquad (6.41d) \end{aligned}$$

where the quantities U and V are defined as

$$U \equiv \frac{d\ln g}{d\ln r}\,, \qquad V \equiv \frac{\rho g r}{p} = -\frac{d\ln P}{d\ln r}\,, \tag{6.42}$$

along with the coefficients α_{1-3}

$$\alpha_1 \equiv \frac{\mu}{P}\,, \qquad \alpha_2 \equiv \Gamma - \frac{2\alpha_1}{3}\,, \qquad \alpha_3 \equiv \Gamma + \frac{4\alpha_1}{3}\,, \tag{6.43}$$

with Γ being the adiabatic index (Section 2.5.2.1).

The ODEs (6.41a) - (6.41d) describe the readjustment of an (accreting) neutron star crust in response to an in-homogeneous source term (highlighted in bold)

$$\mathbf{\Delta S} = \frac{\Delta P}{P} = \left.\frac{\partial \ln P}{\partial \ln T}\right|_{\rho} \frac{\Delta T}{T}\,, \tag{6.44}$$

which arises from the temperature dependence of the equation of state in Eq. (6.1). In our specific case, this source term is derived from the thermal pressure perturbations generated in the crystal lattice of the crust (i.e. $\Delta P \equiv \Delta P_{\rm th}$; Sec. 6.1.1) from temperature perturbations produced as a result of anisotropic heat conduction due to quadrupolar magnetic fields (Sec. 5.1).

It should be noted that, whilst very similar to the equations of UCB, our perturbation equations for a source term derived from the existence of a temperature perturbation are not identical. Specifically, the elastic perturbation equations derived by UCB (*cf.* their Eqs (43a) - (43d)) include an additional term, that they refer to as α_4, given by

$$\alpha_4 = \left.\frac{\partial \ln P}{\partial \ln T}\right|_{\rho} \frac{d \ln T}{d \ln r}\,, \tag{6.45}$$

which does not appear in our system of equations (6.41a) - (6.41d). The reason for this discrepancy is as follows. The temperature perturbations computed in Chapter 5 (denoted as δT) were computed for a *fixed crust*, i.e. not allowing for elastic readjustment. Now, however, we are truly seeking to quantify the response of fluid elements in the crust to these temperature perturbations; solving for the *Lagrangian* displacement field ξ^i that brings the crust back into equilibrium. We therefore identify these temperature perturbations with the *Lagrangian* temperature perturbations of the elastically deformed star. We do this as we wish our final solution to be self-consistent with respect to both thermal and elastic perturbations, with a temperature profile given by the calculations of Chapter 5 *after the elastic readjustment of the star*. In fact, this is exactly the procedure followed by UCB when considering perturbations due to a lateral composition gradient $\Delta\mu_{\rm e}/\mu_{\rm e}$. However, UCB chose to identify their fixed-crust *temperature perturbations* with the *Eulerian* perturbations of the elastically deformed star. Why they made such a choice is unclear to us. We do not think this is the correct thing to do, and we are unsure as to why they treated compositional and temperature perturbations differently.

Nevertheless, in order to see where the additional term Eq. (6.45) originates, we refer back to the Lagrangian pressure perturbation equation (6.1), for the two cases whereby the temperature perturbations of the fixed crust are identified with the Lagrangian, or Eulerian, temperature perturbations of the elastically deformed crust. These are written as

$$\Delta P = \left.\frac{\partial P}{\partial \rho}\right|_{T} \Delta\rho + \left.\frac{\partial P}{\partial T}\right|_{\rho} \Delta T\,, \tag{6.46}$$

and

$$\Delta P = \left.\frac{\partial P}{\partial \rho}\right|_T \Delta\rho + \left.\frac{\partial P}{\partial T}\right|_\rho \left[\delta T + \xi^r_{\ell m}(r)\frac{dT}{dr}\right], \tag{6.47}$$

respectively, where we have made use of the definition in Eq. (6.25) to write $\Delta T \equiv \delta T + \xi^r_{\ell m}(r)T'$. These two different identifications of the temperature perturbation may be unified into a single expression for ΔP by making a change in notation as

$$\Delta P = \left.\frac{\partial P}{\partial \rho}\right|_T \Delta\rho + P\boldsymbol{\Delta S} + P z_1 \alpha_4\,, \tag{6.48}$$

where

$$\boldsymbol{\Delta S} = \left.\frac{\partial \ln P}{\partial \ln T}\right|_\rho \frac{\Delta T}{T}\,, \qquad \alpha_4 = 0 \tag{6.49}$$

for a Lagrangian temperature perturbation of the elastically deformed star, and

$$\boldsymbol{\Delta S} = \left.\frac{\partial \ln P}{\partial \ln T}\right|_\rho \frac{\delta T}{T}\,, \qquad \alpha_4 = \left.\frac{\partial \ln P}{\partial \ln T}\right|_\rho \frac{d\ln T}{d\ln r}\,, \tag{6.50}$$

for an Eulerian temperature perturbation. In this sense, our perturbation equations are the same as UCB's when $\alpha_4 = 0$.

6.2.1.1 Boundary conditions and method of solution

The system of coupled equations (6.41a) - (6.41d) presents another boundary value problem which requires a set of four boundary conditions. As we saw in Section 4.8, generally speaking neutron stars are composed of a solid crust bounded by a fluid core and fluid ocean. The computational domain of the elastic calculation is confined to the solid region of the crust, since fluids are incapable of supporting shear stresses (i.e. $\mu = 0$ in the fluid), and therefore cannot contribute to the formation of the mountain.

More precisely, the inner and outer boundaries are determined by the location of the crust-core transition and the crust-ocean transition respectively. Both the crust-core and crust-ocean transitions are determined by the EoS. The location of the crust-core transition for each of the BSk19, BSk20, and BSk21 equations of state are given in Table 2.6.

Determining the location of the crust-ocean transition, however, is a little more complicated. As discussed in Section 4.8, accretion of matter onto the neutron star can cause the outer layers of the crust to melt. Therefore, depending on the assumed rate of accretion of matter onto the neutron star, one should expect that the crust will solidify at different depths (recall Figs 4.19, 4.20, and 4.21 where the solid regions of the star are denoted by dashed lines).

As a reminder, we assume the solid crust to begin at the crust-ocean interface when the ratio of Coulomb energy to thermal energy (Eq. (2.9)),

$$\Gamma_{\mathrm{Coul}} = \frac{Z^2 e^2}{k_B T}\left(\frac{4\pi n_b}{3}\right)^{1/3}, \tag{6.51}$$

exceeds the canonical value 175 for a one component plasma (Haensel et al., 2007).

The boundary conditions which we shall adopt at the two fluid-solid interfaces are taken from UCB. Consider the perturbed Euler equation (6.30), and recall the definitions of the substitution values $z_1 - z_4$ given in Eq. (6.40). At an interface, the radial displacement ξ_r (z_1), as well as both the radial and tangential components of the perturbed traction $\Delta\tau_{rr}$ (z_2) and $\Delta\tau_{r\perp}$ (z_4) must be *continuous*.

At the fluid side of the interface, we require that the Eulerian pressure perturbation $\delta P \equiv 0$. This is a result that we must impose, since we seek to only compute static $(l \neq 0)$ perturbations of the star. Non-zero pressure perturbations in any fluid regions, would, in the absence of any perturbations in the gravitational potential (recall we make the Cowling approximation), or shear stresses $(\mu = 0$ in the fluid) to counterbalance δP, lead to displacements of the fluid and no longer give a static solution.

At each solid-liquid boundary, we must therefore have $\Delta\tau_{rr}(\mathrm{solid}) = \Delta\tau_{rr}(\mathrm{fluid})$. Using the definitions Eq. (6.33) and Eq. (6.25), and the fact that $\delta P \equiv 0$, we can write

$$\begin{aligned} & \Delta\tau_{rr}(\mathrm{solid}) = -\Delta P(\mathrm{liquid}) \\ \Longrightarrow\ & \delta\tau_{rr}(\mathrm{solid}) - \frac{dP}{dr}\xi_{rE} = -\delta P - \frac{dP}{dr}\xi_{rF} \\ \Longrightarrow\ & \delta\tau_{rr} \equiv 0\,. \end{aligned} \tag{6.52}$$

where the subscripts E and F denote the radial displacement on the elastic and fluid sides of the interface respectively. The above result tells us that in order to obtain a static solution, in the Cowling approximation the radial component of the perturbed traction vector $\delta\tau_{rr}$ must be zero at the top and bottom of the crust. This result, combined with the fact that the tangential component of the perturbed traction vector $\delta\tau_{r\perp}$ must vanish in the fluid (see Eq. (6.34) with $\mu = 0$), leads to the set of four boundary conditions

$$
\begin{aligned}
z_2^{\text{crust-ocean}} &= -z_1^{\text{crust-ocean}} \frac{d\ln P}{d\ln r}\,, & z_4^{\text{crust-ocean}} &= 0\,,\\
z_2^{\text{crust-core}} &= -z_1^{\text{crust-core}} \frac{d\ln P}{d\ln r}\,, & z_4^{\text{crust-core}} &= 0\,.
\end{aligned}
\tag{6.53}
$$

We will again use `solve_BVP` for the integration, with initial guesses for z_{1-4} constructed by fixing them to an order of magnitude estimate of the results ofUCB (*cf.* their Figs. 10 - 12).

6.2.1.2 Computing the mass quadrupole moment

From the solution of Eqs. (6.41a) and (6.41d), we then require a method to obtain the corresponding density perturbation $\delta\rho$ associated with the pressure perturbations in the crustal lattice from the local temperature variations. This may be done in two separate ways, either using the perturbed continuity equation (6.31), or the radial projection of the perturbed Euler equation (6.38), and writing them down in terms of the substitution variables z_{1-4}. These methods yield the respective result

$$
\delta\rho_{\ell m}(r) = -\left[z_1 r\frac{d\rho}{dr} - \rho\left(r\frac{dz_1}{dr} + 3z_1 - \beta^2 z_3\right)\right],
\tag{6.54}
$$

or

$$
\begin{aligned}
\delta\rho_{\ell m}(r) = \frac{1}{g}\Bigg[&\frac{d(Pz_2)}{dr} + \frac{d(PVz_1)}{dr}\\
&- \frac{4\mu}{r}\left(z_1 + \frac{d(z_1 r)}{dr}\right) - \frac{\beta^2}{r}\left(Pz_4 + 2\mu z_3\right)\Bigg].
\end{aligned}
\tag{6.55}
$$

The mass quadrupole Q_{22} may then be obtained by integrating either of Eqs. (6.54) - (6.55), as per Eq. (3.34). The resulting expressions are (Ushomirsky et al., 2000)

$$
Q_{22} = 2\int_{r_{\text{crust-core}}}^{r_{\text{crust-ocean}}} \rho[z_1 + 3z_3]r^4 dr - (\rho z_1 r^5)|_{r_{\text{crust-core}}}^{r_{\text{crust-ocean}}}\,,
\tag{6.56}
$$

and

$$
\begin{aligned}
Q_{22} = -\int_{r_{\text{crust-core}}}^{r_{\text{crust-ocean}}} \frac{\rho}{\tilde{V}}\Bigg\{&6z_4 - 2\frac{\mu}{p}\left[2\frac{dz_1}{d\ln r} + 6z_3\right]\\
&+ (6-\tilde{U})(z_2 - \tilde{V}z_1)\Bigg\} r^4 dr\,,
\end{aligned}
\tag{6.57}
$$

where $\tilde{U} = (d \ln g / d \ln r) + 2$, from which the final ellipticity ε may then be computed as (Eq. (3.37))

$$\varepsilon = \sqrt{\frac{8\pi}{15}} \frac{Q_{22}}{I_{zz}}, \tag{6.58}$$

with $I_{zz} \approx 10^{45}$ g cm^{-3}. To test the accuracy of our solver, we use both Eqs (6.56) and (6.57) in order to calculate the mass quadrupole, which we obtain via a simple Simpson's method using the values of $z_1 - z_4$ computed via `solve_BVP`. Whilst Eqs (6.56) - (6.57) are mathematically equivalent, in general we find agreement between the two methods to be in the region $\lesssim 1\%$ for all of our NS models.

To provide further confidence in our results, it is possible to recast Eq. (6.57) as an additional ODE by taking derivatives of both sides, such that

$$\begin{aligned} \frac{dQ_{22}(r)}{d \ln r} = -\frac{\rho}{\tilde{V}} \Bigg\{ & 6z_4 - 2\frac{\mu}{p}\left[2\frac{dz_1}{d\ln r} + 6z_3\right] \\ & + (6 - \tilde{U})(z_2 - \tilde{V} z_1) \Bigg\} r^5, \end{aligned} \tag{6.59}$$

where $Q_{22}(r)$ is the *cumulative* mass quadrupole, with the *total* mass quadrupole (equivalent to both Eqs (6.56) and (6.57)) being $Q_{22} = Q_{22}(r = r_{\text{crust-ocean}})$, the value of $Q_{22}(r)$ at the crust-ocean interface.

This additional ODE may be solved simultaneously in conjunction with the perturbation equations (6.41a) - (6.41d) once an additional boundary condition has been specified (since the system becomes a total of five equations rather than just four). A natural choice is the condition that $Q_{22}(r = r_{\text{crust-core}}) = 0$, since at the transition from the base of the solid crust to the liquid core the shear stresses must vanish.

The benefit of this approach is that it eliminates any potential truncation errors when numerically integrating Eqs (6.56) - (6.57), which is a possible cause for the discrepancies between the two results. Instead, errors are controlled internally by the `solve_BVP` method itself on the same mesh used to compute $z_1 - z_4$, where the desired tolerance of the solution is controlled manually.

Encouragingly, we find agreement between the solution to Eq. (6.59) obtained from `solve_BVP` and Eq. (6.57) obtained via the Simpson rule to be $\lesssim 0.1\%$. This suggests that a truncation error is not the cause of the discrepancy between Eqs. (6.56) - (6.57). Instead, we attribute the difference to round-off errors in computing Eq. (6.56), which essentially involves subtracting two large numbers (in excess of 10^{30}) to get a single, smaller number. This was a similar problem encountered by UCB themselves, where it was noted that 'round-off errors [on Eq. (6.56)] can cause trouble if the relaxation mesh is not fine enough and uniform'.

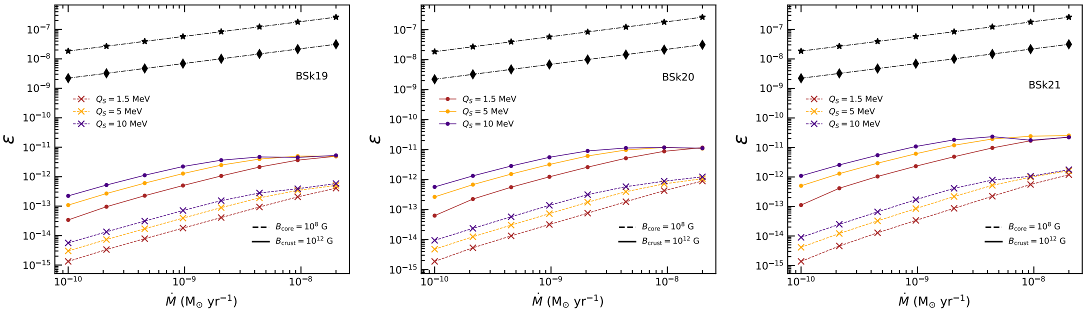

FIGURE 6.3: Ellipticity of a number of magnetised neutron stars assuming the BSk19 (*left*), BSk20 (*centre*) and BSk21 (*right*) equations of state (with properties listed in Table 4.3) as a function of the mass accretion rate $\dot{M}$. Different amounts of assumed shallow crustal heating, ranging from 1.5 - 10 MeV, are indicated in the legend. Solid lines (filled circles) denote NS models that assume a $B = 10^8$ G internal *core* toroidal magnetic field (Eq. (5.41) with $R_{\rm B,\,min} = R_{\rm IB}$), whilst dashed lines (crosses) denote models that assume a $B = 2 \times 10^{12}$ G internal *crustal* toroidal magnetic field (Eq. (5.41) with $R_{\rm B,\,min} = R_{\rm crust-core}$). Dashed-dotted lines show the ellipticity required for gravitational-wave torques to determine the spin-equilibrium (as calculated via Eq. (3.38)) of accreting neutron stars with spin frequencies 300 Hz (filled stars) and 700Hz (filled diamonds), as a function of $\dot{M}$.

6.3 Thermal mountains on accreting neutron stars

With all the necessary pieces assembled, we now outline solutions to the crustal perturbation equations (6.41a) - (6.41d). In Section 5.5 we identified that the assumed level of accretion and amount of shallow heating were crucial to producing larger temperature perturbations for a given magnetic field configuration (recall Figs 5.3, 5.4, and 5.8). In Fig. 6.3, we therefore present results for the ellipticity ε, computed from Eqs (6.56) - (6.57), via Eq. (3.37), for each of the low-mass neutron star models listed in Table 4.3 (i.e. the same as those considered in Fig. 4.19 for the background thermal structure) as a function of the mass accretion rate $\dot{M}$, for different assumed values of the shallow crustal heating parameter $Q_{\rm S}$. Solid lines correspond to models assuming a $B = 2 \times 10^{12}$ G *crustal* magnetic field, whilst dashed lines indicate models that assume a $B = 10^8$ *core* magnetic field, as per Eq. (5.41).

The ellipticities generated via the thermal lattice pressure perturbations (sourced via anisotropic heat conduction) are small - at least relative to theoretical ‘maximum’ elastic mountain[8] $\varepsilon_{\rm max} \sim 10^{-7}$ - and particularly negligible ($\varepsilon \lesssim 10^{-12}$) at low accretion rates ($\dot{M} \lesssim 10^{-10}\, M_\odot$ yr^{-1}) for both the core and crustal magnetic fields. This is for two reasons, which can be understood in reference to the source term Eq. (6.44), and the fact that the majority of the mass quadrupole is likely built in the deep crust, since this is where the majority of the crust’s mass is contained (and hence where the largest density perturbations should be generated).

---

[8] Though, one should again bear in mind that the maximum mountain estimates assume that the ‘forcing term’ that gives the star its non-spherical shape can be arbitrarily large, unlike the source terms we consider here which are fixed by a number of different physical constraints (e.g. temperature, magnetic field strengths, shallow crustal heating, etc.).

First of all, the ratio $P_{\rm th}/P$ in the deep crust is $\lesssim 10^{-5}$ for the temperatures $T < 10^9$ K relevant to our accreting stars (Figs 6.2 and 4.19). This suggests that the lattice pressure in this region is inconsequential to the total pressure, which is instead overwhelmingly dominated by the contribution from unbound neutrons. Secondly, in the case of the core magnetic field, the temperature asymmetry in the deep crust is only $\delta T/T \lesssim 10^{-2}$ % (Fig. 5.3; and recall that we are restricted to $B_{\rm core} \lesssim 10^8$ G in order for the thermal perturbation equations (5.29) - (5.38) to be valid; Sec. 5.3.1). A similar situation persists in the case of the crustal magnetic field, although the temperature asymmetry near the neutron drip point ($\sim 10^{11}$ g cm^{-3}) is ~ 1%, in the deep crust it is only $\lesssim 0.1$% (Fig. 5.4).

The general behavior is for ε to increase with the rate of mass accretion, as well as being enhanced for greater amounts of shallow crustal heating at a given accretion rate. This is simply because the amount of heat deposited in the crust is measured per accreted nucleon, and therefore the crust is naturally hotter when the accretion rate is larger. We find the largest ellipticity to be $\varepsilon_{\rm max} = 2.32 \times 10^{-11}$, obtained with the BSk21 equation of state with an accretion rate $\dot{M} = 4.4 \times 10^{-9}\, M_\odot$ yr^{-1} and shallow heating term $Q_{\rm S} = 10$ MeV.

While the *general* trend is for the ellipticity to increase with the accretion rate, there is in fact a cut off point at $\sim 5 \times 10^{-9}\, M_\odot$ yr^{-1}, where ε for different values of the shallow heating parameter converge for a given magnetic field configuration. The reason for this behavior is that at such high accretion rates the amount of heat being deposited into the crust is in fact large enough to melt the crust at densities $\rho \lesssim 10^{12}$ g cm^{-3}, and so only the inner crust contributes to the formation of the mass quadrupole. The temperature in the deep crust ($\sim 10^{14}$ g cm^3) is relatively insensitive to the amount of shallow crustal heating (see the left-hand panel of Fig. 4.21) since the additional heat is only deposited at densities $\rho < 10^{10}$ g cm^{-3} (Sec. 4.3.2). Since the lattice pressure is very much dependent on the temperature (Fig. 6.2), the ratio $P_{\rm th}/P$ in the deep crust is therefore effectively independent of $Q_{\rm S}$ at high accretion rates. For similar reasons, the temperature perturbations in the deep crust are also largely independent of $Q_{\rm S}$ (at least at high accretion rates). This is especially true of the perturbations sourced by the crust-only magnetic field, since the inner boundary condition in the perturbed thermal structure model (Sec. 5.4.1) requires that $\delta T \to 0$ at the crust-core transition (see Fig. 5.4), irrespective of $Q_{\rm S}$ (and in fact $\dot{M}$ as well).

6.3.1 The torque balance limit

In order to gauge the significance of these results, we also plot in each panel of Fig. 6.3 the value of the ellipticity required to reach the gravitational-wave torque-balance limit Eq. (3.38) (recall the discussion surrounding the torque-balance limit in Sec. 3.2.1) as a function of the accretion rate, assuming rotation at 300 Hz (filled stars) and 700 Hz (filled diamonds). The ellipticity required to dictate the spin-equilibrium from GW emission is in the region $\tilde{\varepsilon} \sim 10^{-9} - 10^{-7}$, and therefore many orders of magnitude larger than the expected ellipticity generated by the magnetic field and thermal lattice pressure.

Despite the ellipticity (mostly) increasing in our model at larger rates of mass accretion (since the star is hotter), the ratio $\tilde{\varepsilon}/\varepsilon$ does not change much as $\dot{M}$ increases. This is because accretion torques on the NS naturally increase with $\dot{M}$ ($N_{\rm GW} \approx \dot{M}\sqrt{GMR}$; Eq. (3.23)), necessitating larger GW torques (and therefore a larger mountain) to maintain torque balance (hence $\tilde{\varepsilon} \propto \dot{M}$ in Eq. (3.38)).

The result Eq. (3.38) however assumes that 100% of the spin-down energy from the NS is radiated away as GWs. Recall that the true picture, however, is complicated by the fact that exactly how matter is transported from an accretion disk to the surface will be determined by the external dipolar magnetic field. The possibility of accretion leading to spin-down torques in the so-called 'propeller regime' (Sec. 3.2.2), can cause the accretion flow to be centrifugally inhibited, resulting in accreted matter being expelled from the disk rather than being brought down to the NS surface.

The ellipticity for torque balance $\tilde{\varepsilon}$ would therefore necessarily be larger or smaller than Eq. (3.38) depending on whether the external magnetic field is providing spin-up or spin-down torques. Recall also from Section 3.2.2 that studies such as Andersson et al. (2005) indicate the magnetic-spin equilibrium model alone cannot uniquely describe the observed spin-rates of *strongly* accreting NSs. It is therefore possible that the mountains generated via the internal magnetic field and the lattice pressure are still playing *some* role in the overall setting of the spin-equilibrium of accreting neutron stars, but are not the 'dominant' source of the spin-down torques.

Indeed, as a result of increasing sensitivity of GW detectors (as well as improved search algorithms), continuous GW searches are now in fact probing the torque balance limit of spinning neutron stars. The most recent example of this was the model-based search for continuous GWs from the LMXB Scorpius X-1 performed by Abbott et al. (2022b). Whilst no concrete detection was made, upper limits on the gravitational-wave strain were set as a function of the GW frequency $f_{\rm GW} = 2\nu_s$ (since the spin-frequency of Scorpius X-1 is currently unknown). Assuming optimal orientation (i.e. where the spin of the NS is aligned with the orbital angular momentum), the most stringent limit on the gravitational-wave amplitude was set in the region $f_{\rm GW} = 100 - 200$ Hz (see their Fig. 6), with $h_0 \sim 4 \times 10^{-26}$ (corresponding to an ellipticity $\varepsilon \sim 7 \times 10^{-6}$), which is below the specific torque-balance predictions for Scorpius X-1 (based on measurements of its X-ray flux) from 40 to 200 Hz.

In addition, whilst it is not an accreting system, another recent study by Abbott et al. (2021c) has as well beaten the GW spin-down limit for the young X-ray pulsar PSR J0537-6910, finding that gravitational-waves from a mountain on the star can only account for less than 14% of the total spin-down energy budget. The spin-down limit for both the Crab and Vela pulsars have also been surpassed, indicating that mountains can only be responsible for $\lesssim 1\%$ and $\lesssim 10\%$ of their respective total energy budgets (Aasi et al., 2014).

6.3.2 Thermal lattice pressure vs. capture layer shifts

To further put our results into perspective, it is helpful to compare the relative sizes of the mass quadrupole generated via the lattice pressure to those generated from the direct shift of capture layers as considered in UCB (and Bildsten, 1998; Sec. 3.2.2.1). The ellipticity associated with the mass quadrupole generated in a *single* capture layer is, as per UCB,

$$\varepsilon_{\mathrm{fid}} = 1.6 \times 10^{-10} \left(\frac{R}{10\,\mathrm{km}}\right)^4 \left(\frac{\delta T/T}{1\%}\right) \left(\frac{E_{\mathrm{cap}}}{30\,\mathrm{MeV}}\right)^3 , \tag{6.60}$$

where E_{cap} is the threshold energy, equivalent to the value of the electron chemical potential μ_e at the nuclear transition $(A_1, Z_1) \longrightarrow (A_2, Z_2)$.

The *total* mass quadrupole of the neutron star is a linear sum of the individual quadrupole moments generated in each capture layer. UCB assumed, in part, the composition of an accreted crust predicted by the HZ90 model. By summing over the total number of capture layers (19) that are listed in Table 2 of Haensel and Zdunik (1990b), an upper limit on the total ellipticity from capture layer shifts can be estimated as

$$\varepsilon^{\mathrm{HZ90}}_{\mathrm{tot}} \sim 1.6 \times 10^{-10} \sum_{i}^{19} \left[\frac{E^{i}_{\mathrm{cap}}}{30\,\mathrm{MeV}}\right]^3 \approx 5.2 \times 10^{-9} . \tag{6.61}$$

Depending on the rate of mass accretion and the spin frequency of the NS, the above result can be anywhere from 1 – 4 orders of magnitude below the torque balance limit Eq. (3.38).

However, the above estimate Eq. (6.61) may become even smaller if one considers more realistic estimates of the temperature asymmetry $\delta T/T$ present within accreting neutron stars. UCB did not model the formation of such asymmetries, instead assuming $\delta T/T \sim 1\%$ *a priori* in Eq. (6.60). Modelling of temperature asymmetries using magnetic fields (Sec. 5.5) suggests that such asymmetries may only be achieved with internal magnetic fields in excess of 10^{12} G, a few orders of magnitude larger than observational inferences of the external field ($\sim 10^9$ G).

In order to generate mass quadrupole moments which *do* probe the torque balance limit, UCB were forced to extrapolate to larger values of E_{cap}, and add additional ‘artificial’ capture layers with A and Z $(88, 22) \longrightarrow (82, 20)$ near the bottom of the crust. They found that captures layers with $E_{\mathrm{cap}} \gtrsim 90$ MeV could (even individually) in fact generate mass quadrupoles in excess of 10^{38} g cm^2 ($\varepsilon \sim 10^{-7}$).

Modern descriptions of the accreted crust, however, do not provide substantiation for the existence of such capture layers. The F+18 model for example - an improvement over the original HZ90 model (Sec. 2.4.2) - predicts the maximum threshold energy to be just $E^{\mathrm{F+18}}_{\mathrm{max}} = 69.10$ MeV. Moreover, recall that the GC20 model (Sec. 2.5.2.1) suggests that actually the EoS of the accreted crust at high density is much closer to that of the non-accreted crust. Their model predicts that unbound neutrons moving freely throughout the inner crust also leads to a composition that is largely similar to that of the ground-state inner crust (see their Fig. 5). Crucially, their model suggests that explicit capture layers only extend to densities $\lesssim 4 \times 10^{11}$ g cm^{-3}, the approximate location of the traditional neutron drip point (see Tables 1 and 2 in Potekhin et al., 2023), and that $E_{\mathrm{max}}^{\mathrm{GC20}} \approx 25.5$ MeV.

If, for the sake of simplicity, one therefore restricts the crustal composition of the HZ90 model to include only capture layers at densities $\rho < 4 \times 10^{11}$ g cm^{-3}, then the estimate Eq. (6.61) reduces to just

$$\varepsilon_{\mathrm{tot}}^{\mathrm{HZ90}} \lesssim 1.6 \times 10^{-10} \sum_{i}^{4} \left[\frac{E_{\mathrm{cap}}^{i}}{30\,\mathrm{MeV}} \right]^{3} \approx 1.1 \times 10^{-10}\,, \tag{6.62}$$

and is therefore well below even the most conservative estimate of the torque-balance limit. The 'less than' symbol in Eq. (6.62) also makes explicit the assumption of $\delta T/T \sim 1\%$, and therefore that the 'true' ellipticity could be many orders of magnitude smaller still.

These differing possibilities are summarised in Table 6.2. Estimates of the neutron star ellipticity via means of physical capture layer shifts (through the estimate Eq. (6.60)) are given, for the cases whereby the capture layers are confined to the outer crust, or extend into the inner crust, following the compositional information found in Haensel and Zdunik (1990a), Fantina et al. (2018), and Potekhin et al. (2023) respectively. The corresponding ellipticity generated via the thermal lattice pressure as presented in this thesis for the F+18 models (i.e. BSk19, BSk20, and BSk21) are also given. For the purposes of a fair comparison, we have assumed a fixed temperature perturbation $\delta T/T = 1\%$ (rather than sourcing the perturbation via the magnetic field), a time-averaged accretion rate of $10^{-8} M_{\odot}$ yr^{-1}, and shallow heating term $Q_{\mathrm{S}} = 0$ MeV, in order to re-create the original choices made in UCB.

Clearly, the ellipticity is largest when capture layers extend into the deep crust, reaffirming the conclusions of UCB that it is the high-density region of the crust where most of the mass quadrupole is generated. It may be seen that there is a reduction in the ellipticity by roughly two orders of magnitude when the capture layers are confined to just the outer crust in each model.

It is also likely that estimates of ε in the outer crust due to capture layer shifts in Tab 6.2 are in fact overestimated by Eq. (6.60), even at a fixed δT. As noted in UCB, there can be a change of sign in Q_{22} when going from shallow to deep capture layers (see their Fig. 14), in which case some capture layers in the outer crust may even cancel each other out, and thus potentially not produce any contribution to the star's total quadrupole moment at all[9]. It is therefore possible that the quadrupole moment generated via perturbations in the crystal lattice pressure is comparable in magnitude to that of the displacement of shallow capture layers. Though, in order to confirm this one would, ideally, compute the mass quadrupole from both the lattice pressure and the

---

[9] This is less likely to be a problem in the deep crust since contributions from individual capture layers there, if they exist, are much larger than those in the outer crust, and thus dominate.

Table 6.2: Comparison of thermal mountain sizes (in terms of the ellipticity ε; Eq. (3.37)) generated via physical capture layer shifts (as derived by Ushomirsky et al., 2000) and thermal lattice pressures (Sec. 6.1.1) for three different equation of state models: GC+20 (Gusakov and Chugunov, 2020, 2021), HZ+90 (Haensel and Zdunik, 1990a,b), and F+18 (Fantina et al., 2018, 2022). The ellipticity from capture layer shifts is computed via Eq. (6.60) in both the full crust, as well as just the outer crust for HZ90 and F+18, in order to compare with the GC20 neutron Hydrostatic and Diffusion model which predicts no capture layers in the inner crust (Sections 2.5.2.1 and 6.3.2). All calculations assume a fixed temperature asymmetry $\delta T/T = 1\%$ and mass accretion rate $\dot{M} = 10^{-8}\,M_\odot\ \mathrm{yr}^{-1}$.

	Ellipticity from Capture Layer Shifts Eq. (6.60)		Ellipticity from Thermal Lattice Pressure Fig. 6.3
EoS	Full Crust	Outer Crust	Full Crust
GC20	-	2.6×10^{-10}	-
HZ90	5.2×10^{-9}	1.1×10^{-10}	-
BSk21 (F+18)	3.9×10^{-9}	9.2×10^{-11}	2.8×10^{-11}
BSk20 (F+18)	3.1×10^{-9}	9.6×10^{-11}	1.5×10^{-11}
BSk19 (F+18)	4.1×10^{-9}	9.2×10^{-11}	8.7×10^{-12}

displacement of capture layers simultaneously (i.e. within the same physical framework), rather than making comparisons with the estimate Eq. (6.60).

6.3.3 Thermal mountains vs magnetic mountains

Lastly, we can make one final comparison of our results of the ellipticities produced via the magnetic field for *thermal* mountains, to those generated by a ‘conventional’ *magnetic mountain* where Lorentz forces directly produce the distortion (Sec. 1.3.3.1). In particular, for a NS with a superconducting core, OJ20 estimated (*cf.* their Eq. (52)), from earlier results obtained by Cutler (2002) (their Eq. (2.6)), that the ellipticity of a magnetic mountain is

$$\varepsilon \sim \frac{BH_{c1}R^4}{GM^2} \approx 2\times10^{-13}\,B_8\,, \tag{6.63}$$

where H_{c1} is the known as the ‘first critical field’ ($\sim 10^{15}$ G).

Since our results depend on additional parameters other than just the magnetic field strength however (i.e the accretion rate, shallow heating, etc.), making such a meaningful comparison is not straightforward. One particular scenario in which a material comparison can be made, however, is if we assume that the accretion rate is quite high, and that there exists a crustal magnetic field $B_\mathrm{crust} = 10^{12}$ G. In this case, we can compare the magnetic mountain Eq. (6.63) with the thermal mountains in Table 6.2, sourced by both the thermal lattice pressure, as well as the estimates of ε from physical capture layer shifts (through Eq. (6.60)), since $\delta T/T \sim 1\%$ when $\dot{M} \sim \dot{M}_\mathrm{Edd}$ and $B_\mathrm{crust} = 10^{12}$ G (Fig. 5.12).

When $B_{\mathrm{crust}} = 10^{12}$ G, we have for the magnetic mountain $\varepsilon_{\mathrm{mag}} = 2 \times 10^{-9}$ as per Eq. (6.63), and, averaging across each EoS model in Table 6.2, we have for each individual case:

- $\bar{\varepsilon}_{\mathrm{cap}} \approx 4 \times 10^{-9}$ for the physical shifts of capture layers in the inner and outer crust (left column),
- $\bar{\varepsilon}_{\mathrm{cap}} \approx 1 \times 10^{-10}$ for the physical shifts of capture layers in just the outer crust (centre column),
- $\bar{\varepsilon}_{\mathrm{lat}} \approx 2 \times 10^{-11}$ for the thermal lattice pressure in the inner and outer crust (right column).

This suggests, assuming temperature asymmetry at the percent level, that the magnetic mountains are comparable in size to thermal mountains generated through the displacements of capture layers in the *inner crust* (assuming capture layers really are present in the inner crust; recall the discussion in the previous section), but an order of magnitude or so larger if the capture layers are confined to just the outer crust, or when the mass quadrupole is assumed to be built from the thermal crustal lattice pressure.

7

Concluding Remarks

In this thesis we have sought to model the interior of accreting neutron stars, which are theorised to have their spin frequencies limited by the emission of gravitational-waves. The work presented here can be divided into the theoretical formulation, and then numerical implementation, of a method to calculate the ellipticity of these stars, which is of observational significance to the LIGO-Virgo-KAGRA Collaboration in their search for continuous GWs.

The main results of this thesis are fourfold. First, we have expanded upon the first-principles mechanism originally developed by Osborne and Jones (2020) for generating asymmetric temperature distributions due to anisotropic heat conduction from quadrupolar toroidal magnetic fields. We have extended the computational domain of the calculation from (only) the crust to the entire star, incorporating more realistic microphysics, and introducing a self-consistent method to include the effects of baryon superfluidity/superconductivity on the background (and perturbed) thermal structure. Second, we have identified a small temperature-sensitive contribution to the total pressure within the crust that originates from the ionic lattice of the crust, in order to generate pressure perturbations from the aforementioned temperature asymmetry. Third, we have combined these two mechanisms to produce the *first fully self-consistent* calculation of the size of thermal mountains that is consistent with known physics of accreting NSs. Fourth, we have found that the size of the mass-quadrupole induced by these two processes are likely insufficient to be dictating the spin-equilibrium of accreting neutron stars.

Over the next few pages we shall briefly summarise some key conclusions (specifically from Chapters 5 and 6) that serves to elucidate the main results listed above. Then, in the final pages of this thesis, we will identify a number of caveats within the current model in order to better understand its current limitations, and outline ways in which, in future work, it might be further refined.

7.1 Summary of temperature asymmetries from magnetic fields

In OJ20, crustal magnetic field strengths in excess of 10^{13} G were required to produce temperature perturbations at the percent level (the minimum amount of asymmetry required by UCB to produce significant GW emission; Sec. 5.6), pushing outside the regime where their method was valid (Sec. 5.3.1). We contrast their results with the ones presented here (Figs 5.3 - 5.11). Under this new analysis, the presence of a magnetic field in at least some region of the core raises the expected level of temperature asymmetry in the deep crust by up to 3 orders of magnitude (depending on the mass of the NS and the mass accretion rate). To provide confidence in these new results, we have also shown that when we again restrict the magnetic field to just the crust (whilst keeping the computational domain the same), the magnitude of the temperature perturbations reduce to the same order of magnitude as those found in OJ20 (compare our Fig. 5.4 with Fig. 5.5; their Fig. 4).

In extending the computational domain of the calculation, we have been able to introduce a more realistic description of the un-magnetised thermal background of the star. We have included many more relevant neutrino emission and thermal transport mechanisms applicable to a NS composed of standard npeμ matter (Secs 4.4 - 4.5), in line with the current understanding of cooling theory of neutron stars in LMXBs (e.g. Ootes et al., 2018). For completeness, we have also implemented a self-consistent calculation on the level of superfluidity to account for the suppression of both thermal transport and neutrino emission mechanisms in sufficiently cool stars.

We have presented our results for three different modern accreting equations of state, provided by Fantina et al. (2018, 2022) (and Potekhin et al., 2013 for calculations associated with the core). One possibility we have not been able to properly explore, given the perturbative nature of our approach, is that the presence of extremely efficient Durca neutrino processes (assuming the BSk21 EoS, for stars heavier than 1.6 $M_{\odot}$) may lead to much larger temperature asymmetries due to enhanced thermal conductivity which raises the magnetisation parameter Eq. (5.8) - which is proportional to the source term Eq. (5.43) - by many orders of magnitude (Fig. 5.2). This means that the same level of asymmetry may be achieved when Durca is active for a comparatively weaker magnetic field than when the process is forbidden, since the magnetisation parameter (Eq. 5.8) is proportional to both the scattering relaxation time τ (which is itself proportional to the thermal conductivity Eq. (4.10)) as well as the strength of the magnetic field B.

For all our background models, we have also computed the Coulomb parameter Eq. (2.9), which tracks the state of the ions in the crust at a given density, and serves to demarcate the computational domain of the elastic calculation (Sec. 6.2.1.1). It is clear that the temperature in the crust depends strongly on the rate of mass accretion and, to a lesser extent, the presence of additional shallow heating in the outer layers of the crust. The heating associated with these two quantities naturally increases the temperature of the crust, which will melt if $\Gamma_{\text{coul}} < 175$ (assuming the one-component plasma approximation). If the inner crust ($\rho \gtrsim 10^{13}$ g cm^{-3}) is molten, a mountain cannot be created since the resultant fluid would not be capable of supporting shear stresses. However, we find that $\Gamma_{\text{coul}} \geq 175$ for all our NS models at densities $\rho \gtrsim 10^{11}$ g cm^{-3} (Fig. 5.8), indicating the inner crust is always solid (at least for temperatures of a typical LMXB) and therefore, in principle, capable of supporting elastic strains.

We choose to quote many of our results for the temperature perturbation δT in Chapter 5 at the fiducial density $\rho = 10^{13}$ g cm^{-3} since it lies near three pycnonuclear reactions in the inner crust (Tables A.1 - A.3). This was a natural choice, for two reasons: (i) it is in this density region in which UCB found the largest mass quadrupoles were generated via physical capture layer shifts, and (ii) these two reactions account for $\sim 80\%$ of the total heat released from deep crustal heating reactions in the entire crust (Sec. 4.3.1).

In comparison to the results obtained by OJ20, we find these new results to be encouraging. Though we have been unable to produce the 1% temperature asymmetry originally required by UCB for the majority of our NS models in order to reach the torque-balance limit Eq. (3.38), we have shown that 1% temperature asymmetry within the accreted crust may be achieved for strongly accreting NSs, if the strength of the *crustal* magnetic field can exceed slightly above 10^{12} G. We have also shown that asymmetries of the order $\sim 10^{-2}\%$ can be produced from *core* magnetic fields of just 10^{8} G. Given that core magnetic fields in principle could be much larger than this, it is not inconceivable that a non-perturbative calculation with stronger magnetic fields could yield temperature asymmetries at the percent level or above.

7.2 Summary of thermal pressure perturbations generated in the crystalline crust

In the first chapter of this thesis (specifically Sec. 1.3.3.2), we outlined two of the primary questions surrounding the feasibility of detecting continuous gravitational-waves from elastic mountains in the near future, namely: (i) the largest possible elastic strains that the neutron star crust could feasibly sustain, and (ii) what physical processes might be taking place inside the star in order to build the necessary strains to begin with.

In answer to the second question, we have sought to produce the first fully self-consistent calculation of the ellipticity of accreting LMXBs due to the formation of a *sourced* ‘thermo-elastic’ mountain. Many aspects of our calculation have drawn inspiration from the seminal model of thermal mountains presented in Ushomirsky et al. (2000) (the UCB model), which we have either sought to improve, or re-work entirely. UCB showed, under certain conditions, that it is possible for the ellipticites of accreting neutron stars to exceed 10^{-7} due to shifts of capture layer in regions of the star that are, on average, locally hotter or colder. This was achieved by introducing some temperature dependence on the cold-matter equation of state as $P = P\big(\rho, \mu_e[\rho, T]\big)$, with $\mu_{\text{e}} \equiv E_{\text{cap}}$ determining at what depth electron captures may take place in the zero-temperature limit (Sec. 2.4.2 and Sec. 3.2.2.1).

Yet, as pointed out in Section 6.3.2, these results are predicated on the assumptions of temperature asymmetry being present at the percent level (i.e. $\delta T/T \sim 1\%$), as well as the existence of capture layers well beyond that predicted by modern equations of state. Indeed, when one considers only the capture layers predicted by such realistic EoSs, the ellipticities are reduced to $\sim 10^{-9}$ in the 'traditional' approach to computing the EoS (i.e. the Fantina et al. (2018) model), and reduced even further to $\sim 10^{-10}$ in the neutron Hydrostatic and Diffusion model of Gusakov and Chugunov (2020) (Table 6.2). It is worth reinforcing that these numbers also represent upper limits, since Table 6.2 also assumes a fixed $\delta T/T \sim 1\%$, and the ellipticity from capture layers shifts Eq. (6.60) scales linearly in $\delta T/T$.

We have instead explored here a method to generate pressure perturbations in the accreted crust via a simpler dependence of temperature on the EoS - $P = P(\rho, T)$ - that does not require the resolution of individual capture layers[1]. Specifically, we have computed the size of the deformations built via elastic strains arising from a thermal contribution to the crustal lattice pressure (produced through interactions of ions with the electron gas, as well as other ions; Sec. 6.1.1), sourced via a *modelled* non-axisymmetric temperature distribution (i.e. rather than assumed, like in UCB) generated by a quadrupolar internal magnetic field (Sec. 5.1).

We have considered the mass quadrupole moment generated in LMXBs accreting at different rates, as well as taking into account the presence of shallow crustal heating, in order to explore the parameter space derived from observations of many different accreting neutron stars. In general, we find that even the most optimistic estimates of the ellipticity (i.e. in strongly accreting neutron stars) from this mechanism are just $\varepsilon \lesssim 10^{-11}$ (Fig. 6.3), and many orders of magnitude away from the torque balance limit Eq. 3.38 ($\tilde{\varepsilon} \sim 10^{-8}$), as well as the theoretical upper limit (or 'maximum mountain') that currently sits at around $\varepsilon \sim 10^{-6} - 10^{-7}$ (Gittins et al., 2021; Gittins and Andersson, 2021; Morales and Horowitz, 2022). Given that the current *observational* upper limit on the ellipticity of accreting millisecond pulsars is $\sim 10^{-7}$ (Abbott et al., 2022a), it could therefore be the case that detecting 'real' thermal mountains will require GW interferometers with much greater sensitivities beyond current and possibly near-future capabilities.

7.3 Outlook

Here we discuss some possible followups to the work presented in this thesis. There are a number of caveats in our current model which we have hinted at throughout the thesis that should not be overlooked. These include, but are not limited to: (i) The use of a simple outer boundary condition in both the background and perturbed problems (Sections 4.7.1 and 5.4.1 respectively), (ii) a lack of an understanding of the magnetic field evolution itself in old accreting neutron stars (Sections 2.3, 5.3, and 5.6), (iii) further improved microphysics (see below), and

---

[1] In the 'traditional' approach to computing the zero-temperature accreted equation of state (HZ90, HZ08, F+18), the capture layers are assumed to be infinitely thin (Sec. 2.4.2). We have made use of this approximation throughout this thesis; most notably to simplify our description of the deep crustal heating processes (Sec. 4.3.1), as well as the crustal thermal conductivity, through the impurity parameter Q_{imp} (Sec. 4.4.1).

(iv) the incongruity in applying the Newtonian heat equation and Newtonian Euler equation on to a general relativistic hydrostatic background (Sec. 6.2).

7.3.1 Extending the background model

First let us review some additional steps necessary towards a more complete calculation of the thermal background, building upon the framework described in Chapter 4.

Outer boundary condition**:** In computing the background thermal structure, we followed the prescription of UCB and assumed that the outer boundary condition was fixed by the temperature at the base of the hydrogen/helium burning layer at $\rho \sim 10^7\ \mathrm{g\,cm^{-3}}$. However, as discussed in Section 4.7.1, the boundary condition Eq. (4.125) is, strictly speaking, only valid when the NS is steadily accreting (i.e. where $\dot{M} \gtrsim 0.1\dot{M}_{\mathrm{Edd}}$). In order to apply the boundary condition at low accretion rates, it was necessary to interpret $\dot{M}$ as a *time-averaged* accretion rate, such that we could, in effect, average over multiple Type-I X-ray bursts that occur when the star is not steadily accreting (Sec. 4.1).

A more rigorous approach would involve further extending the computational domain of the calculation to include the low-density ocean, where the temperature would be determined by the compression of accreted material as it arrives at the star's surface (see Bildsten and Cutler, 1995 and Brown and Bildsten, 1998).

Microphysics**:** Throughout our analysis we have adopted the equations of state derived from the set of Brussels–Montreal energy-density functionals BSk19, BSk20, and BSk21. The composition tables provided by Fantina et al. (2018) and unified pressure-density relations presented in Fantina et al. (2022) allowed us to implement a realistic and self-consistent calculation of the crust *and* core that has been absent in previous works on modelling neutron star thermal mountains.

These models, however, are to some degree restrictive, and do not capture a number of pieces of physics that are expected to affect the thermal structure. For one, the BSk models assume the one-component approximation at each crustal layer. More realistic *multicomponent* models have recently recently been considered by a number of authors (e.g. Lau et al., 2018; Shchechilin and Chugunov, 2019; Schatz et al., 2022). Incorporating such models into our work would not only allow for a better justification of the method to smear heat deposited via DCH reactions (Sec. 4.3.1), but also provide a better description of the effects on thermal conductivity due to the presence of impurities in the crustal layers (see Eq. (4.15) and Fig. 5.8).

Additionally, the BSk models also neglect the redistribution of unbound neutrons in the deep crust. Such an effect, particularly in the presence of neutron superfluidity, has been shown by Gusakov and Chugunov (2020) to affect the EoS and composition (recall the discussion in Sec. 2.5.2.1), as well as the net heat generation within the accreted crust (Gusakov and Chugunov, 2021).

It is also possible that our treatment of transport properties in the core may be improved in a couple of ways. Firstly, as part of our thermal model we implemented the results of Gnedin and Yakovlev (1995) to describe lepton conduction in the core. More recent analysis by Shternin and Yakovlev (2007), however, has studied the inclusion of Landau damping on interactions involving relativistic electrons, which has been shown to modify the temperature dependence of the scattering frequencies. Whilst we have also sought to include the effects of baryon superfluidity in our thermal calculation, effects of proton superconductivity on transport properties was neglected since electrons and neutrons are the primary carriers of heat. Proton superconductivity can however affect the temperature dependence of scattering mechanisms involving protons due to screening effects (recall Sec. 4.6.4.1), which could in turn have consequences for the un-magnetised thermal structure.

7.3.2 Extending the perturbed model

Next we shall review some additional steps towards a more complete calculation of the perturbed thermal structure, building upon the framework outlined in Chapter 5.

***Outer boundary condition*:** Much like the outer boundary condition assumed for the background calculation, the assumed outer boundary condition in the perturbed problem is also somewhat rudimentary. It was shown in Fig. 5.7 that the temperature perturbations in the deep crust are insensitive to the choice of outer boundary condition. And, since the deep crust is where most of the mass quadrupole is built, the lack of a rigorous outer boundary condition is, in practice, not overly restrictive. The 'true' outer boundary condition, however, would follow from the correspondingly more physically motivated outer boundary in the background calculation as described above.

***Magnetic field evolution*:** The lack of knowledge surrounding the nature of the evolution of the internal magnetic field means we cannot faithfully comment on the true nature of its structure inside old ($\sim 10^9$ yr) accreting NSs. Ambipolar diffusion is thought to be the main driver of the magnetic field evolution in the core of the star, whilst Ohmic decay (resulting due to finite electrical conductivity) and Hall drift are responsible for the evolution of the crustal field (recall Sec. 2.3, and see Igoshev et al. (2021) for an additional review). Calculating the magnetic field evolution is beyond the scope of this thesis, and as such we have calculated the level of temperature asymmetry in the presence of a magnetic field that extends over the entire star, when it is confined the crust, and when it is able to permeate the outermost region of the core (Sec. 5.3). This therefore represents three regimes of possibility, with the actual level of temperature asymmetry resulting from a the magnetic field most likely existing somewhere between the two extremes.

***A non-perturbative approach*:** The equations derived to calculate the level of asymmetry induced by magnetic fields was done so perturbatively (i.e. where the condition on the magnetisation parameter Eq. (5.8) - $\omega_B \tau \ll 1$ - is always be obeyed). This limited the strength of core magnetic fields in which the equations remain valid to $\sim 10^8$ G (Fig. 5.2), since the relaxation time τ is much shorter in the crust than in the core. However, if magnetic fields do indeed exist in the cores of accreting NSs, then they will almost certainly be stronger than this, and therefore the temperature asymmetry is likely larger than what we have already estimated.

In addition, using our perturbative results, we found that neutrino emission from highly-efficient Durca processes may limit the strength of the magnetic field required to reproduce the upper-limit on the ellipticity of IGR J00291+5934 to just $\sim 10^{11}$ G (Sec. 5.6). However such a strong magnetic field pushes us out of the perturbative regime, and so should be viewed with caution. In order to asses the role of Durca properly, a reformulation of the anisotropic heat conduction mechanism non-perturbatively could be a new method to constrain the (largely unknown) internal magnetic field strength, where the condition $\omega_B \tau \ll 1$ would no longer be required.

***Superfluid phonons*:** The possibly of heat conduction via superfluid phonons is potentially an important piece of the crustal physics that is missing from our current model. The asymmetry-inducing mechanism considered here relies on the fact that the heat flow orthogonal to the magnetic field is suppressed since the heat-carrying electrons are charged (Sec. 5.1). Conduction by electrically-neutral superfluid phonons may therefore enhance the heat flow orthogonal to the magnetic field line that would otherwise be suppressed. A significant 'short circuiting' of our asymmetry-inducing mechanism however is still unlikely, since Aguilera et al. (2009) have shown magnetic field strengths in excess of 10^{13} G - much larger than those associated with LMXBs - would be required to significantly enhance conduction by these superfluid phonons to a level where it might compete with the electron conductivity.

7.3.3 Extending the elastic problem

Finally, we will review some of the finer details of our model of the elastic response of the crust to the temperature perturbations described in Chapter 5, building upon the framework from Chapter 6.

***Improved analytical representations of the EoS*:** The fundamental building block of our model is the equation of state. Whilst it is only the crust of the star that is relevant to building *elastic* mountains, we have shown that the properties of the core can significantly impact the behavior of temperature perturbations in the crust which source the (thermal) mountain to begin with. The BSk equations of state that we have employed here (the F+18 models) may be applied not only to nuclear clusters in the crust, but also to homogeneous nuclear matter in the core (Sec. 2.6.4). This has therefore allowed us to describe all regions of the neutron star interior in a consistent manner.

However, the large density discontinuities present in the region $\rho \sim 10^{12} - 10^{13}$ g cm^{-3} initially led to severe issues in achieving numerical convergence when computing the mass quadrupole via Eqs (6.56) - (6.57) (which, strictly speaking, are mathematically equivalent) from solving the elastic perturbation equations (6.41a) - (6.41d). One solution to this was to therefore take the approach of approximating the EoS with the analytical fit described in Section 2.5. Whilst this method was successful in achieving agreement in Eqs (6.56) - (6.57) at the level of $\lesssim 1\%$, the procedure was found to introduce a systematic error in the calculation of the adiabatic index $\Gamma_{\mathrm{AC}}^{\mathrm{Fit}}$ as compared to the tabulated data Γ_{AC} (Sec. 2.5.2.1). The smoothing of density discontinuities in the crust essentially equates to a softening of the EoS, leading to the sharp decline in $\Gamma_{\mathrm{AC}}^{\mathrm{Fit}}$, comparable to that of the equation of state of catalysed matter (i.e. a non-accreted crust).

The ‘brute force’ approach of the least-squares method, whilst simple, is not a necessarily robust method to fitting the accreted EoS, given the 23-parameter space in Eq. (2.26) needed to adequately fit the catalysed crust (Potekhin et al., 2013). It would, therefore, be worthwhile amending the analytical representation of the EoS Eq. (2.26) explicitly to further improve the accuracy of the fit, or implement a different method entirely to carry out the optimisation process on the tabulated data. Alternatively, given the implications of the more recent GC20 nHD model (Sec. 2.5.2.1), the ground-state BSk models could serve as an adequate approximation of the EoS in the inner crust, where the analytical representations are better defined.

***Fully relativistic calculation*:** Currently we use general relativity to compute only the hydrostatic structure of the neutron star. This is required in order to make use of realistic EoSs, which would otherwise have led to unphysical density profiles in Newtonian theory. We do however employ Newtonian theory to compute both the thermal structure of the star (Sec. 4.2), as well as the elastic readjustment of the crust (Sec. 6.2.1) in response to the temperature perturbations also derived in the Newtonian framework. Given the compactness of a typical neutron star is $M/R \sim 0.2$, one should probably expect some fractional errors in the thermal structure when neglecting GR.

We have refrained from solving the relativistic (perturbed) Euler equation so that we might focus on prescribing a realistic source term, which has been missing in the literature until now (Sec. 1.3.3.2 and Sec. 3.2.2.1.1). In principle, this could be rectified by following Gittins and Andersson (2021), who outline a procedure for obtaining the multipole moments of the neutron star in general relativity. This would also allow for a more consistent treatment of the gravitational acceleration ($g \equiv \nabla_j \Phi$) in our model, where, rather than being defined in terms of a ‘pseudo acceleration’ as in Sec. 6.2, the effects of self-gravity would be encoded in the spacetime metric g_{ab}.

One additional intermediary step, however, could be to remain in the Newtonian setting, but relax the Cowling approximation. In the current framework, this would add an extra term in the Euler equation (6.30) which accounts for small perturbations in the gravitational potential, and introduce an additional two ODEs in the system of equations (6.41a) - (6.41d) that would derive from Poisson's equation for gravity Eq. (2.43). Whilst not implemented in UCB explicitly, they estimate that inclusion of the effects of self-gravity might increase the resulting mass quadrupole moment by $20-200\%$. These conclusions have been more recently (effectively) reconfirmed in Haskell et al. (2006) and Johnson-McDaniel and Owen (2013), with both studies showing that including the perturbations of the gravitational potential reduce the size of the mass quadrupole by a factor of a few[2].

7.4 Final thoughts

With ever-more accurate theoretical models and the continuing increase in the sensitivity of instruments for observations, the likelihood of a detection of continuous gravitational radiation from deformed neutron stars will continue to grow. And, as it does so, it is of great importance that we continue to refine our physical models as we enter into the era of the next generation of GW detectors.

Looking ahead, one final (and hopefully exciting!) outcome of this thesis is the potential for the general method to compute the ellipticity of accreting LMXBs using a realistic equation of state presented here may be extended to include other mechanisms which generate temperature and/or density perturbations in a self-consistent way.

That said, in the continued search for evidence of a continuous GW signal, it may also be beneficial to consider other sources for neutron star mountains beyond the traditional accreting millisecond pulsar we have considered here. The GW signal from a rigidly rotating deformed NS scales as $h_0 \propto \epsilon \nu_s^2$ (Eq. (3.35)), and therefore these systems are targeted (at least in part) due to their rapid rotation rates.

Ultraluminous X-ray sources (ULXs) are a separate class of astrophysical objects (see e.g King et al., 2023), with some thought to contain systems of very strongly accreting neutron stars. Unlike a traditional LMXB, these systems may accrete at super-Eddington rates ($\dot{M} > 2\times 10^{-8} M_\odot\,\mathrm{yr}^{-1}$), and posses magnetic fields in excess of 10^{12} G (compared to that of 10^{9} G for an LMXB). Not only does this make neutron star ULXs excellent potential sources for *magnetic mountains* (i.e. where the mass distortion is supported by Lorentz forces; Sec. 1.3.3.1), but specific to the thermo-elastic mountain formation mechanism described here; the temperature asymmetry is linear in magnetic field strength, as well as approximately linear in the mass accretion rate (Sec. 5.6). The thermal lattice pressure is also proportional to the temperature (Fig. 6.2) and therefore to the rate of mass accretion.

---

[2] Note, however, that both these studies are concerned with evaluating the 'maximum' mountain that the crust can sustain, rather than exploring the elastic readjustment of the crust from an explicit source term as we have here.

Neutron star ULXs could, at least in principle, therefore play host to significantly larger mountains than their LMXB counterparts. On account of their exceedingly strong magnetic fields, however, the NSs in these systems typically spin much slower than those typically found in LMXBs ($\nu_s \lesssim 50$ Hz as opposed to $\sim 300 - 700$ Hz). It is therefore immediately unclear as to whether the greater mass quadrupole generated as a result of strong magnetic fields and enhanced accretion is counteracted by the low spin-rate, and thus not lead to a stronger signal in the detector. If this counteraction is not present, then ULX systems could be excellent candidates for future targeted searches of advanced detectors such as Einstein telescope (Maggiore et al., 2020) and Cosmic Explorer (Evans et al., 2023; Gupta et al., 2023), with their increased sensitivity at low frequency ($\nu_s \sim 50$ Hz $\rightarrow f_{\rm GW} \sim 100$ Hz).

In short, whilst there is still much work to be done, the results here should be seen as encouraging as we enter deeper into the era of gravitational-wave astronomy. With the proposed third-generation ground-based interferometers, the increased sensitivity of such instruments should lead to a wealth of new data, including perhaps, just maybe, a *continuous* gravitational-wave signal.

Appendix A

A.1 Composition tables

We include for convenience the set of tables showing the properties of the non-equilibrium reactions which take place in the crust an accreted neutron star as predicted by the Brussels-Montreal energy density functionals BSk19, BSk20 and BSk21, reproduced from Fantina et al. (2018).

Columns 1 and 2 show, respectively, the pressure P and density ρ at which each particular nuclear reaction (given in column 3) occurs. Column 4 gives the fraction of free neutrons X_{n} among nucleons in a given capture layer, whilst column 5 shows the relative density jump that occurs at the transition between nuclei. Column 6 then gives the value of the electron chemical potential μ_e at each capture layer, and Finally column 7 shows the heat deposited per accreted nucleon ϵ_{nuc} (originally 'q' in Fantina et al., 2018) for a given reaction.

TABLE A.1: Non-equilibrium processes in the crust of an accreting neutron stars assuming ashes of pure ^{56}Fe using the EDF BSk19. Reproduction of Table A.3 from Fantina et al. (2018).

P (dyn cm^{-2})	ρ (g cm^{-3})	Reactions	X_n	$\Delta\rho/\rho$	μ_e (MeV)	ϵ_{nuc} (keV)
6.48×10^{26}	1.38×10^{9}	$^{56}\mathrm{Fe} \rightarrow^{56} \mathrm{Cr} - 2e^- + 2\nu_e$	0	0.08	4.47	37.0
1.83×10^{28}	1.81×10^{10}	$^{56}\mathrm{Cr} \rightarrow {}^{56}\mathrm{Ti} - 2e^- + 2\nu_e$	0	0.09	10.22	41.2
1.06×10^{29}	7.37×10^{10}	$^{56}\mathrm{Ti} \rightarrow {}^{56}\mathrm{Ca} - 2e^- + 2\nu_e$	0	0.10	15.83	62.3
3.44×10^{29}	1.96×10^{11}	$^{56}\mathrm{Ca} \rightarrow^{56} \mathrm{Ar} - 2e^- + 2\nu_e$	0	0.11	21.22	11.6
9.02×10^{29}	4.48×10^{11}	$^{56}\mathrm{Ar} \rightarrow {}^{55}\mathrm{Cl} + n - e^- + \nu_e$	0	0.06	26.74	0
9.30×10^{29}	4.75×10^{11}	$^{55}\mathrm{Cl} \rightarrow {}^{54}\mathrm{S} + \Delta N \cdot n - e^- + 2\nu_e$	0.04	0.06	27.04	0
1.22×10^{30}	6.20×10^{11}	$^{54}\mathrm{S} \rightarrow {}^{48}\mathrm{Si} + \Delta N \cdot n - 2e^- + 2\nu_e$	0.14	0.14	28.63	50.4
2.48×10^{30}	1.20×10^{12}	$^{48}\mathrm{Si} \rightarrow {}^{30}\mathrm{O} + \Delta N \cdot n - 6e^- + 2\nu_e$				
		$^{30}\mathrm{O} + {}^{30}\mathrm{O} \rightarrow {}^{51}\mathrm{Si} + \Delta N \cdot n - 2e^- + 2\nu_e$	0.54	0.72	32.72	932.1
4.87×10^{30}	3.38×10^{12}	$^{52}\mathrm{Si} \rightarrow {}^{32}\mathrm{O} + \Delta N \cdot n - 6e^- + 2\nu_e$				
		$^{32}\mathrm{O} + {}^{32}\mathrm{O} \rightarrow {}^{61}\mathrm{S} + \Delta N \cdot n$	0.73	0.28	34.76	376.8
6.36×10^{30}	5.23×10^{12}	$^{62}\mathrm{S} \rightarrow {}^{55}\mathrm{Si} + \Delta N \cdot n - 2e^- + 2\nu_e$	0.75	0.04	35.85	7.4
1.96×10^{31}	1.21×10^{13}	$^{58}\mathrm{Si} \rightarrow {}^{35}\mathrm{O} + \Delta N \cdot n - 6e^- + 2\nu_e$				
		$^{35}\mathrm{O} + {}^{35}\mathrm{O} \rightarrow {}^{68}\mathrm{S} + \Delta N \cdot n$	0.85	0.07	39.72	132.0
8.57×10^{31}	3.69×10^{13}	$^{75}\mathrm{S} \rightarrow {}^{71}\mathrm{P} + \Delta N \cdot n - e^- + \nu_e$	0.84	0.003	55.11	0
1.39×10^{32}	5.21×10^{13}	$^{72}\mathrm{P} \rightarrow {}^{68}\mathrm{Si} + \Delta N \cdot n - e^- + \nu_e$	0.85	0.001	60.38	0

TABLE A.2: Non-equilibrium processes in the crust of an accreting neutron stars assuming ashes of pure ^{56}Fe using the EDF BSk20. Reproduction of Table A.2 from Fantina et al. (2018).

P (dyn cm^{-2})	ρ (g cm^{-3})	Reactions	X_n	$\Delta\rho/\rho$	μ_e (MeV)	$\epsilon_{\rm nuc}$ (keV)
6.48×10^{26}	1.38×10^{9}	$^{56}\mathrm{Fe}\rightarrow{}^{56}\mathrm{Cr}-2e^-+2\nu_e$	0	0.08	4.47	37.0
1.83×10^{28}	1.81×10^{10}	$^{56}\mathrm{Cr}\rightarrow{}^{56}\mathrm{Ti}-2e^-+2\nu_e$	0	0.09	10.22	41.2
1.06×10^{29}	7.37×10^{10}	$^{56}\mathrm{Ti}\rightarrow{}^{56}\mathrm{Ca}-2e^-+2\nu_e$	0	0.10	15.82	53.4
3.44×10^{29}	1.96×10^{11}	$^{56}\mathrm{Ca}\rightarrow{}^{56}\mathrm{Ar}-2e^-+2\nu_e$	0	0.11	21.73	12.4
9.06×10^{29}	4.50×10^{11}	$^{56}\mathrm{Ar}\rightarrow{}^{55}\mathrm{Cl}+n-e^-+\nu_e$	0	0.06	26.50	0
9.32×10^{29}	4.76×10^{11}	$^{55}\mathrm{Cl}\rightarrow{}^{54}\mathrm{S}+\Delta N\cdot n-e^-+2\nu_e$	0.04	0.06	26.98	0
1.22×10^{30}	6.17×10^{11}	$^{54}\mathrm{S}\rightarrow{}^{48}\mathrm{Si}+\Delta N\cdot n-2e^-+2\nu_e$	0.14	0.13	28.78	49.1
2.51×10^{30}	1.21×10^{12}	$^{48}\mathrm{Si}\rightarrow{}^{30}\mathrm{O}+\Delta N\cdot n-6e^-+2\nu_e$				
		$^{30}\mathrm{O}+{}^{30}\mathrm{O}\rightarrow{}^{52}\mathrm{Si}-2e^-+2\nu_e$	0.55	0.71	32.71	924.8
5.15×10^{30}	3.49×10^{12}	$^{52}\mathrm{Si}\rightarrow{}^{32}\mathrm{O}+\Delta N\cdot n-6e^-+2\nu_e$				
		$^{32}\mathrm{O}+{}^{32}\mathrm{O}\rightarrow{}^{61}\mathrm{S}$	0.73	0.27	34.98	369.7
7.06×10^{30}	5.53×10^{12}	$^{62}\mathrm{S}\rightarrow{}^{56}\mathrm{Si}+\Delta N\cdot n-2e^-+2\nu_e$	0.75	0.04	36.47	6.3
2.26×10^{31}	1.32×10^{13}	$^{60}\mathrm{Si}\rightarrow{}^{36}\mathrm{O}+\Delta N\cdot n-6e^-+2\nu_e$				
		$^{36}\mathrm{O}+{}^{36}\mathrm{O}\rightarrow{}^{61}\mathrm{S}$	0.84	0.07	40.81	120.7
1.29×10^{32}	5.08×10^{13}	$^{80}\mathrm{S}\rightarrow{}^{75}\mathrm{P}+\Delta N\cdot n-e^-+\nu_e$	0.83	0.003	61.31	0

TABLE A.3: Non-equilibrium processes in the crust of an accreting neutron stars assuming ashes of pure ^{56}Fe using the EDF BSk21. Reproduction of Table A.1 from Fantina et al. (2018).

P (dyn cm^{-2})	ρ (g cm^{-3})	Reactions	X_n	$\Delta\rho/\rho$	μ_e (MeV)	$\epsilon_{\rm nuc}$ (keV)
6.50×10^{26}	1.38×10^{9}	$^{56}\mathrm{Fe}\rightarrow{}^{56}\mathrm{Cr}-2e^-+2\nu_e$	0	0.08	4.47	37.0
1.84×10^{28}	1.82×10^{10}	$^{56}\mathrm{Cr}\rightarrow{}^{56}\mathrm{Ti}-2e^-+2\nu_e$	0	0.09	10.22	41.2
1.06×10^{29}	7.38×10^{10}	$^{56}\mathrm{Ti}\rightarrow{}^{56}\mathrm{Ca}-2e^-+2\nu_e$	0	0.10	15.83	39.1
3.44×10^{29}	1.96×10^{11}	$^{56}\mathrm{Ca}\rightarrow^{56}\mathrm{Ar}-2e^-+2\nu_e$	0	0.11	21.22	8.1
8.75×10^{29}	4.38×10^{11}	$^{56}\mathrm{Ar}\rightarrow{}^{55}\mathrm{Cl}+n-e^-+\nu_e$	0	0.06	26.55	0
9.40×10^{29}	4.79×10^{11}	$^{55}\mathrm{Cl}\rightarrow{}^{53}\mathrm{S}+\Delta N\cdot n-e^-+2\nu_e$	0.05	0.06	27.04	0
1.18×10^{30}	6.04×10^{11}	$^{53}\mathrm{S}\rightarrow{}^{47}\mathrm{Si}+\Delta N\cdot n-2e^-+2\nu_e$	0.15	0.14	28.57	45.0
2.54×10^{30}	1.22×10^{12}	$^{48}\mathrm{Si}\rightarrow{}^{30}\mathrm{O}+\Delta N\cdot n-6e^-+2\nu_e$				
		$^{30}\mathrm{O}+{}^{30}\mathrm{O}\rightarrow{}^{51}\mathrm{Si}+\Delta N\cdot n-2e^-+2\nu_e$	0.54	0.68	32.64	908.1
5.78×10^{30}	3.73×10^{12}	$^{53}\mathrm{Si}\rightarrow{}^{32}\mathrm{O}+\Delta N\cdot n-6e^-+2\nu_e$				
		$^{32}\mathrm{O}+{}^{32}\mathrm{O}\rightarrow{}^{62}\mathrm{S}+\Delta N\cdot n$	0.72	0.23	35.47	355.9
8.69×10^{30}	6.16×10^{12}	$^{66}\mathrm{S}\rightarrow{}^{57}\mathrm{Si}+\Delta N\cdot n-2e^-+2\nu_e$	0.74	0.03	37.74	3.5
3.20×10^{31}	1.65×10^{13}	$^{65}\mathrm{Si}\rightarrow{}^{40}\mathrm{O}+\Delta N\cdot n-6e^-+2\nu_e$				
		$^{40}\mathrm{O}+{}^{40}\mathrm{O}\rightarrow{}^{76}\mathrm{S}+\Delta N\cdot n$	0.83	0.05	43.8	98.2
1.85×10^{32}	7.26×10^{13}	$^{91}\mathrm{S}\rightarrow{}^{86}\mathrm{P}+\Delta N\cdot n-e^-+\nu_e$	0.81	0.006	69.10	0

References

J. Aasi et al. Gravitational waves from known pulsars: Results from the initial detector era. *The Astrophysical Journal*, 785(2):119, Apr 2014. . URL https://doi.org/10.1088%2F0004-637x%2F785%2F2%2F119.

B. Abbott et al. Observing gravitational-wave transient GW150914 with minimal assumptions. *Physical Review D*, 93(12), Jun 2016a. . URL https://doi.org/10.1103/physrevd.93.122004.

B. Abbott et al. Properties of the binary black hole merger GW150914. *Physical Review Letters*, 116(24), Jun 2016b. . URL https://doi.org/10.1103/physrevlett.116.241102.

B. P. Abbott et al. Observation of gravitational waves from a binary black hole merger. *Phys. Rev. Lett.*, 116:061102, Feb 2016c. . URL https://doi.org/10.1103/PhysRevLett.116.061102.

B. P. Abbott et al. A gravitational-wave standard siren measurement of the hubble constant. *Nature*, 551(7678):85–88, Oct 2017a. . URL https://doi.org/10.1038/nature24471.

B. P. Abbott et al. GW170817: Observation of gravitational waves from a binary neutron star inspiral. *Phys. Rev. Lett.*, 119:161101, Oct 2017b. . URL https://doi.org/10.1103/physrevlett.119.161101.

B. P. Abbott et al. Gravitational waves and gamma-rays from a binary neutron star merger: GW170817 and GRB 170817a. *The Astrophysical Journal*, 848(2):L13, Oct 2017c. . URL https://doi.org/10.3847/2041-8213/aa920c.

B. P. Abbott et al. GW170817: Measurements of neutron star radii and equation of state. *Phys. Rev. Lett.*, 121:161101, Oct 2018. . URL https://doi.org/10.1103/PhysRevLett.121.161101.

R. Abbott et al. Observation of gravitational waves from two neutron star–black hole coalescences. *The Astrophysical Journal Letters*, 915(1):L5, Jun 2021a. . URL https://doi.org/10.3847/2041-8213/ac082e.

R. Abbott et al. Constraints from LIGO O3 data on gravitational-wave emission due to r-modes in the glitching pulsar PSR J0537–6910. *The Astrophysical Journal*, 922(1):71, Nov 2021b. . URL https://doi.org/10.3847/1538-4357/ac0d52.

R. Abbott et al. Diving below the spin-down limit: Constraints on gravitational waves from the energetic young pulsar PSR J0537-6910. *The Astrophysical Journal Letters*, 913(2):L27, May 2021c. . URL `https://doi.org/10.3847%2F2041-8213%2Fabffcd`.

R. Abbott et al. Search for continuous gravitational waves from 20 accreting millisecond X-ray pulsars in O3 LIGO data. *Phys. Rev. D*, 105:022002, Jan 2022a. . URL `https://doi.org/10.1103/physrevd.105.022002`.

R. Abbott et al. Model-based cross-correlation search for gravitational waves from the low-mass X-ray binary Scorpius X-1 in LIGO O3 data. *The Astrophysical Journal Letters*, 941(2): L30, Dec 2022b. . URL `https://doi.org/10.3847/2041-8213/aca1b0`.

R. Abbott et al. Constraints on the cosmic expansion history from GWTC–3. *The Astrophysical Journal*, 949(2):76, Jun 2023. . URL `https://dx.doi.org/10.3847/1538-4357/ac74bb`.

D. Adhikari et al. Accurate determination of the neutron skin thickness of ^{208}Pb through parity-violation in electron scattering. *Phys. Rev. Lett.*, 126:172502, Apr 2021. . URL `https://doi.org/10.1103/PhysRevLett.126.172502`.

G. Agazie et al. The NANOGrav 15 yr data set: Observations and timing of 68 millisecond pulsars. *The Astrophysical Journal Letters*, 951(1):L9, Jun 2023a. . URL `https://dx.doi.org/10.3847/2041-8213/acda9a`.

G. Agazie et al. The NANOGrav 15 yr data set: Evidence for a gravitational-wave background. *The Astrophysical Journal Letters*, 951(1):L8, Jun 2023b. . URL `https://dx.doi.org/10.3847/2041-8213/acdac6`.

G. Agazie et al. The NANOGrav 15 yr data set: Constraints on supermassive black hole binaries from the gravitational-wave background. *The Astrophysical Journal Letters*, 952(2):L37, Aug 2023c. . URL `https://dx.doi.org/10.3847/2041-8213/ace18b`.

D. N. Aguilera, J. A. Pons, and J. A. Miralles. 2d cooling of magnetized neutron stars. *Astron. Astrophys.*, 486(1):255–271, Apr 2008. . URL `https://doi.org/10.1051/0004-6361:20078786`.

D. N. Aguilera, V. Cirigliano, J. A. Pons, S. Reddy, and R. Sharma. Superfluid heat conduction and the cooling of magnetized neutron stars. *Phys. Rev. Lett.*, 102:091101, Mar 2009. . URL `https://doi.org/10.1103/PhysRevLett.102.091101`.

T. Ainsworth, J. Wambach, and D. Pines. Effective interactions and superfluid energy gaps for low density neutron matter. *Physics Letters B*, 222(2):173–178, 1989. ISSN 0370-2693. . URL `https://www.sciencedirect.com/science/article/pii/037026938991246X`.

T. Akgün and I. Wasserman. Toroidal magnetic fields in type ii superconducting neutron stars. *Mon. Not. Roy. Astron. Soc.*, 383(4):1551–1580, Jan 2008. ISSN 0035-8711. . URL `http://dx.doi.org/10.1111/j.1365-2966.2007.12660.x`.

Z. Alterman, H. Jarosch, and C. L. Pekeris. Oscillations of the earth. *Proceedings of the Royal Society of London. Series A, Mathematical and Physical Sciences*, 252(1268):80–95, 1959. URL `https://doi.org/10.1098/rspa.1959.0138`.

L. Amundsen and E. Østgaard. Superfluidity of neutron matter: (I). Singlet pairing. *Nuclear Physics A*, 437(2):487–508, Apr 1985a. URL `https://doi.org/10.1016/s0375-9474(85)90103-4`.

L. Amundsen and E. Østgaard. Superfluidity of neutron matter: (ii). triplet pairing. *Nuclear Physics A*, 442(1):163–188, Aug 1985b. . URL `https://doi.org/10.1016/0375-9474(85)90140-x`.

N. Andersson. A new class of unstable modes of rotating relativistic stars. *The Astrophysical Journal*, 502(2):708–713, Aug 1998. . URL `https://doi.org/10.1086/305919`.

N. Andersson. Gravitational waves from instabilities in relativistic stars. *Classical and Quantum Gravity*, 20(7):R105–R144, Mar 2003. . URL `https://doi.org/10.10882F0264-93812F202F72F201`.

N. Andersson. *Gravitational-Wave Astronomy: Exploring the Dark Side of the Universe*. Oxford University Press, Nov 2019. ISBN 9780198568032. . URL `https://doi.org/10.1093/oso/9780198568032.001.0001`.

N. Andersson and G. L. Comer. Relativistic fluid dynamics: physics for many different scales. *Living Reviews in Relativity*, 24(1), Jun 2021. . URL `https://doi.org/10.1007/s41114-021-00031-6`.

N. Andersson, K. Glampedakis, B. Haskell, and A. L. Watts. Modelling the spin equilibrium of neutron stars in low-mass X-ray binaries without gravitational radiation. *Mon. Not. Roy. Astron. Soc.*, 361(4):1153–1164, Aug 2005. . URL `https://doi.org/10.1111/j.1365-2966.2005.09167.x`.

Avakyan, A., Neumann, M., Zainab, A., Doroshenko, V., Wilms, J., and Santangelo, A. XRBcats: Galactic low-mass X-ray binary catalogue. *Astron. Astrophys.*, 675:A199, 2023. . URL `https://doi.org/10.1051/0004-6361/202346522`.

W. Baade and F. Zwicky. On Super-novae. *Proceedings of the National Academy of Science*, 20 (5):254–259, May 1934a. . URL `https://doi.org/10.1073/pnas.20.5.25`.

W. Baade and F. Zwicky. Cosmic Rays from Super-novae. *Proceedings of the National Academy of Science*, 20(5):259–263, May 1934b. . URL `https://doi.org/10.1073/pnas.20.5.259`.

A. Bahramian and N. Degenaar. Low-mass x-ray binaries. In *Handbook of X-ray and Gamma-ray Astrophysics*, pages 1–62. Springer Nature Singapore, 2023. . URL `https://doi.org/10.1007%2F978-981-16-4544-0_94-1`.

D. A. Baiko and D. G. Yakovlev. Thermal and electric conductivities of Coulomb crystals in the inner crust of a neutron star. *Astronomy Letters*, 22(5):708–714, Sep 1996. . URL http://arxiv.org/abs/astro-ph/9604165.

D. A. Baiko, P. Haensel, and D. G. Yakovlev. Thermal conductivity of neutrons in neutron star cores. *Astron. Astrophys.*, 374(1):151–163, Jul 2001. . URL https://doi.org/10.1051/0004-6361:20010621.

D. A. Baiko, A. Y. Potekhin, and D. G. Yakovlev. Thermodynamic functions of harmonic Coulomb crystals. *Phys. Rev. E*, 64(5):057402, Nov 2001. . URL https://doi.org/10.1103/PhysRevE.64.057402.

M. Baldo and H.-J. Schulze. Proton pairing in neutron stars. *Phys. Rev. C*, 75:025802, Feb 2007. . URL https://doi.org/10.1103/PhysRevC.75.025802.

M. Baldo, J. Cugnon, A. Lejeune, and U. Lombardo. Proton and neutron superfluidity in neutron star matter. *Nucl. Phys. A.*, 536(2):349–365, Jan 1992. . URL https://doi.org/10.1016/0375-9474(92)90387-Y.

M. Baldo, Ø. Elgarøy, L. Engvik, M. Hjorth-Jensen, and H. J. Schulze. $^3P_2$-$^3F_2$ pairing in neutron matter with modern nucleon-nucleon potentials. *Phys. Rev. C*, 58(4):1921–1928, Oct 1998. . URL https://doi.org/10.1103/PhysRevC.58.1921.

M. Baldo, E. E. Saperstein, and S. V. Tolokonnikov. A realistic model of superfluidity in the neutron star inner crust. *The European Physical Journal A*, 32(1):97–108, Apr 2007a. . URL https://doi.org/10.1140/epja/i2006-10356-5.

M. Baldo, E. E. Saperstein, and S. V. Tolokonnikov. Upper edge of the neutron star inner crust: The drip point and its vicinity. *Physical Review C*, 76(2), Aug 2007b. . URL https://doi.org/10.1103/PhysRevC.76.025803.

C. Bambi. *Classical Tests of General Relativity*, pages 163–178. Springer Singapore, Singapore, 2018. ISBN 978-981-13-1090-4. . URL https://doi.org/10.1007/978-981-13-1090-4_9.

J. Bardeen, L. N. Cooper, and J. R. Schrieffer. Microscopic theory of superconductivity. *Phys. Rev.*, 106:162–164, Apr 1957. . URL https://link.aps.org/doi/10.1103/PhysRev.106.162.

G. Baym, C. Pethick, and D. Pines. Superfluidity in Neutron Stars. *Nature*, 224(5220):673–674, Nov 1969. . URL https://doi.org/10.1038/224673a0.

G. Baym, C. Pethick, and P. Sutherland. The Ground State of Matter at High Densities: Equation of State and Stellar Models. *Astrophys. J.*, 170:299, Dec 1971. . URL https://doi.org/10.1086/151216.

M. Bender, P.-H. Heenen, and P.-G. Reinhard. Self-consistent mean-field models for nuclear structure. *Reviews of Modern Physics*, 75(1):121–180, Jan 2003. . URL https://doi.org/10.1103/RevModPhys.75.121.

E. Berger, W. Fong, and R. Chornock. An r-process kilonova associated with the short-hard GRB 130603B. *Astrophys. J. Lett.*, 774(2):L23, Sep 2013. . URL https://doi.org/10.1088/2041-8205/774/2/l23.

D. Bhattacharya and E. van den Heuvel. Formation and evolution of binary and millisecond radio pulsars. *Physics Reports*, 203(1):1–124, 1991. . URL https://doi.org/10.1016/0370-1573(91)90064-S.

S. Bhattacharyya and D. Chakrabarty. The effect of transient accretion on the spin-up of millisecond pulsars. *Astrophys. J.*, 835(1):4, Jan 2017. . URL https://doi.org/10.3847%2F1538-4357%2F835%2F1%2F4.

L. Bildsten. Gravitational radiation and rotation of accreting neutron stars. *The Astrophysical Journal*, 501(1):L89, Jun 1998. . URL https://dx.doi.org/10.1086/311440.

L. Bildsten and A. Cumming. Hydrogen electron capture in accreting neutron stars and the resulting g-Mode oscillation spectrum. *Astrophys. J.*, 506(2):842–862, Oct 1998. . URL https://doi.org/10.1086/306279.

L. Bildsten and C. Cutler. Nonradial oscillations in neutron star oceans: A source of quasi-periodic X-ray oscillations? *Astrophys. J.*, 449:800, Aug 1995. . URL https://ui.adsabs.harvard.edu/abs/1995ApJ...449..800B.

S. I. Blinnikov, I. D. Novikov, T. V. Perevodchikova, and A. G. Polnarev. Exploding neutron stars in close binaries. *Soviet Astronomy Letters*, 10:177–179, Apr 1984. . URL https://ui.adsabs.harvard.edu/abs/1984SvAL...10..177B.

E. F. Brown. Nuclear heating and melted layers in the inner crust of an accreting neutron star. *Astrophys. J.*, 531(2):988–1002, Mar 2000. . URL https://doi.org/10.1086/308487.

E. F. Brown and L. Bildsten. The ocean and crust of a rapidly accreting neutron star: Implications for magnetic field evolution and thermonuclear flashes. *Astrophys. J.*, 496:915–933, 1998. URL https://doi.org/10.1086/305419.

E. F. Brown and A. Cumming. Mapping crustal heating with the cooling light curves of quasi-persistent transients. *Astrophys. J.*, 698(2):1020–1032, Jun 2009. . URL https://doi.org/10.1088/0004-637x/698/2/1020.

M. Caplan, A. Schneider, and C. Horowitz. Elasticity of nuclear pasta. *Phys. Rev. Lett.*, 121(13), Sep 2018. . URL https://doi.org/10.1103/PhysRevLett.121.132701.

N. Chamel and P. Haensel. Physics of neutron star crusts. *Living Reviews in Relativity*, 11(1), Dec 2008. . URL https://doi.org/10.12942/lrr-2008-10.

N. Chamel, A. F. Fantina, J. L. Zdunik, and P. Haensel. Experimental constraints on shallow heating in accreting neutron-star crusts. *Phys. Rev. C*, 102:015804, Jul 2020. . URL https://link.aps.org/doi/10.1103/PhysRevC.102.015804.

S. Chandrasekhar. Solutions of two problems in the theory of gravitational radiation. *Phys. Rev. Lett.*, 24:611–615, Mar 1970. . URL https://link.aps.org/doi/10.1103/PhysRevLett.24.611.

J. M. C. Chen, J. W. Clark, R. D. Davé, and V. V. Khodel. Pairing gaps in nucleonic superfluids. *Nucl. Phys. A.*, 555(1):59–89, Apr 1993. . URL https://doi.org/10.1016/0375-9474(93)90314-N.

H.-Y. Chiu and E. E. Salpeter. Surface x-ray emission from neutron stars. *Phys. Rev. Lett.*, 12:413–415, Apr 1964. . URL https://link.aps.org/doi/10.1103/PhysRevLett.12.413.

A. I. Chugunov and P. Haensel. Thermal conductivity of ions in a neutron star envelope. *Mon. Not. Roy. Astron. Soc.*, 381(3):1143–1153, Sep 2007. ISSN 1365-2966. . URL http://dx.doi.org/10.1111/j.1365-2966.2007.12301.x.

N. J. Cornish and T. B. Littenberg. Bayeswave: Bayesian inference for gravitational wave bursts and instrument glitches. *Classical and Quantum Gravity*, 32(13):135012, Jun 2015. . URL https://doi.org/10.1088/0264-9381/32/13/135012.

P. B. Covas, M. A. Papa, R. Prix, and B. J. Owen. Constraints on r-modes and mountains on millisecond neutron stars in binary systems. *The Astrophysical Journal Letters*, 929(2): L19, apr 2022. . URL https://dx.doi.org/10.3847/2041-8213/ac62d7.

C. Cutler. Gravitational waves from neutron stars with large toroidal *B* fields. *Phys. Rev. D*, 66: 084025, Oct 2002. . URL https://doi.org/10.1103%2Fphysrevd.66.084025.

C. Cutler and D. I. Jones. Gravitational wave damping of neutron star wobble. *Physical Review D*, 63(2), Dec 2000. . URL https://doi.org/10.1103/PhysRevD.63.024002.

Dai, H.-L. and Li, X.-D. Accretion torque on magnetized neutron stars. *A&A*, 451(2):581–585, 2006. . URL https://doi.org/10.1051/0004-6361:20053907.

A. K. Dutta, M. Onsi, and J. M. Pearson. Proton-shell effects in neutron-star matter. *Phys. Rev. C*, 69:052801, May 2004. . URL https://doi.org/10.1103/PhysRevC.69.052801.

A. Eddington. The propagation of gravitational waves. *Proceedings of the Royal Society A*, page 102(706), Dec 1922. URL https://doi.org/10.1098/rspa.1922.0085.

D. Eichler, M. Livio, T. Piran, and D. N. Schramm. Nucleosynthesis, neutrino bursts and γ-rays from coalescing neutron stars. *Nature*, 340(6229):126–128, Jul 1989. . URL https://doi.org/10.1038/340126a0.

A. Einstein. Zur allgemeinen Relativitätstheorie. *Sitzungsberichte der Kölniglich Preussischen Akademie der Wissenschaften*, pages 778–786, Jan 1915a. URL `https://ui.adsabs.harvard.edu/abs/1915SPAW.......778E`.

A. Einstein. Zur allgemeinen Relativitätstheorie (Nachtrag). *Sitzungsberichte der Kölniglich Preussischen Akademie der Wissenschaften*, pages 799–801, Jan 1915b. URL `https://ui.adsabs.harvard.edu/abs/1915SPAW.......799E`.

A. Einstein. Die Feldgleichungen der Gravitation. *Sitzungsberichte der Kölniglich Preussischen Akademie der Wissenschaften*, pages 844–847, Jan 1915c. URL `https://ui.adsabs.harvard.edu/abs/1915SPAW.......844E`.

A. Einstein. Erklärung der Perihelbewegung des Merkur aus der allgemeinen Relativitätstheorie. *Sitzungsberichte der Kölniglich Preussischen Akademie der Wissenschaften*, pages 831–839, Jan 1915d. URL `https://ui.adsabs.harvard.edu/abs/1915SPAW.......831E`.

M. Evans et al. Cosmic explorer: A submission to the NSF MPSAC ngGW subcommittee. Jun 2023. URL `https://arxiv.org/abs/2306.13745`.

V. D. Falco, L. Kuiper, E. Bozzo, D. K. Galloway, J. Poutanen, C. Ferrigno, L. Stella, and M. Falanga. The 2015 outburst of the accretion-powered pulsar IGR J00291+5934. *Astron. Astrophys.*, 599:A88, Mar 2017. . URL `https://doi.org/10.1051/0004-6361/201629575`.

A. F. Fantina, J. L. Zdunik, N. Chamel, J. M. Pearson, P. Haensel, and S. Goriely. Crustal heating in accreting neutron stars from the nuclear energy-density functional theory. *Astron. Astrophys.*, 620:A105, Dec 2018. . URL `https://doi.org/10.1051/0004-6361/201833605`.

A. F. Fantina, S. De Ridder, N. Chamel, and F. Gulminelli. Crystallization of the outer crust of a non-accreting neutron star. *Astron. Astrophys.*, 633:A149, Jan 2020. . URL `https://doi.org/10.1051/0004-6361/201936359`.

A. F. Fantina, J. L. Zdunik, N. Chamel, J. M. Pearson, L. Suleiman, and S. Goriely. Accreting neutron stars from the nuclear energy-density functional theory. *Astron. Astrophys.*, 665:A74, Sep 2022. . URL `https://doi.org/10.1051/0004-6361/202243715`.

L. Fesik and M. A. Papa. First search for r-mode gravitational waves from psr j0537–6910. *The Astrophysical Journal*, 895(1):11, May 2020. . URL `https://dx.doi.org/10.3847/1538-4357/ab8193`.

M. Fortin, C. Providência, A. R. Raduta, F. Gulminelli, J. L. Zdunik, P. Haensel, and M. Bejger. Neutron star radii and crusts: Uncertainties and unified equations of state. *Phys. Rev. C*, 94:035804, Sep 2016. . URL `https://doi.org/10.1103/PhysRevC.94.035804`.

J. L. Friedman and B. F. Schutz. Secular instability of rotating Newtonian stars. *Astrophys. J.*, 222:281–296, May 1978. . URL https://doi.org/10.1086/156143.

B. L. Friman and O. V. Maxwell. Neutrino emissivities of neutron stars. *Astrophys. J.*, 232: 541–557, Sep 1979. . URL https://ui.adsabs.harvard.edu/abs/1979ApJ...232..541F.

D. K. Galloway, A. J. Goodwin, and L. Keek. Thermonuclear Burst Observations for Model Comparisons: A Reference Sample. *Publications of the Astronomical Society of Australia*, 34:e019, Apr 2017. . URL https://ui.adsabs.harvard.edu/abs/2017PASA...34...19G.

S. Gandolfi, A. Y. Illarionov, S. Fantoni, F. Pederiva, and K. E. Schmidt. Equation of state of superfluid neutron matter and the calculation of the $^1s_0$ pairing gap. *Phys. Rev. Lett.*, 101: 132501, Sep 2008. . URL https://doi.org/10.1103/PhysRevLett.101.132501.

U. Geppert, M. Küker, and D. Page. Temperature distribution in magnetized neutron star crusts. *Astron. Astrophys.*, 426(1):267–277, Oct 2004. . URL https://doi.org/10.1051/0004-6361:20040455.

P. Ghosh and F. K. Lamb. Accretion by rotating magnetic neutron stars. II. Radial and vertical structure of the transition zone in disk accretion. *Astrophys. J.*, 232:259–276, Aug 1979a. . URL https://doi.org/10.1086/157285.

P. Ghosh and F. K. Lamb. Accretion by rotating magnetic neutron stars. III. Accretion torques and period changes in pulsating X-ray sources. *Astrophys. J.*, 234:296–316, Nov 1979b. . URL https://doi.org/10.1086/157498.

P. Ghosh, F. K. Lamb, and C. J. Pethick. Accretion by rotating magnetic neutron stars. I. Flow of matter inside the magnetosphere and its implications for spin-up and spin-down of the star. *Astrophys. J.*, 217:578–596, Oct 1977. . URL https://doi.org/10.1086/155606.

R. Giacconi, H. Gursky, F. R. Paolini, and B. B. Rossi. Evidence for x-rays from sources outside the solar system. *Phys. Rev. Lett.*, 9:439–443, Dec 1962. . URL https://doi.org/10.1103/PhysRevLett.9.439.

F. Gittins and N. Andersson. Modelling neutron star mountains in relativity. *Mon. Not. Roy. Astron. Soc.*, 507(1):116–128, Oct 2021. . URL https://doi.org/10.1093/mnras/stab2048.

F. Gittins, N. Andersson, and D. I. Jones. Modelling neutron star mountains. *Mon. Not. Roy. Astron. Soc.*, 500(4):5570–5582, Jan 2021. . URL https://doi.org/10.1093/mnras/staa3635.

K. Glampedakis and L. Gualtieri. *Gravitational Waves from Single Neutron Stars: An Advanced Detector Era Survey*, pages 673–736. Springer International Publishing, Cham, 2018. . URL https://doi.org/10.1007/978-3-319-97616-7_12.

O. Gnedin and D. Yakovlev. Thermal conductivity of electrons and muons in neutron star cores. *Nucl. Phys. A.*, 582(3):697–716, 1995. . URL https://doi.org/10.1016/0375-9474(94)00503-F.

S. Goriely, N. Chamel, and J. M. Pearson. Further explorations of skyrme-hartree-fock-bogoliubov mass formulas. XII. stiffness and stability of neutron-star matter. *Phys. Rev. C*, 82:035804, Sep 2010. . URL https://doi.org/10.1103/PhysRevC.82.035804.

K. N. Gourgouliatos, D. D. Grandis, and A. Igoshev. Magnetic field evolution in neutron star crusts: Beyond the hall effect. *Symmetry*, 14(1):130, Jan 2022. . URL https://doi.org/10.3390/sym14010130.

I. Gupta et al. Characterizing gravitational wave detector networks: From a$^\sharp$ to cosmic explorer. July 2023. URL https://arxiv.org/abs/2307.10421.

S. S. Gupta, T. Kawano, and P. Möller. Neutron Reactions in Accreting Neutron Stars: A New Pathway to Efficient Crust Heating. *Phys. Rev. Lett.*, 101(23):231101, Dec 2008. . URL https://doi.org/10.1103/PhysRevLett.101.231101.

M. E. Gusakov and A. I. Chugunov. Thermodynamically Consistent Equation of State for an Accreted Neutron Star Crust. *Phys. Rev. Lett.*, 124(19):191101, May 2020. . URL https://doi.org/10.1103/PhysRevLett.124.191101.

M. E. Gusakov and A. I. Chugunov. Heat release in accreting neutron stars. *Phys. Rev. D*, 103(10):L101301, May 2021. . URL https://doi.org/10.1103/PhysRevD.103.L101301.

M. C. Guzzetti, N. Bartolo, M. Liguori, and S. Matarrese. Gravitational waves from inflation. *La Rivista del Nuovo Cimento*, 39(9):399–495, Aug 2016. ISSN 0393697X, 0393697X. . URL https://doi.org/10.1393/ncr/i2016-10127-1.

P. Haensel. Equation of state of dense matter and maximum mass of neutron stars. *EAS Publications Series*, 7:249–249, 2003. . URL https://doi.org/10.1051%2Feas%3A2003043.

P. Haensel and B. Pichon. Experimental nuclear masses and the ground state of cold dense matter. *Astron. Astrophys.*, 283(1):313–318, Mar 1994. . URL https://ui.adsabs.harvard.edu/abs/1994A&A...283..313H.

P. Haensel and J. L. Zdunik. Non-equilibrium processes in the crust of an accreting neutron star. *Astron. Astrophys.*, 227(2):431–436, Jan 1990a. URL https://ui.adsabs.harvard.edu/abs/1990A&A...227..431H.

P. Haensel and J. L. Zdunik. Equation of state and structure of the crust of an accreting neutron star. *Astron. Astrophys.*, 229(1):117–122, Mar 1990b. URL https://ui.adsabs.harvard.edu/abs/1990A&A...229..117H.

P. Haensel and J. L. Zdunik. Nuclear composition and heating in accreting neutron-star crusts. *Astron. Astrophys.*, 404(2):L33–L36, Jun 2003. . URL https://doi.org/10.1051/0004-6361:20030708.

P. Haensel and J. L. Zdunik. Models of crustal heating in accreting neutron stars. *Astron. Astrophys.*, 480(2):459–464, Mar 2008. . URL https://doi.org/10.1051/0004-6361:20078578.

P. Haensel, A. D. Kaminker, and D. G. Yakovlev. Electron neutrino-antineutrino bremsstrahlung in a liquid phase of neutron star crusts. *Astron. Astrophys.*, 314:328–340, Oct 1996. URL https://ui.adsabs.harvard.edu/abs/1996A&A...314..328H.

P. Haensel, A. Y. Potekhin, and D. G. Yakovlev. *Neutron stars 1: Equation of state and structure*, volume 326. Springer, New York, USA, 2007. . URL https://doi.org/10.1007/978-0-387-47301-7.

C. J. Hansen and H. M. van Horn. White dwarfs seimology. *Astrophys. J.*, 233:253–258, Oct 1979. . URL https://ui.adsabs.harvard.edu/abs/1979ApJ...233..253H.

A. Harpole. *Multiscale modelling of neutron star oceans*. PhD thesis, University of Southampton, June 2018. URL https://eprints.soton.ac.uk/422175/.

J. B. Hartle. *Gravity: An Introduction to Einstein's General Relativity*. Cambridge University Press, 2021. .

B. Haskell and A. Patruno. Are gravitational waves spinning down PSR J1023+0038 ? *Physical Review Letters*, 119(16), Oct 2017. ISSN 1079-7114. . URL http://dx.doi.org/10.1103/PhysRevLett.119.161103.

B. Haskell and A. Sedrakian. Superfluidity and superconductivity in neutron stars. In *The Physics and Astrophysics of Neutron Stars*, pages 401–454. Springer International Publishing, 2018. . URL https://doi.org/10.1007%2F978-3-319-97616-7_8.

B. Haskell, D. I. Jones, and N. Andersson. Mountains on neutron stars: accreted versus non-accreted crusts. *Mon. Not. Roy. Astron. Soc.*, 373(4):1423–1439, Dec 2006. . URL https://doi.org/10.1111/j.1365-2966.2006.10998.x.

O. Heaviside. A gravitational and electromagnetic analogy. *Electromagnetic Theory*, page 1:455–466, Jan 1893.

C. O. Heinke and W. C. G. Ho. Direct observation of the cooling of the Cassiopeia A neutron star. *The Astrophysical Journal Letters*, 719(2):L167, Aug 2010. . URL https://dx.doi.org/10.1088/2041-8205/719/2/L167.

C. O. Heinke, P. G. Jonker, R. Wijnands, C. J. Deloye, and R. E. Taam. Further constraints on thermal quiescent X-ray emission from SAX J1808.4-3658. *Astrophys. J.*, 691(2):1035–1041, Feb 2009. . URL https://doi.org/10.1088/0004-637x/691/2/1035.

J. W. T. Hessels. A radio pulsar spinning at 716 Hz. *Science*, 311(5769):1901–1904, Mar 2006. ISSN 1095-9203. . URL http://dx.doi.org/10.1126/science.1123430.

W. C. G. Ho, H. Klus, M. J. Coe, and N. Andersson. Equilibrium spin pulsars unite neutron star populations. *Monthly Notices of the Royal Astronomical Society*, 437(4):3664–3669, Dec 2013. ISSN 0035-8711. . URL https://doi.org/10.1093/mnras/stt2193.

W. C. G. Ho, N. Andersson, and V. Graber. Dynamical onset of superconductivity and retention of magnetic fields in cooling neutron stars. *Phys. Rev. C*, 96(6), Dec 2017. ISSN 2469-9993. . URL http://dx.doi.org/10.1103/PhysRevC.96.065801.

M. Hoffberg, A. E. Glassgold, R. W. Richardson, and M. Ruderman. Anisotropic Superfluidity in Neutron Star Matter. *Phys. Rev. Lett.*, 24(14):775, 1970. . URL https://doi.org/10.1103/PhysRevLett.24.775.

R. Hulse and J. Taylor. Discovery of a pulsar in a binary system. *Astrophys. J. Lett.*, 195: L51–L53, Jan 1975. . URL https://doi.org/10.1086/181708.

T. J. Hutchins and D. I. Jones. Accretion-driven thermal mountains in magnetic neutron stars. *Monthly Notices of the Royal Astronomical Society*, 494(2):2839–2850, Jan 2023. . URL https://doi.org/10.1093/mnras/stad967.

A. Idrisy, B. J. Owen, and D. I. Jones. r-mode frequencies of slowly rotating relativistic neutron stars with realistic equations of state. *Phys. Rev. D*, 91:024001, Jan 2015. . URL https://doi.org/10.1103/PhysRevD.91.024001.

A. P. Igoshev, S. B. Popov, and R. Hollerbach. Evolution of neutron star magnetic fields. *Universe*, 7(9), 2021. . URL https://doi.org/10.3390/universe7090351.

N. Inogamov and R. Sunyaev. Spread of matter over a neutron-star surface during disk accretion: Deceleration of rapid rotation. *Astronomy Letters - Journal of Astronomy and Space Astrophysics*, 36, Feb 2011. . URL https://doi.org/10.1134/S1063773710120029.

J. J. M. in't Zand, T. Bagnoli, C. D'Angelo, A. Patruno, D. K. Galloway, M. B. M. van der Klis, A. L. Watts, and H. L. Marshall. Chandra spectroscopy of Rapid Burster type-I X-ray bursts, 2017. URL https://doi.org/10.48550/arXiv.1703.07221.

N. K. Johnson-McDaniel and B. J. Owen. Maximum elastic deformations of relativistic stars. *Phys. Rev. D*, 88(4):044004, Aug 2013. . URL https://doi.org/10.1103%2Fphysrevd.88.044004.

D. I. Jones and N. Andersson. Freely precessing neutron stars: model and observations. *Monthly Notices of the Royal Astronomical Society*, 324(4):811–824, Jul 2001. . URL doi:10.1046/j.1365-8711.2001.04251.x.

D. I. Jones and N. Andersson. Gravitational waves from freely precessing neutron stars. *Monthly Notices of the Royal Astronomical Society*, 331(1):203–220, Mar 2002. . URL https://doi.org/10.1046/j.1365-8711.2002.05180.x.

A. Kamada and M. Yamada. Gravitational wave signals from short-lived topological defects in the MSSM. *Cosmology and Astrophysics*, 2015(10):021–021, Oct 2015. . URL https://doi.org/10.1088/1475-7516/2015/10/021.

D. Kasen, B. Metzger, J. Barnes, E. Quataert, and E. Ramirez-Ruiz. Origin of the heavy elements in binary neutron-star mergers from a gravitational-wave event. *Nature*, 551(7678):80–84, Oct 2017. . URL https://doi.org/10.1038/nature24453.

H. Khan. Superconductivity. In R. A. Meyers, editor, *Encyclopedia of Physical Science and Technology (Third Edition)*, pages 235–250. Academic Press, New York, third edition edition, 2003. ISBN 978-0-12-227410-7. . URL https://doi.org/10.1016/B0-12-227410-5/00749-3.

J. Kierzenka and L. F. Shampine. A BVP solver based on residual control and the maltab PSE. *ACM Trans. Math. Softw.*, 27(3):299–316, Sep 2001. ISSN 0098-3500. . URL https://doi.org/10.1145/502800.502801.

A. King, J.-P. Lasota, and M. Middleton. Ultraluminous X-ray sources. *New Astronomy Reviews*, 96:101672, Jun 2023. . URL https://doi.org/10.1016/j.newar.2022.101672.

K. D. Kokkotas and J. Ruoff. Instabilities of relativistic stars. In *2001: A Relativistic Spacetime Odyssey*. World Scientific, Jan 2003. . URL https://doi.org/10.1142/9789812791368_0019.

S. K. Lander and D. I. Jones. Magnetic fields in axisymmetric neutron stars. *Monthly Notices of the Royal Astronomical Society*, 395(4):2162–2176, Jun 2009. . URL https://doi.org/10.1111/j.1365-2966.2009.14667.x.

S. K. Lander, D. I. Jones, and A. Passamonti. Oscillations of rotating magnetized neutron stars with purely toroidal magnetic fields. *Monthly Notices of the Royal Astronomical Society*, Mar 2010. . URL https://doi.org/10.11112Fj.1365-2966.2010.16435.x.

J. Lattimer and M. Prakash. Neutron star observations: Prognosis for equation of state constraints. *Physics Reports*, 442(1-6):109–165, Apr 2007. ISSN 0370-1573. . URL http://dx.doi.org/10.1016/j.physrep.2007.02.003.

J. M. Lattimer, C. J. Pethick, M. Prakash, and P. Haensel. Direct URCA process in neutron stars. *Phys. Rev. Lett.*, 66:2701–2704, May 1991. . URL https://doi.org/10.1103/PhysRevLett.66.2701.

R. Lau, M. Beard, S. S. Gupta, H. Schatz, A. V. Afanasjev, E. F. Brown, A. Deibel, L. R. Gasques, G. W. Hitt, W. R. Hix, L. Keek, P. Möller, P. S. Shternin, A. W. Steiner, M. Wiescher, and Y. Xu. Nuclear Reactions in the Crusts of Accreting Neutron Stars. *Astrophys. J.*, 859(1): 62, May 2018. . URL https://doi.org/10.3847/1538-4357/aabfe0.

M. Y. Leung, A. K. L. Yip, P. C.-K. Cheong, and T. G. F. Li. Oscillations of highly magnetized non-rotating neutron stars. *Communications Physics*, 5(1), Dec 2022. . URL https://doi.org/10.1038/s42005-022-01112-w.

K. P. Levenfish and D. G. Yakovlev. Suppression of neutrino energy losses in reactions of direct URCA processes by superfluidity in neutron star nuclei. *Astronomy Letters*, 20(1):43–51, Jan 1994. URL https://ui.adsabs.harvard.edu/abs/1994AstL...20...43L.

K. P. Levenfish and D. G. Yakovlev. Standard and enhanced cooling of neutron stars with superfluid cores. *Astronomy Letters*, 22(1):49–57, Jan 1996. . URL https://ui.adsabs.harvard.edu/abs/1996AstL...22...49L.

Q. Z. Liu, J. van Paradijs, and E. P. J. van den Heuvel. A catalogue of low-mass X-ray binaries in the galaxy, LMC, and SMC (fourth edition). *Astron. Astrophys.*, 469(2):807–810, Apr 2007. . URL https://doi.org/10.1051/0004-6361:20077303.

M. Maggiore. *Gravitational Waves: Volume 1: Theory and Experiments*. Oxford University Press, Oct 2007. ISBN 9780198570745. . URL https://doi.org/10.1093/acprof:oso/9780198570745.001.0001.

M. Maggiore et al. Science case for the Einstein Telescope. *Journal of Cosmology and Astroparticle Physics*, 2020(03):050, Mar 2020. . URL https://dx.doi.org/10.1088/1475-7516/2020/03/050.

J. Margueron, H. Sagawa, and K. Hagino. Effective pairing interactions with isospin density dependence. *Phys. Rev. C*, 77(5):054309, May 2008. . URL https://doi.org/10.1103/PhysRevC.77.054309.

P. N. McDermott, H. M. van Horn, and C. J. Hansen. Nonradial Oscillations of Neutron Stars. *Astrophys. J.*, 325:725, Feb 1988. . URL https://doi.org/10.1086/166044.

Z. Medin and A. Cumming. Time-dependent, compositionally driven convection in the oceans of accreting neutron stars. *Astrophys. J.*, 802(1):29, Mar 2015. ISSN 1538-4357. . URL http://dx.doi.org/10.1088/0004-637X/802/1/29.

A. Melatos and D. J. B. Payne. Gravitational Radiation from an Accreting Millisecond Pulsar with a Magnetically Confined Mountain. *Astrophys. J.*, 623(2):1044–1050, Apr 2005. . URL https://doi.org/10.1086/428600.

A. B. Migdal. Superfluidity and the moments of inertia of nuclei. *Nuclear Physics*, 13(5):655–674, Nov 1959. . URL https://doi.org/10.1016/0029-5582(59)90264-0.

M. C. Miller et al. The Radius of PSR J0740+6620 from NICER and XMM-Newton Data. *Astrophys. J. Lett.*, 918(2):L28, Sep 2021. . URL https://doi.org/10.3847/2041-8213/ac089b.

J. A. Miralles, V. Urpin, and D. Konenkov. Joule Heating and the Thermal Evolution of Old Neutron Stars. *Astrophys. J.*, 503(1):368–373, Aug 1998. . URL https://doi.org/10.1086/305967.

C. W. Misner, K. S. Thorne, and J. A. Wheeler. *Gravitation*. W. H. Freeman, San Francisco, 1973. ISBN 978-0-7167-0344-0, 978-0-691-17779-3.

J. A. Morales and C. J. Horowitz. Neutron star crust can support a large ellipticity. *Monthly Notices of the Royal Astronomical Society*, 517(4):5610–5616, Oct 2022. . URL `https://doi.org/10.1093/mnras/stac3058`.

D. C. Morton. Neutron stars as X-ray sources. *Nature*, 201:1308–1309, 1964. URL `https://doi.org/10.1038/2011308a0`.

A. H. Mroué et al. Catalog of 174 binary black hole simulations for gravitational wave astronomy. *Phys. Rev. Lett.*, 111:241104, Dec 2013. . URL `https://doi.org/10.1103/PhysRevLett.111.241104`.

J. W. Negele and D. Vautherin. Neutron star matter at sub-nuclear densities. *Nucl. Phys. A.*, 207 (2):298–320, Jun 1973. . URL `https://ui.adsabs.harvard.edu/abs/1973NuPhA.207..298N`.

W. G. Newton. Neutron stars: A taste of pasta? *Nature Physics*, 9(7):396–397, Jul 2013. . URL `https://doi.org/10.1038/nphys2663`.

S. Ogata and S. Ichimaru. First-principles calculations of shear moduli for monte carlo–simulated coulomb solids. *Phys. Rev. A*, 42:4867–4870, Oct 1990. . URL `https://doi.org/10.1103/PhysRevA.42.4867`.

L. Ootes, D. Page, R. Wijnands, and N. Degenaar. Neutron star crust cooling in KS 1731-260: The influence of accretion outburst variability on the crustal temperature evolution. *Mon. Not. Roy. Astron. Soc.*, 461:4400–4405, Oct 2016. . URL `https://doi.org/10.1093/mnrasl/slw131`.

L. S. Ootes, R. Wijnands, D. Page, and N. Degenaar. A cooling neutron star crust after recurrent outbursts: modelling the accretion outburst history of Aql X-1. *Mon. Not. Roy. Astron. Soc.*, 477(3):2900–2916, Jul 2018. . URL `https://doi.org/10.1093/mnras/sty825`.

J. R. Oppenheimer and G. M. Volkoff. On massive neutron cores. *Phys. Rev.*, 55:374–381, Feb 1939. . URL `https://doi.org/10.1103/PhysRev.55.374`.

E. L. Osborne and D. I. Jones. Gravitational waves from magnetically induced thermal neutron star mountains. *Monthly Notices of the Royal Astronomical Society*, 494(2):2839–2850, Mar 2020. . URL `https://doi.org/10.1093/mnras/staa858`.

B. J. Owen. Maximum elastic deformations of compact stars with exotic equations of state. *Physical Review Letters*, 95(21), Nov 2005. ISSN 1079-7114. . URL `http://dx.doi.org/10.1103/PhysRevLett.95.211101`.

B. J. Owen and B. S. Sathyaprakash. Matched filtering of gravitational waves from inspiraling compact binaries: Computational cost and template placement. *Physical Review D*, 60(2), Jun 1999. . URL `https://doi.org/10.1103/PhysRevD.60.022002`.

D. Page. Thermal evolution of isolated neutron stars, 1997. URL `https://doi.org/10.48550/arXiv.astro-ph/9706259`.

D. Page and S. Reddy. Dense matter in compact stars: Theoretical developments and observational constraints. *Annual Review of Nuclear and Particle Science*, 56(1):327–374, Nov 2006. . URL `https://doi.org/10.1146/annurev.nucl.56.080805.140600`.

D. Page and S. Reddy. Forecasting neutron star temperatures: Predictability and variability. *Phys. Rev. Lett.*, 111(24), Dec 2013. . URL `https://doi.org/10.1103/PhysRevLett.111.241102`.

D. Page, U. Geppert, and F. Weber. The cooling of compact stars. *Nucl. Phys. A.*, 777:497–530, Oct 2006. . URL `https://doi.org/10.1016/j.nuclphysa.2005.09.019`.

D. Page, U. Geppert, and M. Küker. Cooling of neutron stars with strong toroidal magnetic fields. *Astrophysics and Space Science*, 308(1-4):403–412, Mar 2007. . URL `https://doi.org/10.1007/s10509-007-9316-z`.

J. Papaloizou and J. E. Pringle. Non-radial oscillations of rotating stars and their relevance to the short-period oscillations of cataclysmic variables. *Mon. Not. Roy. Astron. Soc.*, 182: 423–442, Feb 1978. . URL `https://doi.org/10.1093/mnras/182.3.423`.

A. Patruno, B. Haskell, and C. D'Angelo. Graviational waves and the maximum spin frequency of neutron stars. *The Astrophysical Journal*, 746(1):9, Jan 2012. . URL `https://doi.org/10.1088%2F0004-637x%2F746%2F1%2F9`.

A. Patruno, B. Haskell, and N. Andersson. The spin distribution of fast-spinning neutron stars in low-mass x-ray binaries: Evidence for two subpopulations. *The Astrophysical Journal*, 850(1):106, Nov 2017. ISSN 1538-4357. . URL `http://dx.doi.org/10.3847/1538-4357/aa927a`.

D. J. B. Payne and A. Melatos. Burial of the polar magnetic field of an accreting neutron star - I. Self-consistent analytic and numerical equilibria. *Mon. Not. Roy. Astron. Soc.*, 351(2):569–584, Jun 2004. . URL `https://doi.org/10.1111/j.1365-2966.2004.07798.x`.

J. M. Pearson, S. Goriely, and N. Chamel. Properties of the outer crust of neutron stars from Hartree-Fock-Bogoliubov mass models. *Phys. Rev. C*, 83(6):065810, Jun 2011. . URL `https://doi.org/10.1103/PhysRevC.83.065810`.

J. M. Pearson, N. Chamel, S. Goriely, and C. Ducoin. Inner crust of neutron stars with mass-fitted Skyrme functionals. *Phys. Rev. C*, 85(6):065803, Jun 2012. . URL `https://doi.org/10.1103/PhysRevC.85.065803`.

F. A. E. Pirani. On the physical significance of the Riemann tensor. *Acta Physica Polonica*, 15: 389–405, Jan 1956. URL `https://doi.org/10.1007/s10714-009-0787-9`.

H. Poincaré. Sur la dynamique de l' electron. *Comptes Rendus de l'Academie des Sciences*, page 1504–1508, Jul 1905. URL `https://doi.org/10.1007/bf03013466`.

J. A. Pons and U. Geppert. Magnetic field dissipation in neutron star crusts: from magnetars to isolated neutron stars. *Astron. Astrophys.*, 470(1):303–315, Jul 2007. . URL `https://doi.org/10.1051/0004-6361:20077456`.

A. Y. Potekhin, D. A. Baiko, P. Haensel, and D. G. Yakovlev. Transport properties of degenerate electrons in neutron star envelopes and white dwarf cores. *Astron. Astrophys.*, 346:345–353, Jun 1999. . URL `https://ui.adsabs.harvard.edu/abs/1999A&A...346..345P`.

A. Y. Potekhin, A. F. Fantina, N. Chamel, J. M. Pearson, and S. Goriely. Analytical representations of unified equations of state for neutron-star matter. *Astron. Astrophys.*, 560:A48, Dec 2013. . URL `https://doi.org/10.1051/0004-6361/201321697`.

A. Y. Potekhin, J. A. Pons, and D. Page. Neutron stars—cooling and transport. *Space Science Reviews*, 191(1-4):239–291, Jul 2015. . URL `https://doi.org/10.1007/s11214-015-0180-9`.

A. Y. Potekhin, M. E. Gusakov, and A. I. Chugunov. Thermal evolution of neutron stars in soft x-ray transients with thermodynamically consistent models of the accreted crust. *Mon. Not. Roy. Astron. Soc.*, 522(4):4830–4840, May 2023. . URL `https://doi.org/10.1093%2Fmnras%2Fstad1309`.

D. Radice, V. Morozova, A. Burrows, D. Vartanyan, and H. Nagakura. Characterizing the gravitational wave signal from core-collapse supernovae. *The Astrophysical Journal*, 876 (1):L9, Apr 2019. . URL `https://doi.org/10.3847/2041-8213/ab191a`.

K.-H. Rädler, H. Fuchs, U. Geppert, M. Rheinhardt, and T. Zannias. General-relativistic free decay of magnetic fields in a spherically symmetric body. *Phys. Rev. D*, 64:083008, Sep 2001. . URL `https://doi.org/10.1103/PhysRevD.64.083008`.

B. Rajbhandari, B. J. Owen, S. Caride, and R. Inta. First searches for gravitational waves from r-modes of the crab pulsar. *Physical Review D*, 104(12), Dec 2021. . URL `https://doi.org/10.1103/PhysRevD.104.122008`.

V. Raymond. *Parameter estimation using markov chain monte carlo methods for gravitational waves from spinning inspirals of compact objects*. PhD thesis, Northwestern University, May 2012.

T. E. Riley et al. A NICER view of the massive pulsar PSR J0740+6620 informed by radio timing and XMM-newton spectroscopy. *Astrophys. J. Lett.*, 918(2):L27, Sep 2021. . URL `https://doi.org/10.3847/2041-8213/ac0a81`.

P. H. B. Rossetto, J. Frauendiener, R. Brunet, and A. Melatos. Magnetically confined mountains on accreting neutron stars in general relativity. *Monthly Notices of the Royal Astronomical Society*, page stad2850, Sep 2023. . URL `https://doi.org/10.1093/mnras/stad2850`.

S. B. Rüster, M. Hempel, and J. Schaffner-Bielich. Outer crust of nonaccreting cold neutron stars. *Phys. Rev. C*, 73:035804, Mar 2006. . URL https://doi.org/10.1103/PhysRevC.73.035804.

R. E. Rutledge, L. Bildsten, E. F. Brown, G. G. Pavlov, V. E. Zavlin, and G. Ushomirsky. Crustal emission and the quiescent spectrum of the neutron star in KS 1731-260. *The Astrophysical Journal*, 580(1):413–422, Nov 2002. . URL https://doi.org/10.1086/342745.

T. D. Salvo and A. Sanna. *Accretion Powered X-ray Millisecond Pulsars*, pages 87–124. Springer International Publishing, 2022. . URL https://doi.org/10.1007/978-3-030-85198-9_4.

H. Schatz, L. Bildsten, A. Cumming, and M. Wiescher. The Rapid Proton Process Ashes from Stable Nuclear Burning on an Accreting Neutron Star. *Astrophys. J.*, 524(2):1014–1029, Oct 1999. . URL https://doi.org/10.1086/307837.

H. Schatz, A. Aprahamian, V. Barnard, L. Bildsten, A. Cumming, M. Ouellette, T. Rauscher, F.-K. Thielemann, and M. Wiescher. End point of the *rp* process on accreting neutron stars. *Phys. Rev. Lett.*, 86:3471–3474, Apr 2001. . URL https://doi.org/10.1103/PhysRevLett.86.3471.

H. Schatz, Z. Meisel, E. F. Brown, S. S. Gupta, G. W. Hitt, W. R. Hix, R. Jain, R. Lau, P. Möller, W. J. Ong, P. S. Shternin, Y. Xu, and M. Wiescher. The impact of neutron transfer reactions on the heating and cooling of accreted neutron star crusts. *Astrophys. J.*, 925(2):205, Feb 2022. . URL https://doi.org/10.3847/1538-4357/ac4271.

A. Schwenk, B. Friman, and G. E. Brown. Renormalization Group Methods for the Nuclear Many-Body Problem. *arXiv e-prints*, art. nucl-th/0302081, Feb 2003. URL https://doi.org/10.48550/arXiv.nucl-th/0302081.

S. L. Shapiro and S. A. Teukolsky. *Cold Equation of State Above Neutron Drip*, chapter 8, pages 188–240. John Wiley & Sons, Ltd, 1983. ISBN 9783527617661. . URL https://onlinelibrary.wiley.com/doi/abs/10.1002/9783527617661.ch8.

N. N. Shchechilin and A. I. Chugunov. Crust of accreting neutron stars within simplified reaction network. *Mon. Not. Roy. Astron. Soc.*, 490(3):3454–3463, Dec 2019. . URL https://doi.org/10.1093/mnras/stz2838.

P. S. Shternin and D. G. Yakovlev. Electron-muon heat conduction in neutron star cores via the exchange of transverse plasmons. *Phys. Rev. D*, 75:103004, May 2007. . URL https://link.aps.org/doi/10.1103/PhysRevD.75.103004.

P. S. Shternin, D. G. Yakovlev, C. O. Heinke, W. C. G. Ho, and D. J. Patnaude. Cooling neutron star in the Cassiopeia A supernova remnant: evidence for superfluidity in the core. *Monthly Notices of the Royal Astronomical Society: Letters*, 412(1):L108–L112, Feb 2011. . URL https://doi.org/10.1111/j.1745-3933.2011.01015.x.

N. Singh, B. Haskell, D. Mukherjee, and T. Bulik. Asymmetric accretion and thermal 'mountains' in magnetized neutron star crusts. *Monthly Notices of the Royal Astronomical Society*, 493 (3):3866–3878, Feb 2020. . URL https://doi.org/10.1093/mnras/staa442.

J. R. Stone and P. G. Reinhard. The Skyrme interaction in finite nuclei and nuclear matter. *Progress in Particle and Nuclear Physics*, 58(2):587–657, Apr 2007. . URL https://doi.org/10.1016/j.ppnp.2006.07.001.

L. Suleiman, M. Fortin, J. L. Zdunik, and P. Haensel. Influence of the crust on the neutron star macrophysical quantities and universal relations. *Phys. Rev. C*, 104:015801, Jul 2021. . URL https://doi.org/10.1103/PhysRevC.104.015801.

A. G. Suvorov and A. Melatos. Relaxation by thermal conduction of a magnetically confined mountain on an accreting neutron star. *Monthly Notices of the Royal Astronomical Society*, 484(1):1079–1099, Dec 2018. . URL https://doi.org/10.1093/mnras/sty3518.

T. Takatsuka and R. Tamagaki. Baryon superfluidity and neutrino emissivity of neutron stars. *Progress of Theoretical Physics*, 112(1):37–72, Jul 2004. . URL https://doi.org/10.1143/PTP.112.37.

R. Tamagaki. Superfluid State in Neutron Star Matter. I: Generalized Bogoliubov Transformation and Existence of 3P2 Gap at High Density*). *Progress of Theoretical Physics*, 44(4):905–928, Oct 1970. ISSN 0033-068X. . URL https://doi.org/10.1143/PTP.44.905.

J. H. Taylor and J. M. Weisberg. A new test of general relativity - Gravitational radiation and the binary pulsar PSR 1913+16. *Astrophys. J.*, 253:908–920, Feb 1982. . URL https://ui.adsabs.harvard.edu/abs/1982ApJ...253..908T.

J. H. Taylor, L. A. Fowler, and P. M. McCulloch. Measurements of general relativistic effects in the binary pulsar PSR1913+16. *Nature*, 277(5696):437–440, Feb 1979. . URL https://doi.org/10.1038/277437a0.

K. S. Thorne. The General Relativistic Theory of Stellar Structure and Dynamics. In C. Dewitt, E. Schatzman, and P. Véron, editors, *High Energy Astrophysics, Volume 3*, volume 3, page V, Jan 1967.

K. S. Thorne. The relativistic equations of stellar structure and evolution. *Astrophys. J.*, 212: 825–831, Mar 1977. . URL https://ui.adsabs.harvard.edu/abs/1977ApJ...212..825T.

R. C. Tolman. Static solutions of einstein's field equations for spheres of fluid. *Phys. Rev.*, 55: 364–373, Feb 1939. . URL https://doi.org/10.1103/PhysRev.55.364.

S. Tsuruta and A. G. W. Cameron. Cooling and detectability of neutron stars. *Canadian Journal of Physics*, 44:1863, Jan 1966. . URL https://doi.org/10.1016/0370-1573(79)90033-4.

G. Ushomirsky, C. Cutler, and L. Bildsten. Deformations of accreting neutron star crusts and gravitational wave emission. *Mon. Not. Roy. Astron. Soc.*, 319(3):902–932, Dec 2000. . URL `https://doi.org/10.1046/j.1365-8711.2000.03938.x`.

M. Vigelius and A. Melatos. Improved estimate of the detectability of gravitational radiation from a magnetically confined mountain on an accreting neutron star. *Mon. Not. Roy. Astron. Soc.*, 395(4):1972–1984, Jun 2009. . URL `https://doi.org/10.1111/j.1365-2966.2009.14690.x`.

R. V. Wagoner. Gravitational radiation from accreting neutron stars. *Astrophys. J.*, 278:345–348, Mar 1984. . URL `https://ui.adsabs.harvard.edu/abs/1984ApJ...278..345W`.

M. Wang, G. Audi, F. G. Kondev, W. J. Huang, S. Naimi, and X. Xu. The AME2016 atomic mass evaluation (II). Tables, graphs and references. *Chinese Physics C*, 41(3):030003, Mar 2017. . URL `https://doi.org/10.1088/1674-1137/41/3/030003`.

J. Weber. Evidence for discovery of gravitational radiation. *Phys. Rev. Lett.*, 22:1320–1324, Jun 1969. . URL `https://doi.org/10.1103/PhysRevLett.22.1320`.

J. M. Weisberg and J. H. Taylor. Relativistic binary pulsar B1913+16: Thirty years of observations and analysis, 2004. URL `https://ui.adsabs.harvard.edu/abs/2005ASPC..328...25W`.

R. Wijnands. Crust cooling curves of accretion-heated neutron stars. *arXiv: Astrophysics*, 2004. URL `https://doi.org/10.48550/arXiv.astro-ph/0405089`.

R. Wijnands, N. Degenaar, and D. Page. Cooling of Accretion-Heated Neutron Stars. *J. Astrophys. Astron.*, 38:49, 2017. .

G. Woan, M. D. Pitkin, B. Haskell, D. I. Jones, and P. D. Lasky. Evidence for a minimum ellipticity in millisecond pulsars. *The Astrophysical Journal*, 863(2):L40, Aug 2018. . URL `https://doi.org/10.3847/2041-8213/aad86a`.

R. A. Wolf. Some Effects of the Strong Interactions on the Properties of Neutron-Star Matter. *Astrophys. J.*, 145:834, Sep 1966. . URL `https://ui.adsabs.harvard.edu/abs/1966ApJ...145..834W`.

D. Yakovlev. Neutrino emission from neutron stars. *Physics Reports*, 354(1-2):1–155, Nov 2001. . URL `https://doi.org/10.1016/S0370-1573(00)00131-9`.

D. G. Yakovlev and A. D. Kaminker. Neutrino-pair emission due to electron-phonon scattering in a neutron-star crust. *Astronomy Letters*, 22(4):491–498, Jul 1996. URL `https://ui.adsabs.harvard.edu/abs/1996AstL...22..491Y`.

D. G. Yakovlev and K. P. Levenfish. Modified URCA process in neutron star cores. *Astron. Astrophys.*, 297:717, May 1995. URL `https://ui.adsabs.harvard.edu/abs/1995A&A...297..717Y`.

D. G. Yakovlev and V. A. Urpin. Thermal and Electrical Conductivity in White Dwarfs and Neutron Stars. , 24:303, Jun 1980.

D. G. Yakovlev, A. D. Kaminker, and K. P. Levenfish. Neutrino emission due to Cooper pairing of nucleons in cooling neutron stars. *Astron. Astrophys.*, 343:650–660, Mar 1999. . URL `https://ui.adsabs.harvard.edu/abs/1999A&A...343..650Y`.

J. L. Zdunik, M. Bejger, and P. Haensel. Deformation and crustal rigidity of rotating neutron stars. *Astron. Astrophys.*, 491(2):489–498, Oct 2008. . URL `https://doi.org/10.1051/0004-6361:200810183`.

S. Zhou, E. Gügercinoğlu, J. Yuan, M. Ge, and C. Yu. Pulsar glitches: A review, 2022. URL `https://doi.org/10.48550/arXiv.2211.13885`.

M. Zimmermann. Gravitational waves from rotating and precessing rigid bodies. II. General solutions and computationally useful formulas. *Phys. Rev. D*, 21(4):891–898, Feb 1980. . URL `https://doi.org/10.1103/PhysRevD.21.891`.

M. Zimmermann and E. Szedenits. Gravitational waves from rotating and precessing rigid bodies: Simple models and applications to pulsars. *Phys. Rev. D*, 20:351–355, Jul 1979. . URL `https://doi.org/10.1103/PhysRevD.20.351`.